ISBN: 978-94-028-1658-7

Transverse pressure effect on superconducting Nb_3Sn Rutherford and *Re*BCO Roebel cables for accelerator magnets Peng Gao 2019

Transverse pressure effect on superconducting Nb_3Sn Rutherford and *Re*BCO Roebel cables for accelerator magnets

PENG GAO

INVITATION

You are cordially invited to the public defence of my PhD thesis entitled:

Transverse pressure effect on superconducting Nb_3Sn Rutherford and *Re*BCO Roebel cables for accelerator magnets

on Wednesday September 18, 2019 at 16:45 in Prof. Dr. G. Berkhoff zaal (Waaier 4) University of Twente.

A brief introduction to the thesis will be given at 16:30.

A reception will follow immediately after the ceremony.

Peng Gao
p.gao@utwente.nl

Paranymphs:
Cris Vermeer
Wanshu Zhang

534875-L-os-Gao

Processed on: 30-8-2019

TRANSVERSE PRESSURE EFFECT ON SUPERCONDUCTING Nb_3Sn RUTHERFORD AND *Re*BCO ROEBEL CABLES FOR ACCELERATOR MAGNETS

Peng Gao

September 18, 2019

Dissertation Graduation Committee:

Chairman:	Prof. dr. J. L. Herek	University of Twente, TNW
Supervisor:	Prof. dr. ir. H. H. J. ten Kate	University of Twente, TNW
Co-supervisor:	Dr. M. M. J. Dhallé	University of Twente, TNW
Co-supervisor:	Dr. A. Kario	GSI Darmstadt
Referee:	Dr. A. Ballarino	CERN, Geneve
Members:	Prof. dr. ir. H. J. M. ter Brake	University of Twente, TNW
	Prof. dr. ing. B. van Eijk	University of Twente, TNW
	Prof. dr. ir. R. Akkerman	University of Twente, ET
	Prof. dr. R. Ross	Delft University of Technology
	Prof. dr. C. Senatore	University of Geneve

The research described in this thesis was carried out at the University of Twente, Faculty of Science and Technology, chair of Industrial Application of Superconductivity and chair Energy-Materials-Systems, Enschede, The Netherlands.

Cover composed of 2 pictures: Nb_3Sn Rutherford (courtesy of Fermilab) and Bruker tape based *Re*BCO Roebel cables (courtesy of A. Kario).

Transverse pressure effect on superconducting Nb_3Sn Rutherford and *Re*BCO Roebel cables for accelerator magnets
Publisher: P. Gao
Ph.D. thesis, University of Twente, The Netherlands

ISBN: 978-94-028-1658-7
Printed by Ipskamp Printing, Enschede, The Netherlands
©P. Gao, Enschede, 2019, The Netherlands. All rights reserved. No parts of this thesis may be reproduced, stored in a retrieval system or transmitted in any form or by any means without permission of the author.

TRANSVERSE PRESSURE EFFECT ON SUPERCONDUCTING Nb_3Sn RUTHERFORD AND *Re*BCO ROEBEL CABLES FOR ACCELERATOR MAGNETS

DISSERTATION

to obtain
the degree of doctor at the University of Twente,
on the authority of the rector magnificus,
prof. dr. T. T. M. Palstra,
on account of the decision of the Doctorate Board,
to be publicly defended
on Wednesday 18th of September 2019 at 16:45

by

Peng Gao

born on the 7th of January 1987
in Shanxi, China

This dissertation has been approved by:

Supervisor:	Prof. dr. ir. H. H. J. ten Kate
Co-supervisor:	Dr. M. M. J. Dhallé
Co-supervisor:	Dr. A. Kario

To my beloved wife, Zunyu
and my parents

Contents

Chapter 1
Introduction

In this introductory chapter, the research described in the thesis is briefly framed and justified. In Section 1.1 how and why the ever increasing particle collision energy asked for by the high-energy physics community requires bending- and focusing magnets that generate higher magnetic fields are sketched. In Section 1.2, the superconducting materials that can, in principle, deliver such fields in state-of-the-art and future accelerators are introduced. In Section 1.3 the investigated central question is sketched: the increase in magnetic field causes a quadratic increase in mechanical stress on the superconductors, whose properties are intrinsically sensitive to mechanical strain. Section 1.4, finally, the main research questions are formulated and the lay-out of the thesis is described.

1.1 Introduction

Ever since the successful commissioning of the 'Energy Doubler' [1] at the Fermilab Tevatron in 1983 [2], which was the first circular collider retrofitted with superconducting magnets, the development of superconducting- and particle-accelerator technology have become increasingly intertwined [3]. Today, in the Large Hadron Collider (LHC) at CERN, more than 10000 superfluid helium-cooled superconducting magnets are used to steer, shape and control the counter-rotating proton-antiproton beams [4] as well as to help detect and identify the collision products [5].

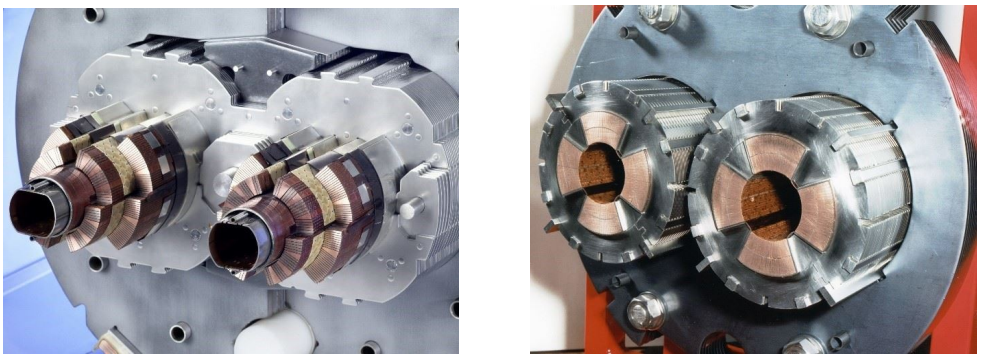

(a) **(b)**

Figure 1.1: *Worked-open cross-sections of the NbTi twin dipole (a, image from* [6]*) and quadrupole (b, image from* [7]*) magnets used in the LHC. Both magnet types have a cold mass that consists of a common iron yoke, collars, main winding packs comprising cables and spacers and beam pipes* [8, 9].

The focus in this thesis is on the superconducting cables used to wind the dipole and quadrupole magnets that bend and focus particle beams, as shown in Figure 1.1. Especially for these magnets, high magnetic fields and high current densities are key. The reason is shown by Equation (1.1) and in Figure 1.2:

$$BR\ (Tm) = \frac{10}{2.998} E\ (GeV). \tag{1.1}$$

The equation is valid for relativistic particles with an electric charge ±e [10]. B is the magnetic field generated by the bending dipoles at the position of the beam, R the radius of a circular collider and E the ultimate energy of the accelerated particles. The drive towards higher B is explained by the decrease in size and hence cost of the accelerator that it allows. Indeed, the equation straightforwardly shows that the cost of engineering works, e.g. the construction of a tunnel, is inversely proportional to the magnetic field. The same holds for the number of bending magnets.

However, a higher B also implies that more ampere-turns are needed per magnet. For a given current density, the winding pack thickness increases linearly with B [10], so that the volume of the winding pack, and hence of the superconducting material, increases as B^2. Taking the engineering and superconductor costs together, this means that there is an optimum field B in terms of cost-effectiveness of a circular accelerator [11]. The relation between critical current density J_c and magnetic field, as shown in Section 1.2, further complicates matters, but Figure 1.2, which surveys some past, present and planned circular accelerators in terms of their bending field and accelerator radius, clearly shows a trendline in which increasing particle energy

E is accompanied by an increase in bending field B, roughly as $B \sim E^{1/3}$.

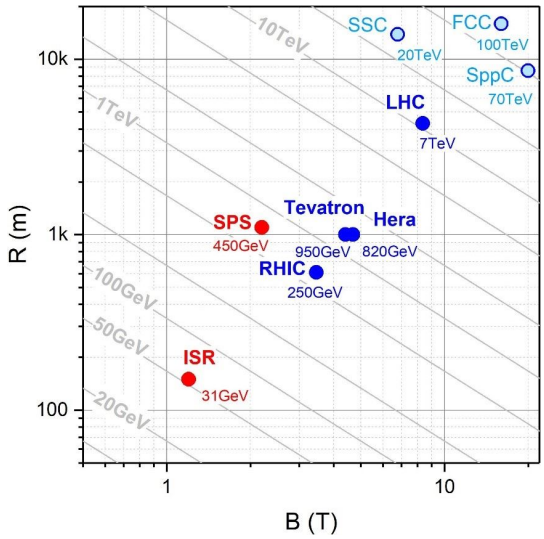

Figure 1.2: *Radius R and bending-dipole field B for some circular accelerators. Red symbols denote machines that rely on copper dipole magnets (ISR* [12] *and SPS* [13]*), blue ones indicate superconducting machines (RHIC* [14], *Tevatron* [1]*, Hera* [15] *and LHC* [8]*). The open symbols indicate projects that were halted (SSC* [16]*) or are still in an early design phase (FCC* [17] *and SppC* [18]*). The grey diagonal lines are particle energy contours calculated with* Equation (1.1).

In this chapter we briefly discuss what this call for higher magnetic fields implies in terms of superconducting material- and cable choices, as shown in Section 1.2, and why these materials are expected to be impacted by the higher transverse pressure levels in such magnets, as shown in Section 1.3. Finally, in Section 1.4, the main research questions are formulated that steered the research described in this thesis and present the thesis lay-out.

1.2 Future accelerators

With LHC now several years in successful operation and seeing that the realization of a new collider typically involves a time-span of 20 years or more [19], the high-energy physics community is thinking ahead towards future machines. Arguably the most publicised success of LHC has been the deepened validation of the Standard Model with the discovery of the Higgs boson [20, 21], but the further detailed study of this particle's interactions as well as the search for answers to open questions such as the nature of dark matter and - energy or the origin of the matter/antimatter asymmetry call for even higher energies [22].

However, as illustrated in Figures 1.3 and 1.4, the bending magnets in the accelerators that enable such energies will necessarily have to rely on other superconductors than NbTi. The target fields and non-copper critical current densities of selected accelerator designs from Figures 1.2 and 1.3 are summarized in Table 1.1. NbTi, with an upper critical field B_{c2} of 13.1 to 13.5 T at 1.9 K [23], is simply no longer superconducting at the fields required by the future machine designs. Instead, the bending magnets in these colliders will need to be wound with Nb_3Sn or with one of the ceramic High Temperature Superconducting (HTS) materials.

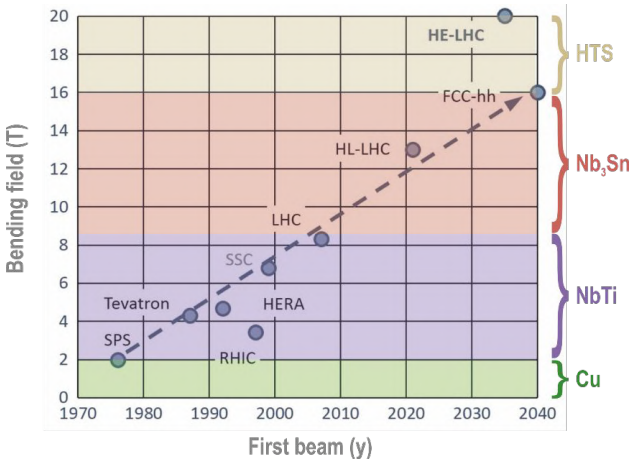

Figure 1.3: *Evolution of bending field strength in circular accelerators. The plot is taken from* [19]*, colouring and conductor material choices have been added. Precise boundaries between materials are indicative only.*

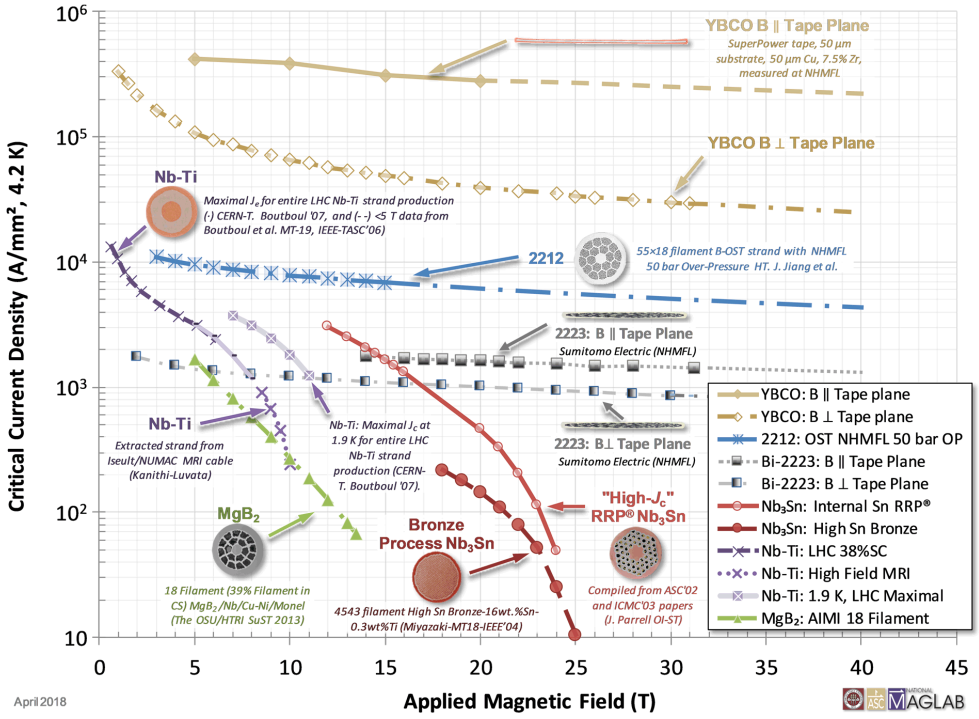

Figure 1.4: *Critical current density versus magnetic field of various state-of-the-art commercial grade superconducting materials, reported, unless stated otherwise, at 4.2 K. The plot is taken from* [24].

Nb_3Sn, with B_{c2} values in the range of about 26 to 28 T at 1.9 K and of about 24 to 26 T at 4.2 K, depending on the precise wire composition and on the manufacturing process, [26] does allow to construct magnets that generate fields well above 10 T. The high-magnetic-field critical cur-

Table 1.1: Magnetic field- and critical current density targets of the bending magnets in selected collider designs.

Collider	Material	Temperature (K)	Magnetic field (T)	J_c (A/mm^2)	Source
LHC	NbTi	1.9	8.33	2400	[25]
HL-LHC	Nb_3Sn	1.9	16	1000	[17]
FCC	Nb_3Sn	1.9	16	1500	[17]
HE-LHC	HTS	4.2	20	50000	[19]
SppC	Nb_3Sn + HTS	4.2	15 20	1500 1300	[18]

rent density that can be achieved in Nb_3Sn wires depends on their detailed composition and on magnetic flux pinning [27]. 'Bronze' wire technology, where during the reaction heat treatment Sn needs to diffuse from the metal matrix into the filaments, leads to significant spatial gradients in the tin composition x throughout the Nb_3Sn_{1-x} filaments, with part of the material having less-than-optimal properties [28]. This problem was circumvented with the 'Internal Tin' [29] and 'Powder-in-Tube' [30] wire production processes, where the tin is brought in much closer proximity of the Nb in the unreacted wires and compositional variations in the final filaments are thus strongly reduced. Both processes have meanwhile been developed into industrial manufacturing techniques [31, 32] producing wires with high-field J_c values well exceeding those of bronze technology, see Figure 1.4. Note that the 'Restacked-Rod-Process' (RRP) is a descendant of the Internal Tin method). Indeed, the first Nb_3Sn wide-bore dipole magnet generating a field well above 10 T was realized with this type of wire [33].

The Nb_3Sn cables presented in Chapter 4 of this thesis are based on such RRP and PIT strands that are further introduced in Section 2.5. It should be noted that state-of-the-art Nb_3Sn technology meets the requirements for HL-LHC in Table 1.1, see Figure 1.4, but not quite yet those for FCC. However, recent developments seem to indicate that there is still room for improvement. Present commercial Nb_3Sn wires rely on compositional control and doping with Ta or Ti to ensure a high B_{c2}-value and on grain-boundary pinning to increase J_c values [34]. Internal oxidation of ternary material doped additionally with Zr not only further refines the Nb_3Sn grains but also forms finely distributed ceramic ZrO_2 particles that act as artificial pinning centers [35].

As Figures 1.3 and 1.4 show, accelerator designs going beyond about 16 T will need to rely on HTS materials, at least for the inner magnet windings that are exposed to the highest magnetic fields. Although it is a robust conductor that is readily available in long lengths [36], $Bi_2Sr_2Ca_2Cu_3O_{10}$ (Bi-2223) is a less-likely candidate material because its multifilamentary tape structure does not allow for the compact cabling which is one of the prerequisites of accelerator magnet technology (see below). Bi-2212, on the other hand, has a similar high irreversibility field B_{irr} at low temperatures (B_{irr} is the magnetic field at which pinning becomes ineffective and J_c becomes zero) [37] and can be melt-processed [38] in the form of reinforced multifilamentary round wires [39] with low filament porosity and the high degree of grain-to-grain connectivity [40] that is needed to achieve high J_c values in HTS. Especially with heat-treatments in pressurized oxygen, current densities far exceeding the target values of Table 1.1 have been demonstrated [41]. This has spurred an active programme aimed at high-field NMR [42] and accelerator magnets [43–45]. However, with the focus of this program mainly situated in the US [19], in this thesis Bi-2212 is not investigated.

One of the main advantages of Bi-2212 round wires in an accelerator context is the possibility to bundle them in a Rutherford-type cable, since accelerators require cables [3]. In order to keep the bending magnets synchronised during the ramp-up of the beam energy, typically several tens of them are energized in series. Such a string of magnets constitutes a sizeable self-inductance and to keep induced voltages manageable during ramping, especially during emergency powering-down following a quench, the number of turns in the windings must be kept low. This is achieved by using cables that typically carry 10 to 20 kA. Furthermore, to keep the cost of the bending and focussing magnets acceptable, it is essential that the field-generating current flows as close as possible to the beam pipe and hence that the overall ('engineering') current density in the winding pack approaches as much as possible the engineering current density in the wires. This implies that the cables must be highly compacted and that it must be possible to stack them efficiently. Already the NbTi-based magnets in the Thevatron were therefore assembled with a Rutherford-type cable [1], essentially a straightforwardly round twisted-strand cable that is passed through a Turks head roller to deform it into a rectangular shape and to compact it to a typical density of about 90% [3]. The layout of the Nb_3Sn Rutherford cables studied in this thesis is presented in Chapter 2.

Re$Ba_2Cu_3O_7$ (*Re*BCO, where *Re* stands for a rare-earth element such as Y or Gd) is a second HTS material that can be assembled into a compact rectangular cable. The development of *Re*BCO conductors is a remarkable story of science and technology feeding back into each other [46, 47], starting in the late eighties with thin film deposition at highly specialized research labs and maturing into the present production of hundreds of meters long piece-lengths with tightly controlled properties commercialized by some ten manufacturers. Several manufacturers already realize the requirements in Table 1.1, offering J_c-values in the range 40 to 50 kA/mm^2 in magnetic fields of 20 T and at a temperature of 4.2 K [48].

By punching coated conductors (CC) into meandering zig-zag ribbon-shaped 'strands' and by interlacing several of these strands together, *Re*BCO cabled structures can be made of typically 10 to 20 strands that, just like the Rutherford cables assembled from round NbTi, Nb_3Sn or Bi-2212 strands, carry currents of the order of 10 kA, have a rectangular cross-section with a packing density close to 90% and in which the strands are fully transposed [49]. Transposition means that each strand experiences the same electro-magnetic environment over one transposition 'pitch' length, which helps to ensure a uniform current distribution among them. This 'Roebel bar' concept of a transposed multi-strand conductor is well-known in the electrotechnical community, where it is used for exactly the same reason. The further development of *Re*BCO Roebel cables has been rapid [50]. Their production has been quasi-automized [51] and can be combined with other CC processing techniques such as striation into filaments to reduce AC loss [52]. Demonstrated or envisaged application areas range from transformers [53] over electrical aircraft [54] and accelerator magnets [55] as shown in Figure 1.5, to fusion magnets [56].

Figure 1.5: *Picture of the 720 mm long HTS dipole coils Feather-M2.1-2, wound with ReBCO Roebel cable within the frame of the European EUCARD-2 collaboration* [19]. *The picture is taken from* [55].

1.3 Transverse pressure in accelerator magnets

In Figure 1.6 the cross sectional lay-outs of the winding packs of several existing or designed bending dipole magnets are shown. Classically, the winding pack of a long dipole is laid out to approach a 'cosine theta' current distribution, with θ the azimuthal position of an axial current line. For a mathematically perfect cosθ distribution, the field B in the aperture is perfectly homogeneous. In reality, the cables are laid out in 'sectors' that are spaced by wedges [57]. For ease of stacking, the Rutherford cables discussed in Section 1.2 are often key-stoned, i.e. they are not exactly rectangular but have one side slightly thicker than the other. The Lorentz force on the conductors has radial and azimuthal components. The radial components are reacted against a collar, a steel or high-strength aluminium laminated cylindrical structure that tightly encloses the winding pack, as shown in Figure 1.1 and keeps it together. The azimuthal stresses, on the other hand, accumulate on the azimuthal midplane $\theta = 0$ and put the cables at this position under significant transverse compression. In principle, the magnitude of these stresses can be estimated analytically [58, 59], but usually they are calculated numerically because the detailed magnet structure quickly becomes complicated [60]. Moreover, numerical modelling allows to incorporate effects of the compressive pre-stress that is typically applied during assembly as well as the thermal stresses that accumulate during cool-down [61]. Modelled stresses on the azimuthal midplane of the designs shown in Figure 1.6 are reported in Table 1.2 and summarized in Figure 1.7.

Table 1.2: Modelled transverse peak pressure on the cables of selected high-field magnet designs.

Collider	Material	Magnetic field (T)	Pressure (MPa)	Design	Institute	Source
LHC	NbTi	8.33	62	cosθ	CERN	[62]
HL-LHC	Nb_3Sn	12	124	cosθ	CERN	[63]
HL-LHC	Nb_3Sn	12	124	cosθ	FNAL	[69]
FCC	Nb_3Sn	15	170	cosθ	FNAL	[65]
FCC	Nb_3Sn	16	135	canted-cosθ-coil	PSI	[68]
FCC	Nb_3Sn	16	155	common-coil	CIEMAT	[67]
FCC	Nb_3Sn	16	180	cosθ	INFN	[64]
FCC	Nb_3Sn	16	194	block-coil	CEA	[66]
FCC	Nb_3Sn	17	224	cosθ	CERN	[70]
HE-LHC	*Re*BCO	17	220	aligned block	FNAL	[65]

The dashed line in Figure 1.7 indicates a quadratic $\sigma(B)$ relation, with σ the transverse peak pressure on the cables, normalized to coincide with the reported LHC dipole values. The modelled peak stress roughly follows this behaviour, as might be expected since the Lorentz force scales as $I \times B$, with I the current, and the magnetic field B itself is also proportional to I. Nevertheless, the 16 T designs fall below this LHC extrapolation, especially the CIEMAT common coil and PSI canted-cosine-theta designs.

Based on modelling predictions, it can be stated that the nominal transverse pressure range for Nb_3Sn dipoles generating a bending field of 11 T may be expected to lie in the range of 100 to 150 MPa; for Nb_3Sn at 16 T between 150 and 200 MPa; and for future HTS inserts in 20 T class magnets between 250 and 300 MPa. To put these values into perspective, they easily exceed the elastic-to-plastic limit of most annealed pure metals and approach it even for several of the hardened alloys that are commonly applied in these magnet [71]. The important question that then arises is whether the superconducting materials that were introduced

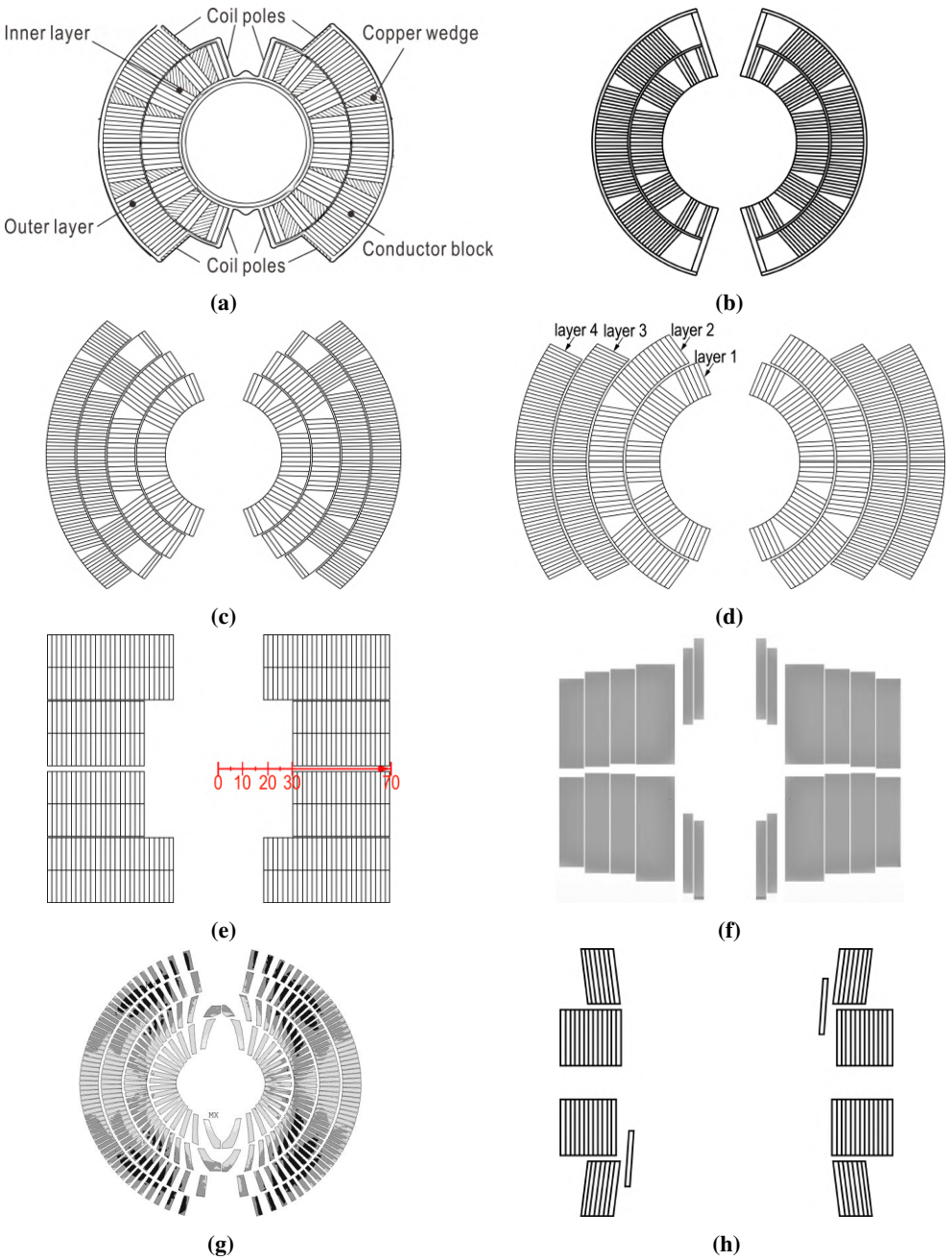

Figure 1.6: *Schematic cross-sectional layouts of the windings packs of various dipole magnets. The picture is compiled from various publications: (a) LHC 8.3 T NbTi cos-theta magnet* [62]*; (b) HL-LHC 11 T Nb_3Sn cos-theta magnet* [63]*; (c) and (d) FCC 16 T and 17 T Nb_3Sn cos-theta designs* [64, 65]*, respectively; (e) FCC 16 T Nb_3Sn block design* [66]*; (f) FCC 16 T Nb_3Sn common-coil design* [67]*; (g) FCC 16 T Nb_3Sn canted-cos-theta design* [68]*; and (h) HE-LHC 20 T ReBCO insert magnet* [55]*. Notice that the last magnet, which is also shown in Fig. 1.5, is just the insert of a hybrid Nb_3Sn/ReBCO system.*

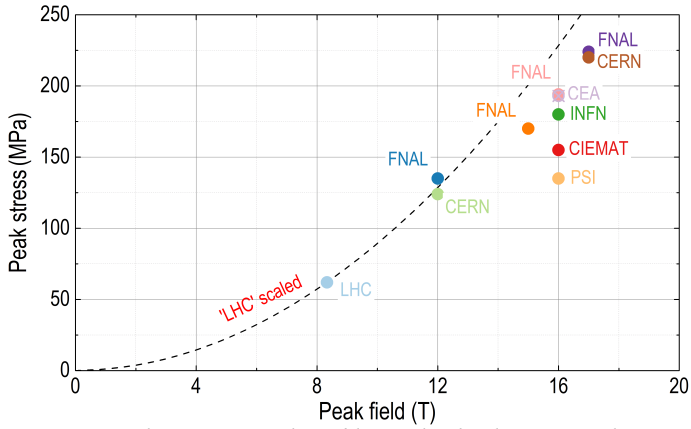

Figure 1.7: *Transverse peak pressure on the cables in the dipole magnets that are presented in Figure 1.6 and in Table 1.2, plotted against the peak field generated by the magnet.*

in Section 1.2 are able to withstand these elevated pressure levels, which is indeed the central question investigated in this thesis.

In order to answer this question, it is important to make the distinction between reversible and irreversible pressure effects on superconducting strands and cables. It is well-known that the superconducting properties of Nb_3Sn change when mechanical strain deforms its crystal lattice. This is illustrated e.g. in Figure 1.8, which shows the variation of the upper critical field B_{c2} of a range of commercial wires with externally applied strain ϵ [72].

In Figure 1.9 the typical behaviour of the critical current I_c in Nb_3Sn strands when they are subjected to axial strain is shown [73]. Just like B_{c2}, I_c decreases with intrinsic strain, defined as the applied strain corrected for residual thermal strain built up during cool-down. The dotted lines in the figure indicate the sequence of the measurements: after each strain excursion, ϵ is again released and I_c is measured at this zero applied strain level. Up till an intrinsic strain level of 0.6%, I_c recovers to its original unstrained value. The origin of the strain-dependence in B_{c2} and I_c, as well as in T_c, in this reversible regime is further discussed in Section 3.2. Closer inspection of Figure 1.9 reveals how strain excursions that exceed an 'irreversible strain limit', for this particular strand 0.6%, lead to irreversible degradation of the current. As illustrated in Figure 1.10, the origin of this degradation is no longer an intrinsic electronic effect but rather a micro-structural failure [74]. When the stress on the brittle Nb_3Sn filaments exceeds their ultimate strength, they crack and locally cease to transport current. Note that the exact moment of filament failure is in general complicated to predict, since it tends to interact with the plastic deformation of the copper matrix [75, 76]. In Section 4.1 it is further reviewed how all these effects may also occur in Nb_3Sn Rutherford cables.

Also *Re*BCO coated conductors exhibit an intrinsic reversible and a micro-structural irreversible strain dependence, although the situation is somewhat complicated by the highly anisotropic layout of the tapes. In Figure 1.11 the excellent current retention under transverse compressive pressure applied normal to the flat tape surface is shown [77], especially when the metal substrate has a superior yield strength [78]. In axial tension or compression, the situation is similar: as shown in Figure 1.12, the critical current varies significantly but reversible for compressive strain as high as -0.9% and up to a tensile irreversible strain limit of +0.6% [79].

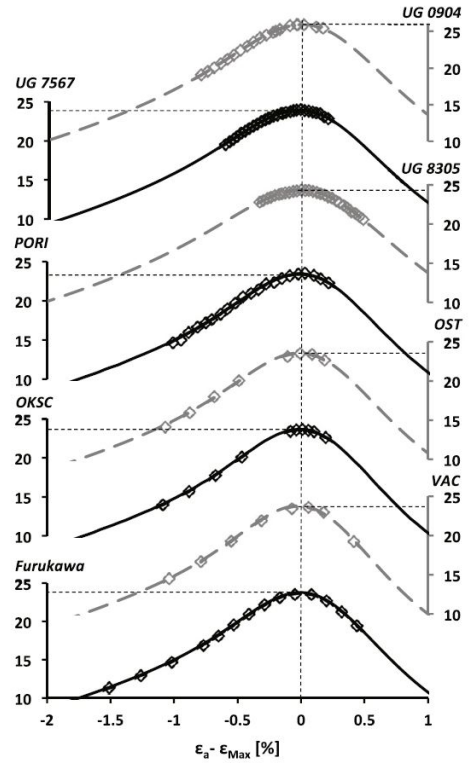

Figure 1.8: *Variation of the upper critical field B_{c2} of several industrial Nb_3Sn strands at 4.2 K when the wires are axially strained. The picture is taken from* [72].

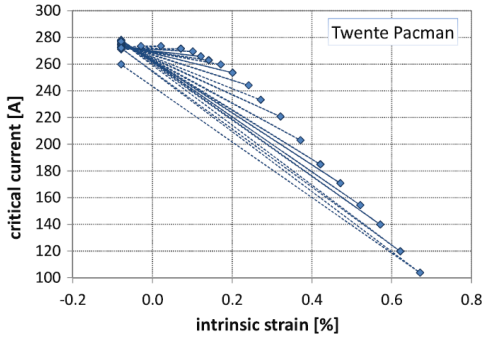

Figure 1.9: *Variation of the critical current of a Nb_3Sn strand at 12 T and 4.2 K when axially strained. The picture is taken from* [73].

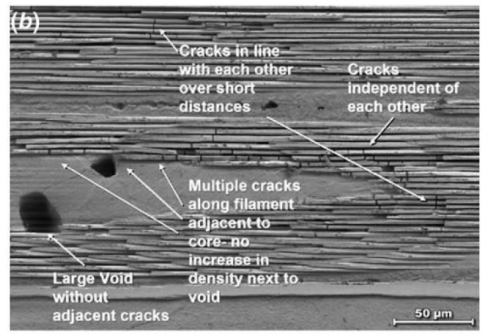

Figure 1.10: *SEM micrograph of a longitudinal section of an internal-tin Nb_3Sn strand subjected to 0.5% bending strain. The picture is taken from* [74].

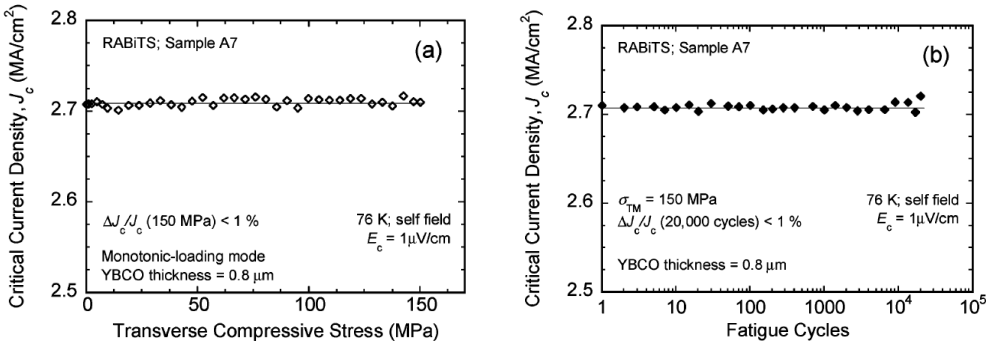

(a) **(b)**

Figure 1.11: *Transverse pressure response of the critical current density in a coated conductor sample. The pictures are taken from* [77].

In terms of stress, these strain values correspond to an overall stress state of several hundreds of MPa, depending mainly on the substrate composition [80]. Indeed, not unlike the Nb_3Sn case described above, the irreversible degradation at higher axial strain values has convinc-

ingly been correlated to plastic yielding of the substrate, which cannot be accommodated by the brittle ceramic *Re*BCO layer [81]. However, as shown in Figure 1.13, the situation is quite different under tensile transverse forces which can cause delamination of the coated conductor structure at stress levels as low as 10 to 20 MPa [82]. Also longitudinal [83] or transverse [84] shear stresses between the layers of a few MPa can lead to delamination with severe irreversible J_c degradation. Although this type of stress can in principle be kept minimal in coiled structures, they do come into play when stress concentration occurs [85] or when a winding pack consists of different materials that exert thermal stresses on each other [86–88]. The implications for Roebel cables are further discussed in Section 5.1.

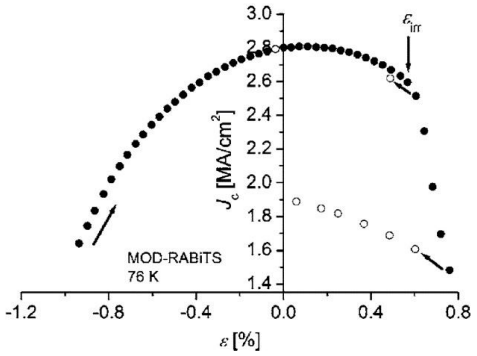

Figure 1.12: *Variation of the critical current density at 77 K of a typical coated conductor under compressive and tensile axial strain. The picture is taken from* [79].

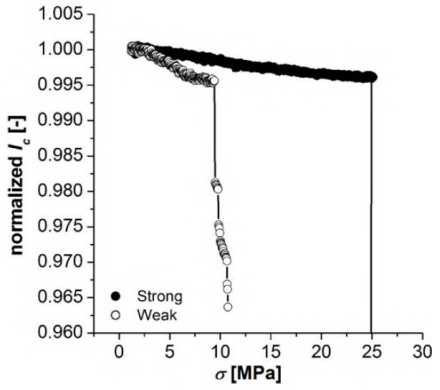

Figure 1.13: *Variation of the critical current at 77 K of different ReBCO coated conductor under transverse tensile stress. The picture is taken from* [82].

1.4 Outline and research questions

The structure of the thesis is summarized in the flow chart shown in Figure 1.14.

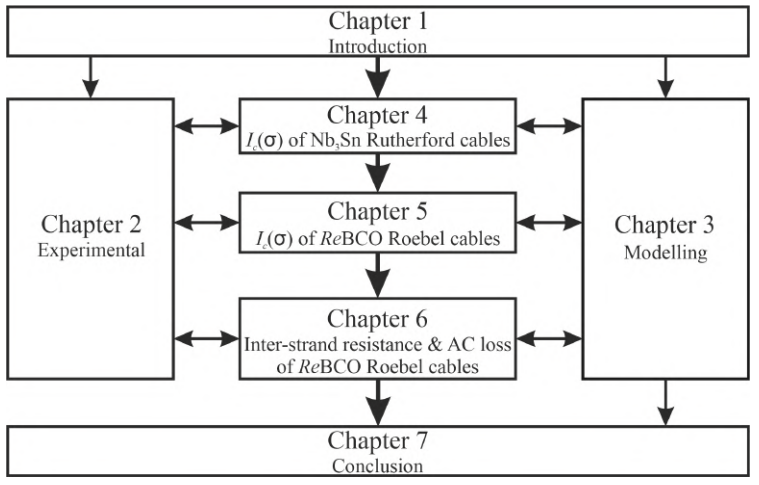

Figure 1.14: *Chart showing the interdependence of chapters and the flow of this thesis.*

The main topic of the thesis is the transverse pressure effect on superconducting Nb_3Sn Rutherford and *Re*BCO Roebel cables for accelerator magnets. A survey of experimental set-ups for measuring the transverse pressure effects on the critical current is presented in Chapter 2, including set-ups for single round wire or flat tape superconductor and cables. Then the direct current transport method for determining the inter-strand resistance of impregnated *Re*BCO Roebel cables is introduced. Moreover, the AC loss measurement methods, especially the magnetic- and calorimetric methods are described. Next, the specification of the measured cable samples is presented, e.g. cable layouts and impregnation methods, and the splice low-resistance process when soldering the cable samples to the terminals of a superconducting transformer for $I_c(\sigma)$ measurement. Finally, the uncertainties in the critical current measurement and transverse pressure calculation are estimated.

In Chapter 3, to support the experimental data analysis, a series of simplified mechanical Nb_3Sn cable models are developed for simulating the influence of the epoxy resin properties, glass reinforcement and confinement geometry on the average deviatoric strain of the strand in a Rutherford cable. Then, the electrical network model of the inter-strand resistance in *Re*BCO Roebel cables is developed to analyze the component contributions to their overall inter-strand resistance. In addition, AC loss models, comprising hysteresis-, coupling- and eddy current loss, are introduced. All the modelling results are compared to experimental data presented in Chapters 4 to 6.

A brief summary of the cause of critical current degradation due to cabling and transverse pressure for Nb_3Sn Rutherford cables is presented in Chapter 4. It is followed by a brief literature review on critical current degradation in Nb_3Sn wires and Rutherford cables when exposed to transverse pressure. Then, the measurement results, including the critical current of witness wires and cable samples, irreversible critical current degradation and decrease of upper critical field due to transverse pressure are presented, as well as a single thermal-cycle and multiple load-cycling effects on critical current of cable samples. In addition, a microscopic anaylsis of the impregnated Nb_3Sn Rutherford cable samples is shown.

Similar to Chapter 4, a review of critical curernt degradation due to Roebel strand preparation and transverse pressure is presented in Chapter 5, followed by a brief summary of critical current degradation in *Re*BCO Roebel cable. The measurement results, including the critical current of single Roebel strand and cable samples, the irreversible critical current degradation and thermal-cycle effect on the critical current of cable samples, are presented. A microscopic analysis of the impregnated *Re*BCO Roebel cable samples is also shown.

In Chapter 6, the measurement results of the inter-strand resistance of impregnated *Re*BCO Roebel cable samples are presented and discussed. Then, the AC loss of the cable samples measured in a perpendicular and parallel transverse magnetic field are shown. In addition, the measurement data of the magnetic field angle dependence of AC loss of the cable samples is presented and discussed.

A series of research questions are outlined and will be addressed in the concluding Chapter 7. The following questions do not cover all details described in this thesis, but they represent a fair summary of its highlights. Regarding the state-of-the-art Nb_3Sn Rutherford and *Re*BCO Roebel cables, the questions are:

1. *Epoxy resin* - Is it possible to fully impregnate the superconducting cables with various epoxy resins?

2. *Critical current* - What is the critical current of the impregnated superconducting cables? How significantly is the critical current density degradation compared to the critical current density of virgin witness wires?

3. *Critical current versus transverse pressure* - How significant is the reversible and irreversible critical current reduction of the impregnated cables, and is it possible to construct high-field accelerator dipole magnets using these kinds of cables view of their of transverse stress limit?

4. *$I_c(\sigma)$ of ReBCO Roebel cable* - How does the critical current behave under transverse pressure at 4.2 K when using various epoxy resins, cable layouts and type of tapes?

5. *B_{c2} of Nb_3Sn Rutherford cable* - How does the upper critical field of cable samples perform when exposed to transverse pressure, is there some reduction, how significant is it?

6. *Simple thermal cycling* - Is there any influence on the critical current of cable samples at successive cool-down cycles? If there is some filaments cracking, is there any evolution of the cracking due to load-cycling?

7. *Load-cycling of Nb_3Sn Rutherford cable* - Is there any evolution of the critical current reduction at high transverse stress level?

8. *Inter-strand resistance of ReBCO Roebel cable* - What is the inter-strand resistance of impregnated cable samples over one transposition length at 4.2 and 77 K? How to estimate the corresponding AC coupling loss in various magnetic fields?

9. *AC loss of ReBCO Roebel cable* - How does the AC loss of impregnated cable samples perform in different magnetic field orientations?

Chapter 2
Experimental aspects

In the chapter, the facilities used to measure the effect of transverse pressure on the critical current of superconducting wires, tapes and cables are presented. In addition, a direct transport-current method used to measure the inter-strand contact resistance of impregnated ReBCO Roebel cables is introduced. The traditional magnetic and calorimetric methods applied for measuring the AC loss of superconductors are briefly described. Furthermore, sample preparation, methods for vacuum impregnation, and characteristics of the investigated cable samples are presented. Finally, an estimate of the measurement errors is presented.

2.1 Introduction

As described in Chapter 1, superconducting cables eventually used for future high-field accelerator magnets have to withstand high-level transverse pressures ranging from 100 to over 200 MPa, which depend on the peak magnetic field and current density in the coil windings [66, 67, 89–91]. The vacuum impregnation technique is generally used to enhance the tolerance of cables comprising brittle superconducting material like Nb_3Sn to transverse pressure [92]. It is essential to investigate and improve the susceptibility of these cables to transverse pressure. By understanding the mechanism behind, it is possible to find a proper way to further enhance the transverse pressure tolerance of cables.

Many groups have developed dedicated equipment for the examination of the critical current in relation to transverse pressure of superconducting wires, tapes and cables. A survey of the facilities is provided early in this chapter. A more detailed description of the set-up used in this study is presented in Section 2.2.

The inter-strand resistance is a key parameter that influences the accelerator magnets' dynamic magnetic field quality. Many studies already reported relevant findings in Nb_3Sn Rutherford cables [93–99]. However, only a few publications concern the investigation of the inter-strand contact resistance of *Re*BCO Roebel cables [100–102] performed on non-impregnated cables at 77 K. The AC loss performance of such cables is reported as well but mostly investigated at 77 K [50].

A direct transport-current method for the determination of the inter-strand resistance of impregnated *Re*BCO Roebel cables at 77 and 4.2 K is introduced in Section 2.3. The measured inter-strand resistance is used to estimate the AC coupling loss in different orientations of magnetic field. For validation purpose, also the AC loss of cables were examined in various orientations of applied magnetic field at 4.2 K. The traditional methods for AC loss measurement are briefly introduced in Section 2.4. In this research both magnetic and calorimetric methods are used and described in detail in this section.

The transverse pressure susceptibility of Nb_3Sn Rutherford- and *Re*BCO Roebel cables was examined at 4.2 K in a solenoid magnet generating a background magnetic field up to 11 T. The Nb_3Sn strands in the Rutherford cables are based on two technologies: the 'Restacked-Rod-Process' (RRP) from Bruker-OST [103] and the 'Powder-In-Tube' (PIT) process from Bruker-EAS [104]. The characteristics of the examined conductors are presented in Section 2.5.1.

In this study, different epoxy impregnation methods are applied for investigating the effect of impregnation on the transverse pressure dependence of the critical current in *Re*BCO Roebel cables, as presented in Section 2.5.2.

For the critical current measurements of cables using a superconducting transformer, see Section 2.2.2.4, it is important to maintain a low joint resistance that is smaller than 10 nΩ when using the UT facility. The methods used for achieving a low joint resistance are presented in Section 2.5.3.

In order to draw proper conclusions regarding the measurement data of the transverse pressure dependence of the critical current, the uncertainties in the measurements are studied and evaluated. Type and sources of the measurement errors are briefly introduced, and a basic error analysis is presented in Section 2.6.

2.2 Survey of experimental set-ups for measuring the transverse pressure effect on the critical current

2.2.1 Set-ups for single round wire or flat tape superconductor

Several facilities were developed worldwide to study the effect of transverse pressure on the critical current of superconductors, for example the drag-free stress test apparatus at the University of Colorado [105], Walters springs at the University of Geneva [106–109] and Durham University [110], the Short Sample Test Facilities (SSTF) at Fermi National Accelerator Laboratory (FNAL) and Lawrence Berkeley National Laboratory (LBNL) [111–113], the straight conductor test set-up at the Sophia University [114–119], and the two-component strain apparatus at the University of Twente [120–122].

2.2.1.1 Drag-free stress test apparatus

The "drag-free stress test apparatus" was designed to simultaneously apply current perpendicular magnetic field and transverse compressive stress to a superconducting wire or tape in a liquid helium bath [105]. The schematic of the transverse stress test apparatus is shown in Figure 2.1. The sample terminals are soldered to copper contacts connecting to a 900 A power supply. The set-up is placed in a split-coil magnet with a magnetic field up to 10 T. The compressive stress acts on short U-shaped samples along a straight length of 9.5 mm through two stainless-steel anvil heads. One head is fixed and the other is connected to a pivot driven by a servo-hydraulic system, which can provide a compressive force of 1.7 kN [123].

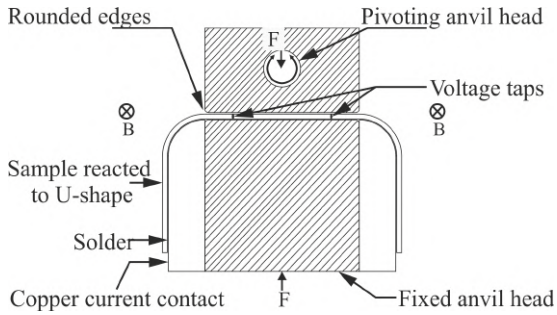

Figure 2.1: *Transverse pressure test apparatus at the University of Colorado* [105].

2.2.1.2 Walters spring devices

The "Walters spring devices" used for critical current measurements on round wires exerted to transverse compressive stress at the University of Geneva have two configurations: a 2- and a 4-wall version shown in Figure 2.2. In the 2-wall version, non-impregnated wires, with cross sections of up to 4 mm^2, are fixed in a one-turn Walters spring and pressed by two parallel stainless-steel walls [106–108]. The 4-wall version makes it possible to measure the critical current of a wire either with or without impregnation under transverse compressive stress [109] as shown in Figure 2.2 as well. The wire samples are constrained in a U-shaped groove at the bottom and pressed by an upper anvil that fits the groove. The groove width is specific for the wire diameter. The wire samples in both configurations are pressed along a length of 126 mm. The probes are located in a 2.2 to 100 K variable temperature insert with a current lead capacity of 1 kA. The spring, with a diameter of 39 mm, is inserted in a 21 T superconducting magnet.

The transverse force up to 40 kN is supplied by a servo motor.

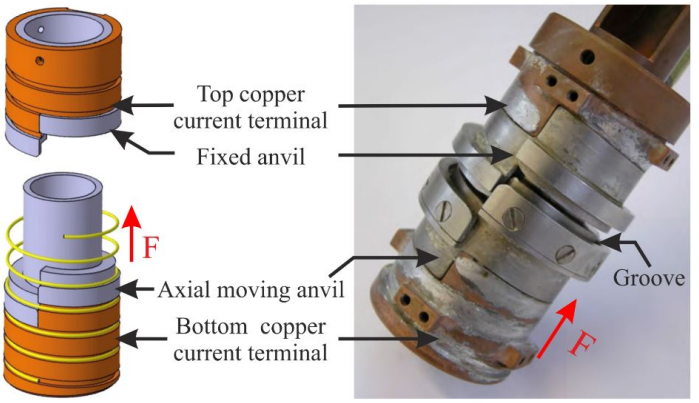

Figure 2.2: *Walters springs for I_c measurements versus transverse pressure at the University of Geneva: (a) 2-wall configuration* [107, 108] *; (b) 4-wall configuration* [109].

2.2.1.3 Short sample test facility

"Short sample test facilities" to assess the critical current performance of a selected strand within a cable under transverse pressure were built at FNAL and at LBNL [111], as shown in Figure 2.3. The cable samples are 53 mm long, with one longer single strand sticking out at both sides. This strand is used for the critical current measurements as a function of transverse pressure applied to the cable surface [112]. Both ends of the selected strand are 200 mm long, which is long enough to ensure current transfer once soldered to the copper current leads carrying current of up to 2 kA. The cable sample is compressed between two Inconel plates. The top plate is welded to an Inconel tube, which is welded itself to the top flange. The bottom plate is driven up by an Inconel rod assembly, which is pulled up by a 20 ton-load hydraulic cylinder mounted on the top flange. A maximum transverse pressure of 200 MPa can be applied [112]. The device was designed to operate at 4.2 K in a 64 mm-bore superconducting solenoid providing a background magnetic field up to 14 T [111, 112].

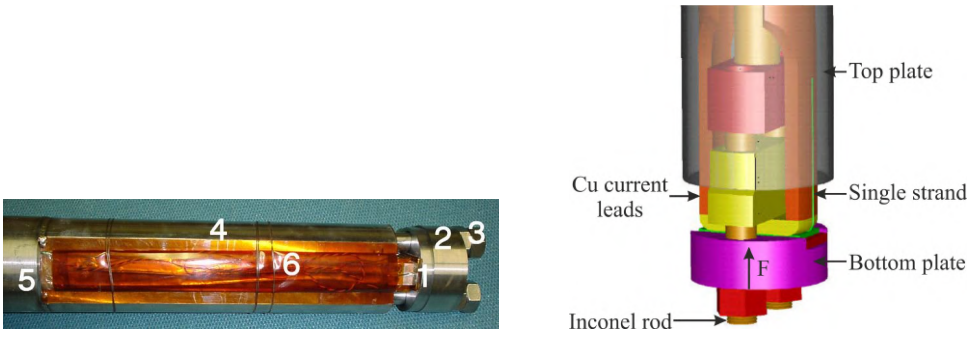

Figure 2.3: *Short sample test facility, transverse pressure experimental setup at FNAL and at LBNL* [111,113]: *(1) cable sample; (2) bottom plate; (3) Inconel rod; (4) top plate; (5) Inconel tube; (6) copper current leads.*

2.2.1.4 Straight conductor test set-up

The "straight conductor test set-ups" were built at the Sophia University [114–119]. Two apparatuses were designed for conductor measurements at 77 K in self-field and at 4.2 K in a 14 T background magnetic field, as shown in Figures 2.4 and 2.5. Samples are limited to a length of 4 mm. For the apparatus in Figure 2.4, the sample is set horizontally and clamped by pushing blocks from upper and lower sides. The top block is fixed, and the bottom block moves upward. The ends of the sample are soldered to copper terminals connected to current leads [116]. Two types of stainless-steel pushing parts covered with insulation film are available: line-contact in Figure 2.4a and face-contact with 5 mm-wide contact surface in Figure 2.5b [115]. The contact force tolerances are 0.3 and 1 kN, respectively. For the apparatus in Figure 2.5, the sample is placed on a glass-fiber reinforced plastic plate with its ends soldered to copper current leads [118]. The sample is uniformly compressed by a pushing head from upper side, which is connected to a load cell to measure the applied compressive force. Various width of pushing heads are available: 0.5, 1, 2, 3, 4, 5 and 6 mm. The maximum force applied to the flat sample is 1.3 kN. This type of apparatus is relatively easy to realize. The Karlsruhe Institute of Technology (KIT) has two similar systems as well, but only designed for 77 K use [100].

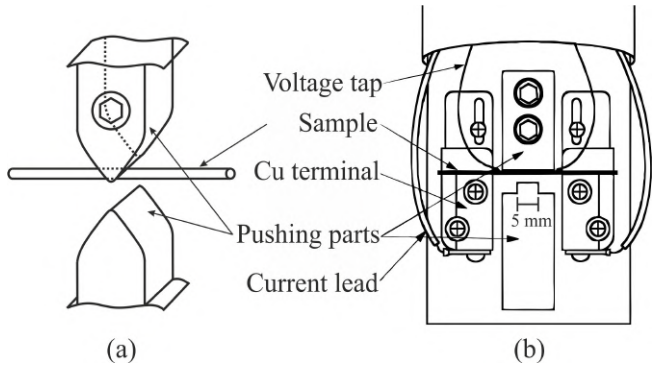

Figure 2.4: *Schematic of the "straight conductor test set-up" at the Sophia University: (a) line-contact pushing parts; (b) assembled setup with face-contact pushing parts* [116].

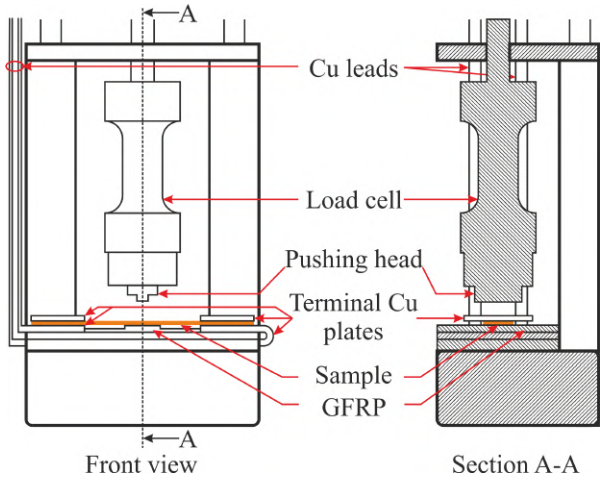

Figure 2.5: *Schematic of the second "straight conductor test set-up" at Sophia University* [117, 118].

2.2.1.5 Two-component strain apparatus

To investigate the axial- and transverse strain susceptibility of a tape conductor, a two component strain apparatus was developed by Ten Haken *et al.* [120] at the University of Twente, as shown in Figure 2.6. The sample has a straight test length of 25 mm and corner bending radius of 15 mm. The ends are soldered to two half-moon shaped pieces, which are connected to copper current leads. The sample can be positioned in two directions as depicted in Figures 2.6a and 2.6b [121]. One of the two legs moves in the sample axial direction through a parallelogram construction hidden inside. A maximum force of up to 0.5 kN can be generated. On the other hand, a transverse press with maximum force of 6 kN can be applied through a wedge driving a lever with an anvil head on top. The pressure surface of the anvil head has a 10×20 mm^2 area. In practice, the load section of the tape can be reduced to less than 20 mm by changing anvils. The measurements are carried out at 77 K in self-field and 4.2 K in a 60 mm-bore magnet providing a background magnetic field up to 15 T.

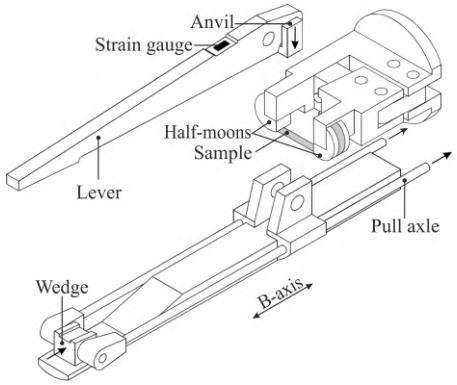

(a) *Magnetic field parallel to the wide face of tape samples.*

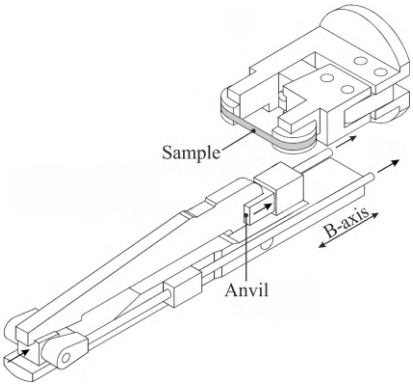

(b) *Magnetic field perpendicular to the wide face of tape samples.*

Figure 2.6: *Schematic of the "two-component strain apparatus" for measuring the critical current as a function of transverse load on flat tapes at the University of Twente* [121].

2.2.2 Set-ups for cables

To the best of our knowledge, only four test facilities worldwide are presently capable to measure the critical current of accelerator-type cables under transverse pressure, located at: the National High Magnetic Field Laboratory (NHMFL) in Tallahassee [124, 125], the Brookhaven National Laboratory (BNL) [126, 127], CERN [128] and the University of Twente [129].

2.2.2.1 NHMFL cable test station

Figure 2.7 shows the cross-sectional schematic of the sample holder used in the NHMFL cable test facility [124], which comprises a stainless steel U-channel and a G-10 top plate. A stack of two active cable samples are placed in the groove. The lower ends of the fixture, with insulation removed, are sheathed in a 125 mm-long Cu box and soldered to create a closed current path [124]. The outer two dummy cables provide a coil-winding block-like environment and protect the active cables during assembly. At the upper end of the fixture, the active cables are extended into a Cu bus plate to which they are soldered while the dummy cables are terminated. The bus plates are connected to the NbTi current leads designed for 10 kA [125]. Two shims are added

in the groove to guarantee sample alignment with the pressure bar. In Figure 2.8, the schematic of the loading assembly is presented [125]. The transverse force is applied by a piston pushed by helium gas. Up to 530 kN can be applied to the sample surface over an area of 122 × 15 mm^2. The force is measured by a capacitive pressure transducer positioned underneath the center of the pressure plate. The facility is designed to operate at 4.2 K in a 150 mm-bore split solenoid providing a background magnetic field up to 14 T.

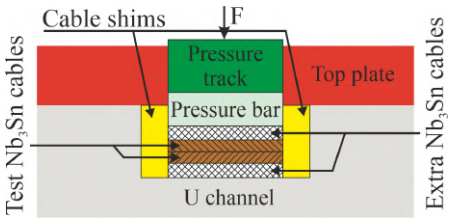

Figure 2.7: *Schematic cross section view of the cable press at the NHMFL* [124].

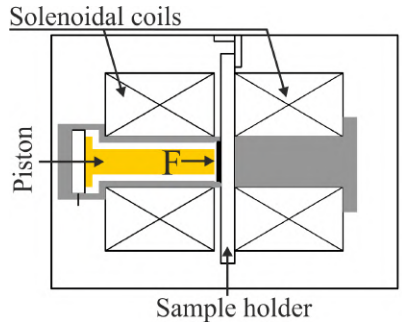

Figure 2.8: *Schematic of the NHMFL transverse force generating system* [125].

2.2.2.2 BNL cable test station

The sample holder used at BNL is similar to the one of the test facility at NHMFL [126, 127], as shown in Figure 2.9. One difference of the sample holder used at BNL is the cover plate, which is made of stainless-steel instead of G-10 [126]. This sample holder is designed to compress cable samples via the cover plate and restraining bolts over the entire cable length of 970 mm, rather than using the pressure track. A pre-stress up to 290 MPa can be applied to the cable broad face at room temperature. Since the thermal contraction of the cable stack is higher than that of the holder, a 4 MPa lower stress acts on the cable surface at 4.2 K. The facility is equipped with three 25 kA current leads allowing testing of two samples during the same cool-down. The sample holder is placed in a 75 mm bore of a one meter long NbTi superconducting dipole magnet, which can generate a background magnetic field up to 7.5 T at 4.3 K and 9 T at 1.9 K. The uniform magnetic field region is 600 mm [127].

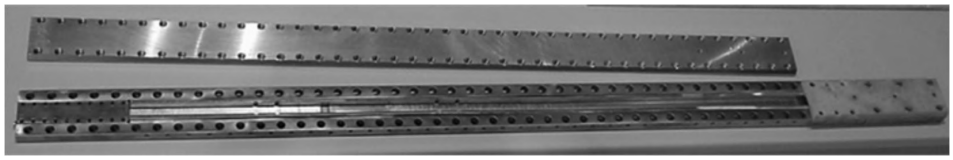

Figure 2.9: *Sample holder used at the BNL cable test station* [127].

2.2.2.3 CERN FRESCA transverse pressure apparatus

Figure 2.10 shows the setup used in the FRESCA test station at CERN [103, 104, 128]. An external aluminum tube houses two pads, a titanium U-cage, two stainless steel keys and cable samples up to 1.8 m long and 20 mm wide. Two active cable samples, placed between two dummy cables, are soldered at the bottom with a joint length of 150 mm; while at the top they are connected to a NbTi bus cable with a joint length of 200 mm. The NbTi bus cable is connected to the current leads of the insert with a maximum current capacity of 32 kA [130].

The pressure is applied at room temperature using the "bladder and key" technology [131]. The pressure bladder is inserted between the U-cage and the lower pad, and then the pads are pushed to the tube. A transverse force up to 1.4 MN over a length of 700 mm can be applied to the cable surface in a magnetic field of 10 T at 4.3 K [103]. Once the target stress is reached, the keys are inserted. The applied stress changes after cooling down, and the thermal contraction coefficients of different materials need to be considered to evaluate the final stress. The applied strain is detected by 12 strain gauges, which are mounted to the inner wall of the aluminum shell.

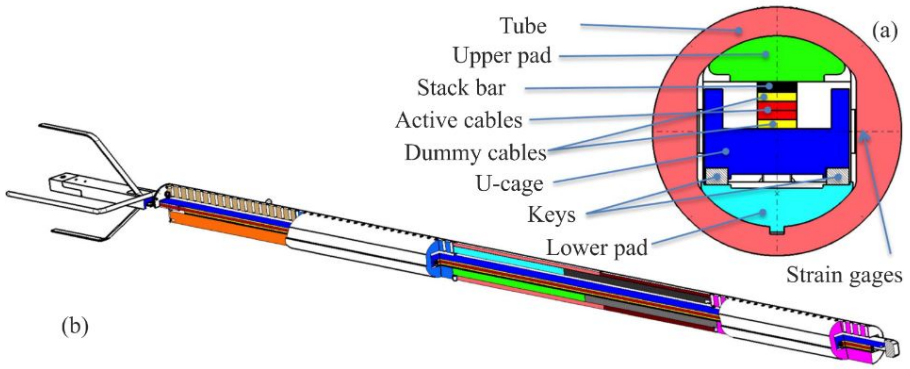

Figure 2.10: *Sketch of the FRESCA sample holder for measurement of critical current under transverse pressure: (a) cross section view of the pressed region; (b) overview of the whole assembly* [104].

2.2.2.4 UT cable test station

The transverse stress measurement setup used extensively for the characterization of superconducting cables at the University of Twente consists of two main parts: a superconducting transformer for injecting the sample current (Figure 2.11a) and an electro-magnetic press generating the transverse force exerted on the cable surface (Figure 2.11b) [129,132]. The primary current of the transformer can be swept from -50 to +50 A, thereby inducing a maximum current of 100 kA in the secondary coil. The mechanically loaded section of the sample is situated in the center of an 11 T solenoid and all measurements are made at 4.2 K. The cable samples are bent into a flat-bottomed “U”-shape, with corners of radius 10 mm for Nb_3Sn Rutherford cables and 20 mm for *Re*BCO Roebel cables. To reduce the influence of friction between the anvil and the two-clamping side-plates, two layers of Kapton cover the inner face of the plates. The ends of the cable sample are soldered to the secondary coil terminals over a length of 165 mm. The press is shown in Figure 2.11b and essentially consists of two anti-series connected NbTi flat coils that repel each other. The top coil pushes the pressure anvil against the sample via a piston; the bottom coil is connected to the sample holder by a thick steel sleeve and fixation pins. A maximum force of 250 kN can be applied to the cable surface over a length of 46 mm for Nb_3Sn Rutherford cables and 26 mm for *Re*BCO Roebel cables. The precise force, also considering a correction for the interaction between the main magnet and the press-coil, is determined with two independent methods [132]. The displacement of the upper coil is measured with an extensometer. In addition, two strain gauges glued to the short sides of the pressure anvil allow to monitor its deformation.

For this thesis, the transverse pressure susceptibility of superconducting cables were all investigated using the UT test apparatus.

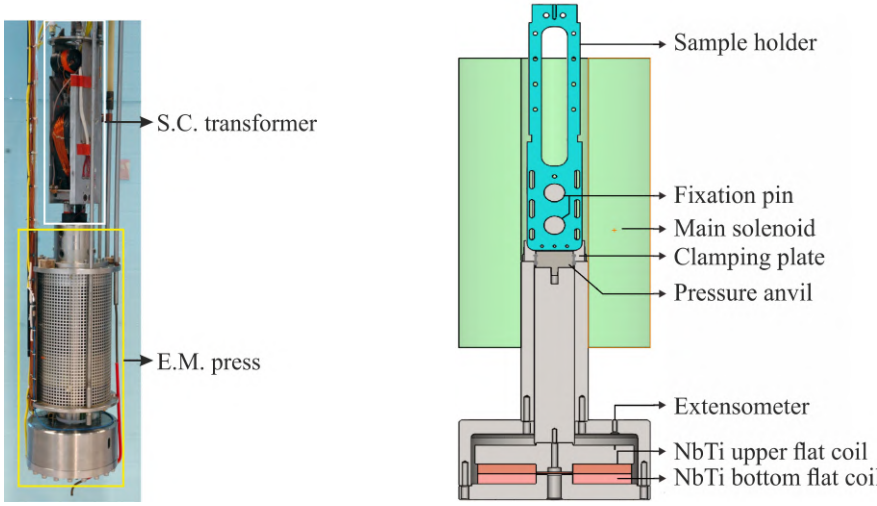

(a) *Assembly of the superconducting transformer and electro-magnetic press.*

(b) *Schematic of the electromagnetic cryo-press, sample holder and main solenoid.*

Figure 2.11: *The facility used for transverse pressure susceptibility investigations of cable critical current at the University of Twente* [129].

2.3 Determination of the inter-strand resistance

Inter-strand resistance of non-impregnated Roebel cables, characterized as a function of transverse pressure, were presented and modeled by Otten *et al.* [100], who showed the resistance to decrease with pressure in bare cables. Here, a series of transport current measurements are presented to determine under self-field condition the tape-to-tape inter-strand resistance of impregnated Roebel cables. The strand in the cable changes position along the longitudinal direction, thus within one transposition length every strand is in contact with two neighboring strands, as shown in Figure 2.12. It is assumed that the *Re*BCO layer in the strand is in equipotential state. One transposition length in a 15-strand cable can then be represented by the equivalent electrical circuit shown in Figure 2.13. The nodes represent the *Re*BCO layers, each at a potential V_i, while R_{ij} represent the cross-over resistances between strands i and j. The sensing wires soldered to all strands at the cable termination are used either as current lead or voltage tap. In Figure 2.13, current is injected in strand 1 and extracted from strand 8, while the electrical potential of all other strands is measured using strand 15 as reference. With the cable at 4.2 K and an injected current of 2 A, this configuration leads to the measured voltage profile indicated by the solid circles in Figure 2.14.

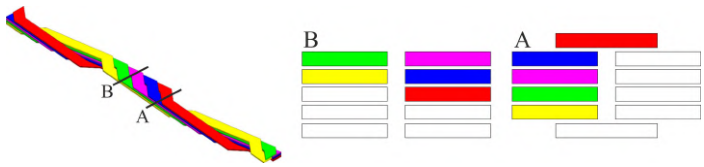

Figure 2.12: *Schematic of the strands layout in a Roebel cable* [133].

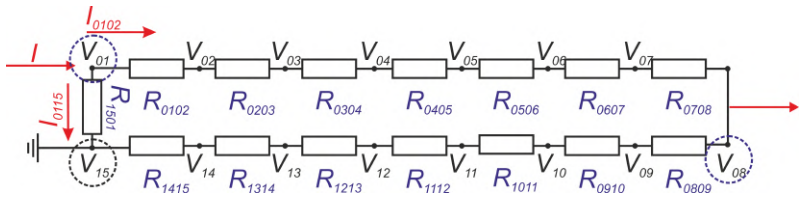

Figure 2.13: *Equivalent circuit of a 15-strand Roebel cable.*

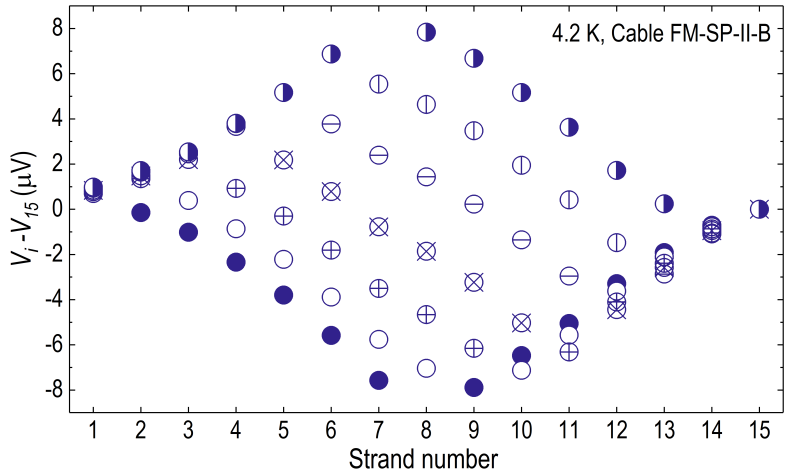

Figure 2.14: *Inter-strand potential differences measured within one transposition length of a 15-strand Roebel cable sample. The symbols indicate different current leads used, e.g. strand 1 and strand 8 used as current leads for the solid circles, strand 2 and strand 9 used as current leads for the hollow circles.*

Indexes refer to strand pairs, with strand 15 as reference. In the example of Figure 2.13, the current can flow from strand 1 to strand 8 through two parallel paths, either via strands 1-2 denoted as current I_{0102} or via strands 1-15 referred to as I_{0115}, as shown in Figure 2.13, with $I_{0102} + I_{0115} = I$. Note that I_{ij} indicates the part of the current that flows from strand i to strand j. Since I_{0102} and I_{0115} are a-priori unknown, the data are not sufficient to determine the inter-strand resistances. Moreover, potentials V_{01} and V_{08} cannot be measured accurately, because of the voltage drop over current leads and contacts. Nevertheless, from this set of potential values we can determine the ratio between successive inter-strand resistances. Since the current through R_{0203} and R_{0304} is the same I_{0102}, the ratio of voltage drops over the two resistors equals their resistance ratio:

$$\frac{V_{04} - V_{03}}{V_{03} - V_{02}} = \frac{R_{0304}}{R_{0203}}. \tag{2.1}$$

Repeating the measurement several times with successive wire pairs 2 and 9; 3 and 10;… 7 and 14 used as current leads, yields the other data in Figure 2.14. In this way all resistance ratios $R_{i,i+1}/R_{i-1,i}$ can be determined. Also the ratio between any pair of resistances is now known, e.g.:

$$R_{0405}/R_{0203} = R_{0405}/R_{0304} \times R_{0304}/R_{0203}. \tag{2.2}$$

For the configuration with current leads 1&8, we can then also determine the ratio of the currents I_{0102} and I_{0115}:

$$\frac{I_{0102}}{I_{0115}} = \frac{R_{0809} + R_{0910} + ... + R_{1501}}{R_{0102} + R_{0203} + ...R_{0708}} = \frac{R_{0809}/R_{1415} + R_{0910}/R_{1415} + ... + R_{1501}/R_{1415}}{R_{0102}/R_{1415} + R_{0203}/R_{1415} + ... + R_{0708}/R_{1415}}, \tag{2.3}$$

where, arbitrarily, R_{1415} is chosen as the reference resistor. With the ratio I_{0102}/I_{0115} worked out and the sum I_{0102} + I_{0115} = 2 A known, we can determine I_{0102} and I_{0115} separately, and finally translate the measured voltage drops to resistances, e.g. R_{0102} = (V_{02}-V_{01})/I_{0102}. The inter-strand resistance results using this method are presented in Chapter 5.

2.4 AC loss measurement methods

Conventional methods for measuring the AC loss in superconductors include electric, magnetic and calorimetric methods [134]. The electric method entails measuring the resistive voltage component along the conductor with AC transport current over a range of frequencies and current amplitudes [135]. For this purpose, lock-in-amplifier and pick-up coil techniques are normally used to separate the real and imaginary part of the conductor voltage [134]. The voltage taps of conductor and compensation coil are then connected in anti-series before connecting them to the input terminals of the lock-in amplifier. The loss generated by the alternating current is called self-field or transport-current loss.

The magnetic method is used to measure the changes in the magnetic moment of the superconducting sample. The so-called magnetization loss, can be measured using pick-up coil- [136] or calibration-free techniques [137]. In the first case, pick-up and compensation coils are wound to the same dimension around the sample and around non-magnetic dummy cables, respectively. The magnetization loss is calculated from the subtracted voltage from the two coils. The measured loss has to be calibrated due to the demagnetization effect [138]. In the calibration-free case, the method uses pick-up coils wound in parallel with the AC field magnet [137]. Two identical systems are used, each consisting of an AC field magnet equipped with a measuring coil. One of the magnets contains the sample and the other one is empty. The two coils are connected in anti-series before connecting them to the lock-in amplifier.

Besides the electric and magnetic methods, a calorimetric method for measuring AC loss can be used. The transport-current and magnetization losses result in temperature rise when the sample in mounted adiabatically [134], which can be measured with a thermometer or by measuring the evaporation of cryogen, the so-called boil-off method [139].

For this thesis, AC loss was measured at 4.2 K on cable samples positioned in a dipole magnet [140], sweeping the transverse magnetic field between ±1.5 T with a frequency of 1 Hz maximum. The samples are immersed in liquid helium and exposed to a transverse magnetic field. The AC loss is measured using the boil-off based calorimetric method as well as magnetic method using pick-up coils [136]. The calorimetric loss data are absolute but less accurate, while the magnetization data show a higher resolution, but require calibration due to the uncertainty in the effective filling factor of the sample in the pick-up coil [138]. The calorimetric method is applied at high loss for calibration purpose while the magnetization method is used to extend the measurement to the low-loss range.

2.4.1 Magnetic method

The lay-out of the 2 orthogonal sets of pick-up coils is shown in Figure 2.15. In-plane coils wound around the wide face of the cable and dummy sample measure the magnetic moment perpendicular to this face. The out-of-plane coils wound around the cable narrow face measure the in-plane component of the magnetization. The in-plane coils and cables are clamped in between two G10 plates. Afterwards, the out-of-plane coils are wound around the cable narrow face, including the two G10 plates. This whole sample assembly is fixed with nylon screws to a Tufnol sample holder, which is inserted into the calorimeter.

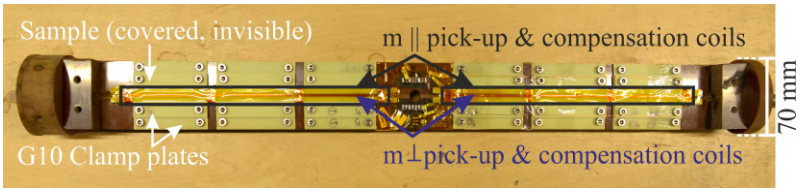

Figure 2.15: *Sample holder for the AC loss measurement of Roebel cable samples. The Roebel cable sample length is 226 mm. The overall size of sample holder is 635 mm × 70 mm.*

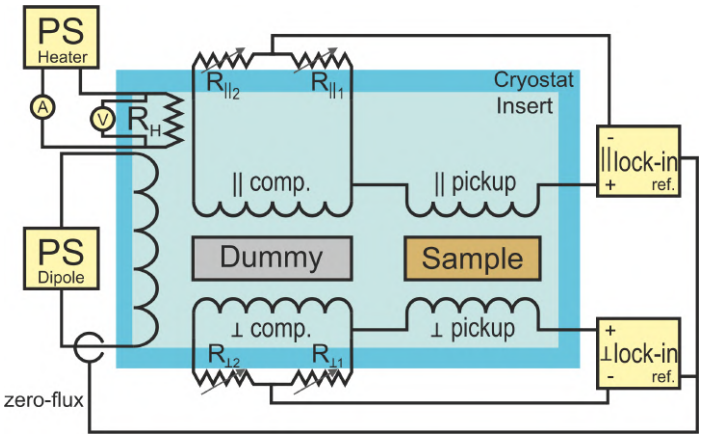

Figure 2.16: *Equivalent circuit for the AC magnetometer. Two power supplies (PS) are used for activating the heater and dipole magnetic field generation, respectively. The magnet direct current is detected by a Hitec MACC Plus 600 A zero-flux, which keeps track of the field amplitude but also serves as reference signal for the lock-in amplifiers that record the induced pick-up voltages. The lock-ins allow to measure both amplitude and phase of the compensated signals from the orthogonal coil sets.*

The electrical circuit of the magnetization method is schematically shown in Figure 2.16. Even if the dummy sample is chosen such that the areas of pick-up and corresponding compensation coils are as similar as possible, they are not identical. Compensation of the out-of-phase magnetization signal hence requires an extra voltage divider. The compensated signals from the two coil sets are fed into a pair of lock-in amplifiers, which measure their amplitude and phase. The volumetric loss density per cycle Q is calculated using formula [141]:

$$Q = \mu_0 \int \boldsymbol{H} d\boldsymbol{M} = \frac{1}{2f}\left[\left(\frac{V_{pucc}H_0}{\alpha N_{pu}A_{pu}}\right)_{\perp} + \left(\frac{V_{pucc}H_0}{\alpha N_{pu}A_{pu}}\right)_{\parallel}\right], \tag{2.4}$$

with $\boldsymbol{M}$ and $\boldsymbol{H}$ the sample magnetization and applied magnetic field, f frequency, H_0 magnetic field amplitude, V_{pucc} amplitude of the in-phase component of the compensated pick-up voltage, N_{pu} and A_{pu} the number of turns and the area of the pick-up coil and α the sample fill factor determined when calibrating with the calorimetrically measured loss. The values of N_{pu} and A_{pu} under corresponding magnetic field orientations are presented in Table 2.1.

Table 2.1: Parameters of the pickup coils.

	Unit	FM-SP-II-B	FM-SP-II-D
$A_{pu\perp}$	mm^2	226 × 13.30	225 × 12.00
$A_{pu\parallel}$	mm^2	233 × 5.15	233 × 5.10
$N_{pu\perp}$	-	50	51
$N_{pu\parallel}$	-	50	40
$\alpha_\perp$	-	0.06	0.07
$\alpha_\parallel$	-	0.002	0.006

2.4.2 Calorimetric method

The calorimetric method is shown schematically in Figure 2.17. Liquid helium from the main magnet bath can flow into the sample chamber through a U-shaped plastic tube at its bottom. The U-shape prevents external bubbles from entering the chamber. An ohmic heater inside the calorimeter allows for accurate calibration of the thermal mass-flow meter [142]. The helium evaporated in the chamber flows through its top outlet to the mass-flow meter and then back to the cryostat. This way, the pressures in and outside the chamber are kept equal so that the liquid level inside remains constant.

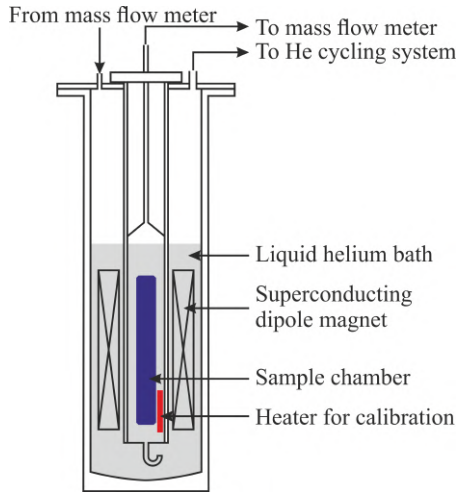

Figure 2.17: *Schematic of the calorimetric AC loss set-up.*

2.5 Specification of cable samples

As explained in Section 1.2, accelerator magnets are built using high-current cables for achieving a compact efficient design and to reduce the self-inductance of magnets. In practice, all

present high-field accelerator magnets use Rutherford-type cables. For use in future accelerators, high-J_c Nb_3Sn Rutherford cables are developed to built the dipole magnets generating magnetic fields of 11 to 16 T [89, 143]. One option for going higher in magnetic field, even up to 20 T or more is using *Re*BCO Roebel cables, which feature a sufficiently high engineering current density [144].

Rutherford-type cables, see Figure 2.18a, are fabricated applying a compaction step using a Turks head on a hollow tubular multi-strand cable. The high compaction not only increases the overall high current density but also reduces the average inter-strand contact resistance [136].

Roebel-type cables, see Figure 2.18b, are manufactured by assembling multiple zig-zag shaped tape-like strands, which are fully transposed. This is beneficial for limiting transient time constants and it improves current sharing [91, 145].

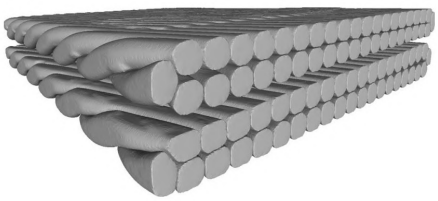

(a) *Nb_3Sn Rutherford-type cable* [146].

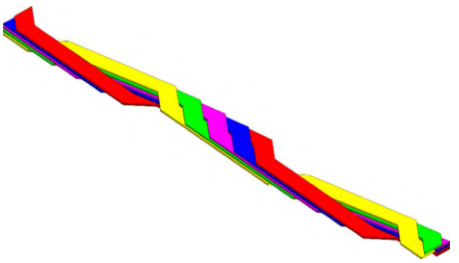

(b) *ReBCO Roebel-type cable* [133].

Figure 2.18: *Cable types presently used for future accelerator magnets.*

2.5.1 Cable layouts

Four different Nb_3Sn type Rutherford cables were investigated to determine their transverse pressure susceptibility. They are based on three types of Nb_3Sn wire technology. Three different *Re*BCO Roebel cables were investigated for the same purpose.

For the HL-LHC project, two Rutherford cables DS-PIT-I and -II developed for the 11 T dipole magnets are investigated. Here DS stands for "Dispersion Suppression", a beam focusing magnet developed for the HL-LHC upgrade [147]. The cables comprise 40 PIT-114 Nb_3Sn strands, with a wire diameter of 0.7 mm and were made at CERN on their cabling machine. Cable DS-PIT-I has a stainless-steel 316L strip core with a cross-section of 12 mm ×25 µm for coupling loss suppression [148].

For the FCC-EuroCirCol project, four Rutherford cables for the development of 16 T dipole magnets are investigated. Cables SMC-RRP-I and -II comprise 10 RRP-132/169 high-J_c Nb_3Sn strands. Cables SMC-PIT-I and -II comprise 10 PIT-192 high-J_c Nb_3Sn wires. SMC stands here for "Short Model Coil", a series of coils built for the Nb_3Sn magnet development program at CERN [149]. The strand diameter in these four cables is 1 mm.

The cross-sections of the three Nb_3Sn wires are shown in Figure 2.19. The wire characteristics are presented in Table 2.2. The sub-element diameter and Cu/non-Cu ratio are 43 µm and 1.33 for PIT-114, 58 µm and 1.22 for RRP-132/169, 48 µm and 1.22 for PIT-192.

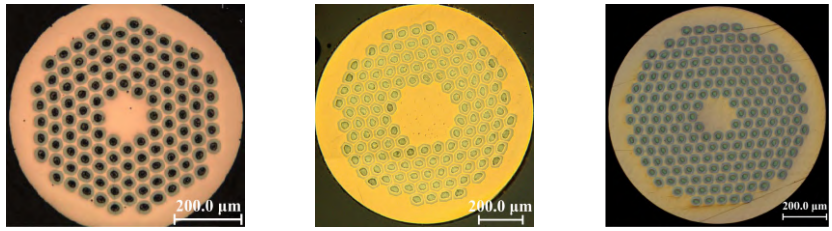

(a) *PIT-114.* **(b)** *RRP-132/169.* **(c)** *PIT-192.*

Figure 2.19: *Cross-section views of the three Nb_3Sn wires: (a) PIT-114 wire with 0.7 mm diameter; (b) RRP-132/169 wire with 1 mm diameter; (c) PIT-192 type wire with 1 mm diameter* [150, 151]. *Wire details are listed in Table 2.2.*

Table 2.2: Characteristics of strands used in the Nb_3Sn Rutherford cables.

Property\Project	DS-PIT-I and DS-PIT-II	SMC-RRP	SMC-PIT
Strand type	PIT-114	RRP-132/169	PIT-192
D_{strand}, (mm)	0.700	1.000	1.000
$D_{filament}$, (μm)	~44	~58	~48
Cu/non-Cu ratio	1.25	1.22	1.22

The cross-sections of Nb_3Sn Rutherford cables are shown in Figure 2.20. The key characteristics of the cables are listed in Table 2.3. All investigated DS-PIT cables are keystoned, with an angle of 0.71°. Their transposition length is 100 mm and cross-section area is 14.70 ×1.25 mm^2. The SMC cables feature a rectangular cross-section, with an area of 10 ×1.8 mm^2. The transposition length of these cables is 63 mm.

Table 2.3: Characteristics of the Nb_3Sn Rutherford cables.

Parameter	used in HL-LHC project		used in FCC-EuroCirCol project	
Serial number	DS-PIT-I	DS-PIT-II	SMC-RRP	SMC-PIT
Cable ID	H15EC01 26AB	H15EC01 26AC	H03EC0 120A	H03EC0 140A
w / t (mm)	14.70 / 1.25	14.70 / 1.25	9.97 / 1.81	9.93 / 1.81
Strand type	PIT-114	PIT-114	RRP-132/169	PIT-192
Core	SS 316L	-	-	-
Core size w / t (mm)	12 / 0.025	-	-	-
Number of strands	40	40	18	18
Keystone angle (°)	0.71	0.71	0	0
Transposition length (mm)	100	100	63	63
Number of samples	1	1	2	2

For the EuCARD2 project, six *Re*BCO Roebel cables were investigated. Three FM-SP-I cables comprise 10 zig-zag shaped strands made of SuperPower tapes with a transposition length of 126 mm. Cables FM-SP-II and -III comprise 15 SuperPower-type meandering strands within a transposition length of 226 mm. Cable FM-BR consists of 15 Bruker-type meandering strands with a same 226 mm transposition length. The top view of the cables are shown in Figure 2.21. An additional copper layer was applied to the punched strands before the cable assembly process in the case of Bruker-type cable, which is called punch-and-coat technique [152]. In the case of SuperPower tape, one edge of the strand is left exposed after punching and may be affected by the environment.

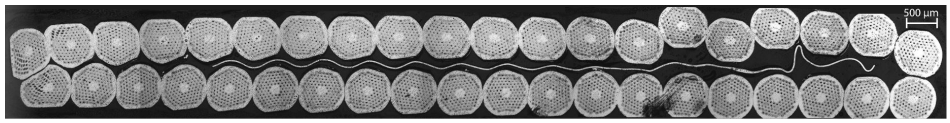

(a) *Nb_3Sn Rutherford cable DS-PIT-I with 40 PIT-114 strands and SS central core. Note the asymmetric position of the core in the cable and its "wrinkled" shape at its right end.*

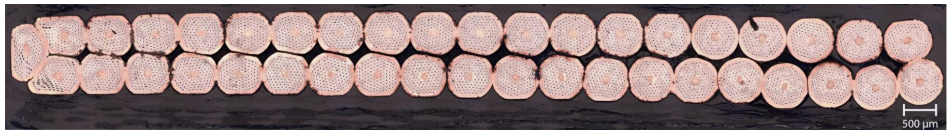

(b) *Nb_3Sn Rutherford cable DS-PIT-II with 40 PIT-114 strands.*

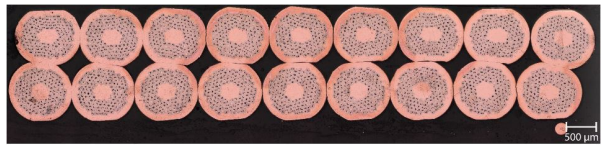

(c) *Nb_3Sn Rutherford cable SMC-RRP with 18 RRP-132/169 strands.*

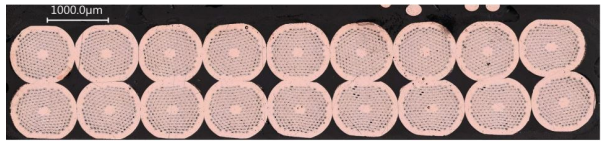

(d) *Nb_3Sn Rutherford cable SMC-PIT with 18 PIT-192 strands.*

Figure 2.20: *Cross-section views of the four investigated Nb_3Sn cables manufactured at CERN; cable details are listed in Table 2.3.*

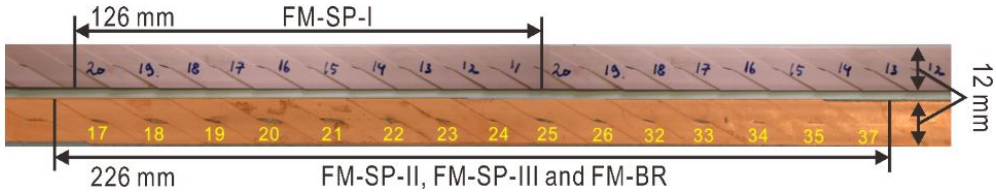

Figure 2.21: *Top view of Roebel cables with different transposition length.*

Table 2.4: Characteristics of the *Re*BCO coated conductors used in the Roebel cables.

Property ⧹ Cable	FM-SP-I, -II and -III	FM-BR
Manufacturer	SuperPower	Bruker
Conductor ID	SCS12050-AP	T284D
Substrate (material / thickness)	Hastelloy / 50 μm	Stainless-steel / 97 μm
Cu stabilizer (type / thickness)	Electroplated / 40 μm	Electroplated / 40 μm
Protection layer (type / thickness)	Ag / 2 μm	Ag / 1.8 μm
*Re*BCO layer thickness	1.0 μm	1.5 μm
Dimensions ($W_t \times t_t$)	12 mm × 0.10 mm	12 mm × 0.14 mm
I_c(77 K, S.F.)	398 A or 393 A	120 A

The characteristics of the coated conductors used for manufacturing Roebel strands are presented in Table 2.4. The substrate of the SuperPower tape is made of Hastelloy, whereas

stainless-steel with a thickness of 97 μm is used for the Bruker tape. The thicknesses of the copper stabilizer, silver and *Re*BCO layers for the two types of tapes are different. The average critical current of the two batches SuperPower tape are 398 and 393 A at 77 K in self-field environment, respectively, while the Bruker tapes features a critical current of 120 A. All *Re*BCO coated conductors have a width of 12 mm and are punched to zig-zag shaped Roebel strand. The punched tape geometry is shown in Figure 2.22 and detailed in Table 2.5.

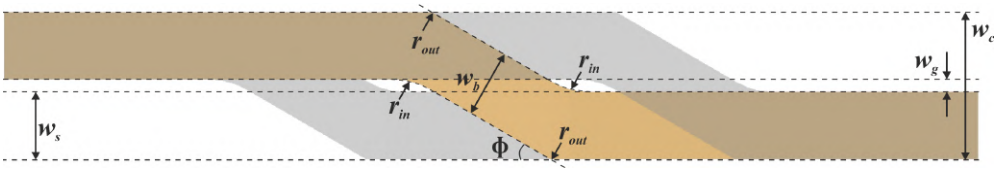

Figure 2.22: *Roebel cable geometry.*

Table 2.5: Parameters of the meandering strand of the EuCARD2 Roebel cable.

Description	Symbol	Value
Strand width	w_s	5.5 mm
Cable width	w_c	12.0 mm
Cross over width	w_b	5.5 mm
Channel width	w_g	1.0 mm
Cross over angle	Φ	30°
Inner radius	r_{in}	6.0 mm
Outer radius	r_{out}	0.0 mm

(a) *ReBCO Roebel cable with 10 SuperPower strands.*

(b) *ReBCO Roebel cable with 15 SuperPower strands.*

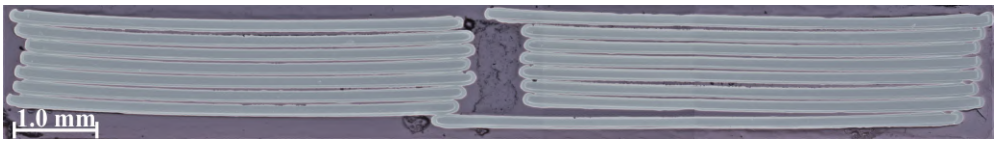

(c) *ReBCO Roebel cable with 15 Bruker strands.*

Figure 2.23: *Cross-section views of the investigated three ReBCO Roebel cables.*

The cross-section of the investigated *Re*BCO Roebel cables are presented in Figure 2.23. The main characteristics of the cables are listed in Table 2.6. Cables FM-SP-I and -II comprise the same batch of SuperPower tape, while cable FM-SP-III consists of two batches of SuperPower tape. The average critical current of the strands in cable FM-SP-III shows a hardly significant 6 A deviation from those in cables FM-SP-I and -II. Cable FM-BR is made of Bruker tape.

The samples used for inter-strand resistance and AC loss measurements are of the type FM-SP-II. Cables FM-SP-II-A, -B and -C were first used for inter-strand resistance measurements, FM-SP-II-B and -D are used for AC loss measurements.

Table 2.6: Characteristics of *Re*BCO Roebel strands and cables.

Serial number	FM-SP-I	FM-SP-II	FM-SP-III	FM-BR
Cable width (mm)	12.0	12.0	12.0	12.0
Cable thickness (mm)	0.5-0.6	0.7-0.9	0.7-0.9	1.5-2.0
Strand batch number	SP-KIT-20131011	SP-KIT-20131011	SP-KIT-20131011 SP-KIT-20141125-2	BR-KIT-20150615
Cu electroplating after punching	No	No	No	Yes
Number of strands	10	15	15	15
Transposition length (mm)	126	226	226	226
Average I_c(77K, S.F.) of strands (A)	152	152	158	54*
Number of samples	3	1	1	1

* The value is not directly measured on the Roebel strand, only approximated from 12 mm tape results, as most of the Roebel strands show 45% of the full tape current at 77 K in self-field.

2.5.2 Cable impregnation methods

Vacuum impregnation is commonly used in Nb_3Sn type of accelerator magnet coils for providing turn-to-turn insulation, prevention of conductor movement, and mechanical reinforcement to avoid Nb_3Sn critical current degradation. It is delicate to choose the right combination of methods due to the thermal expansion differences of the impregnation material and superconducting cable. As discussed in Section 1.3, in high-field accelerator type magnets, a fairly large transverse pressure is applied to the surface of Nb_3Sn Rutherford and *Re*BCO Roebel cables, which will affect the cable transport properties. The design requirements for sustaining the transverse pressure are as follows. The Nb_3Sn Rutherford cables investigated here have to withstand 150 MPa at 11 T and 200 MPa at 16 T [153, 154]; *Re*BCO Roebel cables have to withstand 110 MPa at 17 T and 150 MPa at 20 T [91].

As further elaborated in Section 3.2, it is well-known that Nb_3Sn superconductors feature a critical current and upper critical field that are intrinsically strain dependent [72, 155, 156]. The intrinsic strain reduction is reversible; but above its limit the superconducting filaments start to crack, and the critical current is not recovered upon strain release and thus the conductor is degraded.

The critical current reduction caused by reversible transverse stress is associated to the deterioration of the upper critical field due to deflection of the Nb_3Sn lattice. This intrinsic susceptibility of the critical field to transverse compressive stress is significantly greater than to axial stress, under which only less than 2% I_c reduction up to 200 MPa was observed [157]. The transverse stress susceptibility of a wire can be reduced significantly by providing a uniform stress distribution around the whole cross-section. Mondonico *et al.* [158] observed that irreversible reduction, thus true degradation due to transverse pressure for epoxy impregnated bronze route wire starts between 165 and 185 MPa at 4.2 K and 19 T, which is three times more than for bare wires (<50 MPa). Comparing the impregnated PIT wire to a corresponding wire, this value has increased to a level between 135 and 165 MPa from less than 20 MPa.

Compared to single bare wire samples, the solder-filled and epoxy-impregnated Nb_3Sn Rutherford cables are significantly less susceptible to transverse stress. At 4.2 K and 10 T, the critical current degradation at 100 MPa decrease from 29% for the wire to 13% for the solder-filled flat cable [157], and even to less than 2% for the epoxy-impregnated cable [159]. Therefore, the transverse pressure susceptibility of Nb_3Sn Rutherford cables can be significantly improved by applying solder or epoxy to the cable. The evidence further showed that cable samples under transverse pressure with a complete impregnation are less affected than with a partial impregnation [160].

Although the flat *Re*BCO tape is much more resilient to transverse pressure than bare Nb_3Sn round wire, there are significant effects due to stress concentrations between the assembled meander-shaped *Re*BCO strands [85, 161–163]. Therefore, Roebel cables used in accelerator type coils must also be impregnated. However, resin impregnation of Roebel cable is not so straightforward since epoxy resin has a different thermal contraction coefficient than *Re*BCO tape, which can cause strand delamination [86]. Such delamination has further influence on the transverse pressure susceptibility of Roebel cables, as well as on the inter-strand contact resistance and AC loss. It is important that epoxy resin impregnation using proper fillers can be better matched to the tape's thermal contraction [164].

2.5.2.1 Impregnation of Nb_3Sn Rutherford cables

The Nb_3Sn cables DS-PIT-I and -II used in the 11 T accelerator dipole magnets were impregnated with an Araldite epoxy resin of CIBA GEIGY with composition MY740 / HY906 / DY062 [165, 166]. This epoxy resin system was used before for the impregnation of Nb_3Sn coils [167–170], and has a pot life of 6 hour at the processing temperature of 55 °C. The specification is shown in Table 2.7.

Table 2.7: Characteristics of epoxy resin CIBA GEIGY MY740 / HY906 / DY062 [165, 166].

	Resin / MY740	Hardener / HY906	Accelerator / DY062
Viscosity at 25 °C (mPa.s)	12000	175-225	≤10
Density at 25 °C (g / cm^3)	1.16	1.14	0.90
Mixing ratio in mass	100	90	0.2
Pot life	6 h at 55 °C		
Curing schedule	4 h at 85 °C+ 16 h at 110 °C		

However, epoxy resin for coil applications requires a long pot life and appropriate low viscosity. CTD-101K [171] has a very low viscosity 400 mPa.s and an extremely long pot life of 60 hour. For this reason, it is used for the vacuum impregnation of large coils for accelerator magnets [171]. The Nb_3Sn cables SMC-RRP and SMC-PIT are impregnated using this epoxy resin. The CTD-101K characteristics are shown in Table 2.8.

Table 2.8: Characteristics of epoxy resin CTD-101K [171].

	CTD-101K
Viscosity at 40 °C (mPa.s)	400
Density at 25 °C (g / cm^3)	1.03
Mixing ratio in mass	Part A: Part B: Part C = 100: 90: 1.5
Pot life	60 h at 40 °C
Curing schedule	5 h at 110 °C + 16 h at 125 °C

The CIBA GEIGY Araldite and CTD-101K epoxy resins have a thermal contraction of more than 1.1% from room temperature to 4.2 K. The value is too big in comparison to heat treated Nb_3Sn Rutherford cables of 0.3% from room temperature to 4.2 K [164]. For this reason, S-2 glass-fiber sleeve is used to decrease the thermal contraction values of the epoxy resin.

For sample preparation, the Nb_3Sn Rutherford cables are bent around a U-shape reaction holder with bending radius of 10 mm following the wind-and-react technology [172]. Next, the cable is reacted following the heat-treatment protocol presented in Table 2.9. When completed, the sample is carefully removed from the reaction holder and transferred to a comparable "Hair-pin" test setup. The sample holder is covered with a Kapton tape for electrical insulation. Several pairs of voltage taps are soldered to the edges of the Rutherford cable. As seen in Figure 2.24, two extra layers of glass-fiber tapes are added to increase the thickness of the cured epoxy at the loading area. A Teflon block placed on the surface of the cable is fixed to the loading area to apply pre-stress, which support the liquid epoxy during the vacuum impregnation. Next, a Kapton tape is glued to the surface of the Teflon block, which is in contact with the cable. This step is performed to provide a smooth interface to the impregnated cable. In addition, three straps of glass-fiber tape are applied to each side of the U-shape sample holder to fix the cable to the sample holder. A PT-100 temperature sensor and two resistive heaters are used to control the temperature of the sample holder during vacuum impregnation and curing.

Table 2.9: Heat treatment protocols used in the Nb_3Sn conductors.

Property\Project	DS-PIT-I and DS-PIT-II	SMC-RRP	SMC-PIT
Strand type	PIT-114	RRP-132/169	PIT-192
Final HT step	200 h at 625°C*	50 h at 665°C**	120 h at 640°C***
Ramp rate	50°C/ h	50°C/ h	50°C/ h

* Intermediate temperature plateau: 100 h at 600°C, ramp 50 °C/ h.
** Intermediate temperature plateau: 72 h at 210°C, ramp 25 °C/ h and 72 h at 400°C, ramp 50 °C/ h.
*** Intermediate temperature plateau: 100 h at 620°C, ramp 50 °C/ h.

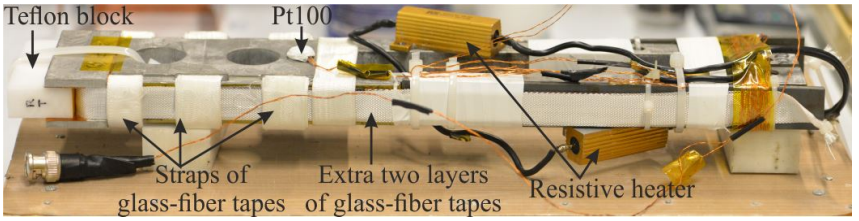

Figure 2.24: *Nb_3Sn U-shaped pressure sample prepared for vacuum impregnation.*

The Nb_3Sn Rutherford cable samples with different impregnation methods are listed in Table 2.10. Two preparation methods for Nb_3Sn Rutherford cables for transverse stress measurements are used, as shown in Figure 2.25. The PIT-114 cables have a keystone angle of 0.71° and are wrapped with a glass-fiber tape with 50% overlap, as shown in Figure 2.25a. The SMC Rutherford cables are prepared as shown in Figure 2.25b, which is representative for coil impregnation. Cables were first inserted into a glass-fiber sleeve where after a stack of two cables were wrapped again with a glass-fiber tape with 50% overlap. A dummy cable is used to transfer pressure to the measured sample placed on the top.

For the CIBA GEIGY Araldite, resin and hardener were heated to 40°C and 45°C, respectively. Before mixing, the hardener was degassed at 33 mbar for 30 minutes. Then the mixture

Table 2.10: Nb_3Sn cables with impregnation methods applied.

Test	Cable samples	Epoxy	Additives
Transverse load	DS-PIT-I DS-PIT-II	CIBA GEIGY MY740 / HY906 / DY062	S-2 glass fiber tapes
	SMC-RRP SMC-PIT	CTD-101K	S-2 glass fiber sleeve

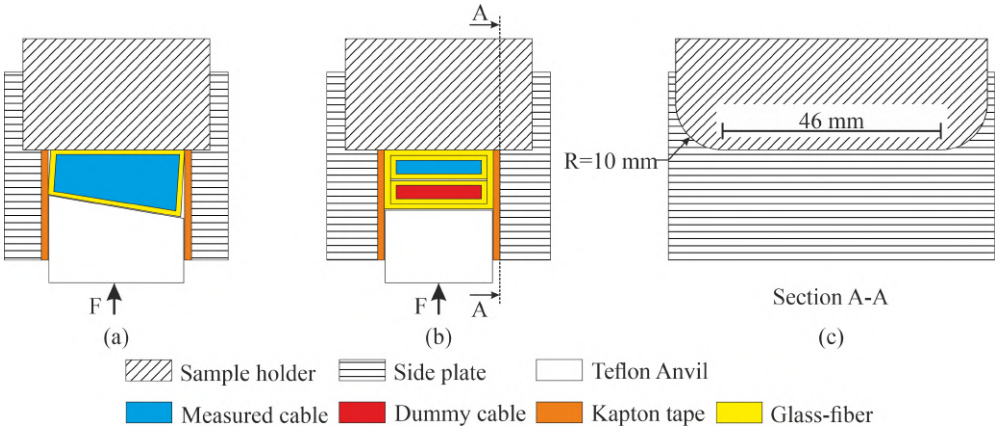

Figure 2.25: *Sketch of Nb_3Sn Rutherford cable cross-sections in the force loaded area. (a) PIT-114 Rutherford cable. (b) RRP-132/169 and PIT-192 Rutherford cables. (c) Section views of sample holder and side plate.*

was heated to 55°C and degassed at 33 mbar for 20 minutes. As to the CTD-101K epoxy, the temperature is always kept at 60°C. Before mixing, Part-B is degassed at 0.4 mbar for 30 minutes and the mixture of Part-A, -B and -C is degassed at 0.4 mbar for 20 minutes. After the preparation for impregnation, the sample holder is inserted with a speed of 1 mm / min into a transparent chamber with epoxy resin, shown in Figure 2.26. Heaters and a PT100 temperature sensor are fixed to the outer surface of the container to control the temperature of the epoxy resin, which is at 55°C for the CIBA GEIGY Araldite and 60°C for CTD-101K. The vacuum pressures are 30 and 0.4 mbar, respectively. After vacuum impregnation, the sample holder is disassembled and put into an oven for the curing process.

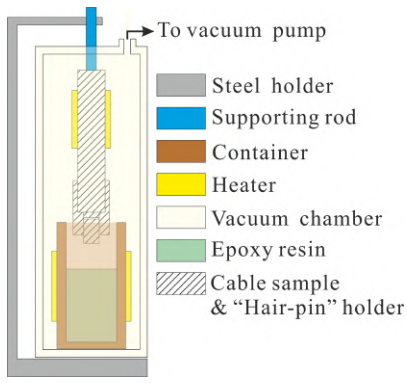

Figure 2.26: *Setup for vacuum impregnation of the U-shaped cable samples.*

In Figure 2.27 the vacuum impregnated samples are shown. In order to apply transversse pressure, the relatively flat surface of Rutherford cables needs to be longer than 46 mm after impregnation. In this case, the whole straight section of the cable is covered. The minimum length of the flat surface after impregnation shown in Figure 2.27 satisfies this requirement.

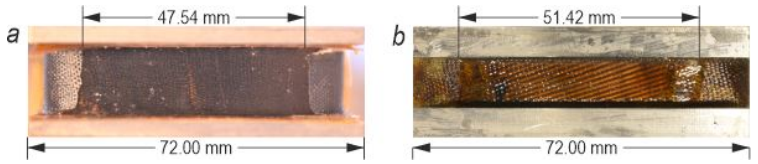

Figure 2.27: *Impregnated Nb_3Sn Rutherford cables showing the area where the transverse pressure is applied: (a) Cable DS-PIT-I; (b) Cable SMC-RRP.*

2.5.2.2 Impregnation of the *Re*BCO Roebel cables

The layered architecture of *Re*BCO tapes is very susceptible to thermal stress. Takematsu *et al.* [86] investigated the performance degradation of a *Re*BCO coil due to epoxy resin impregnation. The observed critical current degradation was explained by the difference in thermal contraction, from room temperature to 4.2 K, between the tapes of 0.25% and pure epoxy resin 1.33%. Kirby *et al.* [173] presented thermal contraction coefficients of *Re*BCO tapes and cables of -0.30% ± 0.05% from room temperature to 4.2 K. To match thermal contraction to the *Re*BCO tapes, the epoxy resin was mixed with powder fillers by Otten *et al.* [174]. The Araldite epoxy resin CY5538 / HY5571 filled to 50 wt% with fused silica powder was recommended for the impregnation of Roebel cables, as shown in Table 2.11. The average particle size of the powder is 4 μm. The epoxy resin has a low thermal contraction of 0.82% and a viscosity of less than 4500 mPa.s at 80 °C.

Table 2.11: Characteristics of Araldite CY5538 / HY5571 with 50 wt% with silica powder filler [174].

	Araldite CY5538 / Araldur HY5571 / Silbond FW600 EST
Viscosity at 80 °C (mPa.s)	< 4500
Mixing ratio in mass	1: 1: 2
Pot life	3 h at 80 °C
Curing schedule	24 h at 100 °C

Another way to influence the thermal contraction properties is adding glass fiber, as already shown in the previous paragraph. Kirby *et al.* [173] demonstrated a thermal contraction of 0.2% for a mixture of CTD-101K resin and glass-fiber. This thermal contraction is closer to *Re*BCO than the impregnation methods used by Otten *et al.* [174] and can also be easily applied for coil winding.

Since vacuum impregnation is essential for successful application of cables in magnets, three impregnation methods were compared for the *Re*BCO Roebel cables see Table 2.12. Note that a glass-fiber rope was inserted into the central gap of Roebel cables to prevent leakage of epoxy resin during the curing process, as well as to decrease the epoxy resins thermal contraction.
The positioning of the *Re*BCO Roebel cables on the sample holder is comparable to Nb_3Sn Rutherford cables, which was described in Section 2.5.2.1. The U-shape sample holder for Nb_3Sn Rutherford cables has a 10 mm bending radius. This value is too low for *Re*BCO Roebel cables. The minimum bending radius of *Re*BCO Roebel cables was measured by Otten *et al.* [174, 175]. Considering the asymmetry of *Re*BCO tapes and the corresponding asymmetry in

Table 2.12: Vacuum impregnation schemes.

Test	Cable samples	Epoxy	Additives
Transverse load	FM-SP-I FM-SP-II	Araldite-CY5538 / HY5571	Silica powder
	FM-SP-III FM-BR	CTD-101K	S-2 glass fiber sleeve & central rope
Inter-strand resistance	FM-SP-II-A FM-SP-II-B FM-SP-II-C	CTD-101K	S-2 glass fiber sleeve & central rope
AC loss	FM-SP-II-B	CTD-101K	S-2 glass fiber sleeve & central rope
	FM-SP-II-D	CTD-101G	Alumina powder & S-2 glass fiber sleeve

Roebel cables, the bending tests of the Roebel cables were performed with the superconducting layer facing inwards and outwards. According to the bending test results, 20 mm is considered a safe bending radius for *Re*BCO Roebel cables, not causing any I_c degradation. Therefore, the corner radius of the sample holder for *Re*BCO Roebel cables was increased to 20 mm.

To reduce the joint resistance between the secondary coil of the superconducting transformer and the Roebel cable sample, the *Re*BCO layer faces the sample holder. In addition, two stainless-steel plates insulated with Kapton tape are used to fix the cable to both sides of the U-shape sample holder, as shown in Figure 2.28. Tie wraps or glass-fiber tape are used to hold the stainless-steel plates and the sample holder during cable impregnations.

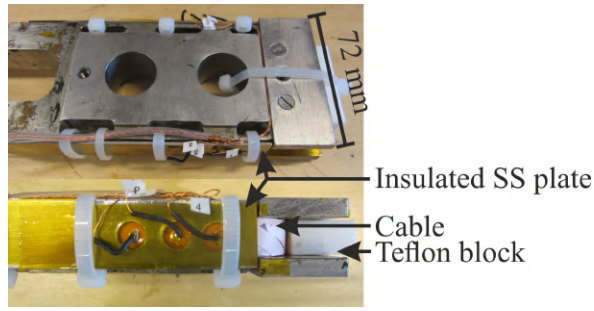

Figure 2.28: *Roebel cable sample before vacuum impregnation, top view and side view.*

The impregnation setup and procedures for Roebel cables is comparable to those used for Rutherford cables presented in Figure 2.26. In Figure 2.29 the vacuum impregnated samples are shown. To be able to apply transverse pressure, the relatively flat surface of Roebel cables needs to be longer than 26 mm after impregnation, and the sample in Figure 2.29 satisfy this requirement.

Samples used for inter-strand resistance and AC loss measurements were prepared at CERN using a different method. For this purpose a special mold for vacuum impregnation was built, as shown in Figure 2.30. To measure the inter-strand resistances, all strands at one cable terminal are connected to copper wires for voltage detection or current injection. A glass-fiber rope was inserted into the central hole of the cable and the cable was inserted in a glass-fiber sleeve.

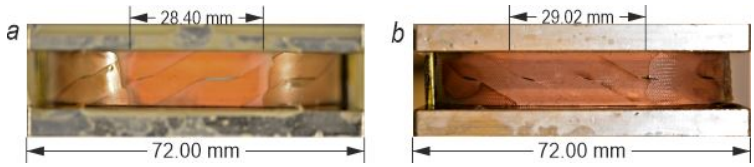

Figure 2.29: *Impregnated ReBCO Roebel cables showing the area where the transverse pressure will be applied: (a) Cable FM-SP-II; (b) Cable FM-SP-III.*

When clamped in the mold, about 5 MPa transverse pressure is applied to the cable surface to make sure that the strands get in touch. As mentioned in Section 2.5.1, cables FM-SP-II-A, -B and -C were prepared for inter-strand resistance measurements, while cables FM-SP-II-B and -D are used for AC loss measurements. The procedure for impregnation of cable FM-SP-II-D is similar as for FM-SP-II-B, but without using central glass-fiber rope and sense wires.

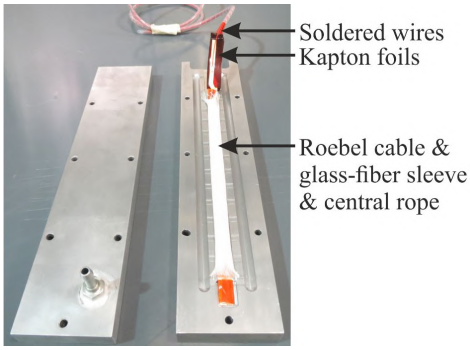

Figure 2.30: *Roebel cable sample prepared for vacuum impregnation used for inter-strand resistance and AC loss measurements.*

2.5.2.3 Alignment impregnation for transverse pressure measurement

The force needs to be applied uniformly over the pressure area during transverse pressure measurement for all cable samples. The alignment of pushing block and pressure surface is therefore crucial. The vacuum impregnation of the sample itself on the "Hair-pin" sample holder with the Teflon block as "placeholder" cannot ensure that the surface is perfectly aligned with the actual pushing block.

The misalignment of pushing block will result in a non-uniform stress distribution along the impregnated cables. A further analysis of this effect is presented in Chapter 3. To improve the alignment of pushing anvil and cable surface, an additional impregnation is applied, and shown in Figure 2.31. Two layers of glass-fiber tapes brushed with degassed Stycast® 2850FT / 23LV are added to the impregnated cable. A layer of Kapton tape is glued on the bottom surface of the anvil, as well as the inside faces of the two clamping plates. The anvil is positioned by using two spark eroded plates, which are fixed to the sample holder by two pins. After the epoxy resin has cured, the side plates and stainless-steel strips are removed. The method ensures that the anvil is now "perfectly" aligned to the pressed section of the sample holder. The transverse pressure can now be applied uniformly on the impregnated cable sections.

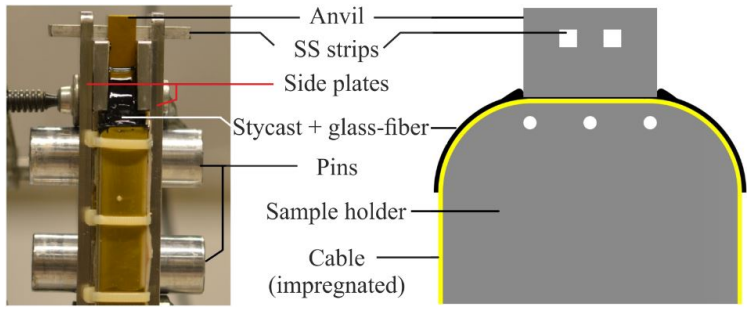

Figure 2.31: *Schematic of the alignment impregnation, to guarantee uniform force distribution of pressure block on the sample surface.*

2.5.3 Splice low-resistance process

Once impregnated, the sample is connected to the superconducting transformer used to introduce the sample current. The joints need to be as low-resistive as possible, since they determine how long a steady test current in the sample can be maintained [129]. The low-resistivity solder of Tin-Silver 96Sn4Ag, with a melting temperature 221 °C, is used for the Nb_3Sn samples. Low temperature solder In97Ag03, which melts at 143 °C, is used for the *Re*BCO since excessive heat may cause current degradation in the strands [176]. Copper plates are used ensuring a flat soldering surface of *Re*BCO cables, providing a homogeneous heat transfer and cable flat soldering surface. The soldered joint is over one transposition length for the Nb_3Sn Rutherford and Roebel FM-SP-I cables, and half transposition length for the Roebel FM-SP-II, -III and FM-BR cables, as shown in Figure 2.32. Glass-fiber tape straps soaked with Stycast and cured are used to fix the splice.

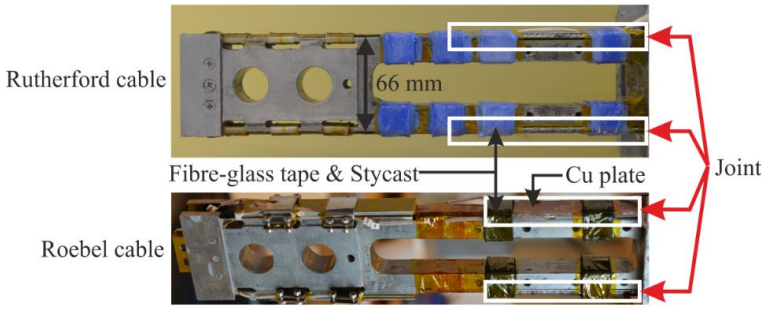

Figure 2.32: *"Hair-pin" sample holder with joints of Nb_3Sn Rutherford cable and ReBCO Roebel cable to the terminals of the transformer secondary coil.*

Another factor to consider in the lay-out of the joints is the current distribution in the cable, which has to be as homogeneous as possible. This requires identical contact resistances to individual strands. For the 10-strand cable FM-SP-I with a transposition length of 126 mm, this is achieved by making the soldered joint length equal to the transposition length, see Figure 2.33. However, this is not possible for the 15-strand cables FM-SP-II, -III and FM-BR, whose transposition length of 226 mm exceeds the length of the secondary transformer terminals. This implies that not every cable strand faces directly the current lead terminal. The solution is to solder only half a transposition length of the cables to the current terminals, while keeping

the cable section length in-between the joints equal to an integer multiple of the transposition length. This way, half the strands face the terminal in one joint, while the other half in the second terminal. As a consequence, all 15 strands will have about the same effective contact resistance. Note that an extra copper plate is used to reduce the overall contact resistance and to ensure a homogeneous heat distribution during soldering.

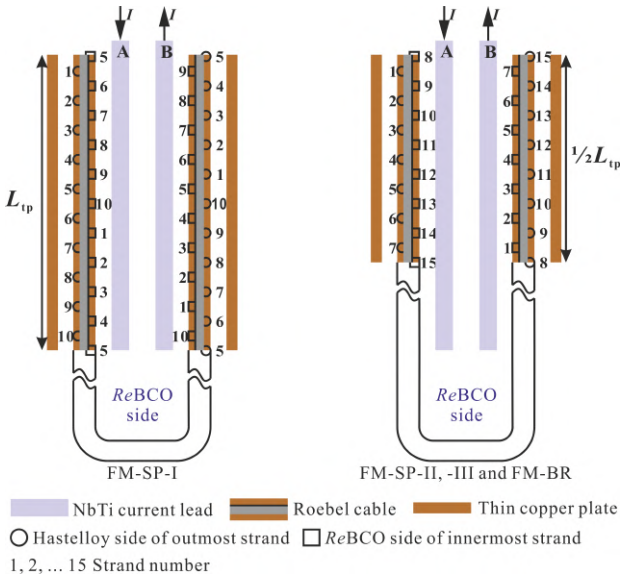

Figure 2.33: *Schematic lay-out of the soldered joints to the secondary of the superconducting transformer for Roebel cables.*

The joint resistances are calculated from the current decay data of the secondary closed loop. The resistance values are listed in Table 2.13. All values are smaller than 10 nΩ, and retain a relatively low level.

Table 2.13: Total joint resistance comprising two splices between the cable and secondary coil.

	Cable	Total circuit resistance (nΩ)
Nb_3Sn Rutherford	DS-PIT-I	3.0 ± 0.2
	DS-PIT-II	6 ± 1
	SMC-RRP	3.5 (3) ± 1.0 (1)
	SMC-PIT	3.0 (2.0) ± 0.5 (0.1)
*Re*BCO Roebel	FM-SP-I	6 ± 1
	FM-SP-II	3.0 ± 0.5
	FM-SP-III	3.0 ± 0.1
	FM-BR	2.0 ± 0.1

2.6 Uncertainty estimates

When determining the critical current of the superconducting Nb_3Sn and *Re*BCO cables under transverse pressure in Chapters 4 and 5, we will typically compare their critical current value at a given pressure with the value measured under 'zero'-stress conditions. To gauge whether

observed variations are significant or not, e.g. to determine the onset of irreversible degradation, it is essential to estimate the uncertainty in the measured critical current value. In this context it is required to differentiate between 'random' and 'systematic' measurement errors [177].

Random errors may originate from limits on the instrumental resolution, from fluctuating environmental factors or from slight variations in data processing. Systematic errors can occur due to less-accurate instrument calibration, to uncertainties in exact voltage tap position, to inaccuracies in models used for data processing etc. Such systematic errors will become especially important when comparing data measured with different set-ups, e.g. cable I_c data obtained at the University of Twente and at CERN; or when comparing experimental results with expectations, e.g. predicting a cable I_c value from single-strand data. On the other hand, systematic errors do not affect relative variations within the same experimental run on the same sample. To gauge the significance of such variations, an estimate of random errors is more important.

Below, the uncertainties involved in the measurement of the two main quantities in Chapters 4 and 5, critical current and transverse pressure, are estimated.

2.6.1 Uncertainty in the critical current

As discussed in Section 2.2.2.4, the critical current is measured with a superconducting transformer set-up in the familiar 4-point configuration, gradually stepping-up the current and each time measuring the corresponding cable voltage. An example of such an *E-I* curve is shown in Figure 2.34. The measured voltage is converted into an electric field E by dividing it by the voltage tap distance and the critical current is then determined as the current corresponding to an electric field criterion E_c, which is 10^{-5} V/m for the Nb_3Sn cables and 10^{-4} V/m for *Re*BCO. This process involves several uncertainties, which are listed below.

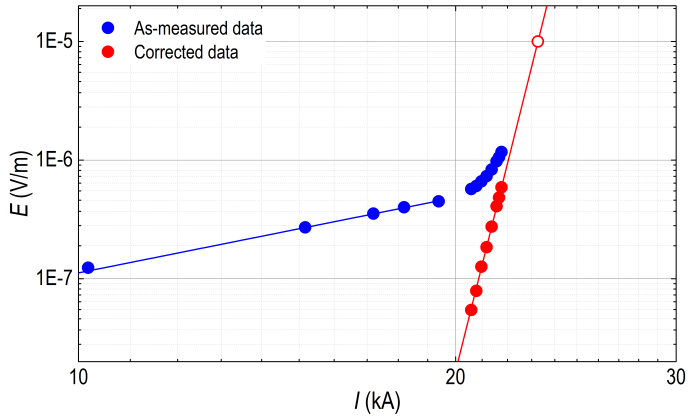

Figure 2.34: *Illustration of a typical E-I curve measured on one of the Nb_3Sn DS cables with an applied field of 10 T and a transverse pressure of 3 MPa. The blue symbols represent the raw data, the blue line is the fitted ohmic 'foot'. Subtracting this foot from the data, one obtains the red data points which can then be fitted with the well-known power-law (red line). The open symbol represents the extrapolated I_c value at an electric-field criterion of 10^{-5} V/m.*

Instrumental calibration and offset **(systematic error)**. The current is read out directly from the control loop that maintains its value in the secondary of the transformer constant by slowly

ramping up the primary current [178]. The control electronics sense the current via a Rogowski coil coupled via a superconducting integrator to a Hall probe. At the beginning of each measurement run, the read-out system is calibrated with a secondary loop that is inductively coupled to the same Rogowski. The corresponding relative error is estimated at 1 to 1.5%. Since the same calibration is used throughout a measurement run, this is a systematic error.

Resistive slope correction **(random error)**. The blue data points below 20 kA in Figure 2.34 correspond to a resistive onset of the *E-I* curve. This resistive slope is typically present in measurements on Nb_3Sn cable samples and originates in inter-strand current re-distribution at the corners of the U-shaped holder, where the relative orientation of the magnetic field changes and at the edges of the pressure anvil, where the stress in the cable changes [136]. It needs to be fitted and subtracted from the data in order to obtain the power-law type *E-I* curve representative for the superconducting transition itself, shown as the red data points in the Figure 2.34. Since the transition from resistive to power-law is gradual, the choice of the fitting interval is somewhat subjective. Trying out several intervals on several cables learns that the corresponding uncertainty in the critical current value introduced by this choice is once more about 0.5 to 1%. Since this procedure is repeated for each *E-I* curve, this error is random.

Uncertainty in voltage tap position **(systematic error)**. For Nb_3Sn cables, the voltage taps nominally span one half to one transposition length and are typically soldered to a single strand on the side of the cable. The transposition length is 100 mm for 40-strand DS cables and 63 mm for 18-strand SMC cables. The axial length of a strand along the cable side (Figure 2.18a) is 2.5 mm for DS cables and 3.5 mm for SMC cables, resulting in an uncertainty in the voltage tap position estimated as 2 mm, i.e. 2 to 4%. This relative uncertainty translates directly into an uncertainty in the electric field. However, since the exponent n of the power-law *E-I* curve is typically 20 to 40, the corresponding uncertainty on the critical current is quite modest, about 0.1%. Since the voltage taps are soldered only once, this is a systematic error.

E-I power law fit / extrapolation **(random error)**. The quality of the fit of the corrected *E-I* curve to the power-law expression and of its extrapolation to the E_c criterion depends on the number of measuring points and typically introduces a random uncertainty estimated at 0.3%.

Bath temperature **(random error)**. The University of Twente uses a closed helium recovery system, with all helium cryostats connected to a central storage balloon. Depending on the number of users and on the stored gas volume, the pressure in the cryostats might vary as much as 1 kPa during a day, leading to a boiling point variation of about 10 mK [179]. With the $J_c(T, B, \epsilon)$ scaling relation discussed in Chapter 3 shown as Equation (3.1), this translates for Nb_3Sn at 4.2 K and 10 T to a modest relative uncertainty of about 0.1% on the critical current value. Since these pressure fluctuations may occur within a given measurement run, this error is considered random.

Magnetic peak field value **(systematic error)**. The magnetic field values reported in Chapters 4 and 5 are peak magnetic fields, i.e. the maximum magnetic field value occurring on the superconductor within the cable. As discussed in these result chapters, the peak magnetic field is estimated by superposition of the applied background magnetic field and the sample's self-field. The self-field is calculated with an electro-magnetic model that assumes a homogeneous current distribution throughout the cable. However, on a local scale the magnetic field value may vary significantly. Assuming that a strand typically carries a current of 500 to 700 A and has a filamentary zone of diameter 600 μm, the self-field contribution of this strand will vary $\pm$ 0.3 to 0.5 T from one side of the zone to the other. Since this is the uncertainty in the peak

magnetic field and once more using the scaling relation expressed as Equation (3.1) discussed in Chapter 3, this translates to a significant critical current uncertainty of about 2 to 4% at a temperature of 4.2 K and an overall field of 10 T. Since the self-field calculation is performed just once for each sample, this error is systematic.

Adding up all the error contributions, we estimate a typical systematic uncertainty of 3 to 5% and a typical random uncertainty of 1 to 1.5% in the Ic-values reported in Chapters 4 and 5. The corresponding error estimates are summarized in Table 2.14.

Table 2.14: Estimated errors in the critical current measurement.

Source	Type (rand. / syst.)	Relative error (%)
Instrumental calibration and offset	systematic	1 to 1.5
Resistive slope correction	random	0.5 to 1
Uncertainty voltage tap position	systematic	0.1
E-I power law fit / extrapolation	random	0.3
Uncertainty bath temperature	random	0.1
Uncertainty peak field value	systematic	2 to 4
Total systematic error		3 to 6
Total random error		1 to 1.5

Especially this latter estimate has a direct impact on the determination of the irreversible pressure limit in the results chapters. At this point, the filaments start to crack and the critical current degrades irreversibly. Similar as with the single-strand experiments shown in Figure 1.9, this is detected by cycling the transverse pressure back to a reference critical current at low-level stress, repeating the low-stress critical current measurement and comparing the outcome with its earlier value. For a possibly observed reduction in critical current to be significant, it has to be larger than the random uncertainty 1 to 1.5%. Hence in Chapters 4 and 5 the criterion for determining the irreversible pressure limit is set as the pressure that causes an irreversible critical current reduction of 2%.

2.6.2 Uncertainty in the transverse pressure

To determine the uncertainty in the transverse pressure a different approach is taken. Rather than estimating different contributions a-priori, e.g. the friction acting on the force transmitting piston in Figure 2.11b, two independent methods are compared to measure the pressure and use the difference between them as an error estimate.

The pressure exerted on the cable can be derived by simply dividing the force with which the two NbTi flat coils described in Section 2.2.2.4 repel each other by the surface area of the pressure anvil. The force is calculated from the current with which the NbTi coils are excited, from their dimensions and from the distance separating them. Measuring this distance accurately with an extensometer and factoring in a correction due to the interaction between the electro-magnetic press and the main magnet [180], the force can be obtained with an accuracy of 2% [132]. The second method to measure the pressure is to monitor the deformation of the steel pressure anvil with the two strain gauges that are glued to its sides and to combine this information with its known Young's modulus to determine the stress state of the anvil, which is assumed to be uniaxial. The estimated accuracy of this method is similar to that of the force calculation, which is 3% [132].

If all the force exerted by the press coils is transmitted friction-less to the anvil and balanced there by the reaction force generated by the cable sample, plotting the outcome of these two pressure measurements against each other should in principle yield a curve with unit slope. Such a curve is indeed all but observed in Figure 2.35 for the SMC-RRP-II cable. In most cases some deviation will occur between the force-derived pressure value and the one determined from the strain gauge readings, e.g. for the DS-PIT-I cable in Figure 2.35. We will use the average intercept of these curves (one for each gauge) with the x-axis as an estimate for the uncertainty in the applied pressure. From Figure 2.35, this estimate is 3 MPa for cable sample SMC-RRP-II and 10 MPa for cable sample DS-PIT-I. In view of the observed linearity of the curves, we take this error to be systematic within a given measurement run.

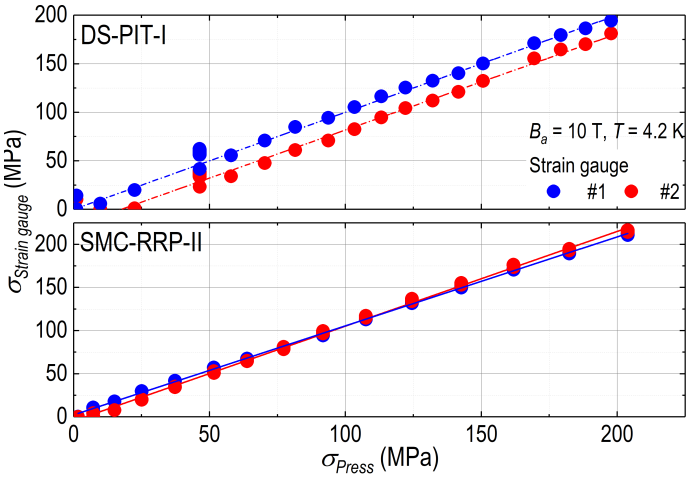

Figure 2.35: *Transverse stress calculated from the strain gauges, plotted against the transverse stress calculated from the current in the press and displacement of the upper press coil detected by the extensometer. The two different colors correspond to the two different strain gauges, one on either side of the pressure anvil.*

This analysis was carried out for all the experiments presented in Chapters 4 and 5, with the resulting uncertainty estimates reported in Table 2.15.

Table 2.15: Estimated errors in the transverse pressure.

Cable sample	Pressure uncertainty (MPa)	Cable sample	Pressure uncertainty (MPa)
DS-PIT-I *	± 10	FM-SP-A	-
DS-PIT-II *	± 30	FM-SP-B	± 5
SMC-RRP-I *	± 32	FM-SP-C	± 15
SMC-PIT-I *	± 23	FM-SP-II	± 3
SMC-RRP-II	± 3	FM-SP-III	± 5
SMC-PIT-II	± 3	FM-BR	± 3

* The cable samples were not prepared with an alignment impregnation, as described in Section 2.5.2.3. For sample SMC-PIT-II, one of the strain gauge readings deviated about 100 MPa from the other one and from the force-derived pressure. This improbable value was likely due to a fault in the gauge wiring and was discarded. The gauge readings for sample FM-SP-I-A were not recorded.

2.7 Summary

Various facilities have been designed worldwide to investigate the critical current degradation of superconducting wires, tapes and cables when exposed to transverse pressure. The test station at the University of Twente is unique worldwide, as the effect of applying transverse pressure on a sample surface of 20 mm × 40 mm with a force of 250 kN at 4.2 K and magnetic field up to 11 T can be investigated while varying the pressure in-situ. The UT test station is equipped with a superconducting transformer to supply the current to cable samples with maximum current capacity of 100 kA, which is much higher than in other test stations. A maximum pressure of 370 MPa for 15 mm-wide and 550 MPa for 10 mm-wide Rutherford cables are applicable, while this is approximately 690 MPa for 12 mm-wide Roebel cables.

The inter-strand contact resistance measurements for impregnated *Re*BCO Roebel cables were carried out using a direct transport-current method at 77 and 4.2 K in self-field environment. The magnetic method based on the pick-up coil technique and the calorimetric method based on boil-off technique are used in this research to examine the AC loss of impregnated Roebel cables at 4.2 K in a dipole magnet generating an AC field up to ±1.5 T and frequency up to 1 Hz.

Six Nb_3Sn Rutherford cables, including two so-called DS cables and four SMC cables, were investigated for their transverse pressure effect. Six *Re*BCO Roebel cables made from SuperPower and Bruker tapes were investigated as well. The DS and SMC cables are impregnated with CIBA GEIGY Araldite and CTD-101K, respectively. For Roebel cables FM-SP-I and -II, the Araldite CY5538 / HY5571 epoxy resin is used. Cables FM-SP-III and FM-BR are impregnated with CTD-101K. All the epoxy resins are mixed with proper fillers, e.g. glass-fiber or silicon powder, to better match the thermal contraction of insulator and tapes. To improve the alignment between pushing block and surface of the impregnated cables, an additional alignment impregnation is applied at room temperature. A low joint resistance, smaller than 10 nΩ is required for maintaining sufficiently long the test current in the sample. For this purpose, the low-resistivity solder 96Sn4Ag is used for Nb_3Sn Rutherford cables. For *Re*BCO Roebel cables, a low-temperature solder like In97Ag03 is used to avoid damage caused by the excessive heat.

The three *Re*BCO Roebel cables FM-SP-II-A, -B and -C impregnated with CTD-101K are used for the inter-strand resistance measurements. Afterwards, two cables FM-SP-II-B and -D are used for AC loss investigation in different magnetic field orientations. Cable FM-SP-II-D has the same architecture as cable -B, but is impregnated with a different epoxy resin CTD-101G, filled with alumina powder.

The random uncertainty in the cable's critical current values was estimated at 1 to 1.5%. Based on this estimate, an irreversible current degradation of 2% was selected as criterion for the determination of the irreversible pressure limit. The systematic uncertainty in I_c was estimated at 3 to 6%. This error value is relevant when comparing measurement results between labs and between cable- and strand data. The systematic uncertainty in the transverse pressure applied to the Nb_3Sn cables is 10 to 30 MPa before the introduction of the alignment impregnation. With this second impregnation, the uncertainty significantly reduced to about 3 MPa. For the *Re*BCO cable samples, the error in the pressure readings is estimated at 5 to 15 MPa.

Chapter 3
Modelling

In this chapter, three types of models are presented that support the later discussion of the results described in Chapters 4 to 6. First, in Section 3.2, three simplified finite-element models of Nb_3Sn Rutherford-type cables are described to demonstrate how their mechanical response is influenced by resin impregnation and by the details of their confinement. Next, in Section 3.3, an electrical network model is drawn up to estimate the various contributions to the inter-strand resistance in a ReBCO Roebel-type of cable. Finally, in Section 3.4, several analytical AC loss models are represented from literature, allowing to estimate and compare the different loss contributions that may occur in Roebel-type of cables.

3.1 Introduction

The mechanical models that are first discussed in this chapter, are aimed at understanding the influence of epoxy resin impregnation, of glass-fiber reinforcement and of the detailed cable confinement on the transverse pressure tolerance of the critical current density in Nb_3Sn Rutherford cables presented in Chapter 4. It is well-understood how the critical current density in Nb_3Sn strands is determined, besides by temperature and magnetic field, by the deviatoric strain that is experienced by the strand's filaments [120, 181]. In accelerator magnets, such strain will typically be due to a combination of stresses imposed during cable- and magnet assembly, of differential thermal contraction during cool-down and of Lorentz force when the magnet is excited. Modelling the resulting strain state of the micron-sized filaments taking into account all the components of a meter-sized magnet as well as their thermo-mechanical history is a daunting task [182–186], which falls beyond the scope of this thesis.

Instead, we limit ourselves in Section 3.2 to strongly simplified 2D plane-strain models of the cable, which we solve numerically using COMSOL Multiphysics. These solutions give semi-quantitative insight in the effect of impregnation and reinforcement on the average deviatoric strain that is experienced by transversely compressed strands, as well as in the importance of possible misalignment of the cable and the resulting stress concentration that may occur in the transverse pressure experiment presented in Section 2.2 of the previous chapter, but also in the winding pack of actual magnets.

The second type of model is an electrical one, aimed at understanding which factors dominate the strand-to-strand contact resistance in the *Re*BCO Roebel cables presented in Chapter 6. Earlier literature on the electrical tape-to-tape resistance in coated conductors mainly focused on soldered or welded lap joints that are needed for current leads or to extend the length of magnet windings [187–195]. However, recent interest in no-insulation pancake- or racetrack-type coils for stationary applications [196–200] as well as the steady development of various *Re*BCO cable types [100, 102, 201–204] has raised the question of how the direct contact resistance between two tapes, i.e. the electrical resistance without intermediate soldering or welding layer, is influenced by the internal layout of the coated conductor and by external factors such as temperature, transverse pressure or surface condition. This question, which has a direct impact on issues such as current sharing, thermal stability and AC loss, is addressed experimentally in Chapter 6.

To answer this question a-priori, in Section 3.3 a straightforward resistor network model is proposed, in which the current path from the superconducting layer in one tape to the following layer in the neighboring tape is split up into several components. The magnitude of each of these components is then estimated based on the layout and on the material properties of a typical *Re*BCO coated conductor.

The third type of models presented in this chapter are analytical predictions of the AC loss in *Re*BCO Roebel cables exposed to an external magnetic field. Such loss is well understood and documented for cabled structures assembled from round multi-filamentary strands [136, 205, 206]. They can be subdivided into three parts: hysteresis loss due to the motion of magnetic flux inside the filaments; ohmic eddy-current loss due to the currents that are induced in metallic parts of the strands and the cable; and coupling loss due to currents that cross over between the filaments within the strands or between the strands within the cable.

For cables based on coated conductors, this classification still holds but the situation is com-

plicated by the intrinsic anisotropy of the *Re*BCO material and by the high aspect ratio of the strands [133]. For these reasons, authors often resort to numerical models to predict the loss in *Re*BCO cables [141, 207–213]. In this thesis however, we limit ourselves to analytical estimates, which are presented in Section 3.4 and compared to the measured data in Chapter 6.

3.2 Mechanical Nb_3Sn cable modelling

3.2.1 Introduction

The inherent assumption behind the mechanical modelling of superconducting cables in order to predict their critical current is the existence of a unique relation between the critical current density J_c and mechanical strain ϵ. In Nb_3Sn, the establishment of such a relation started with the observation by Ekin *et al.* [214] that the strain susceptibility of Nb_3Sn wires increases as one approaches the upper critical field B_{c2}. This lead him to suggest that $B_{c2}(T, \epsilon)$ itself was strain-susceptible and to formulate a Fietz-Webb type [215] of scaling approach to describe the strain susceptibility of $J_c(T, B, \epsilon)$ throughout the temperature-magnetic field domain [155]. Ten Haken *et al.* [121] picked up on this idea and showed that the key factor in this description is the deviatoric strain component ϵ_{dev}. Meanwhile, this type of scaling description has been refined by further experimental observations [216, 217] and the role of deviatoric strain has been understood a-priori in terms of the disruption that it causes in the crystal structure and hence in the electronic density of states [181, 218–220].

A widely-used form of the strain scaling relation is [216]:

$$J_c(T,B,\epsilon) = \frac{C_1}{B} s(\epsilon_{dev}) \left(1-t^{1.52}\right)\left(1-t^2\right) b^p (1-b)^q, \tag{3.1}$$

where the strain function $s(\epsilon_{dev})$ describes the strain-dependence not just of J_c, but also of the critical field $B_{c2}(T, \epsilon)$ and of the critical temperature $T_c(B, \epsilon)$. It can be expressed as:

$$s(\epsilon_{dev}) = \frac{J_c(T,B,\epsilon_{dev})}{J_c(T,B,0)} = \frac{B_{c2}(0,\epsilon_{dev})}{B_{c2}(0,0)} = \left[\frac{T_c(0,\epsilon_{dev})}{T_c(0,0)}\right]^3, \tag{3.2}$$

where $s(\epsilon_{dev})$ depends on what is often loosely referred to as the 'deviatoric strain', more precisely on the square root of the second strain invariant [221]:

$$\epsilon_{dev} = \frac{2}{3}\sqrt{(\epsilon_x-\epsilon_y)^2+(\epsilon_y-\epsilon_z)^2+(\epsilon_z-\epsilon_x)^2}, \tag{3.3}$$

while t and b are the reduced temperature and magnetic field, respectively:

$$t = \frac{T}{T_c(0,\epsilon_{dev})}; \quad b = \frac{B}{B_{c2}(T,\epsilon_{dev})}. \tag{3.4}$$

C_1, p and q are strand-specific fitting parameters. Several forms of varying sophistication and complexity have been proposed for the strain function $s(\epsilon_{dev})$ [216]. For the purpose of our J_c estimates in Section 3.2.4, we use the straightforward form that was originally suggested in [120]:

$$s(\epsilon_{dev}) = 1 - \frac{C_{dev}}{B_{c2}(0,0)}\sqrt{\epsilon_{dev}^2+\epsilon_{0,d}^2}, \tag{3.5}$$

where C_{dev} is a fitting constant and $\epsilon_{0,d}$ is the residual strain.

Having established the current-strain relation, we can turn our attention to the influence of impregnation on the deviatoric strain. To investigate the effect of epoxy resin on the strain state of a single Nb_3Sn wire, Ten Haken *et al.* [120] modeled a homogeneous cylinder surrounded by epoxy resin and pressed between two rigid plates, as shown in Figure 3.1. He found that impregnation reduces the deviatoric strain throughout the cylinder considerably, especially on its mid-plane, and becomes nearly uniform already for epoxies with a moderate Young's modulus (>10 GPa).

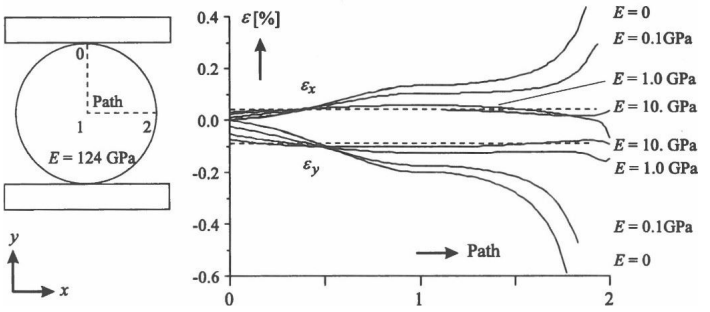

Figure 3.1: *Straightforward model of a single strand embedded in epoxy resin and pressed, laterally unconstrained, between two plates with a pressure of 100 MPa. The dashed lines in the right graph represent the limit where the Young's modulus of the epoxy resin equals the one of the strand (from* [120]).

More recently, at CERN [222] and at the University of Geneva [109] more detailed 2D FE modelling of a similar transverse loading situation essentially has led to the same qualitative conclusion, with taking into account the internal strand architecture. However, these detailed simulations also yield the strain distribution among the filaments and can be combined with the current-strain relation presented in Figure 3.1 to predict the reversible critical current reduction of the transversely stressed impregnated strands quantitively. When comparing such predictions with experimental data on various PIT-type strands, both papers report satisfactory agreement with experiments, certainly for un-twisted filaments. Moreover, by comparing the modelled Von Misses stress with the elastic-to-plastic yield limit of the copper matrix and with the ultimate strength of the filaments, the University of Geneva group was also able to predict the irreversible strain limit, including its correlation with strand diameter [109] and with stress concentrations at filament voids [223]. Turning our attention to impregnated Rutherford-type cables, Van Oort *et al.* [224] also used a straightforward 2D FE model with homogeneous cylindrical strands to investigate the effect of the epoxy. He reported a decreasing stress susceptibility of reversible J_c with increasing epoxy stiffness and a higher irreversible stress limit with increasing yield strength of the resin. Lately, this was confirmed at CERN on more realistic cable lay-outs by comparing FE modelling both with measured stress distribution profiles [146] and with measured critical current data [184].

From this brief and far from comprehensive literature review, it is clear that FE modelling has evolved into a powerful tool that is able to predict the critical current of mechanically loaded Nb_3Sn Rutherford-type cables quantitatively, especially when combining detailed knowledge of cable- and strand layouts and accurate material properties with state-of-the-art computation power. However, as the earlier work in [120,224] shows, even relatively straightforward models

yield a semi-quantitative insight into the role of the various geometrical and material-specific parameters involved. Below, we follow such a semi-quantitative approach to evaluate the role of the epoxy stiffness and Poisson ratio; of the glass reinforcement that is used both in the experiments in this thesis and in actual magnets; and of the details of the cable's geometrical confinement.

All mechanical models in this chapter are constructed with COMSOL Multiphysics as 2D plane-strain problems, i.e. assuming that the tensile strain ϵ_z, the shear strains ϵ_{yz} and ϵ_{zx} are zero taking z as the axial cable direction [221]. This assumption is appropriate for the experiments described in Chapters 4 and 5, where the cable samples are axially fixed on a holder over a length that is much larger than their thickness and width. To simplify modelling further, the mechanical properties of Nb_3Sn are applied uniformly across the cross-section of the strands, just like in [120, 224]. The impact of this uniform-strand assumption is investigated in the 18-strand cable model of Section 3.2.4, where the deviatoric strain variations due to misalignment angle are modelled with and without internal strand structure. All models assume a symmetrical cable architecture. The cross-section of the glass-fiber sleeve is assumed to be rectangular with round corners following the diameter of the strands.

3.2.2 Influence of the epoxy properties on the deviatoric strain

The straightforward isotropic 2-strand model presented in Figure 3.2 is a simulation of the 'hair-pin' sample holder that is used in the transverse pressure experiments. The uniform strands have a diameter of 1 mm and are fully surrounded by an epoxy resin with a Young's modulus ranging from 1 to 40 GPa and a Poisson's ratio ranging from 0.1 to 0.4. A normal pressure of 100 MPa is applied to the top of the impregnated sample over a section of 1.2 × 46 mm^2 with a stainless-steel anvil. The total thickness of the impregnated stack is 2.6 mm, with a distance of 0.1 mm in-between the two strands. The assumed mechanical properties of various materials at 4.2 K are presented in Table 3.1. The bottom edge of the epoxy is fixed, the left and right sides of the stack and of the anvil are modelled as 'sliding boundaries', which implies that no displacement in horizontal direction can occur at these boundaries.

Table 3.1: Mechanical properties of various materials used in the 2-strand model.

T = 4.2 K	E (GPa)	ν
Nb_3Sn	75[225]	0.36[109]
Epoxy	1 to 40	0.1 to 0.4
Stainless steel 316L	207[225]	0.284[225]

Due to the symmetry in the model, only the average deviatoric strain $<\epsilon_{dev}>$ acting on strand-1 is calculated and presented in Figure 3.3 as a function of the Young's modulus E_{epoxy} and the Poisson's ratio ν_{epoxy} of the epoxy resin. With increasing Young's modulus and Poisson's ratio, $<\epsilon_{dev}>$ decreases. This can be understood intuitively. As the epoxy becomes stiffer (larger E_{epoxy}) it carries a larger fraction of the force and the stress exerted on the strand becomes smaller, causing a corresponding reduction of the strain in the strand. A larger Poisson's ratio of the epoxy resin on the other hand, increases its bulk modulus [221], as defined following Equation (3.6), and thus renders the stress distribution more hydrostatic:

$$k_{epxoy} = \frac{E_{epoxy}}{3\left(1-2\nu_{epoxy}\right)}. \tag{3.6}$$

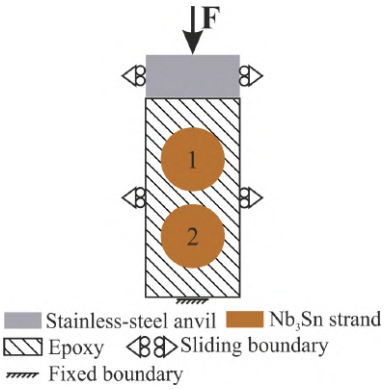

Figure 3.2: *2D mechanical model comprising a stack of two Nb_3Sn strands.*

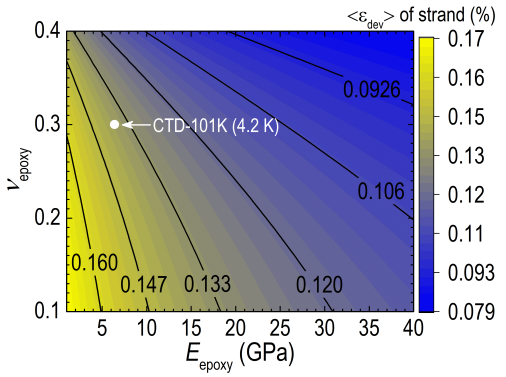

Figure 3.3: *Variation of average deviatoric strain acting on strand-1 with respect to the Young's modulus and Poisson's ratio of epoxy resin.*

Correspondingly, the x- and y-strains inside the strand become more similar, which also results in a reduction of $<\epsilon_{dev}>$. It can thus be concluded that using an epoxy resin with either a large Young's modulus or a large Poisson's ratio reduces the deviatoric strain component acting on the strand and hence increases its critical current. In the transverse pressure experiments of Chapters 4 and 5, the epoxy resin CTD-101K is used, with a reported Young's modulus E_{epoxy} of 6.44 GPa and a Poisson's ratio ν_{epoxy} of 0.3 at 4.2 K [144]. These values are indicated by the dot in Figure 3.3.

3.2.3 Influence of a glass reinforcement on the deviatoric strain

As discussed in Section 2.5.2, vacuum impregnation with epoxy is commonly applied in accelerator magnets to enhance the coils' mechanical properties. For large-scale magnets, the epoxy resin CTD-101K [171] is often used due to its long pot life and low viscosity at 40 °C (60 h and 400 mPa.s, respectively, as presented in Table 2.8). In addition, a glass-fiber sleeve is often applied around the cables to ensure adequate electrical turn-to-turn isolation. As added advantages, compared to the pure epoxy resin the combination of CTD-101K and glass-fiber not only has a thermal contraction coefficient that is much closer to the one of the Nb_3Sn cables, but also a larger Young's modulus. The orthotropic mechanical properties of the glass-resin composite are presented in Table 3.2.

Table 3.2: Mechanical properties of CTD-101K with S-2 glass-fiber sleeve [144].

T = 4.2 K	E_x / E_y / E_z (GPa)	ν_x / ν_y / ν_z	G_x / G_y / G_z (GPa)
CTD-101K & glass-fiber sleeve	39.4 / 19.7 / 32.9	0.21 / 0.12 / 0.22	9 / 4.917 / 9

We can adapt our simple cable model of Figure 3.2 to include the glass and thus to estimate the change in the average deviatoric strain in the strand due to the glass-fiber. The resulting 2D mechanical model is presented in Figure 3.4. It has the same size and boundary constraints as the 2-strand model of Figure 3.2, but this time the medium enclosing the strands has three different regions: the epoxy resin mixed with glass-fiber, the pure epoxy resin inside- and outside the glass-fiber. The thickness of the glass-fiber is taken to be 50 μm, the minimum distance between glass-fiber and strand is also 50 μm. As before, transverse pressure is applied to the

top surface of the impregnated sample stack through the anvil.

The average deviatoric strain $<\epsilon_{dev}>$ acting on strand-1 with and without the glass-fiber is plotted against applied pressure in Figure 3.5. The difference in deviatoric strain with and without glass is proportional to the applied pressure, with the strands in the sample impregnated with CTD-101K mixed with glass-fiber experiencing a 5% lower average deviatoric strain compared to the sample impregnated with pure CTD-101K.

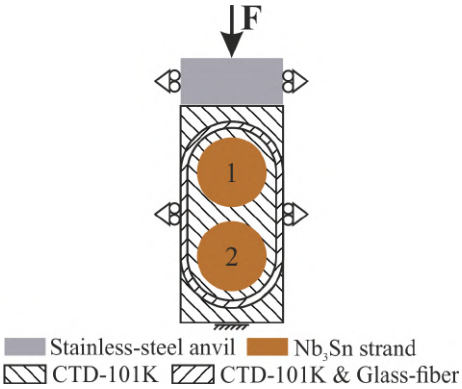

Figure 3.4: *2-strand model including epoxy resin & glass-fiber sleeve.*

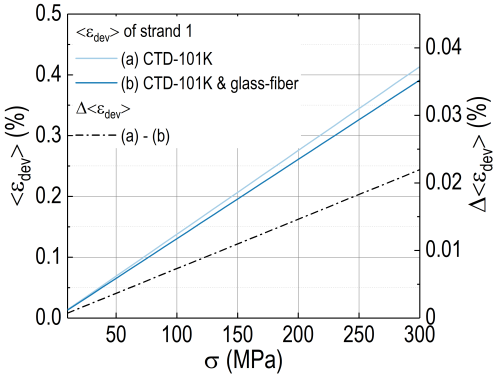

Figure 3.5: *Average deviatoric strain acting on strand-1 with and without using the glass-fiber (left axis) and the difference between both (right axis) plotted against the applied pressure.*

3.2.4 Influence of the confinement geometry on the deviatoric strain (effect of the alignment impregnation)

As discussed in Chapter 4, the Nb_3Sn cable samples SMC-RRP-I and -PIT-I initially showed an irreversible pressure limit 170 ± 25 and 125 ±10 MPa, respectively, which is considerably lower than expected. A possible reason for this is a misalignment between the impregnated cable and the pressure anvil. For cable samples SMC-RRP-II and -PIT-II, an additional 'alignment impregnation' step, described in Section 2.5.2.3, was introduced to improve the interface parallelism. As a result, the measured transverse pressure tolerance of these two types of cable improved significantly to an irreversible pressure limit larger than 190 ± 3 and 150 ± 3 MPa, respectively.

To estimate how significant the effect of misalignment is on the deviatoric strain in the strands of the measured Nb_3Sn cables, as well as to understand better how the alignment impregnation improves the transverse stress tolerance of the cables, a 2D mechanical model for impregnated cables was developed, as shown in Figure 3.6. Just like in the previous models, a constant force is applied to the stainless steel anvil while the left and right boundaries of both the anvil and the impregnated cable sample are defined as sliding. Also like in the models above, the strands are represented as uniform Nb_3Sn cylinders. The input variable d_s in the COMSOL simulations is the vertical displacement of the anvil, while g_s is the initial vertical gap that is left on the "non-touching" edge of the cable when d_s is zero, the anvil first comes into contact with the sample at the other edge. θ is the misalignment angle between the anvil and the sample surface.

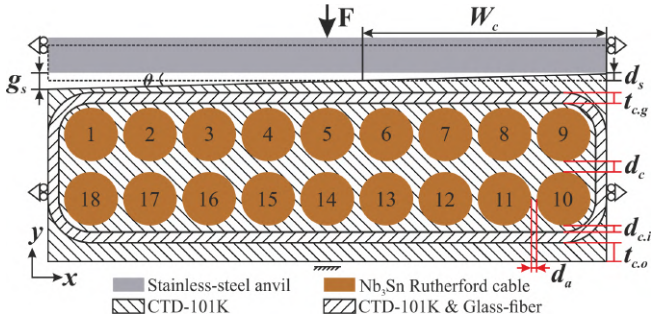

Figure 3.6: *2D mechanical model with misalignment interface.*

The various geometrical parameters of the cable model of Figure 3.6 are summarized in Table 3.3. The 1 mm diameter strands are surrounded by pure CTD-101K epoxy resin. The minimum distance $d_{c.i}$ between strands and the glass sleeve is 50 μm. Within one strand layer, neighboring strands are separated a distance d_a of 50 μm apart while the vertical distance dc between the strands in the two layers is 100 μm. This structure is enveloped in a glass-fiber sheet with a thickness $t_{c.g}$ of 50 μm. An additional 100 μm thick pure epoxy resin layer is assumed outside the glass at the top and the bottom of the resulting sample stack. Nb_3Sn, epoxy resin and glass-fiber properties are taken the same as in the previous models, as listed in Tables 3.1 and 3.2.

Table 3.3: Dimensional parameters of the 2D mechanical model of the cable architecture.

Parameter	Description	Unit	Value
r	Radius of the strand	mm	0.5
$t_{c.o}$	Thickness of the outer CTD-101K	mm	0.1
$t_{c.g}$	Thickness of CTD-101K & glass-fiber	μm	50
$d_{c.i}$	Distance between strand and glass-fiber	μm	50
d_a	Distance between neighboring strands in the same layer	μm	50
d_c	Distance between neighboring strands in different layers	mm	0.1

In Figure 3.7 the calculated average deviatoric strain acting on the strands in the top layer of the cable is shown for a perfectly aligned experiment ($\theta = 0°$) and for an experiment with a small misalignment angle ($\theta = 0.2°$). In both cases, the force applied by the anvil is 20 kN, corresponding to a nominal pressure of 40 MPa. Strikingly, in the misaligned case the deviatoric strain in strand 9, the strand situated directly below the 'first contact' area of the anvil, is about 3 to 3.5 times higher than in the 'perfect' experiment. As we move from the right to the left (from strand 9 to strand 3 in Figure 3.6), the deviatoric strain decreases approximately linearly. For the left-most strands 1 and 2 the strain becomes less position-dependent. These observations can be understood in terms of geometrical factors, as sketched in Figure 3.8. For a non-zero misalignment and relatively low anvil displacement d_s, only part of the anvil is in contact with the sample, with an "overall" strain $\epsilon_y(x)$ that decreases linearly from right to left over the width of the contact area w_c. As long as $d_s < g_s$, w_c will be smaller than the sample width and a gap remains between the anvil and sample on the left-hand side.

In reality, the strain concentration shown in Figure 3.7 can be expected to be even larger on a filament level. The figure shows the modelled deviatoric strain in homogeneous Nb_3Sn cylindrical 'strands', not taking into account the internal strand composition. More detailed FE

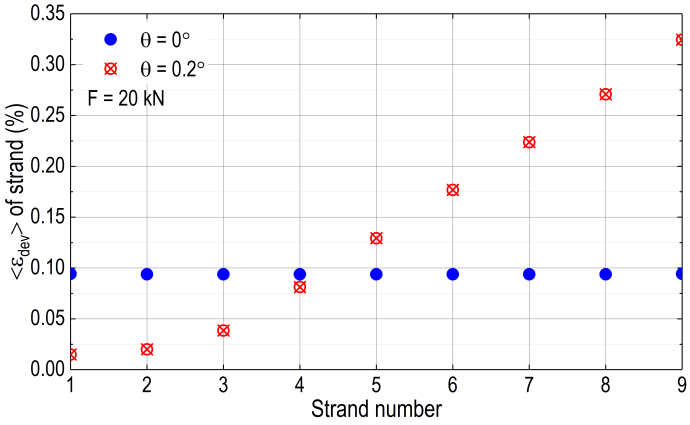

Figure 3.7: *Comparison of the average deviatoric strain distributions.*

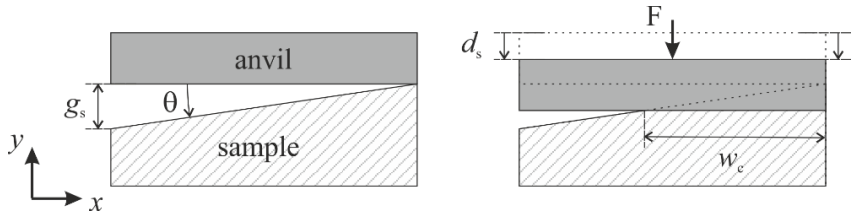

Figure 3.8: *Schematic geometry of the compressed sample in the case of a non-zero misalignment angle θ.*

modelling shows that further stress- and strain- concentrations occurs within the filamentary zone of the strands [109,186,223]. As mentioned in the Section 3.1, such detailed level of modelling falls outside the scope of this thesis, but also here we can get a feeling for the magnitude of this effect from a strongly simplified model. The strain calculation using the cable model shown in Figure 3.6 was repeated, but this time replacing the homogeneous Nb_3Sn cylinders by strands modelled as in Figure 3.9.

In this simple refinement, the 1 mm diameter strand is modelled as an octagonal uniform Nb_3Sn zone surrounded by a cylindrical copper matrix, and containing a central copper core. The Cu to non-Cu ratio of 1.22 is taken from the SMC-RRP strand presented in Section 2.5 (Figure 2.19 and Table 2.2). The diameter of the copper core r_i is 200 μm. The Young's modulus and Possion's ratio of the copper are set to 137 GPa and 0.35 [109], respectively. Running the calculations of the model in Figure 3.6 again and comparing the average deviatoric strain in the filamentary zone of this refined strand model with the one in the homogeneous strand, reveals a further increase of $<\epsilon_{dev}>$ with about 33%, as shown in Figure 3.10.

The model outcomes presented in Figures 3.7 and 3.10 can now be combined with the strain scaling relation for the critical current density $J_c(T, B, \epsilon)$ introduced in Section 3.2.1, following Equation (3.1), to obtain a rough estimate of the effect of sample-anvil misalignment on the critical current measured in the press experiment, as described in Section 2.2.2.4. Once more, we take an as simple as possible approach: the calculated average deviatoric strain in the

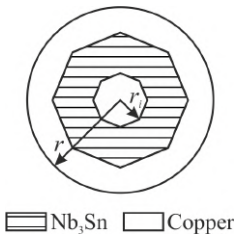

Figure 3.9: *Layout of the refined strand model.*

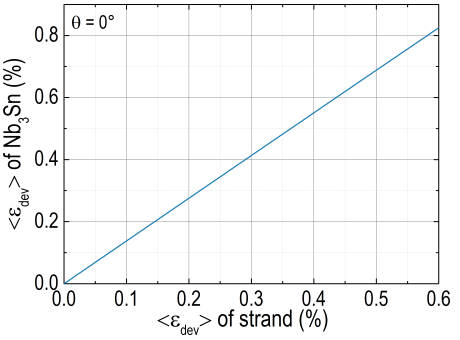

Figure 3.10: *Average deviatoric strain in the filamentary zone of the refined strand model, plotted against the average deviatoric strain in the uniform strand model.*

filamentary zone of model strand 9 is inserted in Equation (3.1), using the typical scaling-law parameters given in Table 3.4, and is assumed to dominate the overall pressure response of the critical current of the whole cable. Note that this is a rather crude approximation, neglecting possible effects of current redistribution among filaments or strands and assuming that the magnetic peak-field location, see Section 4.2.1, coincides with the region of maximum stress concentration. The result is shown as the solid lines in Figure 3.11. The blue line is calculated for perfect alignment when θ is 0°, while the green curve is obtained with a misalignment angle θ of 0.15°. Strikingly, even this small a misalignment causes a 13% lower I_c value at a transverse pressure of 200 MPa compared to the perfectly aligned case.

Table 3.4: Scaling-law parameters (Equation (3.1)) used to calculate the effect of strain on I_c [120].

Parameter	Description	Unit	Value
$B_{c2}(4.2\ K,\ 0)$	Upper critical magnetic field at 4.2 K and zero strain	T	26.38
$T_{c2}(0,\ 0)$	Critical temperature at zero field and strain	K	16.8
B	Applied magnetic field	T	11.63
T	Operation temperature	K	4.2
C_1	Scaling constant	AT/mm^2	46300
C_{dev}	Strain constant	-	1000
p	Low field exponent of the pinning force	-	0.5
q	High field exponent of the pinning force	-	2
e_{0d}	Residual strain component	%	0.09

The symbols in Figure 3.11 represent measurements on SMC-RRP cables that will further be discussed in Chapter 4. Here we suffice to say that the only difference between the two cable experiments is the alignment impregnation, as shown in Section 2.5.2.3, that was applied to cable sample SMC-RRP-II but not to the identical cable SMC-RRP-I. The exact shape of the calculated $I_c(\sigma)$ curve when θ is 0.15° differs from the detailed trend in the SMC-RRP-I data, which is not too surprising given the crudeness of the mechanical and electrical models. But at higher pressures the I_c magnitude of the calculated reduction compared to the simulation when θ is 0° and of the measured SMC-RRP-I data compared to the SMC-RRP-II data is similar. This suggests that the alignment impregnation is indeed effective in avoiding strain concentrations in the cable samples.

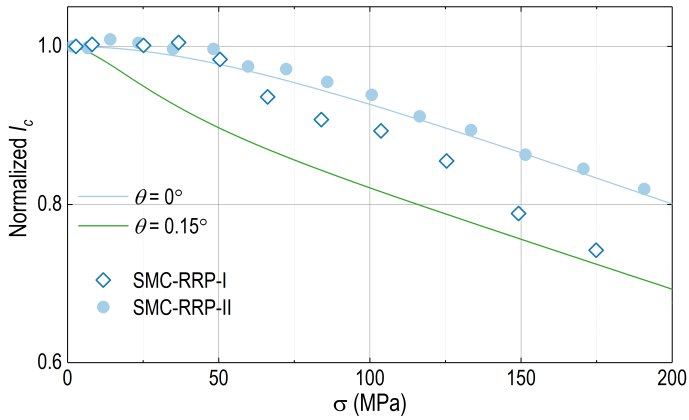

Figure 3.11: *Normalized critical current versus transverse stress. Influence of a small misalignment angle on the pressure-dependence of the critical current. The lines represent model calculations, the symbols experimental data obtained for cable samples SMC-RRP-I without the alignment impregnation and -RRP-II with the alignment impregnation.*

To investigate the effect of the alignment impregnation further, the calculations on the cable model of Figure 3.6 are repeated once more, but this time filling the gap between the anvil and the sample with a mixture of Stycast 2850FT and glass fiber, as shown in Figure 3.12. No literature data was found on the mechanical properties of a Stycast and glass-fiber mixture at 4.2 K. Instead, we used data published in [146], reporting a Young's modulus of pure Stycast at 77 K in the range 22 to 29 GPa. To account for the lower temperature of 4.2 K and for the glass layers, we assume a high-end value of 30 GPa. Since no published data was found for the Poisson's ratio, two extreme values are used: 0.1 and 0.4.

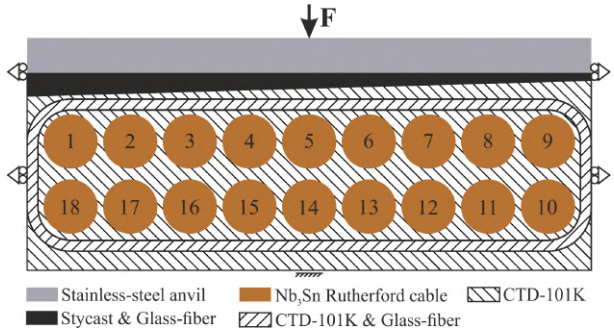

Figure 3.12: *2D mechanical model with alignment impregnation.*

The results calculated for this model are presented in Figure 3.13, including, for comparison, also the previously shown results of the model in Figure 3.6. Both models were simulated assuming a misalignment angle θ of 0.2°. Clearly, also in the model the alignment impregnation virtually eliminates the effect of the misalignment angle, reducing the variation of the deviatoric strain between the strands to less than 1%, and yielding a $<\epsilon_{dev}>$ value that is near-identical to the one found for θ is equal to 0°.

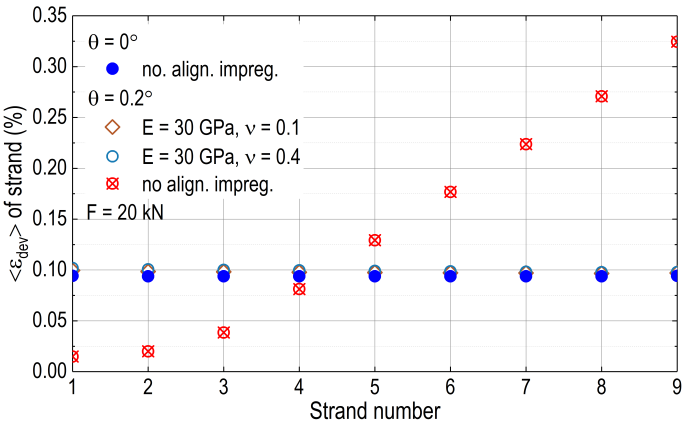

Figure 3.13: *Average deviatoric strain variation among strands with and without misalignment and with and without alignment impregnation.*

3.3 Electrical network model of the inter-strand resistance in *Re*BCO Roebel cables

In Chapter 6, experimental values of the inter-strand resistance in *Re*BCO Roebel cables are presented and discussed in terms of the properties of the copper-to-copper interface between two neighboring strands. However, the current path involved in these measurements actually runs from the superconducting *Re*BCO layer within one strand to the neighboring layer inside the next strand. In order to separate out just the copper-to-copper interface resistance, we need to be able to estimate the internal resistance contributions to this overall current path. To do this, a network model of the strands is constructed and the various components of the current path are considered one by one.

A schematic of the cross-sectional layout of two neighboring strands in a Roebel cable, as shown in Figure 2.23 and the corresponding resistor network connecting them, are sketched in Figure 3.14. The points "A" and "G" represent the *Re*BCO layers. The electrical resistance R_a between them can be expressed as:

$$R_a = \frac{1}{\dfrac{1}{R_{AB}+R_{BC}+R_{CD}+R_{DE}}+\dfrac{1}{R_{AE}}} + R_{EF} + R_{FG}. \tag{3.7}$$

The first term on the right-hand side of Equation (3.7) is the resistance between the *Re*BCO layer in the upper tape and the bottom part "E" of its copper stabilizer. In principle, the current can follow two paths. R_{AE} represents the direct path through the Hastelloy substrate, while R_{AB} + ... + R_{DE} is the resistance of the path from the *Re*BCO into the upper part of the copper stabilizer R_{AB}, along the stabilizer to the non-punched edge of the tape R_{BC}, down this edge R_{CD} and finally along the bottom part of the stabilizer R_{DB}. Since the electrical resistivity of Hastelloy is at least three (at 77 K) to four (at 4.2 K) orders of magnitude higher than the resistivity of silver and copper [226] at those temperatures, the direct path through the substrate

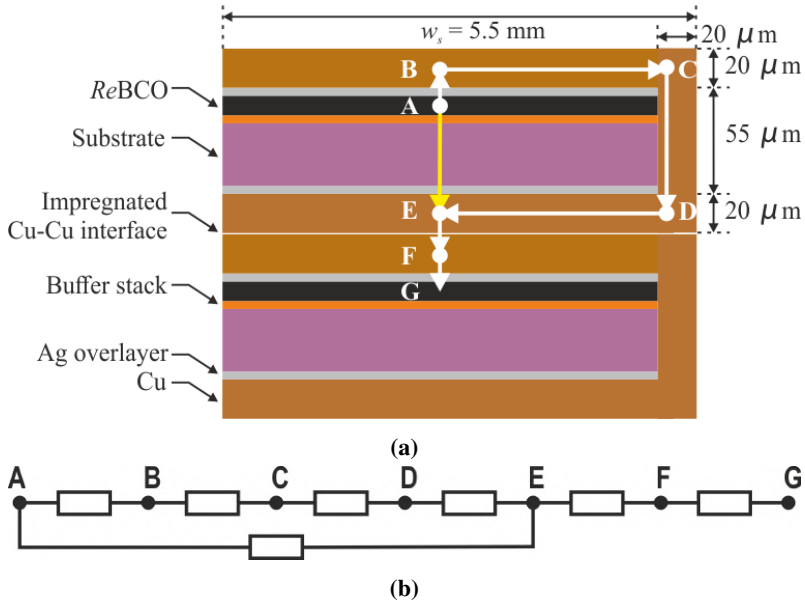

Figure 3.14: *Schematic of current path from one ReBCO strand to an adjacent one in cross-sectional view. a) Cross-section view of two adjacent ReBCO strands, b) Mechanism of coupling current path between two adjacent ReBCO strands.*

can be neglected. Equation (3.7) can then be simplified to the simple serial form:

$$R_a = R_{AB} + R_{BC} + R_{CD} + R_{DE} + R_{EF} + R_{FG}. \tag{3.8}$$

The current path A→B→C is described by the well-known problem of current transfer from a superconductor to a normal metal [205,227,228]. In such a configuration, the current density in the metal will increase exponentially from the center of the tape to its edge over a characteristic length scale λ, the current transfer length. The corresponding contact resistance between the *Re*BCO layer and its silver layer is calculated following [205]:

$$R_{ReBCO/Ag} = \frac{R\square}{A} = \frac{R\square}{w_{sc}l}\frac{w_{sc}}{\lambda} cotanh\left(\frac{w_{sc}}{\lambda}\right), \tag{3.9}$$

where $R_\square$ given in Ωm^2 is the surface resistance per unit area of contact and A is the effective contact area. w_{sc} and l are the transverse width and axial length of the superconducting layer, respectively. Limiting cases for Equation (3.9) can be written as:

$$\begin{aligned} R_{ReBCO/Ag} &= \frac{R\square}{w_c l}, \quad when\, \lambda \gg w_{sc}, \\ R_{ReBCO/Ag} &= \frac{R\square}{\lambda l}, \quad when\, \lambda \ll w_{sc}. \end{aligned} \tag{3.10}$$

Typical $R_\square$ values for an interface between *Re*BCO and Ag range from 1 to 100 × 10^{-14} Ωm^2 at 4.2 K and 0.7 to 4 × 10^{-11} Ωm^2 at 77 K [227, 229, 230]. With these literature values, the current transfer length λ can be determined using the model originally proposed by Lucas *et*

al. [231]:

$$\lambda = \sqrt{\frac{R_{\square} t}{\rho}}, \tag{3.11}$$

where t is the silver layer thickness of 2 μm and ρ in Ωm its resistivity, which is 2 nΩm at 4.2 K and 2.5 nΩm at 77 K. These values yield an estimated transfer length λ of 3 to 30 μm at 4.2 K and 70 to 100 μm at 77 K. λ is thus 500 to 50 times smaller than the width of the superconducting layer $w_{sc} \approx 5$ mm, as listed in Table 6.2, so that the limiting case of Equation (3.10) applies. Physically, this means that the current only leaves the *Re*BCO layer in a narrow region at the edge of the tape, i.e. on the right-hand side in the sketch of Figure 3.14a with a width of 10 μm at 4.2 K and of 100 μm at 77 K. The corresponding resistance then becomes:

$$R_{AB} + R_{BC} \approx \frac{R_{\square}}{w_{sc} l} \frac{w_{sc}}{\lambda} cotanh\left(\frac{w_{sc}}{\lambda}\right) + \frac{\rho_{Cu} \lambda}{l t_{Cu}} \approx \frac{R_{\square}}{\lambda l}, \tag{3.12}$$

where ρ_{Cu} is the electrical resistivity of copper. Based on the data presented in Chapter 6, the RRR value of the copper stabilizer in the Roebel cables investigated in this thesis is 10, which corresponds to a resistivity of 1.5 nΩm at 4.2 K and of 3.5 nΩm at 77 K [232]. t_{Cu} is the 20 μm thickness of the copper stabilizer.

The resistance of the downward current path through the stabilizer at the non-punched side of the tape, R_{CD}, is estimated straightforwardly as:

$$R_{CD} \approx \frac{\rho_{Cu} t_s}{l t_{Cu}}, \tag{3.13}$$

where $t_s \approx 100$ μm is the tape thickness, as listed in Table 6.2.

Next, the current has to flow back from the side towards the center of the tape through the bottom layer of the stabilizer of the top strand and then across the actual copper-to-copper interface between the two strands. This case is a similar to the one encountered at the *Re*BCO/Ag interface described above. Just how far the current flows towards the center before it crosses over to the other tape, depends on the balance between the Cu stabilizer resistance and the interface resistance. The general Equation (3.9) also here yields the combined resistance of R_{DE} and R_{EF}:

$$R_{DE} + R_{EF} = \frac{R_{\square,tt}}{w_{sc} l} \frac{w_{sc}}{\lambda_{tt}} cotanh\left(\frac{w_{sc}}{\lambda_{tt}}\right), \tag{3.14}$$

where $R_{\square,tt}$ is the surface resistivity of the copper-to-copper interface and λ_{tt} is the corresponding transfer length:

$$\lambda_{tt} = \sqrt{\frac{R_{\square,tt} t_{Cu}}{\rho_{Cu}}}. \tag{3.15}$$

Note that the value of $R_{\square,tt}$ is a-priori unknown and indeed it is exactly this parameter that we aim to derive from the data in Chapter 6. Also note that the use of the Equation (3.14) only holds for this metal-to-metal case on condition that the resistance R_{FG} is negligible, i.e. on condition that the top layer of the Cu stabilizer in the bottom tape can be considered to be in equipotential with its underlying *Re*BCO layer. The justification of this assumption is deferred to Chapter 6, in the discussion of the interstrand-resistance data.

To estimate the resistance of this final contribution to the current path, R_{FG}, it is assumed that

the current flows straight down, which will be the case if the tape-to-tape transfer length λ_{tt} is much larger than the tape width w_{sc}. Also this assumption will be justified in Chapter 6. R_{FG} is then the straightforward series addition of the resistance of the stabilizer and of the contact resistance between the stabilizer and the *Re*BCO layer:

$$R_{FG} \approx \frac{\rho_{Cu} * t_{Cu} + R_{\square}}{l * w_{sc}}. \tag{3.16}$$

To summarize the resistor network model, the derived expressions for the various contributions in the *Re*BCO layer-to-layer current path in terms of the tape's geometrical factors and material properties are presented in Table 3.5.

Table 3.5: Overview of the resistance components that contribute to the inter-strand resistance.

Component	Description	Formula	Equation
$R_{AB} + R_{BC}$	*Re*BCO layer to strand edge	$\frac{R_{\square}}{l\lambda}$	3.12
R_{CD}	Strand edge	$\frac{\rho_{Cu} t_s}{l t_C u}$	3.13
$R_{DE} + R_{EF}$	Strand edge to next stabilizer	$\frac{R_{\square,tt}}{\lambda l} cotanh\left(\frac{w_{sc}}{\lambda}\right)$	3.14
R_{FG}	Stabilizer to *Re*BCO layer	$\frac{\rho_{Cu} t_{Cu} + R_{\square}}{l w_{sc}}$	3.16
R_{AE}	Hastelloy	∞	-

3.4 Analytical AC loss models for *Re*BCO Roebel cable

The AC loss of *Re*BCO Roebel cables is presented in Chapter 6. The basic mechanisms causing AC loss in superconductors are well understood. Under influence of time-varying magnetic self- or applied magnetic fields, quantized magnetic flux lines move in or out of the filaments but are hampered by flux pinning, leading to viscous loss and hysteresis. On a macroscopic level, this magnetic behavior is accurately described by Bean's Critical State Model [233]. A second mechanism involves induced currents that flow partly through the filaments, partly through metallic parts of the strands or of the cable. The corresponding ohmic loss in the metal is called coupling loss [234, 235]. The third contribution is caused by induced eddy current loss in purely metallic parts of strands and cables.

Although the loss mechanisms themselves are well-described, the accurate prediction of AC loss in a cabled structure can become complicated, typically due to the system's geometry, due to non-linear interactions between various currents and magnetic fields or due to intrinsic anisotropy of the material involved. This is especially the case for HTS materials [133]. As mentioned in Section 3.1 these complications, together with advances in numerical methods and with the availability of ever-increasing computation power, have led to a clear trend towards numerical modelling of AC loss. However, as with the detailed mechanical modelling in Section 3.2, such a detailed numerical approach falls outside the scope of this thesis. Instead, analytical expressions that allow to incorporate the main features of *Re*BCO cables are selected from literature and their predictions are compared to the measured data in Chapter 6.

Hysteresis loss

Hysteresis loss in superconductors with various cross-sectional shapes exposed to high-symmetry magnetic field directions is extensively presented in literature [205,233,236–240]. Here, three analytical models for infinite long superconductors are considered: an ellipse model developed by Ten Haken *et al.* [239] for conductors with an elliptical transverse cross-section; a rectangle model for strips reported by Carr [240] and the original slab model from Bean [233]. The ellipse model and rectangle models are, in principle, applicable to magnetization loss for fields applied both perpendicular and parallel to the cable's broad face. The slab model ignores demagnetizing effects at the edges of the strands and cables and is thus only suitable for parallel applied magnetic fields.

When the applied magnetic field is perpendicular to the wide face of a superconductor that has a large cross-sectional aspect ratio, these demagnetizing effects play an important role and the loss depends on its cross-sectional shape. For an elliptical cross-section, Ten Haken *et al.* [239] predict the loss as:

$$Q_h(H_0) = \begin{cases} 4\mu_0 M_p H_p(\beta)\left[\dfrac{2}{1-m_0'}\left((1-b)^{1-m_0'}-1\right)+b(1-b)^{-m_0'}+b\right], & \\ & when\ 0 \le b < 1, \\ 4\mu_0 M_p H_p(\beta)\left(b-\dfrac{2}{1-m_0'}\right), & when\ b \ge 1, \end{cases} \tag{3.17}$$

where β is the aspect ratio of the cross-section, w is its width and βw is its thickness. M_p in A/m is the magnetization of the fully penetrated ellipse and $\mu_0 H_p(\beta)$ in tesla is the shape-dependent penetration field; b is the normalized field amplitude and m_0' is a geometrical factor:

$$M_p = \frac{2}{3\pi} J_c w, \tag{3.18}$$

$$H_p(\beta) = \begin{cases} \dfrac{J_c w}{\pi}\dfrac{\beta}{2\sqrt{1-\beta^2}}\ln\left(\dfrac{1+\sqrt{1-\beta^2}}{1-\sqrt{1-\beta^2}}\right), & when\ 0 < \beta < 1 \\ \dfrac{J_c w}{\pi}, & when\ \beta = 1 \\ \dfrac{J_c w}{2}, & when\ \beta = \infty \end{cases} \tag{3.19}$$

$$b = \frac{H_0}{H_p(\beta)}, \tag{3.20}$$

$$m_0' = -\frac{1+\beta}{\beta}\frac{H_p}{M_p}, \tag{3.21}$$

whereμ_0 in $J{\cdot}A^{-2}{\cdot}m^{-1}$ is the vacuum permeability, $\mu_0 H_0$ is the applied magnetic field. Due to magnetic coupling of the strands in a Roebel cable [241], the aspect ratio β depends on the direction of the applied magnetic field in a non-trivial way. With the magnetic field perpendicular to the broad face of the cable, the strands that lie stacked on top of each other are fully coupled and the aspect ratio becomes:

$$\beta = \frac{\frac{N_s+1}{2}t_{Re}}{w_s - t_{Cu}} \approx \frac{N_s+1}{2}\frac{tR_e}{w_s}, \tag{3.22}$$

where N_s the number of strands in the cable, w_s their width and t_{Re} or t_{Cu} the thickness of the *Re*BCO layer and of the copper stabilizer, respectively. Thus in the 15-strand cables considered in this thesis, seven or eight *Re*BCO layers contribute to the effective thickness. In the parallel field orientation, the *Re*BCO layers of individual strands are magnetically decoupled and the aspect ratio becomes:

$$\beta = \frac{w_s - t_{Cu}}{t_{Re}} \approx \frac{w_s c}{t R_e}. \tag{3.23}$$

AC magnetization loss in a superconducting strip with a rectangular cross-section of width w and thickness t is treated by Carr [240]. We refer to this as the rectangle model. When the magnetic field is applied normal to the broad face of the strip, the hysteresis loss is derived as:

$$Q_{h\perp}(B_0) = \begin{cases} \frac{1}{3}\mu_0 w J_c \frac{H_0^3}{H_{p\perp}^2}, & when\ H_0 < H_{p\perp} \\ \mu_0 w J_c \left(H_0 - \frac{2}{3}H_{p\perp}\right), & when\ H_0 > H_{p\perp} \end{cases}. \tag{3.24}$$

The penetration field $H_{p\perp}$ is calculated as:

$$H_{p\perp} = J_c \frac{t}{\pi}\left\{ ln\left[1 + \left(\frac{w}{t}\right)^2\right] + 2\frac{w}{t} arctg \frac{t}{w}\right\}. \tag{3.25}$$

With the magnetic field parallel to the wide face of strip, Carr predicted for the hysteresis loss:

$$Q_{h\parallel}(H_0) = \begin{cases} \frac{4\mu_0 H_0^3}{3\iota_c}, & when\ H_0 < H_{p\parallel} \\ \iota_c \mu_0 \left(H_0 - \frac{1}{3}\iota_c\right), & when\ H_0 > H_{p\parallel} \end{cases}, \tag{3.26}$$

where $\iota_c = j_c * 2t$ is the critical sheet current. The penetration field is:

$$H_{p\parallel} = \frac{J_c t}{2}, \tag{3.27}$$

where t in meter is the thickness of the *Re*BCO layer.

The third model that will be compared to the data in Chapter 6 is the original Bean model, which gives an estimate for the hysteresis loss in a superconducting slab placed in a parallel magnetic field [237]. In this thesis, we refer to it as the parallel slab Model. The parallel loss $Q_{h\parallel}$ in J·cycle^{-1}· m^{-3} is written as [205, 238]:

$$Q_{h\parallel}(H_0) = \begin{cases} \frac{2\mu_0 H_0^3}{3H_p}, & H_0 < H_p \\ 2\mu_0 \left(H_p H_0 - \frac{2}{3}H_p^2\right), & H_0 > H_p \end{cases}, \tag{3.28}$$

where H_p once more given by Equation (3.27).

Eddy current loss

Since the low-temperatue electrical resistance of the Hastelloy substrate in the strands is several orders of magnitude larger than of copper [226], eddy current loss in *Re*BCO Roebel cables is mainly generated in the copper stabilizer layers of the strands. Lakshmi *et al.* [242] estimated this loss as:

$$Q_{eddy}(H_0, f) = \frac{\pi^2 N_s \mu_0^2 H_0^2 f}{6 A_{Cu} \rho_{Cu}} \sum_m \frac{w_m^3}{t_m}, \tag{3.29}$$

where f is the frequency, N_s is the number of strands, A_{Cu} is the cross-sectional area and ρ_{Cu} is the resistivity of the copper in the strands, w_m is the width and t_m is the thickness of the individual copper layers in the strands.

Coupling loss

Coupling loss in a *Re*BCO Roebel cable can be calculated from the inter-strand resistance R_a and from the area A of the elementary inductive pick-up loop formed by two coupled strands. It is expressed as:

$$Q_c = \frac{2\pi^2 \mu_0^2 H_0^2 f n A^2}{V R_a}, \tag{3.30}$$

where V is the volume of the sample and n is the number of elementary loops present in the tested length [243].

In Chapter 6, independent measurements of the inter-strand resistance are presented. The coupling current loop area A depends on the magnetic field direction and can be derived from the cable geometry, as shown in Figure 6.1. Some authors use the center-to-center spacing of the strands in the cable to estimate the coupling loss in the normal magnetic field direction [242]. However, as shown by several model calculations [141, 244], magnetization currents mainly run along the edges of the zig-zag shaped *Re*BCO layers and are relatively high in the cross-over section. The area of the coupling current loop between adjacent strands is therefore simply put equal to:

$$A_\perp = l_g w_g, \tag{3.31}$$

where l_g and w_g are length and width of the central gaps in-between the crossing strands, as indicated in Figure 6.1 and given in Table 6.2. Within one transposition length, there are two of such coupling current loops between two adjacent strands, so that the area value is multiplied by two.

When the applied magnetic field is parallel to the broad face of the cable and perpendicular to its axis, we assume the coupling current flows along the broad surfaces of the *Re*BCO layer and transfers to neighboring strand along the whole transposition length. Consequently, the corresponding area is estimated as:

$$A_\parallel = (L_{tp} - 2l_g) * d_s, \tag{3.32}$$

where d_s is illustrated in Table 6.2. The value of d_s can be approximated as $2t_c/N_s$, where t_c is the thickness of the cable and N_s is the number of strands.

3.5 Conclusion

The simplified 2D FE modelling of impregnated and transversely loaded Nb_3Sn Rutherford cables presented in Section 3.2 shows that the average deviatoric strain acting on its strands decreases with increasing Young's modulus of the epoxy resin, as the resin increasingly carries part of the transverse load. An increasing epoxy resin Poisson's ratio, and therefore an increasing bulk modulus, renders the stress on the strand more hydrostatic and thus also reduces the deviatoric strain component. Since the deviatoric strain of Nb_3Sn filaments has a direct impact on their critical current density, the use of a stiff and relatively incompressible resin significantly improves the pressure tolerance of the cables. The mechanical effect of an insulating glass sleeve around the cable is relatively small.

The same type of mechanical model was also used to quantify the effect of a possible misalignment between the cable surface and the pressure anvil used in the experiments that are presented in Chapters 4 and 5. For a typical Nb_3Sn cable layout, even a misalignment angle as small as 0.2° can cause a strain concentration with a factor 3 in the strands at the side of the cable that comes into contact with the anvil first. It should be noted that similar imperfect stress- and strain concentrations may well occur also in the winding pack of real magnets, which the experiment is designed to mimic. The alignment impregnation described in Chapter 2 significantly improves the strain homogeneity in the transverse press experiments, rendering it essentially equal to the strain modelled for the perfectly aligned situation.

With the electrical network model of Section 3.3, the different contributions to the inter-strand resistance between adjacent strands in impregnated *Re*BCO Roebel cables were estimated. The direct path through the Hastelloy substrate plays no role, instead the current transfers from the *Re*BCO layer to the copper stabilizer in a narrow zone at the edge of the strand, flows down the edge and then spreads out evenly through the bottom layer of the stabilizer before crossing over to the next strand across the actual copper-to-copper interface between the stands.

In Section 3.4, three analytical models were presented that are used to predict hysteresis loss in strongly asymmetric structures such as *Re*BCO Roebel cables. Also eddy current loss in the stabilizer of the flat strands can be analytically estimated based on the geometry, while inter-strand coupling loss may be estimated based on the measured inter-strand resistance and on the cable architecture.

Chapter 4

Transverse pressure affecting the critical current of Nb_3Sn Rutherford cables

In this chapter the transverse pressure influence on the critical current of Nb_3Sn Rutherford cables is presented. The reversible critical current reduction or irreversible degradation effects known in literature are described. The average non-copper current density of virgin witness wires is compared to the critical current density of cable samples. No significant critical current degradation due to cabling and impregnation is observed, except in cable DS-PIT-I with a stainless-steel core, which showed a 20% critical current degradation. Measured data of critical current versus transverse pressure and the effect of a thermal cycle, as well as of load cycling for selected cable samples are presented. The various cross-sections of measured cable samples are analyzed microscopically afterwards.

4.1 Introduction

In the frame of the High-Luminosity LHC upgrade and the Future Circular Collider development program, the magnetic field in the accelerator dipole magnets is enhanced to 11 T and 15-16 T level, respectively [89, 143]. For this purpose, advanced Nb_3Sn conductors, with non-copper critical current density exceeding 2500 A/mm^2 at 4.2 K and 12 T, are being developed using the "Restacked-Rod-Process" (RRP) [245] and "Powder-In-Tube" (PIT) process [246] technology from Bruker-OST and Bruker-EAS, respectively. Nb_3Sn is a brittle material, and it is a significant challenge to construct high-field dipole magnets with such strain-susceptible superconductor. Two approaches for fabricating Nb_3Sn magnet coils were developed: React-and-Wind (R&W) [247] and Wind-and-React (W&R) [248]. The R&W technique is sometimes used for large coils with a large bending radius like the common coil type of dipole magnets [249–252]. Even then, it is still difficult to avoid conductor damage introduced in the coil winding process. The W&R technique is therefore widely used for Nb_3Sn coils that involve relatively tight conductor bending [253–259]. The investigation of Nb_3Sn conductors presented in this chapter is focused on the W&R technique.

For high-field accelerator magnets, the high-level of stress acting on the wide face of the Rutherford cables of 125 to 200 MPa [66, 67, 89, 90, 260] generated by the high Lorentz force initially causes a reversible reduction and at higher stress level eventually a permanent degradation of J_c. This study sets out to examine the critical current and upper critical field performance of state-of-the-art RRP and PIT Nb_3Sn type Rutherford cables exposed to transverse pressure.

The cause of the critical current degradation in Nb_3Sn strands of Rutherford cable is briefly presented. The relevant literature on the transverse pressure dependence of the critical current of wires and Rutherford cable samples is reviewed. First a comparison of non-copper $J_c(B_{peak})$ results of witness strands and impregnated Rutherford cables is presented in Section 4.2.1. Then, in Sections 4.2.2 and 4.2.3 the irreversible critical current reduction of cable samples under transverse pressure, and the effect of one thermal-cycle on the critical current, as well as the load-cycling effect on the critical current are presented. Finally, a microscopic analysis of sample cross-sections is presented in order to check for the presence of visible voids and strand damage.

4.1.1 Cause of I_c degradation due to Rutherford cable preparation and transverse pressure

All present high-field accelerator magnets use Rutherford-type cables, in which the strands are fully transposed and a large engineering critical current density can be achieved with high cable compaction [261]. Although the unreacted Nb_3Sn wire is robust enough to withstand the plastic deformation due to tension, bending and compaction during the cabling process, sub-elements in strands close to the edge of the cable are significantly deformed, as shown in Figure 4.1, resulting in locally degraded superconductivity. Defining the compaction factor as the thickness at a certain point of the cable divided by two times the strand diameter in virgin state, in the crosssection of a key-stoned cable it increases from the thick edge towards the thin edge:

$$C_t = \frac{t}{2 * d}, \tag{4.1}$$

where t is the thickness at a certain position in the cable, and d is the diameter of the strand. The compaction factor of a whole Rutherford cable is proportional to the cross-sectional area of the cable divided by the cross-sectional area of the strands in the virgin state. For a key-stoned cable, it can be calculated following [262]:

$$C_c = \frac{2w\,(t_1 + t_2)\,cos\varphi}{n\pi d^2} \cdot \frac{\pi}{4} \cdot 100\%, \tag{4.2}$$

where w is the cable width, t_1 is the thin-edge thickness, t_2 is the thick-edge thickness and φ is the cabling pitch angle defined as:

$$\varphi = arctan\frac{2w}{L_{tp}}, \tag{4.3}$$

where L_{tp} is the transposition length. In order to avoid damage to the diffusion barriers in the strands and to safeguard the engineering critical current density of the magnet coil windings, the Nb_3Sn Rutherford cables require to be compacted appropriately [263, 264]. Moreover, additional thermal strain is generated in the Nb_3Sn strand during the heat treatment due to the diverse thermal expansion coefficients of the various material components in the strand. Afterwards, compressive stress is applied to the coil and vacuum impregnation with epoxy resin is implemented to prevent possible quench training caused by micro-movement or deflection of cable strands or entire coil windings. Another function of the impregnation is to reduce the stress concentrations caused by Lorentz force when energizing the dipole magnet. The Lorentz force acting on the wide surface of coil conductors can, just like with the strands discussed in Section 1.3, cause a reversible reduction of the critical current and upper critical field at stress levels below the irreversible transverse stress limit, beyond which a permanent critical current reduction occurs due to cracks in filaments.

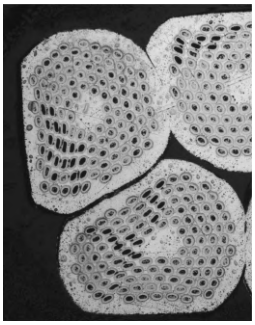

Figure 4.1: *Deformed Nb_3Sn strands nominal diameter 0.7 mm at the edge of a Rutherford-type cable.*

The cause of strain-induced critical current reduction in Nb_3Sn conductors during dipole magnet fabrication can be summarized as follows: (1) mechanical stress applied to strands and cables during cabling, coil winding and magnet assembly process; (2) thermal strain generated during conductor and coil heat-treatments and cool-down; (3) Lorentz force acting on the wide surface of the impregnated coil turns. The pre-stress applied on the heat-treated coils has to be kept to below the irreversible transverse stress limit, taking into account the possible thermal stress generated during cool-down. For high-field Nb_3Sn dipole magnets, ensuring that the superconducting Nb_3Sn in the coils is capable to sustain the high-level transverse stress caused by the Lorentz force remains a significant challenge.

4.1.2 Review of I_c degradation of Nb_3Sn wire due to transverse pressure

The unreacted Nb_3Sn wires are significantly compacted in the cabling process, which can cause a decrease of the critical current in the reacted strands of the Rutherford cable. Therefore, it is essential to control the wire deformation within a reasonable range, in order to balance the reduction of the critical current against the gain in engineering critical current of Rutherford cables. Barzi *et al.* [265] investigated the critical current performance of various RRP Nb_3Sn wire samples with respect to wire deformation at 4.2 K and 14 T. The wire deformation is defined as the reduction of wire thickness divided by the initial diameter of the round wire. The unreacted RRP wires were rolled with 10% and more wire deformation, then heat treated on a grooved cylindrical barrel. No critical current reduction was observed at wire deformation below 20% for various RRP Nb_3Sn wire samples. However, at more than 30% deformation, a decrease in the Residual Resistance Ratio (RRR) occurred. At 40% wire deformation, more than 20 to 40% I_c reduction and 60% RRR decrease were observed. The RRR of the stabilizing copper strand matrix is well known as an important factor affecting the quench performance of superconductors and stability of magnets [266]. Brown *et al.* [267] observed that wire rolling induces non-uniform shear bands that generate greater distortion of inner ring filaments, which locally causes damage of the diffusion barrier and leads to local Sn leakage during the reaction heat treatment, causing a degradation of RRR. It is concluded that in order to preserve RRR in the investigated RRP and PIT conductors, the wire deformation needs to be kept below 10%.

Note that the critical current reduction of different strand designs can behave quite differently, which was observed in early work by Turrioni *et al.* [268]. It was found that ciritical current degradation due to cabling depends more on to strand design than on cable geometry. Another comparison of the critical current and RRR performances between RRP and PIT Nb_3Sn wires with respect to wire deformation was reported by Bordini *et al.* [150, 269]. The unreacted round wires were rolled to reduce their thickness permanently by 15% or more. The rolled wires were then reacted on their sample holders and finally I_c was measured at 4.2 K. It is concluded that RRP type Nb_3Sn wire is very robust in terms of critical current performance and no I_c degradation was observed when rolling the wire up to 20% deformation. However, about 1 to 4% and 5 to 8% of I_c degradation occurred in PIT Nb_3Sn wires when rolled to 15 and 20% deformation. All wires showed significant RRR degradation between 35 and 50% for 15 and 20% rolling-deformed RRP wires, and from 45 to 55% and 65 to 75% for 15 and 20% rolled PIT wires, respectively.

For reacted bronze-processed [270,271] Nb_3Sn round wires and flat tapes, a study from Ekin *et al.* [157] showed that critical current and upper critical field of the Nb_3Sn conductors are more susceptible to transverse stress when compared to axial stress at 4.2 K in transverse magnetic field of 8 and 11 T. Both conductors showed a critical current reduction of 20 to 30% and an upper critical field reduction of 10 to 15% at a transverse stress up to 100 MPa, but less than 1% reduction of both properties was observed at the same level of axial stress.

In order to reduce the transverse stress susceptibility of Nb_3Sn round wire samples, Mondonico *et al.* [158] studied the critical current performance of bronze-processed and PIT Nb_3Sn wire samples with respect to transverse pressure using the 2- and 4- wall Walters spring setups presented in Section 2.2.1.2. A permanent critical current reduction occurred at a transverse pressure of 20 MPa for "bare" bronze-processed sample and as low as 5 MPa for the "bare" PIT sample when transverse pressure is applied with the anvil in the 2-wall Walters spring at 4.2 K and 19 T. These transverse stress limits increase to 50 and 15 MPa, respectively, when transverse pressure is applied with the anvil in the 4-wall Walters spring. Eventually,

the transverse stress limit reached to 165 and 135 MPa for epoxy resin impregnated bronze-processed and PIT wire samples, respectively, which were also measured in the 4-wall Walters spring. From these observations, it is concluded that the transverse pressure susceptibility can be reduced by providing a relatively uniform stress distribution around the entire wire cross-section. Also, Calzolaio *et al.* [109] investigated the critical current performance of three PIT Nb_3Sn round wire samples at 4.2 K and 19 T, all wire samples were impregnated with epoxy resin in the U-shaped groove of the 4-wall Walters spring. The impregnated PIT round wire samples showed irreversible transverse stress limits of 110 ± 6% to 145 ± 4% MPa. A finite element mechanical model analysis further indicated that the improvement in the transverse stress limit is due to the different stress sensed by the superconducting filaments. Bordini *et al.* [151] also reported the transverse stress limit of an impregnated PIT round wire sample of 110 MPa is enhanced by 40 MPa when the unreacted wire sample is rolled to 15% deformation; and even by more than 50 MPa when the round wire is covered with a glass-fiber sleeve or using the loaded epoxy resin Stycast instead of a pure epoxy resin.

4.1.3 Review of I_c degradation of Nb_3Sn Rutherford cable due to transverse pressure

Comparing the bronze-processed Nb_3Sn single round strand data reported by Ekin *et al.* [157] with the results on solder-filled rectangular Rutherford cables made from the same wires presented by Jakob *et al.* [272], the experimental results indicated that, at least up to 150 MPa, the cable samples (30% I_c reduction) exhibited less degradation than round wire samples, i.e. 40% I_c reduction, when subjected to the same transverse stress at 4.2 K and 10 T. Moreover, the critical current of a similar cable without solder-filler started to degrade significantly beyond 70 MPa and critical current reduction reached to 60% at 150 MPa. The reason for this behavior may be that in the cable with a relatively soft solder matrix, the load is distributed between different strands. This can result in a lower local pressure on strands in the solder-filled cable compared to a cable subjected directly to the transverse force. Further research on the same type of key-stoned Rutherford cables by Jakob *et al.* [273] indicated that with epoxy resin impregnation, the critical current reduction of cables is reduced to 5% at 150 MPa.

As mentioned in Section 4.1.1, a significant transverse force is applied to strands in the cabling process in order to increase the engineering critical current density and mechanical stability of the Nb_3Sn Rutherford cables, as reported by Andreev *et al.* [274]. For a key-stoned cable, the transverse force varies along the cable width direction. This results not only in difference in mechanical stability [275], but also in variations in transverse stress susceptibility between the edge and the center of the cable. Pasztor *et al.* [276] presented that the thin-edge exhibited 15% more critical current reduction than the center in a bare bronze-processed Nb_3Sn Rutherford cable at 160 MPa at 4.2 K, 11.5 T. After filling with solder, variation in reduction decreased to 3% at the same level stress. The critical current reduction of the thin-edge in the cable decreases from 35% to 16%.

To reduce the transverse stress susceptibility of Nb_3Sn Rutherford cables, a complete and perfect epoxy resin impregnation is very important. Boschman *et al.* [160] compared the critical current performance of a key-stoned cable with a rectangular cable. Both cables were manufactured using PIT strands. For key-stoned cables, only the outside was covered with Stycast 2850 FT; while the rectangular cable was fully impregnated. It was observed that about 30% critical current reduction appeared in the cable sample with full impregnation at 160 MPa at 4.2 K and 11 T, while 80% reduction was found in a cable sample with partial impregnation.

All the transverse stress susceptibility investigations mentioned above are based on the typical method by which the ratio of the critical current measured at applied transverse pressure and the critical current measured at 'zero'-stress is compared. Another method, which is a more accurate representation of the physical process, refers to the reversible degradation as the difference between the irreversible reduction $\Delta I_c = I_c(0 \rightarrow \sigma \rightarrow 0)/I_c(0)$ and the normalized critical current reduction $I_c(\sigma)/I_c(0)$. A quantitative investigation by Van Oort *et al.* [224] on transverse stress susceptibility of Rutherford cables manufactured with different types of Nb_3Sn wires, i.e. Modified Jelly-roll (MJR) [277], Internal-Tin (IT) [278] and PIT, indicated that the reversible critical current reduction and irreversible critical current degradation due to transverse stress varies in Rutherford cables with different strand-type and cable-layout, and is difficult to predict. Other relevant researches to determine the reversible and irreversible critical current reduction of different types of Nb_3Sn cables were presented in [103, 104, 129, 279–281].

4.2 Transverse pressure susceptibility of Nb_3Sn Rutherford cables

The exploration of critical current and upper critical field reduction of state-of-the-art high-J_c Nb_3Sn Rutherford cables is one of the key issues that require deeper understanding to support the dipole magnet development programs underway. The comparison of the critical current of wires and Rutherford cables also provides valuable experimental data for optimizing the cabling parameters, like the rolling compaction factor and key-stone angle. Finally the characterization of advanced Nb_3Sn properties also generates further experimental data, that fosters the material technology development.

The critical current performance of six state-of-the-art Nb_3Sn Rutherford cables subjected to transverse pressure are presented here. Two key-stoned cable samples comprising 40 strands of PIT-114 are representative for the cable layout used in the Dispersion Suppression (DS) demonstrator dipole magnet studies. The first cable sample DS-PIT-I contains a 25 μm-thick stainless-steel core, in order to control the inter-strand resistance in the cable to reduce the coupling current during a magnet current ramp, while the second cable sample DS-PIT-II has no core. Four rectangular cable samples comprising 18 RRP-132/169 and PIT-192 strands are typical examples of the cables used in the Short Model Coil (SMC) demonstrator dipole magnets. The characteristics of the cables and corresponding Nb_3Sn wires are listed in Tables 2.2 and 2.3, respectively. All cable samples are fully impregnated with epoxy resin to enhance their mechanical properties. The epoxy resins Araldite of CIBA GEIGY and CTD-101K were used in combination with glass-fibers. More detailed information was presented in Section 2.5.2.1.

All measurements were carried out in boiling liquid helium at 4.2 K, focusing on four aspects: (1) critical current of witness wires and cables in various transverse magnetic field strengths, as well as the RRR of their stabilizing copper matrix at 20 K; (2) transverse pressure susceptibility of cable samples in a background magnetic field of 10 T; (3) comparison of the upper critical field of cable samples with and without transverse stress; (4) effect of one thermal cycle and load-cycling on the critical current performance of cable samples. As explained in Section 2.6 the critical current is determined as the current corresponding to an electric-field criterion E_c of 10^{-5} V/m. The 3 to 6% systematic error in the critical current is applied when comparing data measured with different set-ups or experimental results of different samples. The 1 to 1.5% random error in the critical current is applied when analyzing the experimental results within one experimental run. The identification of the samples and measurements are

listed in Table 4.1.

Table 4.1: Identification and type of critical current measurements on Nb_3Sn witness wire and Rutherford cable samples.

Sample *	Number of strands	Impregnation material	Alignment impregnation	Measurement	Figure
Wire					
DS-PIT	-	-	-		4.6
SMC-RRP	-	-	-	I_c(B)	4.7
SMC-PIT	-	-	-		4.7
Cable					
DS-PIT-I DS-PIT-II	40	Araldite CIBA GEIGY	No	$I_c(\sigma)$	4.10
SMC-RRP-I SMC-PIT-I	18	CTD-101K	No	$I_c(\sigma)$	4.12
SMC-RRP-II	18	CTD-101K	Yes	I_c(B) $I_c(\sigma)$ $B_{c2}(\sigma)$ thermal-cycle	4.8 4.11 4.13 4.15
SMC-PIT-II	18	CTD-101K	Yes	$I_c(B)$ $I_c(\sigma)$ $B_{c2}(\sigma)$	4.9 4.13 4.14

∗ DS = Dispersion Suppression magnet, SMC = Short Model Coil magnet.

4.2.1 Critical current of witness wires and cables

By comparing the critical current of witness wires and cable samples, the effect of cabling and vacuum impregnation on the current transport properties of cable samples can be investigated. The virgin wire sample is wound on a titanium ITER-type barrel [26], as shown in Figure 4.2. It was heat treated together with a U-shaped cable sample and two protected 300 mm-long straight wire samples used for RRR measurement following the recipe listed in Table 2.9. After heat-treatment, the witness wire is soldered to the copper terminals of the sample holder and is mechanically fixed with Stycast 2850FT / 23LV. Excess epoxy is wiped off to maximize heat transfer from the wire to the liquid helium bath. The wire samples were measured in a 15 T solenoid, with a magnetic field oriented practically transverse to the wire sample.

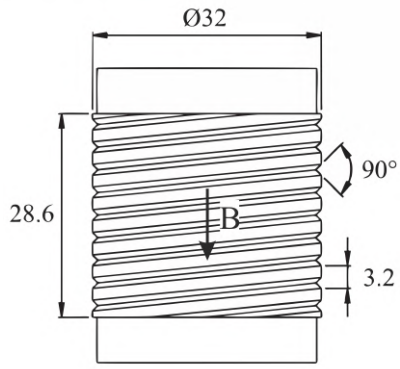

Figure 4.2: *Standard Ti-6Al-4V helical sample holder* [26]. Dimensions are in mm.

In order to compare the critical current of wire and cable samples directly, it is customary to report the critical current data not in terms of the background magnetic field B_a, but rather in terms of the peak magnetic field B_{peak}, the maximum value of the total magnetic field experienced by the superconducting filaments. For a wire sample on the sample holder, the location of the peak field is at the outer edge of the filamentary zone and the self-field correction is made using the widely used formula [282]:

$$B_{peak,wire} = B_a + B_{sf,wire} = B_a + \left(\frac{\mu_0}{2\pi R} - 0.09\right) I_{wire} \times 10^{-3}, \tag{4.4}$$

where $B_{sf,wire}$ in tesla is the self-field of the wire sample, μ_0 in H/m is the magnetic permeability of the vacuum, R in mm is the radius of the fliamentary zone, I_{wire} in ampere is the current flowing in the sample. The formula is valid only when the Lorentz force tends to push the sample onto the barrel. This equation comprises two terms: the first represents the self-field of a straight wire and the second is a correction of the self-field taking in account the helical shape of the sample. The value of R is 0.29 mm for PIT-114, 0.4 mm for RRP-132/169 and 0.42 for PIT-192 wire samples estimated by using the cross-section views of the virgin wires, as shown in Figure 4.3.

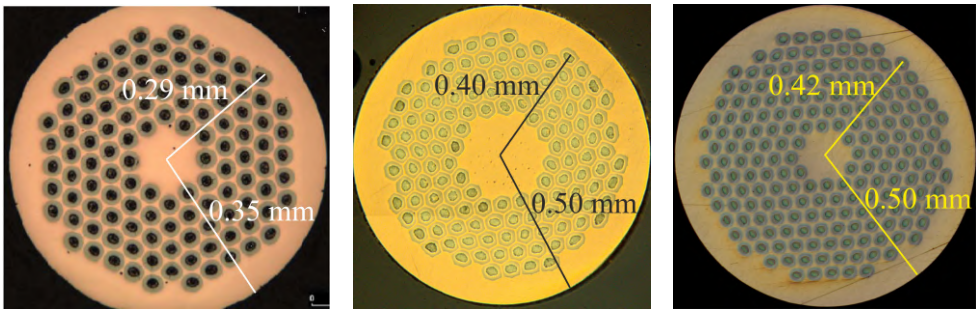

(a) **(b)** **(c)**

Figure 4.3: *Cross-section views of the virgin wire samples* [150, 151]*: (a) PIT-114, $\phi = 0.7$ mm; (b) RRP-132/169, $\phi = 1.0$ mm; (c) PIT-192, $\phi = 1.0$ mm.*

In the case of cable, a 2D finite element COMSOL model was used to estimate the peak magnetic field in the filaments, as shown in Figures 4.4 and 4.5, yielding a self-field correction of:

$$B_{peak,cable} = B_a + \eta \times I_{cable}, \tag{4.5}$$

where I_{cable} is the current flowing in the cable sample and η is 0.061 mT/A for DS-PIT cable samples and 0.078 mT/A for SMC-RRP and -PIT cable samples.

For further ease of a direct comparison between strand- and cable data, "non-copper" critical current density values $J_{c,wire}$ are reported. For a strand, this value is calculated following:

$$Non-copper J_{c,wire} = \frac{I_{c,wire}(1+\zeta)}{A_{wire}}, \tag{4.6}$$

where $I_{c,wire}$ in ampere is the measured critical current of a wire sample, A_{strand} in mm^2 is the cross-sectional area of the wire and ζ is its Cu to non-Cu ratio, as listed in Table 2.2. In the case of a cable, $J_{c,cable}$ is calculated following:

$$Non-copper J_{c,cable} = \frac{I_{c,cable}(1+\zeta)}{N * A_{wire}}, \tag{4.7}$$

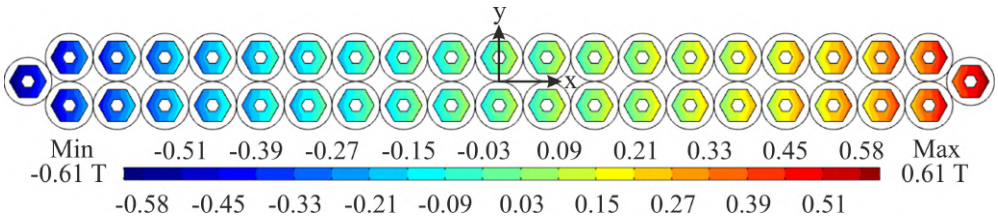

Figure 4.4: *Calculated y-component (i.e. perpendicular component) of the self-field of the cable sample DS-PIT with injection current of 10 kA pointing out from the page.*

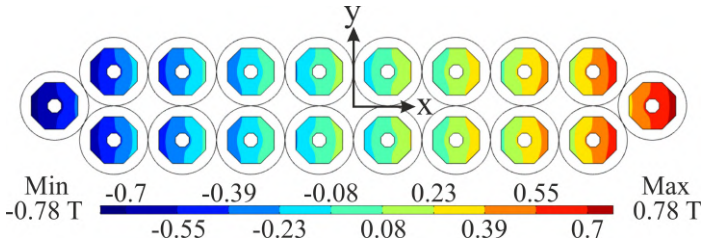

Figure 4.5: *Calculated y-component (i.e. perpendicular component) of the self-field of the SMC cable sample with injection current of 10 kA pointing out from the page.*

where $I_{c,cable}$ in ampere is the cable's measured critical current and N is the number of strands in the cable, as listed in Table 2.3. For reference, the $J_c(B_{peak})$ curves are also fitted to a widely used variation on the Kramer expression [283] introduced in Section 3.2:

$$Non-copper\,J_c(B_{peak},T) = \frac{C}{B_{peak}} \times B_{c2}(T)^2 \times h^p(1-h)^q, \tag{4.8}$$

$$h = \frac{B_{peak}}{B_{c2}(T)}, \tag{4.9}$$

where C in A/(mm^2·T) is a fitting constant, $B_{c2}(T)$ is the upper critical field at temperature T, p and q are the low- and high-field exponents of the pinning force for a specific wire, respectively. In the Kramer extrapolation used in this thesis, p and q are fixed at 0.5 and 2 [284], respectively. The fit curves are added to the $J_c(B_{peak})$ graphs below and the fit parameters are reported in Table 4.2.

4.2.1.1 PIT-114 Nb_3Sn wire and cables

The field-dependent critical current density of the PIT-114 wire used for the DS-PIT cables is shown in Figure 4.6. The critical current density points of cable samples DS-PIT-I with a stainless-steel core and -II without core are added in the graph for comparison. The critical current of the cables were also measured when exposed to transverse pressure, reported in Section 4.2.2, and no magnetic field dependence was characterized. Nevertheless, the $I_c(\sigma)$ measurements were carried out in a background magnetic field of 10 T and the relevant non-copper J_c were determined at the low-level pressure of 3 MPa for cable sample DS-PIT-I and 2 MPa for cable sample DS-PIT-II. The critical current density is 2480 ± 75 A/mm^2 at 11.1 ± 0.3 T and 2860 ± 85 A/mm^2 at 11.2 ± 0.3 T for cable samples DS-PIT-I and -II, respectively. Given the 3% systematic error in the critical current as described in Section 2.6.1, a significant

non-copper J_c degradation of some 20% was observed in cable sample DS-PIT-I when compared to the wire sample in the same magnetic field. No significant degradation was observed in cable sample DS-PIT-II. It is concluded that the cabling of the PIT-114 wires caused about 20% critical current degradation in cable sample DS-PIT-I, but no reduction in cable sample DS-PIT-II.

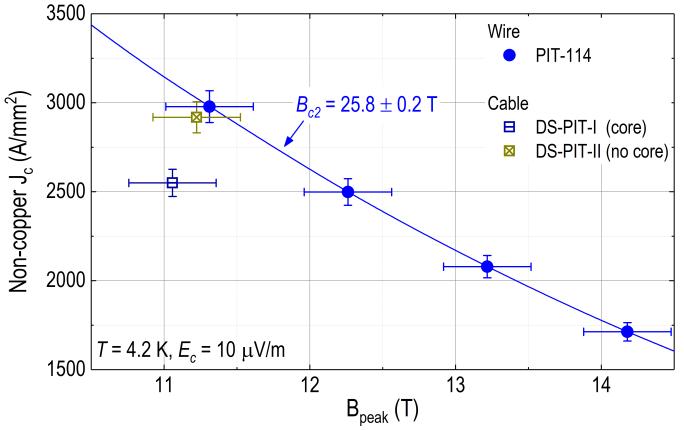

Figure 4.6: *Non-copper critical current density of the DS-PIT witness wire (circles), plotted against the peak magnetic field on the sample. The discrete symbols represent the experimental data, the solid line is a fit of the data following the Kramer expression Equation* (4.8)*. Also indicated is the upper critical field B_{c2} value that results from this fit. For comparison, non-copper J_c values of the DS-PIT cables (squares, at one single magnetic field) are also included in the graph, measured at low-level stress in the $I_c(\sigma)$ campaign. The critical current density and peak magnetic field error bars are determined using the systematic errors of 3% and 0.3 T, respectively, as described in Section 2.6.1.*

The thick- and thin edge compaction are 4.2% and 17.2%, respectively, estimated following Equation (4.1). The overall compaction of the DS-PIT cable samples is about 10% calculated following Equation (4.2). Referring to the investigation by Fleiter *et al.* [285] on the critical current degradation of PIT cable samples, cable sample DS-PIT-I has a 10% larger critical current degradation at the same thin-edge compaction, which is not understood. The possible cause of this significant I_c degradation is the abnormally positioned stainless-steel core, as shown later in Figure 4.16. The upper critical field is 25.8 ± 0.2 T estimated following Equation (4.8).

4.2.1.2 RRP-132/169 and PIT-192 Nb_3Sn wires and cables

In Figure 4.7 the non-copper $J_c(B)$ behavior of two types of Nb_3Sn wires used for the SMC cables are compared. Two RRP-132/169 and two PIT-192 witness wires were heat treated independently and measured at the University of Twente. For comparison, the non-copper J_c of a third RRP-132/169 virgin wire prepared, heat treated and measured at CERN [103] is included in the graph.

The three RRP-132/169 wire samples behave in a very similar way, critical current density differences between them fall within the 6% systematic error estimate and are thus negligible. The critical current density at 12 T is 3200 ± 190, 3180 ± 190 and 3100 ± 190 A/mm^2 for 'CERN', 'UT wire1' and 'UT wire2' RRP-132/169 wire samples, respectively. This increases confidence in both sample-to-sample and lab-to-lab reproducibility of the measurements, as

well as in the level of quality control mastered by the wire producer. A similar conclusion can be drawn for the PIT-192 witness wire samples: no significant difference in the critical current density between two PIT wire samples is observed. The non-copper J_c values at 12 T are 2490 ± 150 and 2460 ± 150 A/mm^2 for 'UT wire1' and 'UT wire2' wire samples, respectively.

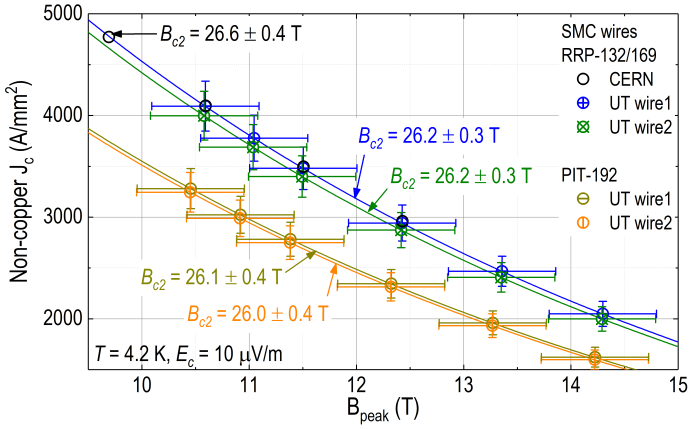

Figure 4.7: *Non-copper critical current density of the SMC witness wires, plotted against the peak magnetic field on the strands. The discrete symbols represent the experimental data, the solid lines are fits of the data following the Kramer expression Equation* (4.8)*. Also indicated are the upper critical field B_{c2} values that result from these fits. The topmost three curves correspond to RRP-132/169 wire samples. For comparison, an independently measured data set of this type of wire recorded at CERN is included in the plot. The two lower curves correspond to PIT-192 wire samples. The critical current density and peak magnetic field error bars are determined using the systematic errors of 6% and 0.5 T, respectively, as described in Section 2.6.1.*

When comparing the SMC-RRP- and PIT wire samples, it is concluded that both Nb_3Sn production processes yield the same average B_{c2} values, but the PIT wire samples have an average non-copper J_c at 12 T that is about 15% lower than the one offered by the RRP wire samples with taking into account the 6% systematic error.

In Figure 4.8 the non-copper $J_c(B)$ values of cable sample SMC-RRP-II and RRP-132/169 wire sample 'UT wire1' are compared. The two data sets of the cable sample SMC-RRP-II correspond to different cool-down cycles.

Differences between wire- and cable samples performance are minor. The average B_{c2} for the cable sample SMC-RRP-II is 25.9 ± 1.1 T. When comparing to the average B_{c2} of the three wire samples of 26.3 ± 0.3 T, the deviation is still within the estimated uncertainty and no significant difference is observed. A similar conclusion can be drawn regarding the comparison of the non-copper J_c values between the wire- and cable samples. It is concluded that there is no significant influence of the cabling process. Differences both in upper critical field and non-copper J_c between the two cool-down runs for the cable are also negligible.

In Figure 4.9 the non-copper $J_c(B)$ of cable SMC-PIT-II and of the PIT-192 virgin wire sample 'UT wire1' is presented. The upper critical field of the cable is about 5% lower than the average value found in the wire samples, but their critical current density values within the measurement range are similar when taking into account the 6% systematic error. It is concluded that the cabling process has no significant influence on the current-carrying capacity of

the material.

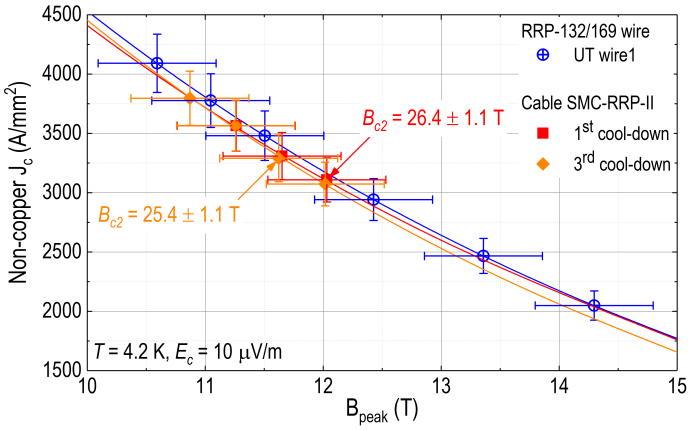

Figure 4.8: *Non-copper critical current density of the SMC-RRP witness wire (circles) and cable (squares and diamonds), plotted against the peak magnetic field on the samples. The discrete symbols represent the experimental data, the solid lines are fits of the data following the Kramer expression Equation* (4.8)*. Also indicated are the upper critical field B_{c2} values that result from these fits. The wire sample data are repeated from Figure 4.7. The two sets of cable data are obtained on the same sample, but in different cool-down runs. The critical current density and peak magnetic field error bars are determined using the systematic errors of 6% and 0.5 T, respectively, as described in Section 2.6.1.*

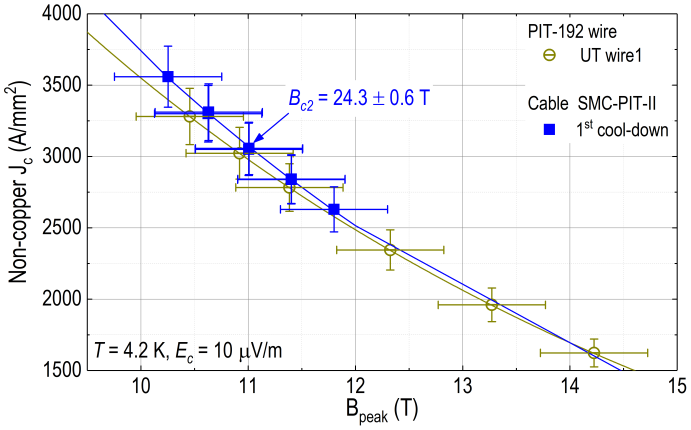

Figure 4.9: *Non-copper critical current density of the SMC-PIT witness wires (circles) and cable (squares), plotted against the peak magnetic field on the samples. The discrete symbols represent the experimental data, the solid lines are fits of the data following the Kramer expression Equation* (4.8)*. Also indicated is the upper critical field B_{c2} value that results from the fits. The strand data are repeated from Figure 4.7. The critical current density and peak magnetic field error bars are determined using the systematic errors of 6% and 0.5 T, respectively, as described in Section 2.6.1.*

For ease of reference, all fitted B_{c2} and J_c(4.2 K, 12 T) values discussed above are summarized in Table 4.2.

The thermal and electrical conductivities of stabilizing copper of the high-J_c Nb_3Sn strand are important parameters to evaluate the stability of a superconducting magnet [266]. The

Table 4.2: Kramer extrapolation of the upper critical field B_{c2} and the non-copper critical current density J_c(*4.2 K, 12 T*) of the various cables and witness wires, obtained by fitting expression Equation (4.8) to the measured data.

		B_{c2} (T)	J_c (A/mm^2)	Figure
DS-PIT	*Wire*			
	PIT-114	25.8 ± 0.2	2620 ± 80	4.6
SMC-RRP	*Wire*			
	RRP-132/169 (CERN)	26.6 ± 0.4	3200 ± 190	4.7 and 4.8
	RRP-132/169 (UT wire1)	26.2 ± 0.3	3180 ± 190	4.7 and 4.8
	RRP-132/169 (UT wire2)	26.2 ± 0.3	3100 ± 190	4.7 and 4.8
	Cable			
	SMC-RRP-II (1st cool-down)	26.4 ± 1.1	3120 ± 190	4.8
	SMC-RRP-II (3rd cool-down)	25.4 ± 1.1	3080 ± 185	4.8
SMC-PIT	*Wire*			
	PIT-192 (UT wire1)	26.1 ± 0.4	2490 ± 150	4.7 and 4.9
	PIT-192 (UT wire2)	26.0 ± 0.4	2460 ± 150	4.7 and 4.9
	Cable			
	SMC-PIT-II	24.3 ± 0.6	2520 ± 150	4.9

copper conductivity at liquid helium is quantified by its RRR value. A larger RRR means a larger conductivity of the copper. An adequate stabilizer for accelerator magnet features a RRR (273.15 K/4.2 K) in excess of 100 [286]. Therefore, the RRR of virgin wire and extracted strand samples of RRP-132/169 and PIT-192 were measured as well and the results are presented in Table 4.3.

Table 4.3: RRR of the virgin wires and extracted strand samples of SMC cables.

SMC cable	RRR(273.15K/20K)							
	RRP-132/169				PIT-192			
	Virgin wires		Extracted strands		Virgin wires		Extracted strands	
	#1	#2	#3	#4	#1	#2	#3	#4
-I	138	125	148	147	178	160	122	168
-II	173	140	109	113	-	-	-	-

Table 4.3 indicates that all measured SMC samples have an adequate copper stabilizer. The measured RRR values for virgin wire samples of cable SMC-RRP-I and cable SMC-PIT-I are reproducible within 10%, which is about 20% for cable SMC-RRP-II. No RRR reduction was found in the extracted strands in comparison with the virgin wires of cable SMC-RRP-I, but up to 40% RRR degradation was observed in the extracted strands of cable SMC-RRP-II. One of the measured extracted strands of cable SMC-PIT-I shows a maximum 30% RRR reduction, while the other one performs similar to the virgin strands. The significant differences do not seem caused by measurement errors, and a possible explanation is that the extracted strand samples were taken from the ends of cable sample, where the cable was bent. Any diffusion barrier damage can cause a decrease of the RRR value. Regardless, the conclusion is that the RRR values of virgin wire and extracted strand samples fulfill the magnet design requirement. Since the J_c(B) of the SMC-RRP cables performs identical to the virgin wires, no critical current degradation due to cabling was observed. The relatively low RRR values of the extracted strands for cable samples SMC-RRP-II and -PIT-I are considered not representative.

4.2.2 Irreversible I_c degradation

A typical measurement session run consists of measuring the critical current of the cable sample at a discrete number of gradually increasing transverse stress. After each measurement, the stress on the cable is released and the critical current at 'zero'-stress is determined. A light pressure is always maintained on the cable sample to prevent various parts in the set-up from losing contact and shifting. The value is compared to the initial critical current at 'zero'-stress, so that possible irreversible I_c reduction due to the earlier pressure excursion can be detected and quantified.

4.2.2.1 PIT-114 Rutherford cables

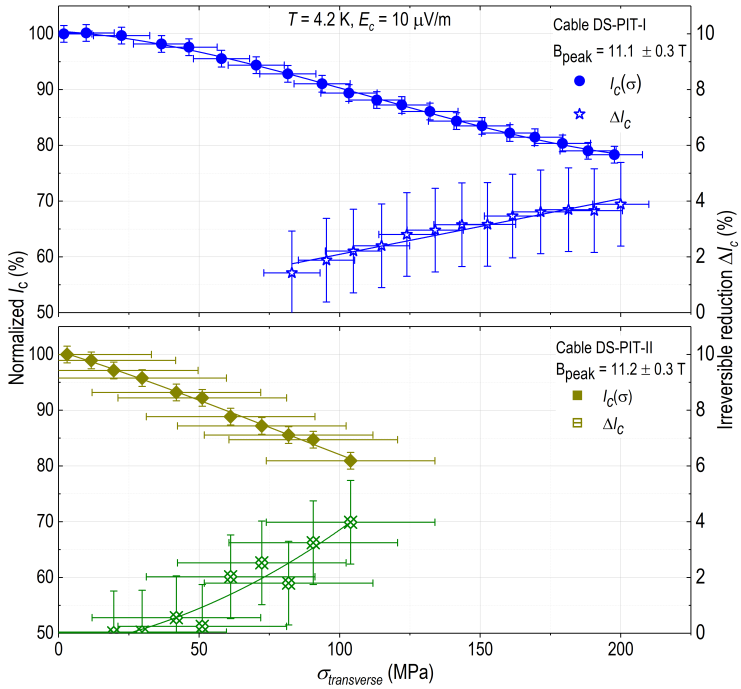

Figure 4.10: *Transverse pressure response of the DS-PIT cable samples in a peak magnetic field of 11.1 ± 0.3 T on cable sample DS-PIT-I and 11.2 ± 0.3 T on cable sample DS-PIT-II. The 'zero'-stress initial critical current is 17.1 ± 0.5 kA for cable sample DS-PIT-I and 19.8 ± 0.6 kA for cable sample DS-PIT-II. The left y-axis corresponds to the normalized critical current $I_c(\sigma)/I_c(0)$ as function of transverse stress σ (solid symbols). The right y-axis reports the irreversible reduction ΔI_c of the critical current referring its unstressed initial value (open symbols). The solid lines are polynomial fits to the data. The critical current random error is ±1.5%; the transverse pressure uncertainties are ±10 and ±30 MPa for cable samples DS-PIT-I and -II, respectively, as described in Section 2.6.*

The initial critical current of cable sample DS-PIT-I with a stainless-steel core, at 4.2 K and a peak magnetic field of 11.1 ± 0.3 T is 17.1 ± 0.5 kA. For DS-PIT-II at a peak magnetic field of 11.2 ± 0.3 T it is 19.8 ± 0.6 kA. The critical current performance of the two cables with respect to transverse pressure is shown in Figure 4.10. Both cables display a relatively steep $I_c(\sigma)$ dependence, falling to 90% of their unstressed value already at 100 ± 10 MPa fore cable sample DS-PIT-I and at 70 ± 30 MPa for cable sample DS-PIT-II. The onset of irreversible critical current reduction is observed at 90 ± 10 MPa for cable sample DS-PIT-I and 70 ±

30 MPa for cable sample DS-PIT-II taking into account the 1.5% random error of critical current measurement and using 2% reduction of the critical current measured at 'zero'-stress as the criterion, as motivated in Section 2.6.1.

4.2.2.2 RRP-132/169 and PIT-192 Rutherford cables

In the case of cable samples SMC-RRP and -PIT, similar $I_c(\sigma)$ measurements were carried out on two samples for each type of cable. Cable samples SMC-RRP-I and -PIT-I were impregnated with CTD-101K. Cable samples SMC-RRP-II and -PIT-II were also first impregnated with CTD-101K but then the 'alignment' impregnation was applied, as described in Section 2.5.2.3, in order to reduce the interface misalignment between anvil and cable surface, which was observed in the impregnated cable samples SMC-RRP-I and -PIT-I. The $I_c(\sigma)$ behavior of cable samples SMC-RRP-II and -PIT-II are reported first in Figure 4.11. Their un-loaded initial I_c is 21.1 ± 1.3 kA for SMC-RRP-II and 18.2 ± 1.1 kA for SMC-PIT-II. 90% of the un-loaded I_c value is reached at 130 ± 3 MPa for SMC-RRP-II and at 90 ± 3 MPa for SMC-PIT-II. The irreversible transverse pressure limit is larger than 190 ± 3 MPa and 150 ± 3 MPa for cable samples SMC-RRP-II and -PIT-II, respectively.

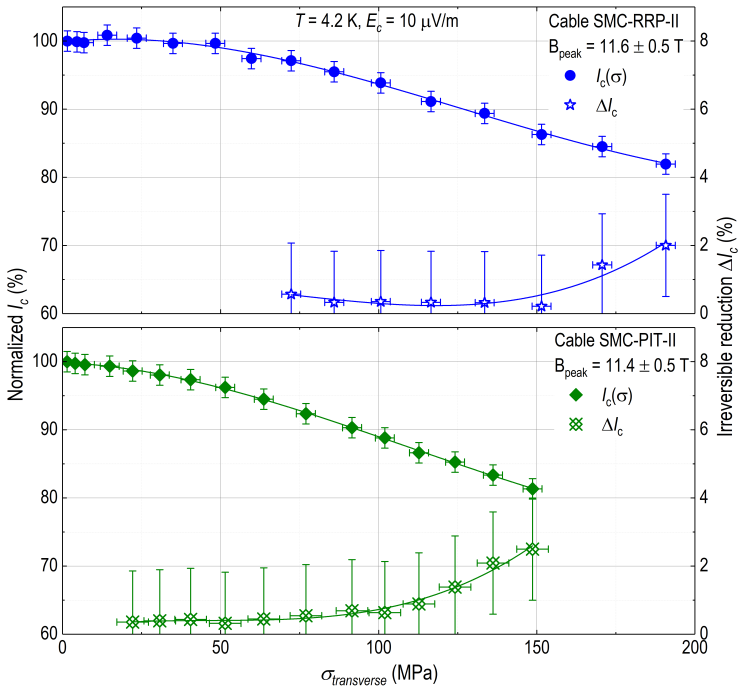

Figure 4.11: *Transverse pressure response of the second set of SMC cables. The peak magnetic field is 11.6 ± 0.5 T for cable sample SMC-RRP-II and 11.4 ± 0.5 T for cable sample SMC-PIT-II. 'Zero'-pressure initial currents $I_c(\sigma=0)$ are 21.1 ± 1.3 kA for SMC-RRP-II and 18.2 ± 1.1 kA for SMC-PIT-II. Solid symbols represent the normalized critical current $I_c(\sigma)/I_c(0)$ as a function of the transverse stress σ (left axis), open symbols the irreversible degradation ΔI_c (right axis). The solid lines are polynomial fits of the data. The uncertainties in the critical current is ±1.5%; the uncertainties in the transverse pressure is ±3 MPa for cable samples SMC-RRP-II and -PIT-II, as described in Section 2.6.*

For ease of reference, all obtained transverse stress limits of the measured Nb_3Sn Rutherford cables are listed in Table 4.4.

Table 4.4: Summary of the transverse stress limit for measured Nb_3Sn Rutherford cables.

Cable sample	$\sigma(\Delta I_c$ = -10%) / MPa	$\sigma(\Delta I_{c,irrev.}$ = -2%) / MPa
DS-PIT-I	100 ± 10	90 ± 10
DS-PIT-II	70 ± 30	70 ± 30
SMC-RRP-II	130 ± 3	>190 ± 3
SMC-PIT-II	90 ± 3	>150 ± 3

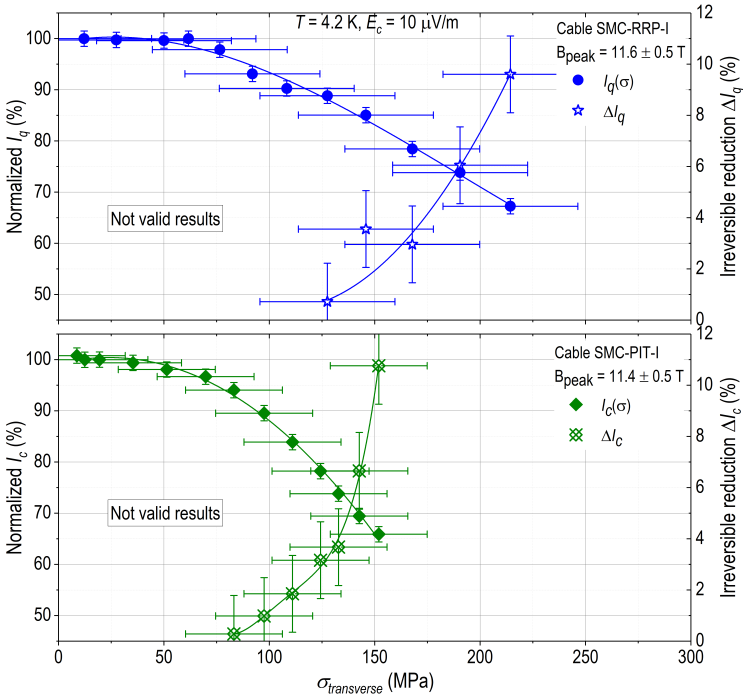

Figure 4.12: *Transverse pressure response of the first set of SMC cables demonstrating that non-representative measurement results can easily be obtained when anvil and cable surface are not well aligned. The peak magnetic field is estimated at 11.6 ± 0.5 T for cable sample SMC-RRP-I and 11.4 ± 0.5 T for cable sample SMC-PIT-I. 'Zero'-pressure initial currents $I_q(\sigma=0)$ are 20.7 ± 1.2 kA for SMC-RRP-I and $I_c(\sigma=0)$ 18 ± 1.1 kA for SMC-PIT-I. Solid symbols represent the normalized $I_q(\sigma)/I_q(0)$ or $I_c(\sigma)/I_c(0)$ as function of transverse stress σ (left axis), open symbols the irreversible degradation ΔI_q or ΔI_c (right axis). The solid lines are polynomial fits of the data. The uncertainties in the critical current is estimated at ±1.5%; the uncertainties of the transverse pressure is ±32 and ±23 MPa for cable samples SMC-RRP-I and -PIT-I, respectively, as described in Section 2.6.*

As discussed also in Section 3.2, the mentioned "alignment" impregnation turned out to be essential to collect reliable transverse pressure results. In order to demonstrate what can happen when this step is omitted an erroneous measurement is presented next. The $I_c(\sigma)$ behavior of cable samples SMC-RRP-I and -PIT-I with no 'alignment' impregnation is presented in Figure 4.12. Note once more, that the results in this figure do not correctly show the true transverse pressure effect due to an imperfectly aligned pressure block and cable surface. Unfortunately, the *V-I* curved based critical current of cable sample SMC-RRP-I could not be measured, so

instead its quench current performance as function of transverse pressure is used. It is observed that the quench and critical current decrease relatively steeply with applied pressure. The reversible critical current reaches 90% of its un-loaded value already at 100 ± 30 MPa for cable sample SMC-RRP-I and at 60 ± 20 MPa for cable sample SMC-PIT-I. Also irreversible reduction sets in quite early, exceeding a level of 2% current degradation at 170 ± 25 MPa for SMC-RRP-I and 125 ± 10 MPa for SMC-PIT-I. The 'zero'-pressure initial quench current of SMC-RRP-I is 20.7 ± 1.2 kA at 11.6 ± 0.5 T. The 'zero'-pressure initial critical current of SMC-PIT-I is 18.0 ± 1.1 kA at 11.4 ± 0.5 T. Both values are similar to the critical currents of the second set of cable samples presented in Figure 4.11. A closer 'post-mortem' inspection of the samples revealed a problem with the alignment between the pushing anvil and the cable surface. Although visual inspection revealed only a small angle of about 0.2°between both, subsequent modelling, as reported in Section 3.2.4, nonetheless indicated that this can have a significant impact on the stress distribution on the cable. It was therefore decided to prepare a second set of cable samples SMC-RRP-II and -PIT-II from the same 'green' cable material and to adopt an extra step in the impregnation procedure to improve parallelism, as presented in Figure 4.11.

4.2.3 Decrease of B_{c2} due to transverse pressure

Additional I_c(B) measurements were carried out on the SMC-RRP-II and -PIT-II cable samples to gauge the reversible effect of pressure on their upper critical field B_{c2}. These are reported in Figures 4.13 and 4.14. The un-loaded $J_c(B_{peak})$ data are discussed in Section 4.2.1, where they are compared to witness strand data and to similar measurements carried out at CERN in the FRESCA test station. The data were obtained with the cables subjected to a transverse pressure of 150 MPa.

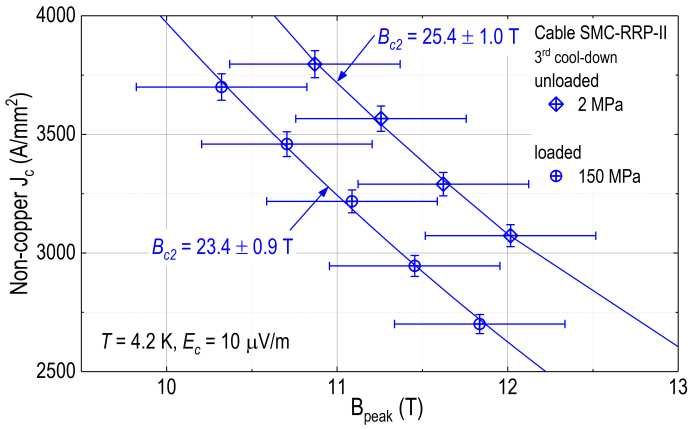

Figure 4.13: *Non-copper critical current density $J_c(B)$ versus magnetic peak field of the SMC-RRP-II cable sample with 'zero' applied stress (about 1 MPa, 'unloaded') and exposed to a transverse pressure of 150 MPa ('loaded'). The unloaded data are measured twice in subsequent cool-down cycles. Solid lines represent the Kramer fit through the data following Equation* (4.8)*. The uncertainties in critical current is ±1.5%, the peak magnetic field error is ±0.5 T, as described in Section 2.6.1.*

The data sets were characterized in terms of upper critical field and non-copper critical current density at 12 T by fitting them to the Kramer-type expression following Equation (4.8), introduced in Section 4.2.1. The results are reported in Table 4.5.

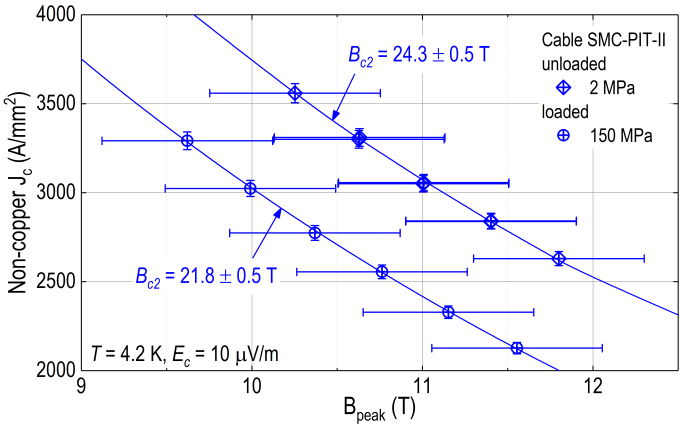

Figure 4.14: *Non-copper critical current density $J_c(B_{peak})$ versus magnetic peak field of the SMC-PIT-II cable with 'zero' applied stress (1 MPa, 'unloaded') and exposed to a transverse pressure of 150 MPa ('loaded'). Solid lines represent a Kramer fit through the data following Equation* (4.8)*. The error in critical current is ±1.5% while the error in peak magnetic field is ±0.5 T, as described in Section 2.6.1.*

Table 4.5: *Upper critical field and critical current density of SMC cables at 4.2 K, 12 T and different transverse pressure levels.*

Cables	σ (MPa)	B_{c2} (T)	J_c (A/mm^2)
SMC-RRP-II (1st cool-down)	2	26.4 ± 1.2	3120 ± 190
SMC-RRP-II (3rd cool-down)	2	25.4 ± 1.0	3080 ± 180
	150 ± 3	23.5 ± 0.8	2630 ± 160
SMC-PIT-II	2	24.2 ± 0.5	2520 ± 150
	150 ± 3	21.8 ± 0.3	1900 ± 110

Given the 1.5% random error in the critical current measurements, the B_{c2} extrapolation shows ±1.0 T error. Taking into account this, some significant reduction in B_{c2} and 15% reduction in J_c at 12 T were observed in the SMC-RRP-II sample by application of a transverse pressure of 150 MPa. For sample SMC-PIT-II, these values for the same pressure level are 6% and 25%, respectively.

4.2.4 One thermal-cycle and load-cycling effects

Cable sample SMC-RRP-II was cooled down a second time and the measurement of critical current versus pressure was repeated in order to check for an influence of thermal relaxation on the pressure-tolerance, as shown also in Section 4.2.1, and to measure the onset of irreversible degradation more accurately. The result is shown in Figure 4.15. No significant increase in I_c was found and also the pressure dependence of the critical current remained virtually the same.

Also, a series of measurements was performed by which the pressure was cycled between 2 and 150 MPa, in order to check for evolution in the irreversible degradation of the cable samples under cyclic loading / unloading, e.g. due to crack growth in the Nb_3Sn filaments. The results are reported in Tables 4.6 and 4.7. No significant evolution was observed.

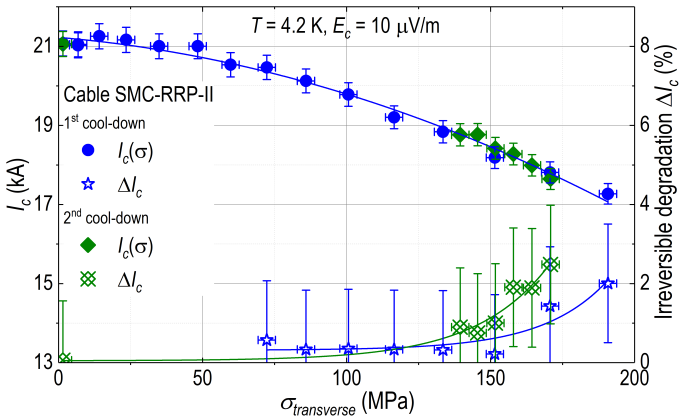

Figure 4.15: *Second measurement of the $I_c(\sigma)$ behavior of cable sample SMC-RRP-II, in order to check for the influence of a thermal cycle and to narrow down the onset of irreversible degradation more accurately. The solid lines are polynomial fits to the data. Solid symbols represent the normalized critical current $I_c(\sigma)/I_c(0)$ as a function of the transverse stress σ (left axis), open symbols the irreversible degradation ΔI_c (right axis). The solid lines are polynomial fits to the data. The error in critical current is ±1.5%; the error in transverse pressure is ±3 MPa for cable samples SMC-RRP-II and -PIT-II, as described in Section 2.6.*

Table 4.6: *Evolution of the critical current of the SMC-RRP-II cable under cyclic loading and unloading. The initial unloaded I_c of SMC-RRP-II is 21.1 ± 1.3 kA.*

Cycle	SMC-RRP-II (2nd cool-down)		SMC-RRP-II (3rd cool-down)	
	I_c(150 MPa) (kA)	I_c(2 MPa) (kA)	I_c(175 MPa) (kA)	I_c(2 MPa) (kA)
1	18.7 ± 1.1	20.9 ± 1.3	18.1 ± 1.1	21.1 ± 1.3
2	18.9 ± 1.1	20.9 ± 1.3	18.1 ± 1.1	21.1 ± 1.3
3	18.7 ± 1.1	20.9 ± 1.3	18.1 ± 1.1	21.1 ± 1.3
4	18.7 ± 1.1	20.9 ± 1.3	18.1 ± 1.1	21.1 ± 1.3

Table 4.7: *Evolution of the critical current of the SMC-PIT-II cable under cyclic loading and unloading. The initial unloaded I_c of SMC-PIT-II was 18.2 ± 1.1 kA.*

Cycle	SMC-PIT-II (1st cool-down)	
	I_c(150 MPa) (kA)	I_c(2 MPa) (kA)
1	14.8 ± 0.9	17.6 ± 1.1
2	14.7 ± 0.9	17.6 ± 1.1
3	14.7 ± 0.9	17.5 ± 1.1
4	14.7 ± 0.9	17.5 ± 1.1
5	14.7 ± 0.9	17.5 ± 1.1

4.2.5 Microscopic analysis of impregnated Nb_3Sn Rutherford cables

After the transverse pressure effect measurements, the samples were carefully removed from the U-shaped holder, cut transversely at the pressed section, embedded in casting epoxy resin and polished. The cross-sections were examined under an optical microscope to verify the impregnation quality and to investigate for damage of the filaments.

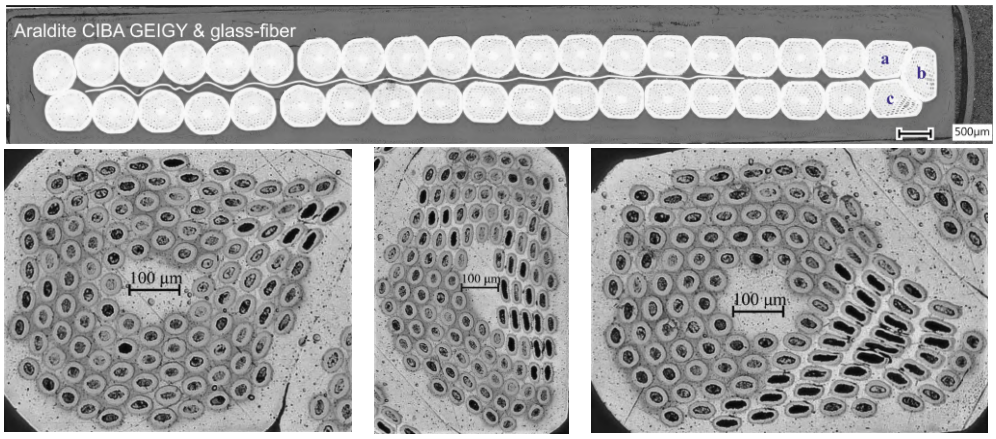

(a) **(b)** **(c)**

Figure 4.16: *Cross-sectional views of the pressed section of cable sample DS-PIT-I. A general overview of the cable layout is presented on the top, while close-ups of strands a, b and c at the thin-edge of the cable are shown in the bottom pictures.*

In Figure 4.16 the cross-sectional views of the pressed section of cable sample DS-PIT-I are shown. The images show that the cable was successfully impregnated as no visible voids are observed. It is found that the stainless-steel core is packed much closer to the left side of the cable with an abnormal "wrinkled-up" shape. The thin-edge of the cable is deformed most where most probably the filament damage occurs. The close-ups of strands a, b and c are presented in Figures 4.16a to 4.16c. Although significant deformations are observed in the three strands, as well as in some filaments, no visible damages can be found.

In the case of cable sample DS-PIT-II, a similar conclusion can be drawn. The cable sample is successfully impregnated and no visible voids and filament damages are observed, as shown in Figure 4.17.

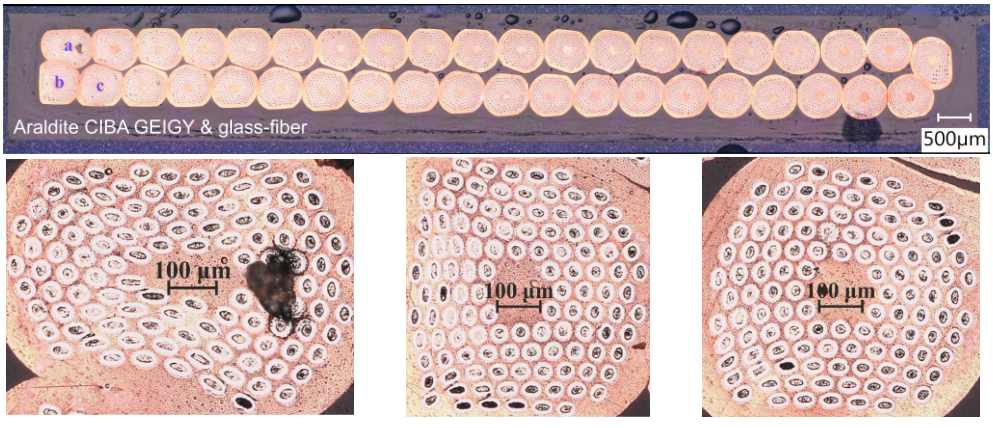

(a) **(b)** **(c)**

Figure 4.17: *Cross-sectional views of the pressed section of cable sample DS-PIT-II. A general overview of the cable layout is presented on the top, while close-ups of strands a, b and c at the thin-edge of the cable are shown in the bottom pictures.*

(a) **(b)**

Figure 4.18: *View of the pressed section of cable samples SMC-RRP-II and -PIT-II: (a) SMC-RRP-II; (b) SMC-PIT-II.*

In Figure 4.18 the cross-section of the pressed sections of cable samples SMC-RRP-II and -PIT-II are shown. A stack of dummy and measured cable samples were vacuum impregnated with CTD-101K in each measurement. Both SMC cable samples are successfully impregnated, no visible voids were observed. In Figures 4.19 and 4.20 the close-ups of cross-sectional views of a, b, c strands in cable samples SMC-RRP-II and -PIT-II are shown, the corresponding position of these strands are shown in Figure 4.18. Once more, it is concluded that no filament damages can be found.

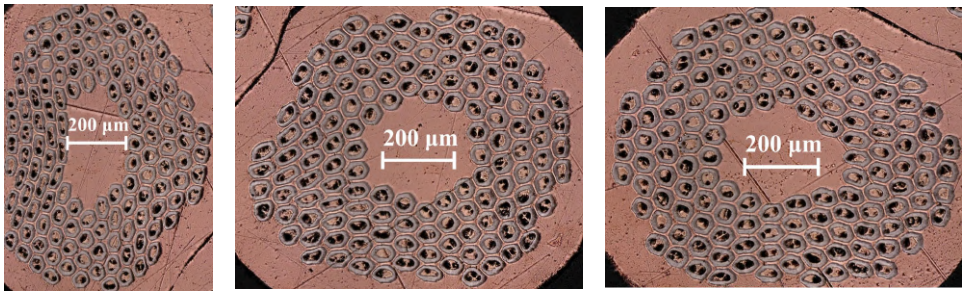

(a) **(b)** **(c)**

Figure 4.19: *Close-ups of cross-sectional views of strands a, b and c at the thin-edge of the cable sample SMC-RRP-II.*

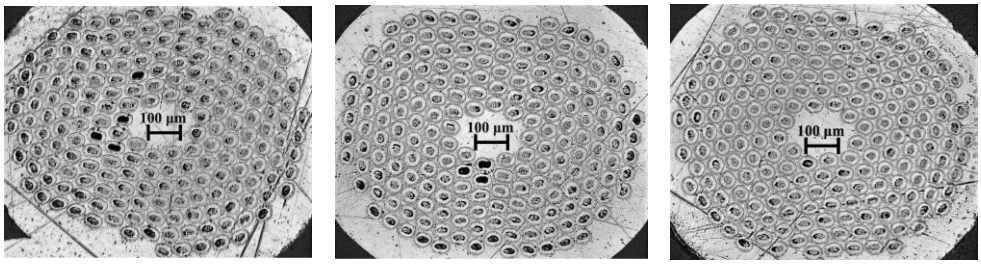

(a) **(b)** **(c)**

Figure 4.20: *Close-ups of cross-sectional views of strands a, b and c at the thin-edge of the cable sample SMC-PIT-II.*

4.3 Conclusion

Two key-stoned Nb_3Sn cable samples DS-PIT-I with a stainless-steel core and -II without core comprising 40 PIT-114 type of strands were vacuum impregnated with epoxy resin CIBA GEIGY Araldite. Four rectangular Nb_3Sn cable samples SMC-RRP-I, -II and -PIT-I, -II comprised of 18 RRP-132/169 and PIT-192 types of strands were vacuum impregnated with epoxy resin CTD-101K. In addition, a second set cable samples SMC-RRP-II and -PIT-II were given an 'alignment' impregnation considered necessary in order to collect reliable measurements of the transverse pressure effect on the critical current [163, 287]. All cables are successfully impregnated, without leaving bubbles or significant residual voids, as reported in Section 4.2.5. The thermal contraction of CIBA GEIGY Araldite and CTD-101K epoxy resins with glass-fiber is about 0.2% from room temperature to 4.2 K, which is similar to the 0.3% of the reacted Nb_3Sn Rutherford cable samples. Both epoxy resins can be used to successfully enhance the transverse pressure tolerance of Rutherford cables. However, in view of actual coils insulation requirements and the longer pot-life of CTD-101K of 60 h at 40 °C in comparison to the silica filled Araldite featuring just 3 h at 80°C, the CTD-101K with glass-fiber sleeve is more suitable for impregnation of large-size magnets.

The critical current of all Nb_3Sn Rutherford cable samples was measured at 4.2 K in a perpendicular applied magnetic field of 10 T. For comparison, the critical current of a virgin witness wire of each cable was measured as a function of the magnetic field. No significant critical current degradation of the cable samples was observed, with exception of cable sample DS-PIT-I that showed a 20% current degradation. The possible reason is due to the abnormal distribution of the stainless-steel core, that may have caused a unwanted stress concentrations during cabling. The 0.7 mm PIT-114 round wire has a non-copper J_c of 2620 ± 80 A/mm^2 at 4.2 K and 12 T. The 1 mm RRP-132/169 round wire has a relatively high non-copper J_c of 3160 ± 190 A/mm^2, while the same size PIT-192 round wire has a lower non-copper J_c of 2480 ± 150 A/mm^2. The RRR values of the SMC virgin wires and extracted strands in the cable samples are larger than 100. Together these satisfy the minimum conductor critical current density and RRR requirements of the 11 and even 16 T accelerator magnet designs presently under development (see also Section 1.2).

Concerning the transverse stress susceptibility of the cable samples, the critical current decreases reversibly to 90% of the initial 'un-loaded' values at 100 ± 10 MPa for cable sample DS-PIT-I, 70 ± 30 MPa for cable sample DS-PIT-II, 130 ± 3 MPa for cable sample SMC-RRP and 90 ± 3 MPa for cable sample SMC-PIT. This reversible critical current reduction has to be taken into account when designing the magnets. The onset of irreversible critical current degradation is determined at 90 ± 10 MPa for cable sample DS-PIT-I and 70 ± 30 MPa for cable sample DS-PIT-II. No irreversible critical current reductions are observed for cable samples SMC-RRP and -PIT for a transverse pressure up to 190 and 150 MPa, respectively. The minimum transverse pressure that Rutherford cable need to sustain is estimated at 100 to 150 MPa for 11 T and 150 to 200 MPa for 16 T dipole magnets (Section 1.3). Therefore, it appears indeed possible to build dipole magnets using the PIT-114 and RRP-132/169 wires provided sufficient margin is taken into account. However, as yet there is insufficient statistical data to draw a solid conclusion. It would be desirable to perform more measurements on similar cables to confirm these results.

The RRR-132/169 wire is more robust than PIT-192 wire. No significant upper critical field reduction is observed at 150 MPa in cable sample SMC-RRP, but 6% reduction occurred in

cable sample SMC-PIT at the same stress level. Since at this pressure no irreversible critical current was observed in cable samples SMC-RRP-II and -PIT-II, this probably means there is no significant filament cracking in the strands of the Rutherford cable due to the transverse pressure. This is also reflected in the effect of load-cycling on the critical current as no significant critical current reduction evolution was observed.

The comparison of the first and second sets of SMC cable samples, supported by the 2D modelling results in Section 3.2.4, shows that special care is needed to avoid stress concentrations. An interface misalignment angle as small as 0.2° can cause the transverse pressure limit to decrease by at least 20 MPa. This demonstrates that measurements of the transverse stress effect on the critical current are delicate and a nearly perfect alignment of pressure block and cable surface must be guaranteed.

Chapter 5

Transverse pressure affecting the critical current of *Re*BCO Roebel cables

In this chapter the transverse pressure influence on the critical current of ReBCO Roebel cables is presented. First, the critical current degradation effects described in literature are reviewed. The local average current density of single Roebel strand is compared to the critical current density of cable samples. The crossover section in the strand shows about 20% lower critical current density than the straight section measured in the magnetic field range of 9 to 12 T. When comparing the bare (not impregnated) SuperPower-type cable sample to the corresponding crossover strand data, no critical current density degradation due to cabling is observed. Also, the results of critical current versus transverse pressure and thermal cycling for selected cable samples are presented. The various cross-sections of cable samples that were compressed are analyzed microscopically after the measurements.

5.1 Introduction

As sketched in Section 1.2, *Re*BCO Roebel cables are being developed to pave the way towards high field magnets for future particle accelerators of 20 T and beyond. The Lorentz force generated in such magnets leads to sizeable transverse pressure on the superconducting cables, in the present 15 to 20 T magnet designs of the order of 150 MPa or even above [91]. Contrary to single *Re*BCO coated conductors, a bare Roebel cable, starts to degrade already under transverse stress below 50 MPa due to stress concentrations [161–163]. In order to use this type of cable in high field magnets additional reinforcement is thus required.

In this chapter, the cause of critical current degradation in *Re*BCO strands of Roebel cable is presented. The $J_c(B_{peak})$ results of single strands in SuperPower-tape *Re*BCO Roebel cables are presented in Section 5.2.1, as well as the average critical current density of cables under transverse pressure. Next, the V-I performance of different strands in cable samples is analyzed. Then, in Sections 5.2.2 and 5.2.3 the irreversible critical current reduction of cable samples under transverse pressure, as well as the effect of a thermal-cycle on the critical current are investigated. Finally, a microscopic analysis of sample cross-sections is presented in order to check for the possible presence of visible voids or strand damage.

5.1.1 Review of I_c degradation due to Roebel strand preparation and transverse pressure

Roebel cables feature a sufficiently high engineering current density to satisfy the requirements for 20+ T accelerator magnets. Moreover, their flat strands are fully transposed, which is beneficial for limiting transient time constants and improving current sharing [91, 145]. Two methods are developed to fabricate the zig-zag strand either by mechanical punching or picosecond-infrared laser cutting technology. The laser cutting produces less defects but is presently not economically attractive in terms of production speed. Therefore, punching has been identified as the best method for manufacturing a Roebel strand with a speed of 50 m/h [50].

The punching die can be replaced according to specific strand-dimensional requirements. Both production methods cause 50 to 60% material loss. Besides material loss, there is a 2 to 3% current reduction due to edge effects such as delamination variation in width. Therefore, a perspective method to reduce the cost of Roebel strand in the future is producing the zig-zag strand already during the *Re*BCO synthesis process using for example a chemical solution deposition, by which the substrate is cut to a zig-zag shape where after buffer layers, as well as the *Re*BCO layer are deposited on the pre-prepared shape [288, 289].

For *Re*BCO tape, a uniform transverse compressive pressure well over 100 MPa can be applied with no irreversible critical current degradation, as reported e.g. by Senatore *et al.* [290]. However, the irreversible stress limit strongly depends on the direction of the force with respect to the broad face of *Re*BCO tape [118, 122]. In SuperPower coated conductor, Otten *et al.* [122] have shown that tape can withstand more than 240 MPa transverse stress when the force is applied to the *Re*BCO side at 77 K and self-field. The limit is as low as 110 MPa when the force is applied to the Hastelloy side. For *Re*BCO Roebel strands, less than 2% critical current degradation was observed when transverse pressure is up to 200 MPa applied to the *Re*BCO side [161].

5.1.2 Sources of I_c degradation in *Re*BCO Roebel cable

In order to identify sources of I_c degradation in Roebel cable used in coils, the process of coil preparation is shortly described. The bending radius and winding direction with respect to the position of the *Re*BCO layer in the tape have an effect on the cable samples' critical current performance and have to be taken into account before winding coils. Bending of coated conductors and Roebel cables in the "easy" bending direction was investigated by Otten *et al.* [175], and in this case, bare Roebel cables exhibit similar properties as a coated conductor. After coil-winding, compressive stress is applied to compact the windings, and the critical current degradation might occur if over-stress is applied to the assembly. Then, vacuum impregnation is required to insulate the coil windings electrically and to fix them. In the case of coated conductor, thermal contraction differences between epoxy resin and tapes do cause critical current reduction due to the thermal stress generated after cooling down [50, 88, 291, 292], see also Section 2.5.2.2. Finally, during excitation of the magnet, the Lorentz force generated in the coils can also affect the critical current performance of the cables.

For achieving optimal performance the Roebel cable is wound in the central section with its broad face parallel to the local magnetic field, the so-called "aligned-block" concept [91]. In the coil heads, the cable is wound with 5°angle with respect to the parallel magnetic field. This structure yields the highest in-field critical current of coated conductor, but also results in a large perpendicular Lorentz force [91]. The bare (not-impregnated) *Re*BCO Roebel cables are much less tolerant to transverse stress than isolated strands, due to local stress concentrations at strand crossovers [85, 88, 161–163]. Fleiter *et al.* [85] investigated the transverse stress distribution locally in two non-impregnated *Re*BCO Roebel cables and showed that the 10-strand cables manufactured by KIT under transverse compression have an effective surface of only 24%, which implies that they locally experience a much higher stress than the average value calculated using the full cable surface. Uglietti *et al.* [161] investigated the critical current under transverse stress of a bare 10-strand *Re*BCO Roebel cables fabricated by the Robinson Research Institute. A significant critical current reduction of some 20% was observed at an average pressure as low as 10 MPa. Further investigation from Talantsev *et al.* [88] showed that a non-impregnated 5-strand Roebel cable has a rather low transverse stress limit in the range of 4 to 34 MPa at 77 K and self-field condition, while more than 270 MPa was measured for cables impregnated with epoxy resin filled with SiO_2 nanopowder. The addition of nanopowder to the epoxy resin leads to a similar thermal contraction coefficient as the metallic substrate of the strands.

5.2 Transverse pressure tolerance of *Re*BCO Roebel cables

In this work, two *Re*BCO Roebel cable samples were vacuum impregnated with a mixture of epoxy resin and fused silica [174] in order to improve their tolerance to transverse stress. Also, a reference cable sample without impregnation is investigated. The three cables comprise 10 SuperPower *Re*BCO Roebel strands. Next, three 15-strand cable samples with an architecture directly relevant for the EuCARD-2 accelerator demonstrator magnet, see Figures 1.5 and 1.6, were impregnated using two methods. The samples comprise either SuperPower (SP), or Bruker (BR) coated conductor. For comparison, one of the 15-strand SuperPower-tape based cables was impregnated with the same resin as the one used for the 10-strand SuperPower cable samples. The other cable samples were impregnated with the preferred and familiar CERN

method using CTD-101K [171], as described in detail in Section 2.5.2. After impregnation, the critical current of the cable samples is measured when exposed to a variable transverse mechanical load at 4.2 K and a 10.5 T perpendicular magnetic field. For reference purpose, as well as to understand the impact of the impregnation on the critical current, the measured field-dependent I_c of short single Roebel cable strands are presented as well. The identification of the samples and measurements are listed in Table 5.1.

Table 5.1: Identification and type of critical current measurements on *Re*BCO Roebel strand and cable samples.

Sample *	Number of strands	Impregnation method	Measurement	Figure
SP-Roebel-strand	-	-	$I_c(B)$	5.2
FM-SP-I-A FM-SP-I-B FM-SP-I-C	10	Araldite CY5538 / HY5571 Bare	$I_c(\sigma)$	5.9
FM-SP-II	15	Araldite CY5538 / HY5571	$I_c(\sigma)$ Thermal cycling	5.9 5.13
FM-SP-III		CTD-101K	$I_c(\sigma)$	5.9
FM-BR			$I_c(\sigma)$ Thermal cycling	5.9 5.12, 5.13

∗ FM = Feather-M0&M2 magnet, SP = SuperPower, BR = Bruker.

5.2.1 Critical current of single Roebel strands and cables

By comparing the critical current of the cable samples with the critical current of single strands at 4.2 K, the effect of vacuum impregnation on the transport properties of the cables can be investigated. The SuperPower strand samples used for the FM-SP cables were taken before assembling the Roebel cables. The strand samples from Bruker-type cable FM-BR were extracted from the cables' end section. All strands were characterized with pairs of voltage taps positioned across both straight- and 'crossover' sections of the punched strands, as shown in Figure 5.1, in a perpendicular magnetic field of up to 11.5 T. The J_c values presented in Figure 5.2, are determined by dividing the critical current by the cross sectional area of the *Re*BCO layer.

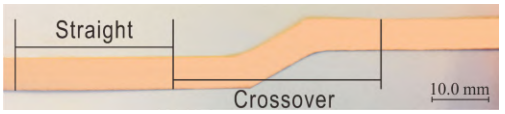

Figure 5.1: *Single strand of SuperPower-type Roebel cable.*

In order to correctly compare the critical current of cables and strands, the self-field contribution to the total magnetic field of both was calculated using COMSOL Multiphysics. A peak self-field factor of 0.24 mT/A was once more calculated for the straight strand section and 0.30 mT/A for the crossover section. For cables FM-SP-I, -II, -III and FM-BR, the values are 0.091, 0.090, 0.087 and 0.098 mT/A, respectively. With these corrections to the background magnetic field applied, the critical current density values of cables FM-SP-I, -II and -III are compared to the $J_c(B_{peak})$ data of the SuperPower strands, as shown in Figure 5.2. The measured J_c values of the crossover strand section are 20% lower than those of the straight sections, illustrating how the crossover sections can affect the overall strand I_c. A possible explanation is that the current in the highly textured *Re*BCO layer of coated conductors displays an in-plane

anisotropy with the current along the tape higher than across the tape. In the crossover section the situation is in-between [293]. Another contributing effect may be the reduced effective width at the crossover section and locally increased damage introduced by the punching process [294]. Comparing the bare sample of cable FM-SP-I with the 'crossover' strand data, no J_c degradation due to cabling is observed. The deviation is within the 6% systematic uncertainty discussed in Section 2.6 and is therefore not significant. Also, the impregnated cable sample FM-SP-I-A shows no J_c degradation due to cabling and impregnation compared to the 'crossover' strand. However, about 1.5% extra critical current density difference between cable samples FM-SP-I-A and -C was observed in excess of the 6% systematic error. This deviation might be caused by non-homogeneity of the current in the tape along the length, which has a standard deviation of 1.5% at 77 K and self-field. The other impregnated cable sample FM-SP-I-B, on the other hand, does show a J_c-reduction of 10% compared to the 'crossover' strand. Similarly, a reduction of about 10% was found in the impregnated cable sample FM-SP-III. For cable FM-SP-II, since the J_c deviation is within the systematic error, no significant critical current density reduction was observed. Cable samples FM-SP-I-A, -B and -II are impregnated with Araldite CY5538 filled with silica powder, while cable FM-SP-III is impregnated with CTD-101K. The comparison indicates that impregnation with Araldite CY5538 doesn't cause critical current degradation in the SuperPower-type Roebel cables. However, whether the 10% critical current degradation in cable sample FM-SP-III is caused by the impregnation with CTD-101K cannot be concluded from a single sample measurement.

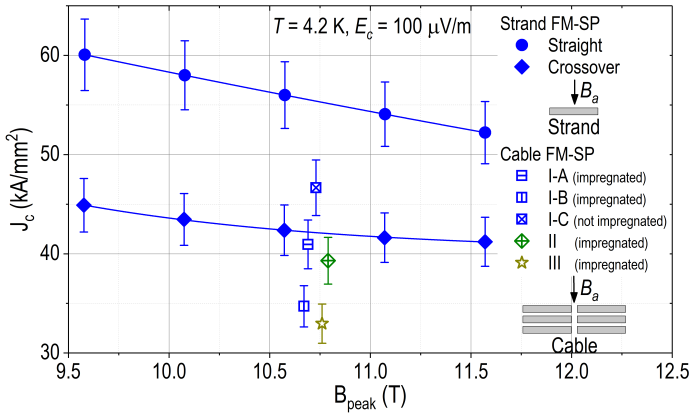

Figure 5.2: *ReBCO layer critical current density versus peak magnetic field in SuperPower-tape single strands and Roebel cables made thereof. The critical current density of cable samples (open squares, diamonds, and stars) was measured when exposed to a transverse stress of 3 MPa. The impregnation of the samples is described in Tables 2.12 and 5.1. Symbols represent the measured data, solid curves represent the curve-fitting. The error bar is taken from the 6% systematic error estimated in Section 2.6.1.*

Unfortunately, a similar analysis for the Bruker-type cable FM-BR was not possible due to limited availability of non-impregnated strand material for measurements.

For the cable measurements, at least three voltage tap pairs are attached, each probing a single strand, over exactly half or one transposition length. In addition, the voltage on the quench detection taps is measured as well and also displayed in the figures. These quench detection signals show partly a resistive behavior since the taps are not positioned on the same strands.

Typical voltage versus current curves measured on the Roebel cables are shown in Figures 5.3 to 5.8. All data were measured at 4.2 K in a perpendicular applied magnetic field of 10.5 T with a rather low 3 MPa transverse pressure applied, just enough to keep the anvil in contact with the sample. In cable FM-SP-I-A and in non-impregnated cable FM-SP-I-C, voltage measurements on several strands did not yield useful data, like strand-1 of cable FM-SP-I-A and strand-3 of cable FM-SP-I-C. Strand-3 of cable FM-SP-II showed a premature transition with a low n-factor, presumably related to a delamination effect, which was confirmed in a post-mortem microscopy analysis. The variations in the onset of the transition are less important for the other cables (about 20% for FM-SP-III and about 10% for FM-BR) and become even insignificant (about 1%) when only the higher-voltage part of the transition is taken into account. The I_c-values are determined at the criterion of 100 μV/m assuming a power-law like V-I behavior. The thus determined I_c-values of Roebel cables are presented in Table 5.2. Compared to the impregnated cables FM-SP-I-A and -B, the non-impregnated cable remarkably has a 10 to 20% higher critical current. The critical current of cable FM-SP-II is 15% higher than cable FM-SP-III. The possible explanation is that cable FM-SP-II is made of the same batch of tapes, while cable FM-SP-III comprises two different tape batches. In cable FM-SP-III, ten strands are from the same tape batch as in cable FM-SP-II and five strands are from another batch of tapes. When comparing cables FM-SP-II and -III with cable FM-BR, a three times higher critical current was observed in cable FM-BR.

Table 5.2: Measured critical current of *Re*BCO Roebel cables at 4.2 K, 10.5 T.

Cable samples	I_c(kA)
FM-SP-I-A	2.2 ± 0.1
FM-SP-I-B	1.9 ± 0.1
FM-SP-I-C (bare)	2.5 ± 0.2
FM-SP-II	3.2 ± 0.2
FM-SP-III	2.7 ± 0.2
FM-BR	7.7 ± 0.5

It has to be emphasized that this striking difference in I_c values at low-temperature, high-magnetic field between SuperPower-tape cables FM-SP-II or -III and the Bruker-tape cable FM-BR directly reflects the different R&D strategies followed by both tape manufacturers. Bruker primarily aims for application in the ultra-high field NMR market at 4.2 K [295], while SuperPower tapes are developed mainly for electrical power applications at low magnetic field and higher operating temperature [296].

5.2.2 Irreversible I_c degradation

Similar to training in some magnets, in order to performing $I_c(\sigma)$ measurements on cable samples correctly, the sample needs to 'settle' against the lateral side-plates after each cool-down before a proper V-I characteristics can be recorded. Once the sample's training behavior subsides and the voltage transition can be measured reproducibly at a 10 to 100 μV level, the transverse pressure susceptibility of the critical current can be measured by gradually stepping up the force transferred by the pressure anvil. The results for all four cables are presented in Figure 5.9.

The difference in critical current between the two impregnated samples A and B of the 10-strand cable FM-SP-I is smaller than 10%. The difference between the two impregnated 15-strand cables FM-SP-II and -III is about 10%. Moreover, the ratio between the I_c-values of

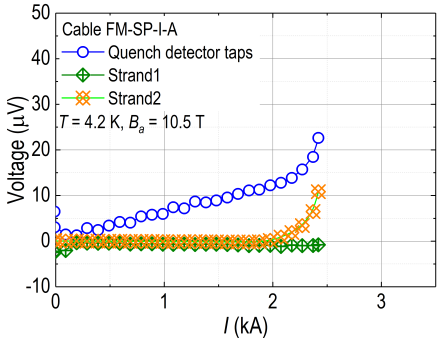

Figure 5.3: Voltage-current curves measured on impregnated cable FM-SP-I-A at an initial reference pressure of 3 MPa.

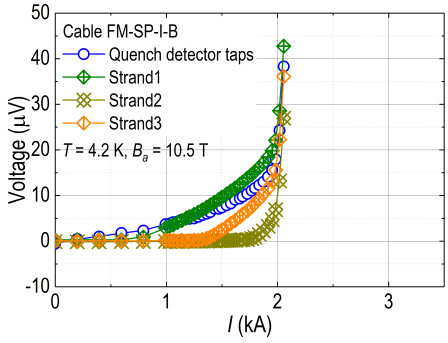

Figure 5.4: Voltage-current curves measured on impregnated cable FM-SP-I-B at an initial reference pressure of 0.5 MPa.

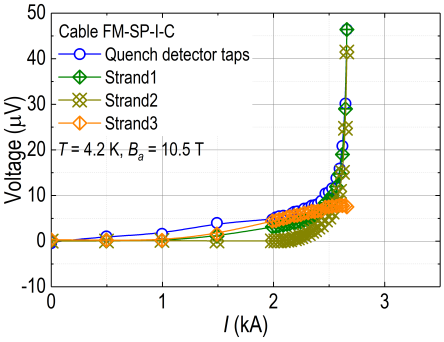

Figure 5.5: Voltage-current curves measured on bare (not impregnated) cable FM-SP-I-C at an initial reference pressure of 10 MPa.

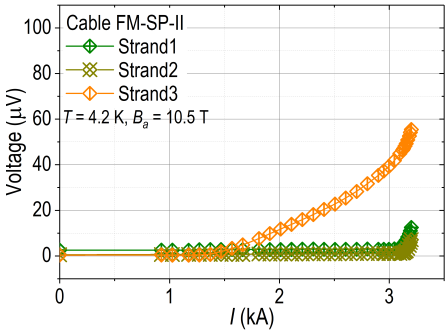

Figure 5.6: Voltage-current curves measured on impregnated cable FM-SP-II at an initial reference pressure of 3 MPa.

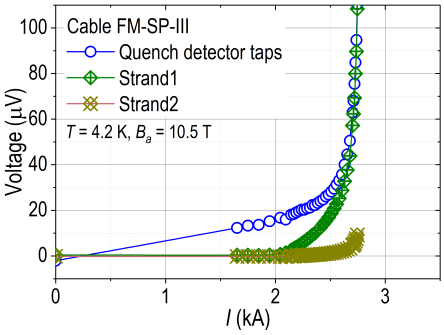

Figure 5.7: Voltage-current curves measured on impregnated cable FM-SP-III at an initial reference pressure of 3 MPa.

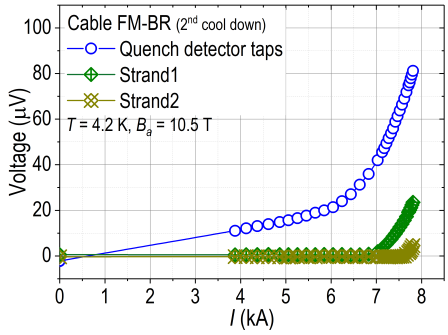

Figure 5.8: Voltage-current curves measured on impregnated cable FM-BR at an initial reference pressure of 3 MPa.

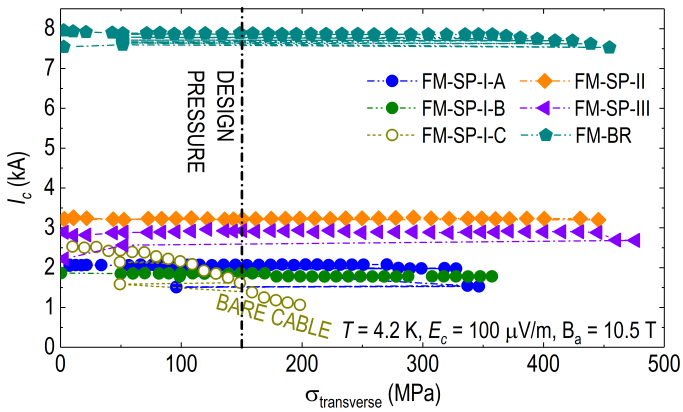

Figure 5.9: *Critical current at T = 4.2 K, Ec = 100 μV/m and B = 10.5 T versus applied transverse pressure of four Roebel cables. The design target of the transverse pressure for the aligned block coil shown in Figure 1.5 when operated as insert in an external magnetic field of 20 T is indicated as well.*

impregnated 15-strand cables FM-SP-II, -III and the 10-strand cables FM-SP-I-A, -B is close to 1.5, i.e. close to the ratio of the number of strands in the cables. This observation shows that the performance of these cables for a given strand type is reproducible, irrespective the cable architecture, used epoxy resin and surrounding insulation material.

Provided the vacuum impregnation is correctly performed, both resins are suitable to enhance the pressure tolerance of the critical current of the cables in comparison to bare cable. All impregnated cable samples easily withstand a transverse pressure of 150 MPa, which is the criterion imposed by the so-called Feather-M2 magnet design [55], see Section 1.2. The critical current reduction of the impregnated cable samples is less than 1% at 150 MPa, at which stress level the critical current of bare cable FM-SP-I-C has already degraded to 65% of the initial critical current, as shown in Figures 5.10 and 5.11. Almost no critical current reduction is observed until the transverse stress reaches 275 MPa for cable sample FM-SP-I-A, 440 MPa for cable sample FM-SP-II and 425 MPa for cable sample FM-BR. The initial decrease of I_c in cable sample FM-SP-I-B between 20 and 50 MPa, its recovery and then second step down at 180 MPa is not explained, however, the effect is within the measurement uncertainty and strictly speaking insignificant. On the other hand, cable sample FM-SP-III displays a somewhat fluctuating critical current with respect to transverse stress, which was not observed in other *Re*BCO Roebel cables investigated. The initial 5% critical current increase when increasing the transverse pressure from 0 to 50 MPa in cable sample FM-SP-III is not understood, but is once more within the measurement error and therefore not statistically insignificant.

The irreversible critical current is determined by repeating the critical current measurement at a relatively low-level transverse stress, i.e. 100 MPa for cable samples FM-SP-I-A and -B, 3 MPa for cable sample FM-SP-II and 50 MPa for cable samples FM-SP-I-C, FM-SP-III and FM-BR, after a measurement at a given stress. The irreversible reduction ΔI_c is derived by calculating the critical current reduction at the cyclic transverse pressure divided by the initial critical current values at the same transverse pressure. As described in Section 2.6, the criterion for determining the irreversible stress limit is taken as 2%, given the 1.5% estimate for the random uncertainty in the critical current. Based on this 2% criterion, the values found for the

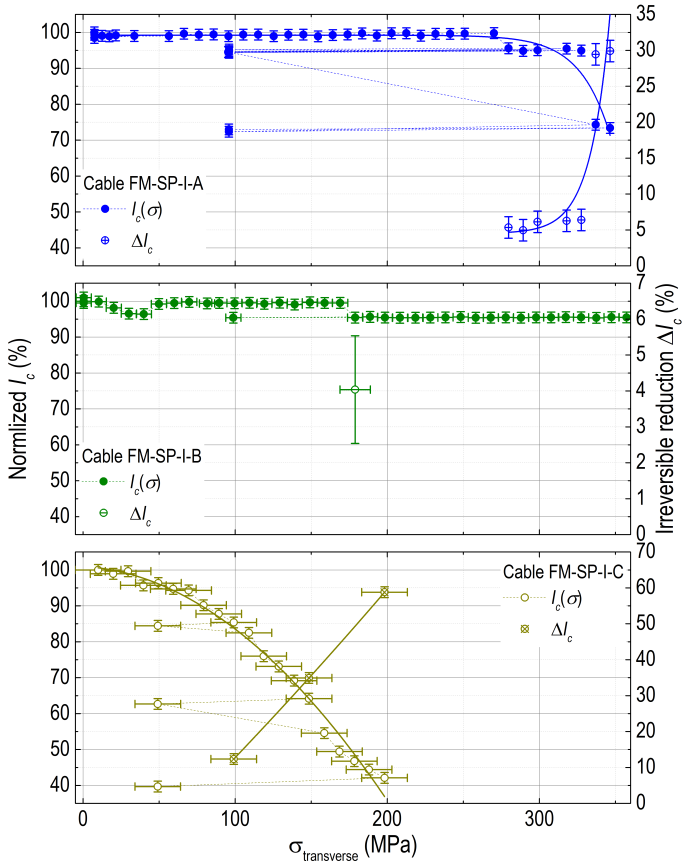

Figure 5.10: *Normalized critical current and irreversible critical current reduction versus applied transverse pressure of impregnated cable samples FM-SP-I-A, -B and bare cable -C. The left-hand axis corresponds to the normalized critical current $I_c(\sigma)/I_c(0)$ in percentage. The right-hand axis reports the irreversible reduction ΔI_c of the critical current with respect to its unstressed initial value. The discrete symbols denote the measurement data with proper curve fitting.*

reversible I_c reduction limit are listed in Table 5.3.

Table 5.3: Irreversible transverse stress limit of *Re*BCO Roebel cables.

Cable samples	Transverse stress limit (MPa)
FM-SP-I-A	<275 ± 10
FM-SP-I-B	170 ± 10
FM-SP-I-C (bare)	<100 ± 15
FM-SP-II	>440 ± 3
FM-SP-III	400 ± 5
FM-BR	455 ± 3

Compared to Nb_3Sn Rutherford cables, the critical current of impregnated *Re*BCO Roeble cables is much less susceptible to transverse stress. However, beyond the irreversible transverse stress limit, no recovery of the critical current is observed when transverse stress is released in *Re*BCO Roebel cables, which is different from the behavior of Nb_3Sn Rutherford cables.

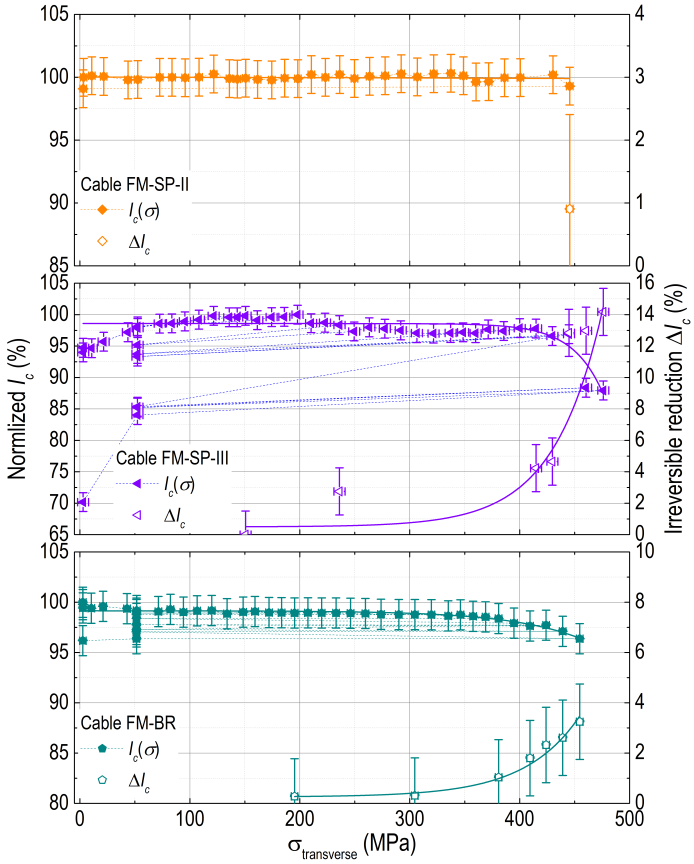

Figure 5.11: *Normalized critical current and irreversible critical current reduction versus applied transverse pressure of impregnated cable samples FM-SP-II, -III and FM-BR. The left-hand axis corresponds to the normalized critical current $I_c(\sigma)/I_c(0)$ in percentage. The right-hand axis reports the irreversible reduction ΔI_c of the critical current with respect to its unstressed initial value. The discrete symbols denote the measurement data with proper curve fitting.*

5.2.3 Single thermal-cycle effect

In Figure 5.12, a comparison between V-I curves registered after the first and the second cool-down (Figure 5.9) of cable FM-BR is shown. Strikingly, from the first to the second cool-down, the critical current degraded by 18%, from 9.5 to 7.8 kA.

The cable samples assembled from SuperPower tapes did not show this effect. Figure 5.13 compares the training quench currents of cable samples FM-SP-II and FM-BR. No reduction in training current is observed from one cool-down to the next for cable FM-SP-II, while cable FM-BR clearly shows the 18% reduction mentioned above. The cause of this temperature cycling effect and its relation to tape architecture and epoxy properties need to be further investigated. It has to noted though that only one single thermal cycle was performed, so there is not enough statistics to make conclusive statements, and further thorough investigation of this issue is needed.

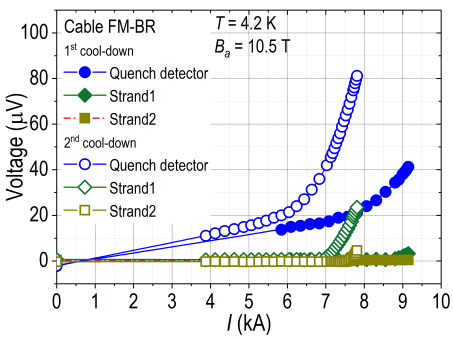

Figure 5.12: *First (solid markers) and second (open markers) V-I curves of cable sample FM-BR illustrating some 18% I_c degradation after one thermal cycle at 4.2 K and 10.5 T.*

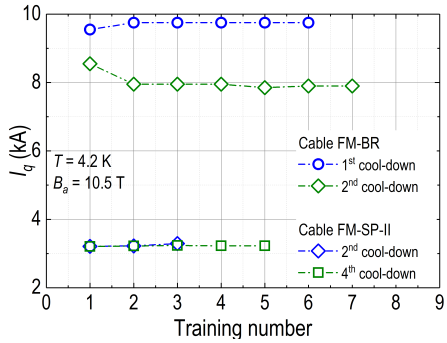

Figure 5.13: *Quench current versus number of training steps showing the effect of a single thermal cycle on cable FM-SP-II and cable FM-BR at 4.2 K and 10.5 T.*

5.2.4 Microscopic analysis of impregnated *Re*BCO Roebel cable samples

After the transverse presssure effect measurements, the samples were carefully removed from the U-shaped holder, cut transversely at the pressed section, embedded in casting epoxy and polished. The cross-sections were examined under an optical microscope to verify the impregnation quality and to investigate for visible damage of the strands.

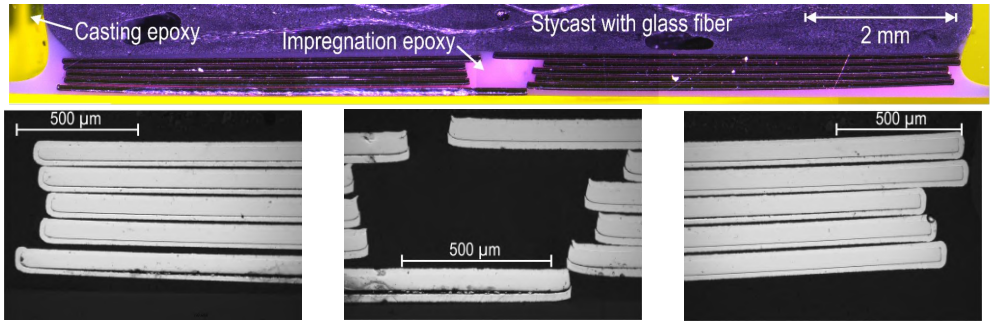

(a) Left **(b)** Middle **(c)** Right

Figure 5.14: *Cross-sectional views of the pressed section of cable FM-SP-I. A general overview of the cable layout is presented on the top, while close-ups of the edges (a, c) and center of the cable (b) are shown in the bottom pictures.*

Figures 5.14 to 5.17 indicate that all cables are fully impregnated, with the epoxy resin filling all intertape space without significant residual voids. In the alignment impregnation Stycast layer of the cable layout overview in Figures 5.14 and 5.17, there are some voids visible because no vacuum impregnation was used to apply this layer. Note that, the impregnated cable is thicker on the left side than on the right side in Figure 5.14. The difference in height is corrected for by gluing the pressure anvil using the so-called alignment impregnation step at room temperature. The only visible damage is delamination of the tape close to the sample holder, clearly visible in the close-ups of the central cable part in Figure 5.14. Several tapes in cable FM-SP-II show clear signs of such layer delamination, especially near to the surface of the

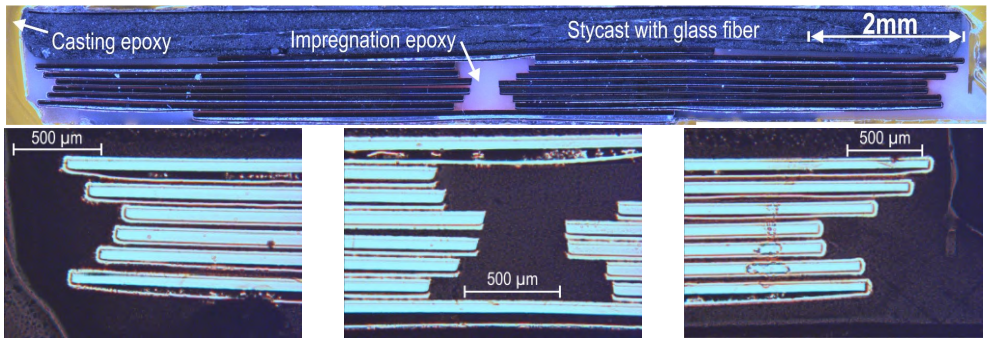

(a) Left **(b)** Middle **(c)** Right

Figure 5.15: *Cross-sectional views of the pressed section of cable FM-SP-II. A general overview of the cable layout is presented on the top, while close-ups of the edges (a, c) and center of the cable (b) are shown in the bottom pictures.*

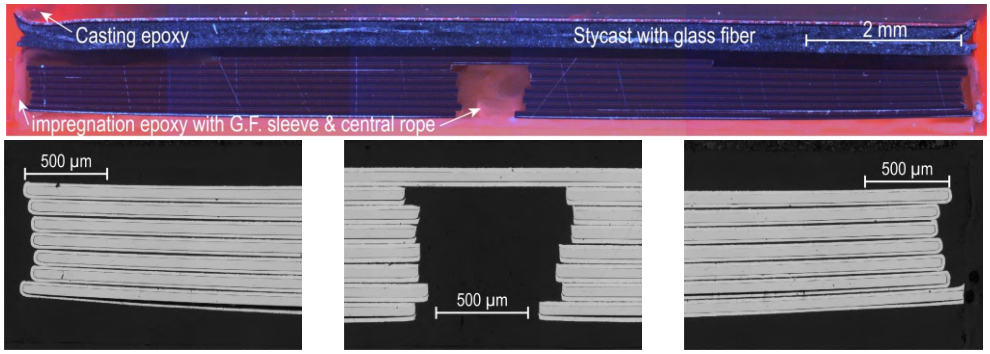

(a) Left **(b)** Middle **(c)** Right

Figure 5.16: *Cross-sectional views of the pressed section of cable FM-SP-III. A general overview of the cable layout is presented on the top, while close-ups of the edges (a, c) and center of the cable (b) are shown in the bottom pictures.*

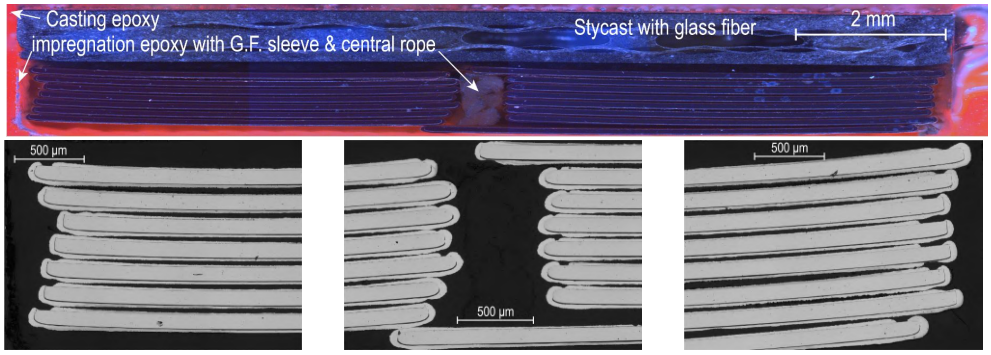

(a) Left **(b)** Middle **(c)** Right

Figure 5.17: *Cross-sectional views of the pressed section of cable FM-BR. A general overview of the cable layout is presented on the top, while close-ups of the edges (a, c) and center of the cable (b) are shown in the bottom pictures.*

cable shown in Figure 5.15. This might be related to the premature V-I transition of strand-3 shown in Figure 5.6. Also cable FM-SP-III shows some signs of delamination in its outermost tapes (Figure 5.16). This is likely a consequence of thermal stress between strands and resin, as discussed in [163] and further corroborated by the difference in the zero-pressure I_c values of bare and impregnated samples of cable FM-SP-I (Figure 5.9). Cable FM-BR does not show any obvious signs of delamination as shown in Figure 5.17. Whether this is a consequence of the different tape architecture or of the extra electroplating step that these strands received after punching, described earlier as the punch-and-coat technique [152], is not clear at this point.

5.3 Conclusion

Two 10-strand *Re*BCO Roebel cable samples FM-SP-I-A and -B were vacuum impregnated with a mixture of epoxy resin and fused silica powder. The critical current of the impregnated cables, as well as a reference bare cable sample FM-SP-I-C, was measured as a function of transverse pressure at 4.2 K and 10.5 T. Also, three new magnet-relevant 15-strand Roebel cable samples were investigated for the effect of vacuum impregnation with epoxy resin on the transverse pressure dependence of the critical current. In order not to change more than one parameter at a time, the 15-strand cable FM-SP-II is assembled from SuperPower tape like the earlier 10-strand cable FM-SP-I and impregnated using the same method. Cable sample FM-SP-III is assembled from the same tape, but impregnated with a different method using CTD-101K and glass fiber. Cable FM-BR comprises Bruker tape using the so-called punch-and-coat process by which the strand is copper plated after punching. The impregnation method used for cable FM-BR is the same as for cable FM-SP-III.

All cables were impregnated successfully, without leaving bubbles or significant residual voids. As reported in Section 2.5.2.2, the thermal contraction of CTD-101K with glass-fiber sleeve is about 0.2% from room temperature to 4.2 K, which is similar to *Re*BCO tapes showing 0.30% ± 0.05%. The value for silica filled Araldite is 0.82%. Both epoxy resins can be used to successfully enhance the transverse pressure tolerance of Roebel cables. However, regarding the coils' insulation requirement and the long pot-life of CTD-101K of 60 h at 40 °C in comparison to the silica filled Araldite featuring 3 h at 80 °C, the CTD-101K with glass-fiber sleeve is more suitable for impregnation of large-size magnets. The critical current of the Roebel cables was measured at 4.2 K in a perpendicular applied magnetic field of 10.5 T. Compared to the 'crossover' region of witness strands, no critical current density reduction was observed in bare cable sample FM-SP-C and only minor and likely insignificant reduction occurred in Araldite CY5538 impregnated cable samples FM-SP-I-A and -II. However, cable samples FM-SP-I-B and -III showed a 10% J_c reduction, which is presently not understood. These observations indicate that the impregnation with Araldite CY5538 doesn't cause the critical current reduction in SuperPower type Roebel cables. No conclusion can be drawn for impregnation with CTD-101K due to lack of sufficient data.

Layer delamination was observed in cable FM-SP-II impregnated with Araldite CY5538 filled with fused silica powder. Whether this is due to the combination of tape punching, which leaves edges of the strands directly exposed to impregnation materials, or to the build-up of thermal stress between resin and strands during cool-down is yet unclear. However, no significant delamination was observed in cables FM-SP-III and FM-BR, which were impregnated using CTD-101K and glass fiber. Therefore, the new impregnation method using a combination of CTD-101K and glass fiber suitable for application in coil windings was convincingly

demonstrated.

A single thermal cycle had no further effect on the critical current of the SuperPower tape based cables, but caused a 20% critical current reduction between first and second cool-down in the Bruker-tape based cable. Since statistics is not sufficient, no further conclusion can be drawn as yet.

In cable FM-SP-I, impregnation caused an increase in the transverse pressure tolerance of the critical current dramatically from <100 to 275 MPa. No critical current degradation was observed in impregnated SuperPower-tape based cables FM-SP-II and -III when loaded with applied transverse pressure up to a record value of 440 MPa. The transverse stress susceptibility of 15-strand SuperPower-tape cables is similar for both impregnation methods. The transverse pressure above which irreversible current reduction starts, is more than 150 MPa higher than for the 10-strand impregnated SuperPower-tape cables. The results are at first instance independent from the type of coated conductor. No critical current degradation was observed for impregnated cable FM-BR up to the very high stress level of 425 MPa. All these values are far beyond the 150 MPa design requirement of the state-of-the art *Re*BCO dipole magnet demonstrator based on using aligned block type of coils and designed for providing 15 to 20 T.

The main conclusions of this study are:

- Epoxy resin CTD-101K is suitable for vacuum impregnation of large-size magnets comprising *Re*BCO Roebel cables enveloped in glass-fiber.
- Provided a correct resin, i.e. CTD-101K and filler-glass-fiber combination, is chosen for vacuum impregnation, *Re*BCO tape based Roebel cables enable the construction of high current density, high-field and thus high-stress magnets i.e. 20+ T class accelerator type magnets.
- 10 and 15-strand *Re*BCO Roebel cables with correct vacuum impregnation are able to withstand transverse pressures far beyond 150 and 300 MPa, respectively, without noticeable degradation in critical current.
- For the first time the transverse pressure effect was measured on 15-strand Roebel cables made from Bruker coated conductor and no critical current degradation was found up to the record of 425 MPa, the irreversible transverse limit was observed up to a record level of 455 MPa.
- The transverse pressure tolerance of 15-strand SuperPower tape based Roebel cables was demonstrated up to 440 MPa.

The transverse pressure effect on the critical current of *Re*BCO Roebel cables presented here are the first ones ever at high stress levels and the number of samples is rather limited. Consequently, it is too early to generalize the unique observations, made and draw hard conclusions with respect to systematic effects, correlation to certain makes of *Re*BCO tape and impregnation constituents. Further investigation are required to broaden the experience database.

Chapter 6
Inter-strand contact resistance and AC loss

In this chapter, the inter-strand resistance of ReBCO Roebel cables measured at 4.2 and 77 K is presented. The samples are impregnated with epoxy resin to reduce the effect of critical current degradation due to Lorentz forces acting on the strands in the Roebel cables. The measured inter-strand resistance is then used to estimate the coupling loss in different magnetic field orientations. Moreover, the contributions of diverse interface contact resistances to the overall inter-strand resistance of Roebel cables were also estimated a-priori using the model presented before in Section 3.3. For validation purpose, the AC loss of cables was examined in various orientations of applied magnetic field at 4.2 K. With three analytical models described earlier in Section 3.4 the hysteresis loss was calculated and compared to the measured data.

6.1 Introduction

Besides a degradation-free critical current behavior under transverse stress, the *Re*BCO cables for accelerator type magnets also require adequate magnetic field quality as well as an optimum balance of coupling loss and current sharing. The work presented here aims to improve and validate the understanding of the relation between inter-strand resistance and coupling loss in impregnated *Re*BCO Roebel cables for magnet applications.

The inter-strand contact resistance of *Re*BCO Roebel cables was reported by several authors [100–102], but mainly on non-impregnated cables. AC loss performance of Roebel cables is reported as well but mostly concentrating on 77 K [50].

Application-oriented Roebel cables when used in accelerator type coils must be impregnated with some loaded resin to enhance the mechanical properties, as described in Chapters 2 and 5. However, resin impregnation of Roebel cable is not straightforward since epoxy resins have a different thermal contraction coefficient to *Re*BCO tape, which can cause layer delamination in cable strand [86]. Resins with proper filler can be better matched to the tape's thermal contraction, as reported by Kirby *et al.* [164]. Two impregnation variants based on using CTD-101K resin [171] with glass-fiber sleeve and CTD-101G resin [297] with Al_2O_3 powder as filler were developed.

Cables FM-SP-II-A, -B and -C with a glass-fiber braid in the central channel, were insulated by a glass-fiber sleeve and vacuum impregnated with epoxy resin CTD-101K, as listed in Table 6.1. The cable samples were impregnated over a length slightly longer than one transposition length. Thin Kapton foils are insulating the excess lengths of strands at one termination, where instrumentation wires are soldered to each strand. The three cables were examined for inter-strand resistance at 4.2 and 77 K, which is defined in this work by the contact resistance over a single tranposition length R_a and determined using a direct transport current measurement, as described in Section 2.3.

Table 6.1: List of *Re*BCO Roebel cables investigated.

Impregnation ⧹ cable	FM-SP-II-A	FM-SP-II-B	FM-SP-II-C	FM-SP-II-D
Epoxy resin	CTD-101K			CTD-101G
Glass-fiber sleeve	Y			Y
Glass-fiber central rope	Y			N
Measurements				
R_a measured	Y			N
AC loss measured	N	Y	N	Y

After the inter-strand resistance measurements, cable FM-SP-II-B was shortened to one transposition length in order to measure its AC loss. A same length of cable FM-SP-II-D was impregnated with CTD-101G filled with alumina powder for AC loss measurements. For all cable samples examined, a 5 MPa transverse pressure was applied perpendicular to their wide face during impregnation. This pressure was chosen to roughly mimic the conditions during magnet coil preparation. All four cable samples have the same geometry using strands made from SuperPower tape with characteristics that were presented in Table 2.4. The cable sample architecture and geometric parameters are shown in Figure 6.1 and Table 6.2, respectively. All AC loss measurements were carried out in a dipole magnet facility at the University of Twente [140], sweeping the transverse magnetic field between ±1.5 T with a frequency of 1 Hz maximum.

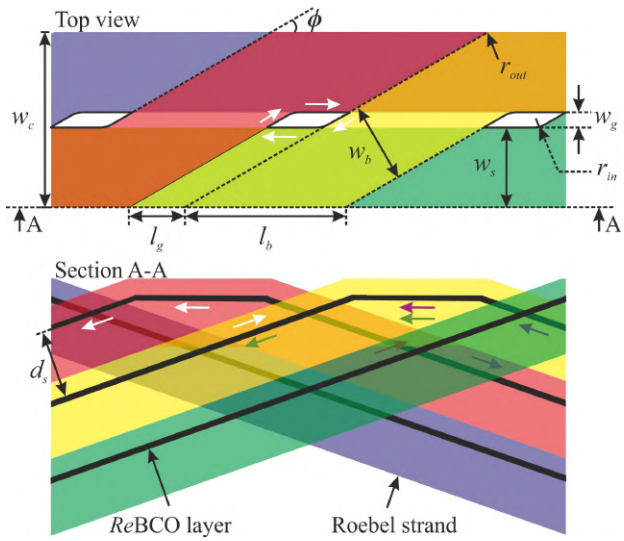

Figure 6.1: *Roebel cable geometry. The cyclic arrows denote the induced current paths used to clarify the estimation of the coupling current loop area of cables. The analytical model was presented in detail in Section 3.4.*

Table 6.2: Parameters of the impregnated SuperPower tape based *Re*BCO Roebel cable.

Description	Symbol	Value
Number of strands	N_s	15
Strand thickness	t_s	0.1 mm
Cable thickness	t_c	0.8 mm
Insulation thickness	t_i	0.1 mm
*Re*BCO layer thickness	t_{Re}	1.0 μm
Copper plating thickness	t_{Cu}	20 μm
Strand width	w_s	5.5 mm
Cable width	w_c	12.0 mm
Cross over width	w_b	5.5 mm
Channel width	w_g	1.0 mm
Cross over angle	Φ	30°
Transposition pitch	L_{tp}	226 mm
Hole length	l_g	4.1 mm
Cross-over length	l_b	11 mm
*Re*BCO layer distance	d_s	0.11 mm
Inner radius	r_{in}	6.0 mm
Outer radius	r_{out}	0.0 mm

The inter-strand resistance and AC loss results were used to validate the electrical network model developed by Van Nugteren *et al.* [141], that allows calculation of the dynamic magnetic field quality, stability and normal zone propagation in Roebel cable. To use the model for exhaustive simulation of various Roebel cables, measured input data as contact-resistance and magnetization are required.

In order to understand the relative contribution of the various layers in a single coated conductor Roebel strand to the overall inter-strand resistance in a cable, the various component materi-

als in the tape were considered separately and a-priori estimates were made of their electrical resistance, see Section 3.3. Also, estimates of the hysteresis loss behavior of the cables based on the analytical ellipse-, rectangle- and slab models described in Section 3.4 are analyzed.

6.2 Inter-strand resistance, results and discussion

6.2.1 Measurement data

The inter-strand resistance per transposition length R_a measured on Roebel cables FM-SP-II-A, -B and -C are shown in Figure 6.2 and summarized in Table 6.3. At 77 K, the resistance ranges from 3 to 16 $\mu\Omega$, with a standard deviation of 1 to 5 $\mu\Omega$, depending on the cable. At 4.2 K, the values are about 2 times lower, ranging from 1.5 to 9 $\mu\Omega$ with a standard deviation of 0.5 to 3 $\mu\Omega$. To check for parasitic contacts at the cable ends, possibly caused by sample cutting, the cable end with no Kapton insulation of sample FM-SP-II-A was polished. The cable sample was measured again and no significant resistance increase was observed.

The resistance ratio of R_a between 77 and at 4.2 K is about 2, see Table 6.3. This corresponds to a RRR value of 10 for the copper stabilizer layer when extrapolating to room temperature using electrical resistivity data of copper [232].

Table 6.3: R_a measured between neighboring strands at 77 and 4.2 K.

Temperature	cable FM-SP-II		
	A	B	C
77 K ($\mu\Omega$)	16 ± 5	2.9 ± 0.9	10 ± 3
77 K polished ($\mu\Omega$)	18 ± 6	-	-
4.2 K ($\mu\Omega$)	9 ± 3	1.4 ± 0.5	5 ± 1
R_a(77 K) / R_a(4.2 K)	1.9 ± 0.1	2.1 ± 0.1	2.2 ± 0.4

6.2.2 Discussion

As described in Section 3.3, a resistor network model is used to estimate the inter-strand resistance components inside *Re*BCO conductors. In Table 3.5, the estimated resistance components that contribute to the inter-strand resistance normalized with respect to the axial length of the superconducting layer l, were summarized. For Roebel type cable samples, two adjacent tapes are in contact everywhere except in the cross-over regions. Since tapes cross twice per transposition length, and for a 15-strand cable it takes 1/15 of transposition length before they cross, the axial length l over which adjacent tapes are in contact can be estimated straightforwardly to be 13/15 of the transposition length L_{tp}, i.e. 196 mm.

Table 6.3 shows that measured R_a values range from 2.9 ± 0.9 to 18 ± 6 $\mu\Omega$ at 77 K and from 1.4 ± 0.5 to 9 ± 3 $\mu\Omega$ at 4.2 K. With the estimates for the different resistance components given in Table 3.5, R_{AE} has such a high resistance that it hardly contributes to the inter-strand resistance current flow. For other resistance components, all but R_{DE} and R_{EF} are too low to contribute significantly to the inter-strand resistance. In other words, we can conclude for the calculated R_a:

$$R_a \approx R_{DE} + R_{EF} = \frac{R_{\square,tt}}{\lambda_{tt} l} cotanh\left(\frac{w_{sc}}{\lambda_{tt}}\right), \tag{6.1}$$

where $R_{\square,tt}$ is the surface resistivity of the tape-to-tape interface and λ_{tt} is the corresponding current transfer length. At 77 K, we can derive from the measured R_a, that $R_{\square,tt}$ is in the range

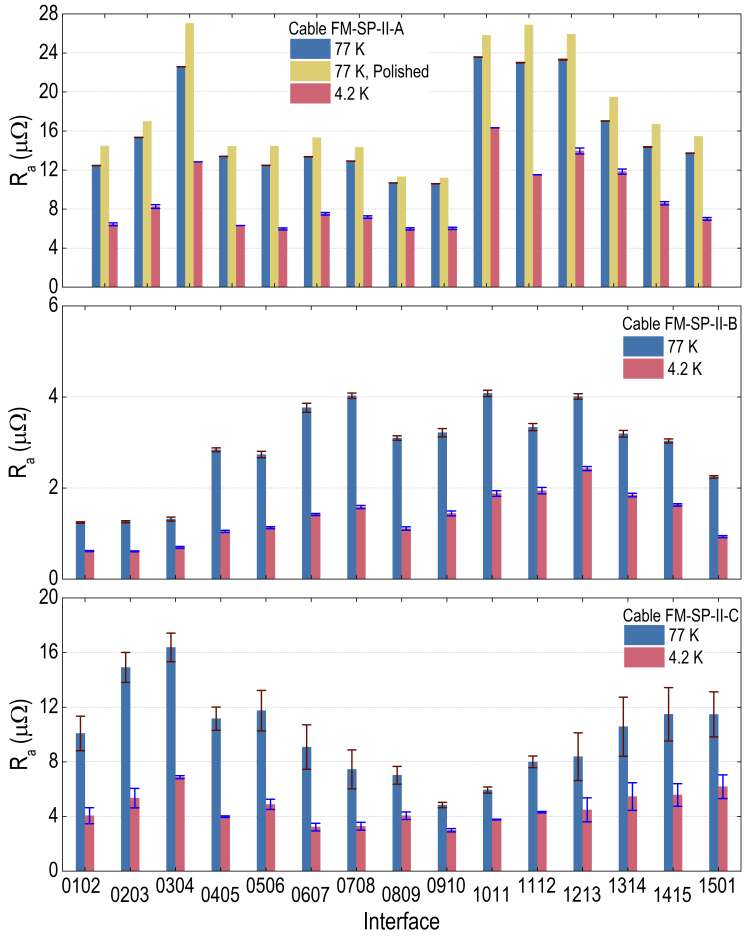

Figure 6.2: *Inter-strand resistances measured at 77 and 4.2 K in the three CTD-101K impregnated Roebel cables. The horizontal axis denotes the interface between strands, i.e. 0102 represents the interface between strands 1 and 2.*

of 1 to 20 nΩm^2 and that λ_{tt} is 4 to 16 mm. This implies that the current transfer length λ_{tt} is indeed larger than or equal to the width of the *Re*BCO layer w_{sc}, so that our earlier assumption made to derive Equation (3.14) in Section 3.3 holds and R_{FG} is negligible. At 4.2 K, $R_{\square,tt}$ is 0.5 to 10 nΩm^2 corresponding to a λ_{tt} of 3 to 11 mm.

Similar contact surface resistivity values at 77 K were measured by Otten *et al.* [100]. With a 5 MPa transverse pressure, the value for SuperPower *Re*BCO tapes is between 7 and 20 nΩm^2, and for a 10-strand bare Roebel cable 5 to 25 nΩm^2. These coherent results obtained in different laboratories with different measurement methods show that surface resistivities can be measured reliably.

The resistance of the impregnated copper to copper interface is determined by the effective contact area between the tapes, which is significantly affected by the roughness of the tape surface, surface copper-oxidation level, applied transverse pressure during impregnation and strand-misalignment. It is difficult to determine analytically what the effective contact between

the surfaces.

6.3 AC loss results and discussion

The AC loss data of the impregnated cable samples FM-SP-II-B and FM-SP-II-D are presented in Figures 6.3 to 6.5. Figure 6.3 shows the loss measured with the AC magnetic field applied perpendicular to the wide face of the cables. In Figure 6.4 the magnetic field is applied parallel to this face, but still perpendicular to the cable axis. Figure 6.5 shows the loss when the magnetic field is rotated in a plane perpendicular to the cable axis and makes an angle θ with the normal to the wide face. All data were collected with the cables fully submerged in boiling helium at a temperature of 4.2 K. In all figures the discrete symbols represent measured data points, while the solid and dashed lines were calculated with the analytical models for hysteresis- and coupling losses, respectively, that were presented in Section 3.4, except for Figures 6.3c and 6.4c, where the lines are just polynomial fits that are used to determine the maximum of the loss function.

In Sections 6.3.1 to 6.3.3, we simply present the data and make some key observations about the observed amplitude-, frequency- and orientation dependences. A more detailed discussion of the measured losses, comparing the cables to each other and commenting on the model predictions, is referred to Section 6.3.4.

6.3.1 Measurement results in perpendicular transverse magnetic field

In Figure 6.3a, the losses of the two cables in a perpendicular AC magnetic field are reported as a function of magnetic field amplitude at several fixed frequencies. Also the frequency-independent hysteresis losses that are predicted by the ellipse- and rectangle models, Equations (3.17) and (3.24) respectively, are presented. The dot-dashed lines correspond to inter-strand coupling loss predictions at selected frequencies, calculated with Equation (3.30) using the independently measured inter-strand resistance R_a of 1.4 $\mu\Omega$ of cable FM-SP-II-B, as presented in Table 6.3 of Section 6.2. We can make several observations:

- The measured AC loss in the two cables are quite similar, especially at magnetic fields above 50 mT;
- Up to 500 mT the measured loss increases with the third power of the magnetic field amplitude, as predicted by most hysteresis loss models for magnetic field amplitudes below the penetration field;
- The amplitude dependence of the loss in cable FM-SP-II-B measured at two different frequencies, 10 and 100 mHz, shows the same result across the investigated range;
- Qualitatively, the model predictions for hysteresis loss follow the shape of the measured data quite well, but quantitatively they over-estimate the perpendicular magnetic field loss, by more than two decades for the ellipse model and by about a factor 4 to 5 for the rectangular model. Note that a penetration field of 1 T was assumed in these model predictions (see below);
- Even at higher frequency, the coupling loss predictions remain several orders of magnitude below the measured data.

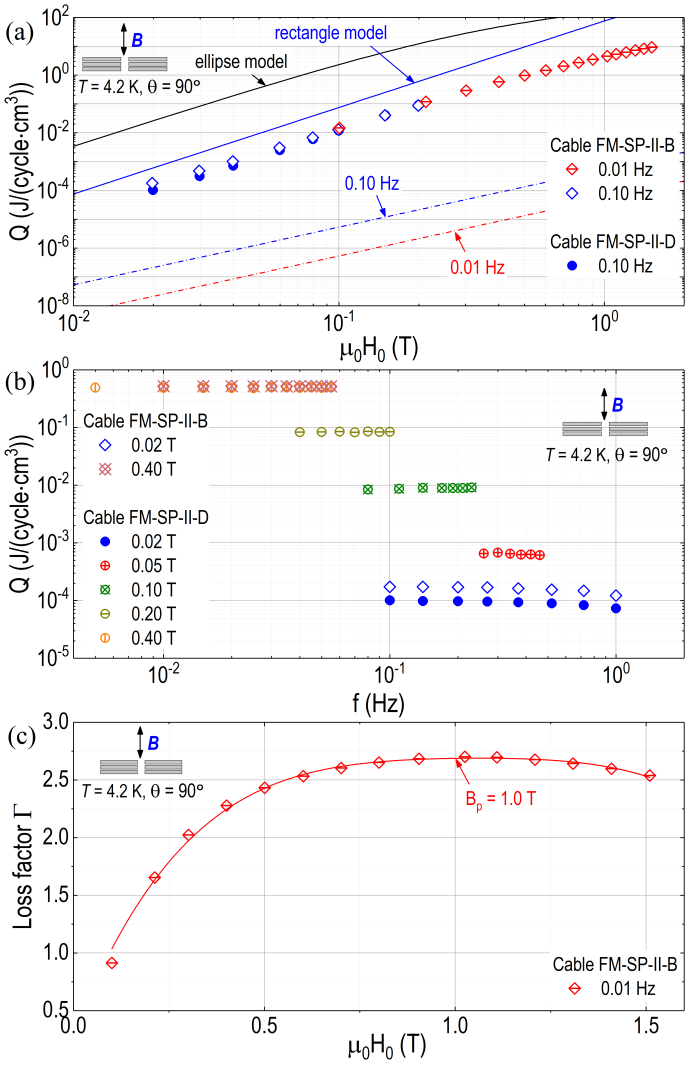

Figure 6.3: *Measured and calculated AC loss of cables FM-SP-II-B and -D at 4.2 K in perpendicular transverse magnetic field: (a) amplitude dependence of AC loss at selected frequencies: symbols represent the measured data, lines represent model predictions of the hysteresis- (solid line) and coupling loss (dot-dashed line); (b) frequency dependence of the loss at selected amplitudes; (c) amplitude-dependent loss factor* Γ *of cable FM-SP-II-B, measured at 0.01 Hz: symbols represent the measured data, the solid line is a polynomial fit made to help determine the maximum in the curve.*

In Figure 6.3b, the measured frequency-dependence of the AC loss in perpendicular magnetic field is presented at a number of selected amplitudes. Again, some straightforward conclusions can be drawn:

- In both cables, the loss does not vary significantly with frequency throughout the investigated amplitude range of 20 to 400 mT. This confirms the main conclusion from Figure 6.3a, that the perpendicular magnetic field loss is dominated by hysteresis loss;

- At 20 mT, the loss level in cable FM-SP-II-D is about a factor 2 lower than in cable FM-SP-II-B, but the losses in both cables virtually coincide at a higher amplitude of 400 mT. Whether or not this is related to the different impregnation resins used in both cables is not clear.

We conclude that for both cables hysteresis is the dominant loss mechanism in perpendicular magnetic field throughout the investigated amplitude- and frequency ranges.

In Figure 6.3c, the amplitude dependence of the measured loss factor Γ of cable FM-SP-II-B is shown, defined as:

$$\Gamma = \frac{Q}{2\mu_0 H_0^2}, \tag{6.2}$$

where Q is the loss per unit volume per cycle, μ_0 is the vacuum permeability and H_0 is the applied field amplitude. The solid line is a polynomial fit to the data, which allows to estimate a perpendicular penetration field of 1.0 ± 0.2 T at 4.2 K, corresponding to the maximum in Γ. Note that this value was used to calculate the hysteresis predictions in Figure 6.3a.

6.3.2 Measurement results in parallel transverse magnetic field

When the AC magnetic field is applied parallel to the wide face of the cables, but still perpendicular to their axis, quite a different loss behavior is observed. Figure 6.4 shows the loss at 4.2 K in this field configuration. Like in Figure 6.3, the amplitude- and frequency dependences were measured separately at selected frequencies and amplitudes, respectively. Also here symbols represent measured data, lines calculated model predictions and the third plot gives the amplitude-dependent loss function of cable FM-SP-II-B.

With reference to the amplitude dependence shown in Figure 6.4a, it is observed that:

- The loss in cable FM-SP-II-B measured at different frequencies of 0.2, 0.5 and 1 Hz coincide within the uncertainty of the measurement;
- Just like in the perpendicular orientation presented above, the amplitude dependence of the loss in this cable follows the hysteresis loss trend also in parallel magnetic field (increasing with the third power of H_0 for amplitudes below 30 mT); At higher amplitudes the loss in this cable FM-SP-II-B changes over to a linear amplitude dependence, in agreement with the well-known fully-penetrated hysteresis behavior described in Section 3.4;
- The hysteresis model calculations, assuming a parallel penetration field of 30 mT, follow the measured data of this cable quite closely, irrespective of the model details (ellipse or rectangle);
- Also in this configuration, the calculated coupling loss of cable FM-SP-II-B using an R_a of 1.4 $\mu\Omega$ lies more than an order of magnitude below the measured data.

We thus conclude that, just like in the perpendicular magnetic field case, the parallel field loss of cable FM-SP-II-B is dominated by hysteresis.

Cable FM-SP-II-D, on the other hand, behaves qualitatively quite different. For this cable the amplitude dependence of the loss, measured at 0.5 Hz, follows a power-law with power two rather than three. Unfortunately, the inter-strand resistance value of this cable was not

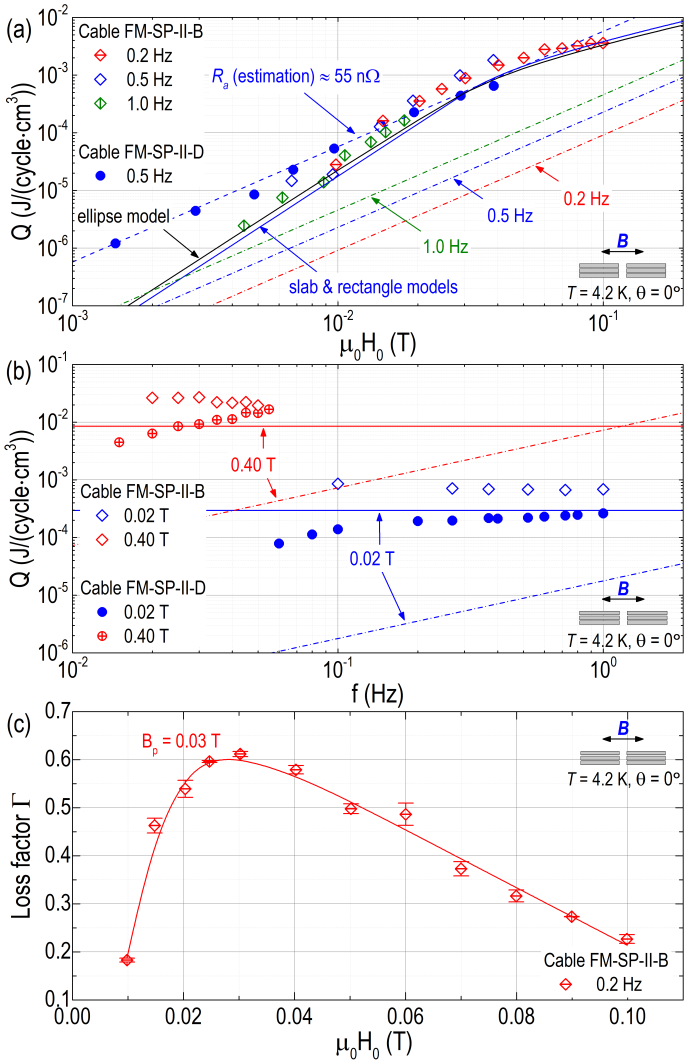

Figure 6.4: *Measured and calculated AC loss of cables FM-SP-II-B and -D at 4.2 K in magnetic field applied perpendicular to the cables' axis but parallel to their wide face: (a) amplitude dependence of the AC loss at selected frequencies: symbols represent the measured values, lines represent model predictions of the hysteresis- (solid line) and coupling loss (dot-dashed line); (b) frequency dependence of the loss in both cables at selected magnetic field amplitudes; (c) amplitude-dependent loss factor* Γ *of cable FM-SP-II-B, measured at 0.2 Hz: symbols are the measured data, the solid line is a polynomial fit to determine the position of its maximum.*

measured independently so that the data cannot be compared with an a-priori prediction of the inter-strand coupling loss. However, following the opposite route, we can take the measured loss and use the coupling loss Equation (3.30) to deduce an inter-strand a contact resistance value of 55 nΩ.

In Figure 6.4b no significant frequency dependence of the loss is observed in cable FM-SP-II-B, confirming the dominance of hysteresis loss in this sample. Cable FM-DP-II-D, however,

shows a weak but significant frequency dependence in the amplitude range of 20 to 400 mT.

Finally, from Figure 6.4c we conclude that the parallel penetration magnetic field of cable FM-SP- II-B is 30 ± 5 mT at 4.2 K.

6.3.3 Magnetic field angle dependence of AC loss

Figure 6.5 shows the angular dependence of the loss $Q(\theta)$ in the two cables, measured at 4.2 K with a fixed magnetic field amplitude of 20 mT and frequency of 1 Hz. θ is defined as the angle between the applied magnetic field, which is kept perpendicular to the cable axis, and the wide face of the cables, i.e. θ = 90° corresponds to the perpendicular case presented in Section 6.3.1 and θ = 0° to the parallel configuration of Section 6.3.2. The diamond- and circle-shaped symbols represent the measured data, which were obtained by processing the voltage signals from the in- and out-of-plane pickup coils separately using Equation (2.4), as described in Section 2.4.1, taking only the applied magnetic field component perpendicular to the corresponding coil, $H_0\sin\theta$ for the in-plane coil and $H_0\cos\theta$ for the out-of-plane one, and using the corresponding fill factors ($\alpha_\perp$ and $\alpha_\parallel$, respectively) that were determined from the calorimetric calibration during the 'pure' perpendicular or parallel loss measurements. The open-square symbols represent the sum of the two contributions. The lines in both graphs are model calculations that are discussed in Section 6.3.4.

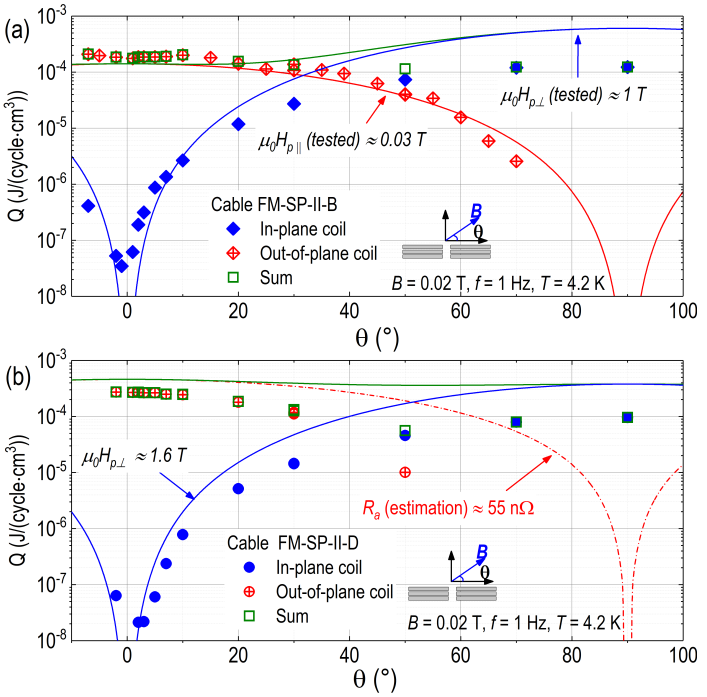

Figure 6.5: *Angular dependence of the measured and calculated AC loss at a fixed magnetic field amplitude 20 mT, frequency 1 Hz and temperature 4.2 K: (a) cable FM-SP-II-B, the blue and red symbols are the loss detected by the in- and out-of-plane coils separately, the green ones are the sum of both. The solid curves represent hysteresis loss calculated with the 'rectangle model'; (b) cable FM-SP-II-D, also with blue and red symbols for the measured data obtained from the two separate coil sets and the green ones representing the sum of both. The solid line is also here calculated with the 'rectangle' model, the dashed one with a coupling loss model.*

Figure 6.5a presents the angular dependence of the loss in cable FM-SP-II-B. From the previous sections we know that in both, in the perpendicular- and in the parallel configuration, the losses in this cable are dominated by hysteresis. Therefore, we model the angle-dependent losses with the same rectangle model Equations (3.24) (the blue line) and (3.26) (the red line) as in Figures 6.3 and 6.4, using the perpendicular and parallel penetration fields found in the previous sections (1 and 0.03 T, respectively, see Figures 6.3c and 6.4c), but this time taking into account the field angle by using the appropriate magnetic field component rather than its full amplitude. In other words, the blue curve is proportional to $|\sin^3\theta|$ and the red one to $|\cos^3\theta|$. The green line is simply the sum of both. The data follow these model predictions reasonably well, especially in the vicinity of $\theta = 0°$. Closer to the perpendicular situation $\theta = 90°$, the correspondence is less good, with a deviation between data and model that is similar to the one observed in the 'pure' perpendicular experiment of Section 6.3.1.

Figure 6.5b shows the measured angular dependence of the loss in cable FM-SP-II-D. From Section 6.3.2 we know that the parallel loss in this cable is dominated by inter-strand coupling. Hence we use coupling loss Equation (3.30) to model the influence of the parallel field component, yielding the red dashed line which is proportional to $|\cos^2\theta|$. For the perpendicular component (the blue line), we still use the hysteresis Equation (3.24) predicting a $|\sin^3\theta|$ behavior. The perpendicular penetration magnetic field is taken to be 1.6 T, reported for similar cable samples that were measured at the University of Southampton [298, 299].

6.3.4 Discussion

Hysteresis loss

The perpendicular and parallel penetration fields of cable FM-SP-II-B were measured to be 1.0 ± 0.2 T and 30 ± 5 mT, as presented in Figures 6.3c and 6.4c, respectively. The perpendicular penetration field of cable FM-SP-II-D was reported by the University of Southampton [298, 299] as 1.6 T. From these measured penetration field values and the cable dimensions presented in Table 6.2, the critical current density J_c can be estimated using the analytical model Equations (3.19), (3.25) and (3.27) for the ellipse, rectangle and slab, respectively. The resulting J_c values are shown in Table 6.4. The ellipse- and rectangle models yield similar values in perpendicular magnetic field, which also closely corresponds to the J_c value derived from the parallel penetration field for all models.

Table 6.4: Derived critical current densities for cable FM-SP-II-B.

$\mu_0 H_p$(T)	j_c($\times 10^{10}$ A / m^2)	Model	External field direction
1	4.3	Ellipse	$\mu_0 \boldsymbol{H}_\perp$
	4.2	Rectangle	
0.03	4.8	Ellipse / rectangle / slab	$\mu_0 \boldsymbol{H}_\parallel$

The hysteresis loss in the 15-strand *Re*BCO Roebel cables can then be calculated and these results were presented in Figures 6.3a and 6.4a as solid lines. In perpendicular field, see Figure 6.3a, the rectangle model approaches the measured data best. This is most likely due to the local magnetization of the cable edges, which is not represented correctly in the elliptic model. In the parallel case, shown in Figure 6.4a, all three analytical models correspond quite closely with the measured data. This is not too surprising, since demagnetization effects at the sample edges only play a minor role in this configuration. In the partial-penetration regime, all mea-

sured losses increase with the cube of the magnetic field amplitude $H_0{}^3$. The $H_0{}^4$ dependence predicted for low magnetic fields by the thin strip model proposed in [236] is not observed in our data set.

Since Carr's rectangle model corresponds best to the measured cable data, the model introduced to describe the angular dependence of the loss in Figure 6.5 is derived from this rectangle model, using the measured penetration fields and j_c-values described above.

To the best of our knowledge, there is no analytical model available that describes the hysteresis loss in a superconductor with an aspect ratio different from 1 as a function of the magnetic field angle. Since the experimental data in Figure 6.5 were obtained with separate in- and out-of-plane coils, we modelled them by simply taking the in-plane and out-of-plane components of the applied magnetic field and inserting these for the amplitude $\mu_0 H_0$ in the rectangle model. Remarkably, the results of such analysis follow the measured data reasonably well, reproducing the parallel component of the magnetization closely and the perpendicular component with the same deviation as the pure perpendicular field case measurement results shown in Figure 6.3. Note that this observation is far from trivial, since the Critical State Model is highly non-linear and the magnetic field penetration profile for intermediate angles could thus be expected not to obey the simple superposition that is inherently assumed in our modelling approach. However, since this assumption does yield a reasonable correspondence to the data, it can be used to make a first straightforward estimate of the loss, e.g. when pre-designing a magnet.

Eddy current loss

The eddy current loss in perpendicular and parallel magnetic fields is calculated from Equation (3.29). Similar to coupling loss, eddy current loss increases with the square of the amplitude at a constant frequency. For example, the eddy current loss in a perpendicular magnetic field of 0.1 T at 0.1 Hz and 4.2 K is calculated to be 1.0×10^{-3} J/(cycle·cm^3), about 200 times higher than the estimated coupling loss 5.5×10^{-6} J/(cycle·cm^3) but is only 10% of the measured hysteresis loss. In a parallel magnetic field, the eddy current loss at 1 Hz and 0.1 T is estimated at 6.3×10^{-9} J/(cycle·cm^3), about 1000 times lower than the corresponding coupling loss 4.6×10^{-6} J/(cycle·cm^3). In both orientations, the estimated eddy current loss is lower than the measured AC loss throughout the investigated experimental window.

Coupling loss

Using Equation (3.30), the AC coupling loss can be derived from the measured inter-strand resistance R_a and from the area A of the elementary inductive 'pick-up loop' formed by two coupled strands. The value of A in perpendicular and parallel magnetic field orientations are reported in Table 6.5, estimated using Equations (3.31) and (3.32).

Table 6.5: Parameters used in coupling model calculation.

	Unit	Value	n
$A_\perp$	mm^2	4.1	2*N_s
$A_\parallel$	mm^2	24	N_s
R_a of cable FM-SP-II-B	$\mu\Omega$	1.4	-

Using the loop areas and average measured R_a value reported in Section 6.2.1, the coupling loss in cable FM-SP-II-B was calculated. The results are included in Figures 6.3 and 6.4 as dot-

dashed lines, yielding for all investigated amplitudes, frequencies and field orientations, loss values that are several orders of magnitude lower than the measured ones. This simple model thus confirms the dominance of hysteresis loss in cable FM-SP-II-B. For cable FM-SP-II-D, on the other hand, a clear signature of coupling loss is observed in the parallel field orientation. Unfortunately, the inter-strand resistance R_a of this cable FM-SP-II-D was not measured, but can be estimated to be 55 nΩ from Equation (3.30) and the loss data presented in Figure 6.4. Note that this is about 30 times lower than the measured R_a values in cable FM-SP-II-B. Possibly, this is related to the different impregnation: in cross-sectional microscopy of the cables no voids were observed in the CTD-101K resin that was used with cable FM-SP-II-B, while in cable FM-SP-II-D the central channel does not contain resin, as shown in Figure 6.6. Presumably, the higher viscosity of the CTD-101G resin with filler particles hampered proper penetration of the epoxy in this cable. Whether this scenario is correct and indeed related to the lower inter-strand resistance needs to be investigated further.

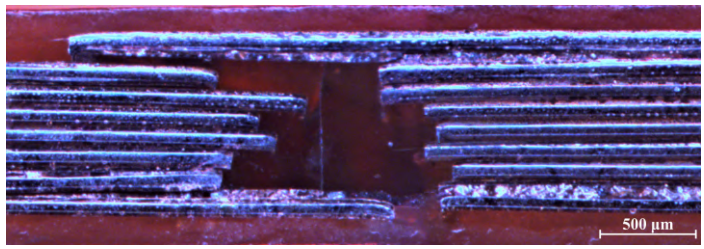

(a)

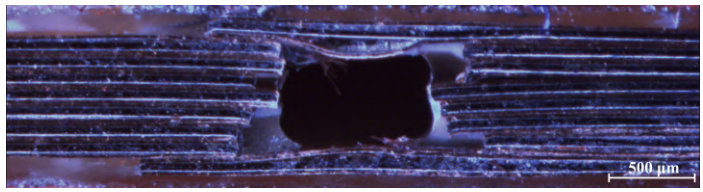

(b)

Figure 6.6: *Cross-sectional views of the center section of investigated Roebel cables: (a) cable FM-SP-II-B; (b) cable FM-SP-II-D. Note that the ReBCO layer is facing upwards in both pictures.*

6.4 Conclusion

Application of *Re*BCO Roebel cable in magnets require characterization of various cables to arrive at high performance coil windings. For enabling accurate *Re*BCO Roebel cable simulation needed for the design of 20+ tesla class superconducting accelerator type magnets, accurate model input is essential. For this reason, the experimental data base has to be extended since the volume of data is quite limited.

Novel resin-filler impregnated *Re*BCO Roebel cables proposed by CERN were characterized in terms of inter-strand contact resistance and AC loss. The inter-strand resistance values within one transposition length of three cables at 77 K, range from 3 to 18 $\mu\Omega$ and the derived mean contact surface resistivity is in the range of 1 to 20 nΩm^2. The inter-strand resistance measured at 4.2 K is in the range of 1 to 10 $\mu\Omega$, leading to a surface resistivity of 0.5 to 10 nΩm^2. Variations in inter-strand resistance values between cables are within 30% and may be caused by variations in strand alignment. The variation in average inter-strand resistance for samples

of three cables is within a factor 6. Analysis of the several contributions to the intra-strand contributions determining the overall inter-strand contact resistance clearly indicates the dominant contribution of the copper-to-copper surface resistance.

AC loss at 4.2 K in impregnated Roebel cables was measured calorimetrically and inductively with alternating magnetic field applied either perpendicular or parallel to the wide face of the cable. In perpendicular field, both amplitude- and frequency dependence of the two cable types show that their loss is dominated by hysteresis. The same is valid for the loss in cable FM-SP-II-B in parallel field, while cable FM-SP-II-D shows a clear sign of inter-strand coupling loss in this orientation. In parallel field, the hysteresis loss of cable FM-SP-II-B is well described by the infinite slab model, while in perpendicular field the best possible description is given by the rectangular strip model. Calculation of the coupling loss in this cable, based on the measured inter-strand contact resistance, confirms that hysteresis loss is dominant for all orientations of magnetic field. Although the inter-strand contact resistance of cable FM-SP-II-D was not measured directly, the observed coupling loss in this cable in parallel magnetic field remarkably shows that it is two orders of magnitude lower than in cable FM-SP-II-B, possibly due to incomplete impregnation.

Magnetization loss in both cable types was also measured as a function of applied magnetic field angle, using an orthogonal set of pick-up coils to record the in-plane and normal components of the magnetization. Somewhat surprisingly, the loss at intermediate magnetic field angles can be predicted quite well by considering the perpendicular and parallel components of the applied magnetic field separately and taking the sum of the corresponding losses.

The inter-strand resistance and magnetization loss experimental results are important as input for advanced electrical cable network simulation models by Van Nugteren *et al.*, for calculating for example the dynamic magnetic field quality, thermal stability and normal zone propagation of *Re*BCO Roebel cables.

Chapter 7
Conclusion

In the previous Chapters several topics important for understanding the transverse pressure effect on superconducting Nb_3Sn Rutherford and ReBCO Roebel cables for accelerator magnets, were presented. In this chapter the main findings and conclusions are summarized. The Chapter ends with recommendations for future research.

7.1 Transverse pressure effect on the critical current of Nb_3Sn Rutherford cables

DS-typed key-stoned Nb_3Sn Rutherford-type cables, comprising 40 PIT-114 strands with a wire diameter of 0.7 mm and impregnated with the CIBA GEIGY Araldite epoxy resin, show a non-copper **critical current density** at 4.2 K of 2480 ± 75 A/mm^2 at 11.1 ± 0.3 T for the cable sample with a stainless-steel core and 2860 ± 85 A/mm^2 at 11.2 ± 0.3 T for the cable sample without core. No critical current reduction was observed in the cable sample without core when compared to a virgin witness wire. However, the cable sample with core showed a 20% critical current reduction, which might be due to the uneven positioning of the stainless-steel core causing unwanted stress concentrations in the cabling process. SMC-type rectangular Nb_3Sn Rutherford-type cables, comprising 18 RRP-132/169 and PIT-192 strands with a wire diameter of 1 mm and impregnated with CTD-101K epoxy resin, have a non-copper critical current density at 4.2 K of 3160 ± 190 A/mm^2 and 2480 ± 150 A/mm^2 at 12 T for RRP- and PIT-type cable samples, respectively. No significant differences in critical current density were observed between both cables and their virgin witness wires. These observations indicated that the impact of the cabling process for Nb_3Sn Rutherford cables can be minimized when using an appropriate cabling method. In addition, the measurement results of RRR values on virgin witness wires and extracted strands of the rectangular cable samples are larger than 100, which satisfies the minimum RRR requirement for a 16 T accelerator magnet design presently under development and confirms the adequate deformation control during cabling.

For the **transverse pressure susceptibility** of the cable samples, the characterization of both reversible and irreversible critical current reduction is crucial. The measurement results show a 90% critical current retention compared to the initial 'un-loaded' values at 100 ± 10 MPa for the key-stoned DS-PIT cable sample with a stainless-steel core; 70 ± 30 MPa for the key-stoned DS-PIT cable sample without core; 130 ± 3 MPa for the rectangular SMC-RRP cable sample and 90 ± 3 MPa for the rectangular SMC-PIT cable sample. This *reversible* critical current reduction caused by Nb_3Sn lattice deformation must be taken into account when designing magnets. In addition, the measurement results illustrate that the DS-PIT cable sample with a stainless-steel core is less susceptible to transverse stress than the DS-PIT cable sample without core for key-stoned Rutherford cables. For the rectangular cable samples, the SMC-RRP cable sample is more robust than the similar cable sample comprising SMC-PIT wires. The onset of *irreversible* critical current reduction due to filament cracking is determined by using 2% reduction of the critical current measured at 'zero'-stress after unloading as criterion. The measurement results of the irreversible critical current reduction of these cables lead to similar conclusions as the results of the reversible critical current reduction. The maximum transverse pressure that a cable can sustain without permanent critical current reduction is 90 ± 10 and 70 ± 30 MPa for key-stoned DS-PIT cable samples with and without core, respectively. The transverse pressure limit for rectangular SMC-RRP and -PIT cable samples are larger than 190 and 150 MPa, respectively.

The minimum transverse stress requirements for designing 11 and 16 T accelerator dipole magnets are 150 and 200 MPa, respectively. Therefore, it is possible to construct dipole magnets using the PIT-114 and RRP-132/169 wires provided sufficient margin is taken into account. However, there is not sufficient statistical data available yet to draw a solid conclusion and more similar experiments need to be performed in order to confirm these results.

The results mentioned above were measured after applying an extra so-called 'alignment' im-

pregnation. Earlier experiments where this extra precaution was not included yielded more scattered data and significantly poorer critical current performance versus the transverse pressure. This illustrates the importance of avoiding stress concentrations in the experiments described in this thesis, but certainly also in magnet windings constructed with these cables.

The **upper critical field** of cable samples is estimated by fitting the critical current data with respect to the peak magnetic field using the Kramer extrapolation function, as described in Section 4.2.1. When comparing the upper critical field values of the rectangular Rutherford SMC cables between 'zero'-stress and 150 MPa, no significant reduction is observed at 150 MPa in the RRP cable sample, but a 6% reduction occurred in the PIT cable sample at the same stress level. In addition, load-cycling of cable samples causes no significant evolution of the critical current reduction. It is concluded that no significant filament cracking occurred in the strands of these rectangular Rutherford cables when transverse pressures reach to 190 and 150 MPa for RRP and PIT cable samples, respectively.

The vacuum impregnation using **epoxy resins** of either CIBY GEIGY Araldite or CTD-101K is successful as no visible voids in the cable were observed. Both impregnation methods reinforce the transverse pressure limit of Rutherford cables. The use of glass-fiber in magnet coil windings not only ensures adequate electrical turn-to-turn insulation, but also reduce the difference in thermal contraction between the pure epoxy resins and the cable itself. Model estimates show that the mechanical effect of an insulating glass-fiber sleeve around the cable is relative small.

7.2 Transverse pressure effect on the critical current of *Re*BCO Roebel cables

For a *Re*BCO Roebel strand, mechanically punched from the investigated SuperPower tapes of 12 mm wide produced in 2016-2017, the **critical current density** is 55 ± 3 and 42 ± 3 kA/mm^2 for its 'straight' and 'crossover' sections, respectively, at 4.2 K and 10.8 ± 0.3 T. The 'crossover' part of the strand has a 20% lower critical current compared to the 'straight' part, which indicates that the overall strand critical current is affected and limited by the critical current locally at the 'crossover' sections. The possible explanation for the critical current deviation is that the critical current in a coated conductor is anisotropic and in-plane direction dependent with the current along the tape higher than across the tape. In the 'crossover' section the situation is somewhere in between.

In the case of the bare (non-impregnated) cable sample, assembled with the same SuperPower *Re*BCO Roebel strands, the **critical current density** at 'zero'-stress is 47 ± 3 kA/mm^2 at 10.7 ± 0.3 T. Compared to the 'crossover' strand sample, no critical current density reduction was observed. A similar conclusion can be drawn regarding most cable samples impregnated with CY5538 Araldite filled with fused silica powder: no significant critical current density reduction occurred in one cable sample comprising 10 SuperPower tape based zig-zag strands. However, a second similar Roebel cable sample impregnated with the same epoxy resin showed a 10% critical current density reduction, which is not understood and might be due to the non-homogeneity in the tape of the critical current along the length. For the 15-strand SuperPower tape based cable samples, one was impregnated with CY5538 Araldite filled with fused silica powder, while the other one was enveloped with a glass-fiber sleeve and impregnated with CTD-101K. Compared to the 'crossover' strand sample, the first one did not show any sig-

nificant critical current reduction, but the second one showed a 10% current reduction. This might be explained by the fact that the second cable sample was not entirely assembled from the same batch of SuperPower tape based strands. These observations indicate that the impregnation with CY5538 Araldite very likely does not cause a critical current reduction in SuperPower tape based cable samples, but no solid conclusion can yet be drawn on impregnation with CTD-101K due to the rather limited number of samples. In addition, compared to the impregnated SuperPower tape based cable samples, the Bruker tape based cable sample, impregnated with CTD-101K, has a 30% larger critical current density at 4.2 K and 11 ± 0.3 T.

Regarding the **transverse pressure susceptibility** of Roebel cable samples, the results show a 90% critical current retention compared to the initial 'un-loaded' values at 80 ± 15 MPa for the bare SuperPower tape based cable sample. In the case of impregnated Roebel cable samples, unlike the bare cable, no significant reduction in critical current appears until the transverse pressure is larger than 170 MPa. The impregnated Roebel cables are less susceptible to transverse pressure than impregnated Nb_3Sn Rutherford cables. The *irreversible* reduction ΔI_c is determined by using the same 2% criterion as for the Nb_3Sn cables in view of the 1.5% random error in critical current measurement. The transverse stress limit was observed at <100 ± 15 MPa for the bare SuperPower tape based cable sample, 170 ± 10 to 275 ± 10 MPa for similar cable samples but impregnated with CY5538 Araldite, and ≥400 ± 5 MPa for 15-strand SuperPower tape base cable samples impregnated with either CY5538 Araldite or CTD-101K. Most importantly, it is the first time the transverse pressure effect was measured on 15-strand Roebel cables made from Bruker coated conductor and no reversible critical current reduction was found up to the record value of 425 ± 3 MPa, while the irreversible transverse limit was observed up to a record value of 455 MPa.

It is concluded that 10- and 15-strand *Re*BCO cables with correct vacuum impregnation are able to withstand transverse pressure far beyond 150 and 300 MPa, respectively, without noticeable degradation in critical current. From a mechanical viewpoint, it is therefore a realistic perspective to build 20+ T class accelerator dipole magnets using state-of-the-art *Re*BCO Roebel cables provided a correct epoxy resin impregnation is applied.

A single **thermal cycle** had no further effect on the critical current of the SuperPower tape based cables, but a 20% critical current reduction was surprisingly observed between first and second cool-down in the Bruker tape based cable. No solid conclusion can be drawn about the cause due to the insufficient statistics.

Vacuum impregnation using **epoxy resins** of CY5538 Araldite filled with fused silica powder and CTD-101K with glass-fiber sleeve are both successful as no visible voids were observed in the cable samples. Epoxy resin CTD-101K with glass-fiber sleeve is suitable to impregnate large-size magnets regarding the coils' insulation requirement and its long pot life of 60 h at 40°C in comparison to the silica filled Araldite featuring 3 h at 80°C only. Layer delamination was observed in a 10-strand SuperPower tape based cable sample impregnated with CY5538 Araldite filled with fused silica powder. Whether this is due to the combination of the tape punching and the subsequent impregnation, which leaves edges of the strands directly exposed to impregnation materials, or to the build-up of thermal stress between resin and strands during cool-down is yet unclear. No significant delamination was observed in cable samples impregnated using CTD-101K and glass-fiber. Therefore, it was convincingly demonstrated that the epoxy resin CTD-101K with glass-fiber sleeve seems suitable for application in coil windings comprising *Re*BCO Roebel cables.

7.3 Inter-strand resistance and AC loss of *Re*BCO Roebel cables

The **inter-strand resistance** measured within one transposition length of three Roebel cables, assembled from 15 standard SuperPower ReBCO tape based strands and impregnated with CTD-101K mixed with glass-fiber, ranges from 3 to 18 $\mu\Omega$ at 77 K and from 1 to 10 $\mu\Omega$ at 4.2 K. The corresponding contact surface resistivities are estimated from an electrical network model, presented in Chapter 3. The values are in the range of 1 to 20 nΩm^2 and of 0.5 to 10 nΩm^2 at 77 and 4.2 K, respectively. The resistivity values at 77 K are comparable to the measurement results from Otten *et al.* [100], who reported resistivity values of 7 to 20 $\mu\Omega$ for SuperPower *Re*BCO tapes and 5 to 25 $\mu\Omega$ for a 10-strand Roebel cable. These coherent conclusions show that surface resistivities can be measured reliably and reproducibly. In addition, analysis of the several contributions to the intra-strand contributions determining the overall inter-strand contact resistance clearly indicate the dominant contribution of the copper-to-copper surface resistance.

The **AC loss** at 4.2 K in impregnated *Re*BCO Roebel cable samples in various orientations of the applied AC magnetic field, is dominated by hysteresis loss. In the impregnation cables, coupling loss can mostly be ignored, only one cable sample, impregnated with CTD-101G and filled with alumina powder, shows a clear sign of inter-strand coupling loss when the magnetic field is parallel to the broad face of the cable sample. Three analytical models taken from literature are used to estimate the hysteresis loss in various magnetic field orientations. The estimates are comparable to the measurement data in a parallel magnetic field, but at least 10 times higher than the measurement data in a perpendicular magnetic field.

Magnetization loss in both cable types was also measured as a function of applied magnetic field angle, using an orthogonal set of pick-up coils to record the in-plane and normal components of the magnetization. Somewhat surprisingly, the loss at intermediate magnetic field angles can be predicted quite well by considering the perpendicular and parallel components of the applied magnetic field separately and taking the sum of the corresponding losses.

7.4 Recommendations

7.4.1 Experiments

The critical current performance at 4.2 K of superconducting cables when exposed to transverse pressure are measured using a superconducting transformer and electromagnetic press system at the University of Twente. The applied force was determined with two independent methods, one is to measure the current that powers the press coils with a zero-flux meter and the displacement of the upper press coil with an extensometer; the second is to monitor the deformation of the pressure anvil with two strain gauges glued to the its short sides. The extensometer can measure with an accuracy of 1 μm within a range of a few millimeters and a sensitivity of 1.046 mV/mm [132]. However, during the cable sample measurement, the extensometer value is fluctuating in a certain range. The first recommendation is to check how significantly the variations of extensometer data affect the calculated force. A method of adding two additional extensometers to the upper press coil is suggested. Three extensometers can be placed at the point of an equilateral triangle and the average value of the extensometer readings used to calculate the applied force. In this case, the error of the force calculation can be further minimized. The misalignment between the upper press coil and piston can be

reduced as well.

As described in Section 2.5.2.3, the contact surface of the side plate is covered with Kapton tapes to decrease the friction between the pressure anvil and two side plates, especially in the case of using the 'alignment' impregnation. The question of how significantly the Stycast applied during the alignment impregnation affects the force applied on the cable sample needs to be answered. Additional stress-strain measurements on samples with a steel-Kapton-Stycast-steel layout are suggested. Another method to reduce the possible friction between the pressure anvil and two side plates is to shorten the current side plates, resulting in less contact surface with the anvil. In this case, more strain gauges can be glued on the long side of the anvil. Then, the stress distribution both along the sample length and -width can be monitored.

In the impregnated *Re*BCO Roebel cable samples used for inter-strand resistance measurement in this thesis, the strands are not aligned with each other and the distances between neighboring strands are not the same. This may cause the observed variation in inter-strand resistances within one cable. To minimize this variation, special care needs to be taken to prepare the cable before impregnation.

The present calorimetric method for measuring the low-level AC loss is not sensitive enough and is easily influenced by the enclosed helium cycle system. It is suggested to use a flow meter with a better resolution or measure the AC loss of stacks of cable samples instead of a single cable sample. Also, the calorimetric data is much more reliable when the pressure of the enclosed helium cycle system is stable, a pressure regulator can be connected to the helium cycle system.

7.4.2 Modelling

The simplified 2D FE mechanical model $I_c(\sigma)$ results, as shown in Section 3.2.4, yields only a semi-quantitative agreement with the measured data. In order to fit better with the measurements data, a more detailed strand model including the filament layout is probably required.

An electrical network model can be developed to estimate the effective length of strands in a Nb_3Sn Rutherford cable determining the overall critical current of the cable, taking into account the deviatoric stain and local magnetic field distributions of the cable.

In the case of AC loss models of *Re*BCO Roebel cables, as described in Section 3.4, the analytical model estimates deviate significantly from the experimental data. Further implementation of the numerical model reported by Van Nugteren *et al.* [141] on different cable layouts, tape types and inter-strand resistance values for *Re*BCO Roebel cables is suggested.

7.4.3 Nb_3Sn Rutherford cables

For key-stoned DS-type Nb_3Sn Rutherford cables, multiple voltage taps can be soldered on both the thin- and thick sides of a cable sample. By switching the orientations of the peak magnetic field position from one side to the other, the critical current performance of both sides when exposed to transverse pressure can be measured. Thereby, the transverse stress susceptibility of both sides in the cable sample can be determined.

To determine the current redistribution in a cable sample, a selected strand can be used for the critical current measurement as a function of transverse pressure applied to the cable surface. The current is injected to the selected strand in the cable sample, and voltage of the strand and

its neighboring strands is detected.

To validate the measurement results in this thesis, more measurements need to be performed on similar cable samples. To determine the irreversible critical current more precisely, small steps of increasing the transverse pressure are needed and a high transverse pressure level needs to be reached. In addition, more critical current measurement as a function of magnetic field when exposed to the transverse pressure can be considered, in order to determine more precisely the relation between upper critical field and transverse pressure.

As to magnet construction, proper methods to monitor and avoid unwanted stress concentrations in magnet assembly are of key importance. One conclusion from this thesis is that the reacted Nb_3Sn Rutherford cables are extremely susceptible to interface misalignment, which causes stress concentrations. This is the essential for the success of high-field Nb_3Sn magnet construction.

To reduce the transverse stress susceptibility of Nb_3Sn wires and cables, one option is using an epoxy resin with a large Young's modulus and Poisson's ratio to impregnate the sample; the second option is to improve the structure of the strands themselves and make it much more robust; the third option is using a different cable architecture, i.e. using rectangular cable with lower cabling compaction instead of a key-stoned cable.

7.4.4 *Re*BCO Roebel cables

Compared to Nb_3Sn based Rutherford cables, the main issue with *Re*BCO coated conductor presently is the relatively high cost. To manufacture a Roebel cable, the traditional methods causes more than 50% material loss. A perspective method to reduce the cost of Roebel strand in the future is producing the zig-zag strand already during the *Re*BCO synthesis process using for example a chemical solution deposition method.

Investigation of current redistribution on *Re*BCO Roeble cables just like Nb_3Sn Rutherford cables is suggested. In general, but in particular, for Bruker tape based Roebel cable, more investigation of the thermal cycling effect on the critical current is also highly recommended.

The investigation of the transverse stress effect on the inter-strand resistance and AC loss of impregnated *Re*BCO Roebel cables with various cable layouts and tape types is suggested as well.

Bibliography

[1] R. R. Wilson. The Tevatron. *Physics Today*, 30(10), 1977.

[2] H. Edwards. The energy saver test and commissioning history. *Proc. 12th Int. Conf. on High-Energy accelerators, Batavia III.*, 1983.

[3] M. Wilson. Superconductivity and accelerators: the good companions. *IEEE Trans. Appl. Supercond.*, 9(2), 1999.

[4] L. Rossi. Superconductivity: its role, its success and its setbacks in the Large Hadron Collider of CERN. *Supercond. Sci. Technol.*, 23(2), 2010.

[5] H. H. J. ten Kate. The ATLAS superconducting magnet system at the Large Hadron Collider. *Physica C*, 468(15-20), 2008.

[6] https://www.noell.bilfinger.com/referenzen/magnettechnik/grundlagenforschung/gallery671, consulted 30th June 2019.

[7] http://irfu.cea.fr/Images/astImg/2411_2.jpg, consulted 30th June 2019.

[8] L. R. Evans. The present status of LHC. *IEEE Trans. Magn.*, 32(4), 1996.

[9] V. Parma, P. Rohmig, M. Peyrot, J. M. Rifflet, P. Védrine, and D. Vincent. The short straight sections for the LHC. *Proc. 1997 IEEE Particle Accelerator Conference*, 1998.

[10] H. Wiedemann. *Particle accelerator physics*. Springer, 2007. ISBN: 978-3-319-18317-6.

[11] P. F. Smit and J. D. Lewin. Superconducting proton synchrotrons. *Nuclear Instruments and Methods*, 52(2), 1967.

[12] K. Johnsen. The CERN intersecting storage rings. *Nuclear Instruments and Methods*, 108(2), 1973.

[13] M. Crowley-Milling. The CERN 400 GeV proton accelerator. *Electronics and Power*, 24(5), 1978.

[14] P. A. Thompson, J. Cottingham, P. Dahl, R. Fernow, M. Garber, A. Ghosh, C. Goodzeit, A. Greene, H. Hahn, J. Herrera, S. Kahn, E. Kelly, G. Morgan, S. Plate, A. Prodell, W. Sampson, W. Schneider, R. Shutt, P. Wanderer, and E. Willen. Superconducting magnet system for RHIC. *IEEE Trans. Nucl. Sci.*, 32(5), 1985.

[15] H. H. J. ten Kate, S.L.Wipf, B. ten Haken, and L. J. M. van de Klundert. Development of a superconducting protection switch for the HERA P-ring. *IEEE Trans. Magn.*, 24(2), 1988.

[16] J. R. Sanford. Civil system aspects of the SSC. *IEEE Trans. Nucl. Sci.*, 32(5), 1985.

[17] D. Schoerling, D. Arbelaez, B. Auchmann, M. Bajko, A. Ballarino, E. Barzi, G. Bellomo, M. Benedikt, S. I. Bermudez, B. Bordini, L. Bottura, L. Brouwer, P. Bruzzone, B. Caiffi, S. Caspi, A. Chakraborti, E. Coatanea, G. de Rijk, M. Dhallé, M. Durante, P. Fabbricatore, S. Farinon, H. Felice, A. Fernandez, I.S. Fernandez, P. Gao, B. Gold, T. Gortsas, S. Gourlay, M. Juchno, V. Kashikhin, C. Kokkinos, S. Kokkinos, K. Koskinen, F. Lackner, C. Lorin, K. Loukas, A. Louzguiti, K. Lyytikainen, S. Mariotto, M. Marchevsky, G. Montenero, J. Munilla, I. Novitski, T. Ogitsu, A. Pampaloni, J. C. Perez, C. Pes, C. Petrone, D. Polyzos, S. Prestemon, M. Prioli, A. M. Ricci, J. M. Rifflet, E. Rochepault, S. Russenschuck, T. Salmi, I. A. Santillana, F. Savary, C. Scheuerlein, M. Segreti, C. Senatore, M. Sorbi, M. Statera, A. Stenvall, L. Tavian, T. Tervoort, D. Tommasini, F. Toral, R. Valente, G. Velev, A. P. Verweij, S. Wessel, F. Wolf, F. Zimmermann, and A. V. Zlobin. The 16 T dipole development program for FCC and HE-LHC. *IEEE Trans. Appl. Supercond.*, 29(5), 2019.

[18] Q. Xu, K. Zhang, C. Wang, Y. Hu, Z. Hou, F. Ning, M. Wang, W. Yao, G. Zhang, L. Zhao, W. Zhao, Z. Zhu, F. Chen, W. Kang, Q. Li, and Q. Peng. 20-T dipole magnet with common-coil configuration: main characteristics and challenges. *IEEE Trans. Appl. Supercond.*, 26(4), 2016.

[19] L. Rossi, A. Badel, M. Bajko, A. Ballarino, L. Bottura, M. Dhallé, M. Durante, Ph. Fazilleau, J. Fleiter, W. Goldacker, E. Härö, A. Kario, G. Kirby, C. Lorin, J. van Nugteren, G. de Rijk, T. Salmi, C. Senatore, A. Stenvall, P. Tixador, A. Usoskin, G. Volpini, Y. Yang, and N. Zangenberg. The EuCARD-2 future magnets European collaboration for accelerator-quality HTS magnets. *IEEE Trans. Appl. Supercond.*, 25(3), 2015.

[20] The ATLAS collaboration. A particle consistent with the Higgs Boson observed with the ATLAS detector at the Large Hadron Collider. *Science*, 338(6114), 2012.

[21] The CMS collaboration. A new Boson with a mass of 125 GeV observed with the CMS experiment at the Large Hadron Collider. *Science*, 338(6114), 2012.

[22] M. Banks and R. Blaustein. CERN beyond the LHC (interview with F. Gianotti). *Physics World*, 32(4), 2019.

[23] L. Bottura. A practical fit for the critical surface of NbTi. *IEEE Trans. Appl. Supercond.*, 10(1), 2000.

[24] P. Lee and co-workers. https://nationalmaglab.org/images/magnet_development/asc /plots, consulted 2th July 2019.

[25] T. Boutboul, S. Le Naour, D. Leroy, L. Oberli, and V. Previtali. Critical current density in superconducting NbTi strands in the 100 mT to 11 T applied field range. *IEEE Trans. Appl. Supercond.*, 16(2), 2006.

[26] A. Godeke. *Performance boundaries in Nb_3Sn superconductors*. PhD dissertation, University of Twente, The Netherlands, 2005.

[27] M. Tinkham. *Introduction to Superconductivity*. McGraw-Hill, 1996. ISBN: 0-07-64878-6.

[28] V. Abacherli, B. Seeber, E. Walker, R. Flükiger, W. Thiele, and J. A. A. J. Perenboom. Development of $(Nb,Ta)_3Sn$ multifilamentary superconductors using osprey bronze with high Tin content. *IEEE Trans. Appl. Supercond.*, 11(1), 2001.

[29] K. Yoshizaki, O. Taguchi, F. Fujiwara, M. Imaizumi, M. Wakata, Y. Hashimoto, K. Wakamoto, T. Yamada, and T. Satow. Nb_3Sn superconducting cables processed by internal tin diffusion. *IEEE Trans. Magn.*, 19(3), 1983.

[30] J. D. Elen, C. A. M. van Beijnen, and C. A. M. van der Klein. Multifilament V_3Ga and Nb_3Sn superconductors produced by the ECN-technique. *IEEE Trans. Magn.*, 13(1), 1977.

[31] E. Barzi, R. Bossert, S. Caspi, D. R. Dietderich, P. Ferracin, A. Ghosh, and D. Turrioni. RRP Nb_3Sn strand studies for LARP. *IEEE Trans. Appl. Supercond.*, 17(2), 2007.

[32] J. L. H. Lindenhovius, E. M. Hornsveld, A. den Ouden, W. A. J. Wessel, and H. H. J. ten Kate. Powder-In-Tube Nb_3Sn conductors for high-field magnets. *IEEE Trans. Appl. Supercond.*, 10(1), 2000.

[33] A. den Ouden, S. Wessel, E. Krooshoop, and H. ten Kate. Application of Nb_3Sn superconductors in high-field accelerator magnets. *IEEE Trans. Appl. Supercond.*, 7(2), 1997.

[34] P. J. Lee, C. M. Fischer, M. T. Naus, A. A. Squitieri, and D. C. Larbalestier. The microstructure and microchemistry of high critical current Nb_3Sn strands manufactured by the bronze, internal-Sn and PIT techniques. *IEEE Trans. Appl. Supercond.*, 13(2), 2003.

[35] X. Xu, J. Rochester, X. Peng, M. Sumption, and M. Tomsic. Ternary Nb_3Sn superconductors with artificial pinning centers and high upper critical fields. *Supercond. Sci. Technol.*, 32(2), 2019.

[36] T. Nakashima, S. Kobayashi, T. Kagiyama, K. Yamazaki, M. Kikuchi, S. Yamade, K. Hayashi, K. Sato, G. Osabe, and J. Fujikami. Overview of the recent performance of DI-BSCCO wire. *Cryogenics*, 15(12), 2012.

[37] H. Kumakura. Development of Bi-2212 conductors and magnets for high-magnetic-field generation. *Supercond. Sci. Technol.*, 13(1), 2000.

[38] M. O. Rikel, D. Wesolowskii, A.A. Polyanskii, X. Y. Cai, K. Marken, H. Miao, and E. E. Hellstrom. Effect of solidification conditions on microstructure of melt processed Bi2212 Ag conductors. *Physica C*, 372-376, 2002.

[39] A. Kajbafvala, W. Nachtrab, X.F. Lu, F. Hunte, X. Liu, N. Cheggour, T. Wong, and J. Schwartz. Dispersion-strengthened silver alumina for sheathing $Bi_2Sr_2CaCu_2O_{8+x}$ multifilamentary wire. *IEEE Trans. Appl. Supercond.*, 22(2), 2012.

[40] A. Matsumoto, H. Kitaguchi, H. Kumakura, J. Nishioka, and T. Hasegawa. Improvement of the microstructure and critical current densities of Bi-2212 round wires with a precisely controlled heat treatment. *Supercond. Sci. Technol.*, 17(8), 2004.

[41] D. C. Larbalestier, J. Jiang, U. P. Trociewitz, F. Kametani, C. Scheuerlein, M. Dalban-Canassy, M. Matras, P. Chen, N. C. Craig, P. J. Lee, and E. E. Hellstrom. Isotropic round-wire multifilament cuprate superconductor for generation of magnetic fields above 30 T. *Nature materials*, 13, 2014.

[42] H. W. Weijers, U. P. Trociewitz, W. D. Markiewicz, J. Jian, D. Myers, E. E. Hellstrom, A. Xu, J. Jaroszynski, P. Noyes, Y. Viouchkov, and D. C. Larbalestier. High field magnets with HTS conductors. *IEEE Trans. Appl. Supercond.*, 20(3), 2010.

[43] A. Godeke, D. Cheng, D. R. Dietderich, C. D. English, H. Felice, C. R. Hannaford, S. O. Prestemon, G. Sabbi, R. M. Scanlan, Y. Hikichi, J. Nishioka, and T. Hasegawa. Development of Wind-and-React Bi-2212 accelerator magnet technology. *IEEE Trans. Appl. Supercond.*, 18(6), 2008.

[44] S. C. Kim, D. W. Ha, S. S. Oh, K. J. Song, S. J. Kim, I. Y. Han, and H. S. Sohn. Fabrication and properties of Bi2212 Rutherford superconducting cable. *IEEE Trans. Appl. Supercond.*, 19(6), 2009.

[45] A. Godeke, L. N. Brouwer, S. Caspi, D. R. Dietderich, S. A. Gourlay, R. R. Hafalia, N. I. Heys, H. C. Higley, T. M. Lipton, M. A. Reynolds, and J. H. Swanson. Bi-2212 Canted-Cosine-Theta Coils for high-field accelerator magnets. *IEEE Trans. Appl. Supercond.*, 25(3), 2015.

[46] Y. Shiohara, M. Yoshizumi, Y. Takagi, and T. Izumi. Future prospects of high Tc superconductors-coated conductors and their applications. *Physica C*, 484, 2013.

[47] X. Obradors and T. Puig. Coated conductors for power applications: materials challenges. *Supercond. Sci. Technol.*, 17(4), 2004.

[48] C. Senatore, M. Bonura, D. Zurmuehle, J. Ferradas, L. Rossi, U. Betz, and A. Usoskin. Recent progress on HTS conductors for high-field magnets: critical surface studies. *Presented at the FCC week 2019, Brussels*, 24-28 June 2019.

[49] W. Goldacker, R. Nast, S.I. Schlachter G. Kotzyba, A. Frank, B. Ringsdorf, C. Schmidt, and P. Komarek. High current DyBCO-ROEBEL assembled coated conductor (RACC). *J. Phys.: Conf. Ser.*, 43, 2006.

[50] W. Goldacker, F. Grilli, E. Pardo, A. Kario, S. I Schlachter, and M. Vojenčiak. Roebel cables from *Re*BCO coated conductors: a one-century-old concept for the superconductivity of the future. *Supercond. Sci. Technol.*, 27(9), 2014.

[51] R. A. Badcock, N. J. Long, M. Mulholland, S. Hellmann, A. Wright, and K.A. Hamilton. Progress in the manufacture of long length YBCO Roebel cables. *IEEE Trans. Appl. Supercond.*, 19(3), 2009.

[52] S. Terzieva, M. Vojenčiak, F. Grilli, R. Nast, J. Šouc, W. Goldacker, A. Jung, A. Kudymow, and A. Kling. Investigation of the effect of striated strands on the AC losses of 2G Roebel cables. *Supercond. Sci. Technol.*, 24(4), 2011.

[53] N. Glasson, M. Staines, N. Allpress, M. Pannu, J. Tanchon, E. Pardo, R. Badcock, and R. Buckley. Test results and conclusions from a 1 MVA superconducting transformer featuring 2G HTS Roebel cable. *IEEE Trans. Appl. Supercond.*, 27(4), 2017.

[54] S. S. Fetisov, V. V. Zubko, S. Yu. Zanegin, A. A. Nosov, V. S. Vysotsky, A. Kario, A. Kling, W. Goldacker, A. Molodyk, A. Mankevich, V. Kalitka, A. Adamenkov, S. Samoilenkov, and D. Melyukov. Development and characterization of a 2G HTS Roebel cable for aircraft power systems. *IEEE Trans. Appl. Supercond.*, 26(3), 2016.

[55] J. van Nugteren, G. Kirby, H. Bajas, M. Bajko, A. Ballarino, L. Bottura, A. Chiuchiolo, P-A Contat, M. Dhallé, M. Durante, P. Fazilleau, A. Fontalva, P. Gao, W. Goldacker, H. ten Kate, A. Kario, V. Lahtinen, C. Lorin, A. Markelov, J. Mazet, J Murtomäki A. Molodyk, N. Long, J. Perez, C. Petrone, F. Pincot, G. de Rijk, L. Rossi, S. Russenschuck, J. Ruuskanen, K. Schmitz, A. Stenvall, A. Usoskin, G. Willering, and Y. Yang. Powering of an HTS dipole insert-magnet operated standalone in helium gas between 5 and 85 K. *Supercond. Sci. Technol.*, 31(6), 2018.

[56] A. Kario, M. Vojenciak, F. Grilli, A. Kling, B. Ringsdorf, U. Walschburger, S. I. Schlachter, and W. Goldacker. Investigation of a Rutherford cable using coated conductor Roebel cables as strands. *Supercond. Sci. Technol.*, 29(8), 2013.

[57] L. Rossi and E. Todesco. Electromagnetic design of superconducting dipoles based on sector coils. *Phys. Rev. Special Topics 10*, 2007.

[58] L. I. Greben, E. S. Mironov, and H. H. Moustafin. Mechanical stresses and strains in superconducting dipole magnets for high energy accelerators. *IEEE Trans. Magn.*, 15(1), 1979.

[59] S. C. Snowdon. Stress analysis for warm iron superconducting dipoles. *IEEE Trans. Nucl. Sci.*, 26(3), 1979.

[60] D. ter Avest. *Properties of the Superconductor in Accelerator Dipole Magnets*. PhD dissertation, University of Twente, The Netherlands, 1991.

[61] S. Caspi and P. Ferracin. Toward integrated design and modeling of high field accelerator magnets. *IEEE Trans. Appl. Supercond.*, 16(2), 2006.

[62] P. Ferracin, W. Scandale, E. Todesco, and D. Tommasini. Azimuthal coil size and field quality in the main CERN Large Hadron Collider dipoles. *Phys. Rev. Special Topics 5*, 2002.

[63] M. Karppinen, N. Andreev, G. Apollinari, B. Auchmann, E. Barzi, R. Bossert, V. V. Kashikhin, A. Nobrega, I. Novitski, L. Rossi, D. Smekens, and A. V. Zlobin. Design of 11 T twin-aperture Nb_3Sn dipole demonstrator magnet for LHC upgrades. *IEEE Trans. Appl. Supercond.*, 22(3), 2012.

[64] V. Marinozzi, G. Bellomo, B. Caiffi, P. Fabbricatore, S. Farinon, A. M. Ricci, M. Sorbi, and M. Statera. Conceptual design of a 16 T $\cos\theta$ bending dipole for the Future Circular Collider. *IEEE Trans. Appl. Supercond.*, 28(3), 2018.

[65] V. V. Kashikhin, N. Andreev, E. Barzi, I. Novitski, and A. V. Zlobin. Magnetic and structural design of a 15 T Nb_3Sn accelerator dipole model. *Materials Science and Engineering*, 101(conference 1), 2015.

[66] C. Lorin, M. Segreti, and M. Durante. Design of a Nb_3Sn 16 T block dipole for the Future Circular Collider. *IEEE Trans. Appl. Supercond.*, 28(3), 2018.

[67] F. Toral, J. Munilla, and T. Salmi. Magnetic and mechanical design of a 16 T common coil dipole for an FCC. *IEEE Trans. Appl. Supercond.*, 28(3), 2018.

[68] B. Auchmann, L. Brouwer, S. Caspi, J. Gao, G. Montenero, M. Negrazus, G. Rolando, and S. Sanfilippo. Electromechanical design of a 16-T CCT twin-aperture dipole for the FCC. *IEEE Trans. Appl. Supercond.*, 28(3), 2018.

[69] I. Novitski, N. Andreev, B. Auchmann, E. Barzi, R. Bossert, M. Karppinen, A. Nobrega, D. Smekens, and A. V. Zlobin. Study of mechanical models of a single-aperture 11 T Nb_3Sn dipole. *IEEE Trans. Appl. Supercond.*, 23(3), 2013.

[70] J. S. Murtomäki, J. van Nugteren, G. Kirby, L. Rossi, J. Ruuskanen, and A. Stenvall. Mechanical effects of the nonuniform current distribution on HTS coils for accelerators wound with *Re*BCO Roebel cable. *IEEE Trans. Appl. Supercond.*, 27(4), 2017.

[71] J. E. Campbell, E. A. Eldridge, and J. K. Thompson. *Handbook on Materials for Superconducting Machinery*. Battelle Columbus Labs., Ohio, 1974. MCIC-HB-04.

[72] B. Bordini, P. Alknes, L. Bottura, L. Rossi, and D. Valentinis. An exponential scaling law for the strain dependence of the Nb_3Sn critical current density. *Supercond. Sci. Technol.*, 26(7), 2013.

[73] A. Nijhuis, R. P. Pompe van Meerdervoort, H. J. G. Krooshoop, W. A. J. Wessel, C. Zhou, G. Rolando, C. Sanabria, P. J. Lee, D. C. Larbalestier, A. Devred, A. Vostner, N. Mitchell, Y. Takahashi, Y. Nabara, T. Boutboul, V. Tronza, S. H. Park, and W. Yu. The effect of axial and transverse loading on the transport properties of ITER Nb_3Sn strands. *Supercond. Sci. Technol.*, 26(8), 2013.

[74] M. C. Jewell, P. J. Lee, and D. C. Larbalestier. The influence of Nb_3Sn strand geometry on filament breakage under bend strain as revealed by metallography. *Supercond. Sci. Technol.*, 16(9), 2003.

[75] N. Mitchell. Finite element simulations of elasto-plastic processes in Nb_3Sn strands. *Cryogenics*, 45(7), 2005.

[76] H. Oguro, S. Awaji, G. Nishijima, K. Takahashi, K. Watanabe, S. Machiya, H. Suzuki, Y. Tsuchiya, and K. Osamura. Residual strain measurement using neutron diffraction for practical Nb_3Sn wires under a tensile load. *Supercond. Sci. Technol.*, 23(2), 2005.

[77] N. Cheggour, J. W. Ekin, C. L. H. Thieme, and Y. Y. Xie. Effect of fatigue under transverse compressive stress on slit Y-Ba-Cu-O coated conductors. *IEEE Trans. Appl. Supercond.*, 17(2), 2007.

[78] N. Cheggour, J.W. Ekin, C. C. Clickner, D. T. Verebelyi, C. L. H. Thieme, R. Feenstra, A. Goyal, and M. Paranthaman. Transverse compressive stress effect in Y-Ba-Cu-O coatings on biaxially textured Ni and Ni-W substrates. *IEEE Trans. Appl. Supercond.*, 13(2), 2003.

[79] D. C. van der Laan, D. Abraimov, A. A. Polyanskii, D. C. Larbalestier, J. F. Douglas, R. Semerad, and M. Bauer. Anisotropic in-plane reversible strain effect in $Y_{0.5}Gd_{0.5}Ba_2Cu_3O_{7-\delta}$ coated conductors. *Supercond. Sci. Technol.*, 24(11), 2011.

[80] K. Ilin, K. A. Yagotintsev, C. Zhou, P. Gao, J. Kosse, S. J. Otten, W. A. J. Wessel, T. J. Haugan, D. C. van der Laan, and A. Nijhuis. Experiments and FE modeling of stress–strain state in *Re*BCO tape under tensile, torsional and transverse load. *Supercond. Sci. Technol.*, 28(5), 2015.

[81] A. Villaume, A. Antonevici, D. Bourgault, L. Porcar, J. P. Leggeri, and C. Villard. Lüders bands in coated conductors: an in-situ strain and transport magneto-optical investigation. *Supercond. Sci. Technol.*, 20(10), 2007.

[82] D. C. van der Laan, J. W. Ekin, C. C. Clickner, and T. C. Stauffer. Delamination strength of YBCO coated conductors under transverse tensile stress. *Supercond. Sci. Technol.*, 20(8), 2007.

[83] N. J. Long, R. C. Mataira, E. Talantsev, and R. A. Badcock. Mode I delamination testing of REBCO coated conductors via climbing drum peel test. *IEEE Trans. Appl. Supercond.*, 28(4), 2018.

[84] L. Liu, Y. Zhu, X. Yang, T. Qiu, and Y. Zhao. Delamination properties of YBCO tapes under shear stress along the width direction. *IEEE Trans. Appl. Supercond.*, 26(6), 2016.

[85] J. Fleiter, A. Ballarino, L. Bottura, and P. Tixador. Electrical characterization of *Re*BCO Roebel cables. *Supercond. Sci. Technol.*, 26(6), 2013.

[86] T. Takematsu, R. Hu, T. Takao, Y. Yanagisawa, H. Nakagome, D. Uglietti, T. Kiyoshi, M. Takahashi, and H. Maeda. Degradation of the performance of a YBCO-coated conductor double pancake coil due to epoxy impregnation. *Physica C: Superconductivity and its Applications*, 470(17-18), 2010.

[87] M. Oomen, W. Herkert, D. Bayer, P. Kummeth, W. Nick, and T. Arndt. Manufacturing and test of 2G-HTS coils for rotating machines: challenges, conductor requirements, realization. *Physica C: Superconductivity and its Applications*, 470, 2012.

[88] E. F. Talantsev, R. A. Badcock, R. Mataira, S. V. Chong, K. Bouloukakis, K. Hamilton, and N. J. Long. Critical current retention of potted and unpotted ReBCO Roebel cables under transverse pressure and thermal cycling. *Supercond. Sci. Technol.*, 30(4), 2017.

[89] F. Savary, E. Barzi, B. Bordini, L. Bottura, G. Chlachidze, D. Ramos, S. Izquierdo Bermudez, M. Karppinen, F. Lackner, C. H. Löffler, R. Moron-Ballester, A. Nobrega, J. C. Perez, H. Prin, D. Smekens, G. de Rijk, S. Redaelli, L. Rossi, G. Willering, A. V. Zlobin, and M. Giovannozzi. The 11 T dipole for HL-LHC: status and plan. *IEEE Trans. Appl. Supercond.*, 26(4), 2016.

[90] V. Marinozzi, G. Bellomo, B. Caiffi, P. Fabbricatore, S. Farinon, A. Maria Ricci, M. Sorbi, and M. Statera. Conceptual design of a 16 T cosθ bending dipole for the Future Circular Collider. *IEEE Trans. Appl. Supercond.*, 28(3), 2018.

[91] G. A. Kirby, J. van Nugteren, A. Ballarino, L. Bottura, N. Chouika, S. Clement, V. Datskov, L. Fajardo, J. Fleiter, R. Gauthier, L. Gentini, L. Lambert, M. Lopes, J. C. Perez, G. de Rijk, A. Rijllart, L. Rossi, H. ten Kate, M. Durante, P. Fazilleau, C. Lorin, E. Härö, A. Stenvall, S. Caspi, M. Marchevsky, W. Goldacker, and A. Kario. Accelerator-quality HTS dipole magnet demonstrator designs for the EuCARD-2 5 T 40 mm clear aperture magnet. *IEEE Trans. Appl. Supercond.*, 25(3), 2015.

[92] H. H. J. ten Kate, H. Weijers, S. Wessel, H. Boschman, and L. J. M van de Klundert. The reduction of the critical current in Nb_3Sn cables under transverse forces. *IEEE Transaction on Magnetics*, 28(1), 1992.

[93] A. Devred, L. Bacquart, P. Bredy, C. E. Bruzek, Y. Laumond, R. Otmani, and T. Schild. Interstrand resistance measurements on Nb_3Sn Rutherford-type cables. *IEEE Trans. Appl. Supercond.*, 9(2), 1999.

[94] E. C. Collings, M. D. Sumption, M. Majoros, X. Wang, D. R. Dietderich, K. Yagotyntsev, and A. Nijhuis. Influence of compaction during reaction heat treatment on the interstrand contact resistances of Nb_3Sn Rutherford cables for accelerator magnets. *IEEE Trans. Appl. Supercond.*, 28(3), 2018.

[95] E. W. Collings, M. D. Sumption, M. A. Susner, D. R. Dietderich, E. Krooshoop, and A. Nijhuis. Inter-strand contact resistance and magnetization of Nb_3Sn Rutherford cables with cores of different materials and widths. *IEEE Trans. Appl. Supercond.*, 22(3), 2012.

[96] E. W. Collings, M. D. Sumption, M. A. Susner, D. R. Dietderich, and A. Nijhuis. Coupling loss, inter-strand contact resistance, and magnetization of Nb_3Sn Rutherford cables with cores of Mgo tape and S-Glass ribbon. *IEEE Trans. Appl. Supercond.*, 21(3), 2011.

[97] M. D. Sumption, E. W. Collings, R. M. Scanlan, A. Nijhuis, and H. H. J. ten Kate. Core-suppressed AC loss and strand-moderated contact resistance in a Nb_3Sn rutherford cable. *Cryogenics*, 39(1), 1999.

[98] A. Nijhuis, H. H. J. ten Kate, V. Pantsyrny, A. K. Shikov, and M. Santini. Inter-strand contact resistance and AC loss of a 48-strands Nb_3Sn CIC Conductor with a Cr/Cr-oxide coating. *IEEE Trans. Appl. Supercond.*, 10(1), 2000.

[99] E. C. Collings, M. D. Sumption, E. Barzi, D. Turrioni, R. Yamada, A. V. Zlobin, and A. Nijhuis. Measurement of AC loss in cored Nb_3Sn Rutherford cables: interstrand contact resistance as function of core width. *AIP Conference Proceedings*, 986(1), 2008.

[100] S. Otten. *Characterisation of ReBCO Roebel cables*. PhD dissertation, Karlsruhe Institute of Technology, Germany, 2019.

[101] M. Majoros, M. D. Sumption, E. W. Collings, and N. J. Long. Stability, inter-strand contact resistance, and AC losses in YBCO Roebel cables. *IEEE Trans. Appl. Supercond.*, 24(3), 2014.

[102] M. Majoros, M. D. Sumption, E. W. Collings, and N. J. Long. Inter-strand current sharing and AC loss measurements in superconducting YBCO Roebel cables. *Supercond. Sci. Technol.*, 28(5), 2015.

[103] J.-E. Duvauchelle, B. Bordini, J. Fleiter, and A. Ballarino. Critical current measurements under transverse pressure of a Nb_3Sn Rutherford cable based on 1 mm RRP wires. *IEEE Trans. Appl. Supercond.*, 28(4), 2018.

[104] B. Bordini, P. Alknes, A. Ballarino, L. Bottura, and L. Oberli. Critical current measurements of high-J_c Nb_3Sn Rutherford cables under transverse compression. *IEEE Trans. Appl. Supercond.*, 24(3), 2014.

[105] J. W. Ekin. Effect of transverse compressive stress on the critical current and upper critical field of Nb_3Sn. *Journal of Applied Physics*, 62(12), 1987.

[106] B. Seeber, A. Ferreira, V. Abächerli, T. Boutboul, L. Oberli, and R. Flükiger. Transport properties up to 1000 A of Nb_3Sn wires under transverse compressive stress. *IEEE Trans. Appl. Supercond.*, 17(2), 2007.

[107] C. Senatore. Superconductors for magnets-from the materials to the technical conductors. *The CERN Accelerator school, University of Geneva, The Switzerland*, CERN indico, February-March 2018.

[108] B. Seeber, A. Ferreira, V. Abächerli, and R. Flükiger. Critical current of a Nb_3Sn bronze route conductor under uniaxial tensile and transverse compressive stress. *Supercond. Sci. Technol.*, 20(9), 2007.

[109] C. Calzolaio, G. Mondonico, A. Ballarino, B. Bordini, L. Bottura, L. Oberli, and C. Senatore. Electro-mechanical properties of PIT Nb_3Sn wires under transverse stress: experimental results and FEM analysis. *Supercond. Sci. Technol.*, 28(5), 2015.

[110] K. S. Alastair. *Temperature and strain scaling laws for the critical current density in Nb_3Sn and Nb_3Al conductors in high magnetic fields*. PhD dissertation, Durham University, England, 2001.

[111] E. Barzi, T. Wokas, and A. V. Zlobin. Sensitivity of Nb_3Sn Rutherford-type cables to transverse pressure. *IEEE Trans. Appl. Supercond.*, 15(2), 2005.

[112] E. Barzi, M. Fratini, and A. V. Zlobin. A device to test critical current sensitivity of Nb_3Sn cables to pressure. *Adv. in Cryog. Eng.*, 48A, 2002.

[113] M. Fratini and E. Barzi. Mechanical and thermal analysis of the cable/strand strain test fixture. *TD-01-001*, 2000.

[114] K. Umekawa, T. Ito, T. Takao, H. Tanaka, and M. Umeda. Transversal compressive force and superconducting transition properties of Bi-2223 tapes. *Physica C: Superconductivity*, 401(1-4), page: 251-254, 2004.

[115] T. Takao, T. Ito, K. Umekawa, Y. Fukasawa, H. Tanaka, and M. Umeda. Influence of transverse compressive strain on degradation of Bi-2223 tapes. *IEEE Trans. Appl. Supercond.*, 14(2), 2004.

[116] T. Takao, T. Ito, K. Umekawa, Y. Fukasawa, H. Tanaka, and M. Umeda. Degradation and reversibility of critical current due to transverse compressive stress in Ta-reinforced Nb_3Sn superconducting strand. *IEEE Trans. Appl. Supercond.*, 15(2), 2005.

[117] T. Takao, T. Ito, K. Umekawa, Y. Fukasawa, H. Tanaka, and M. Umeda. Influence of compressive length of normal stress on degradation in Bi-2223 tapes. *IEEE Trans. Appl. Supercond.*, 15(2), 2005.

[118] T. Takao, S. Koizuka, K. Oi, A. Ishiyama, J. Kato, T. Machi, K. Nakao, and Y. Shiohara. Characteristics of compressive strain and superconducting property in YBCO coated conductor. *Supercond. Sci. Technol.*, 17(2), 2007.

[119] T. Takao, Y. Takahashi, T. Ito, M. Yamaguchi, K. Umekawa, J. Kondo, and M. Umeda. Compressive strain and critical current properties of Nb_3Sn conductors reinforced by center-arranged and distributed Ta. *IEEE Trans. Appl. Supercond.*, 13(2), 2003.

[120] B. ten Haken. *Strain effects on the critical properties of high-field superconductors*. PhD dissertation, University of Twente, The Netherlands, 1994.

[121] B. ten Haken and H. H. J. ten Kate. The degradation of the critical current density in a Nb_3Sn tape conductor due to parallel and transversal strain. *Fusion Engineering and Design.*, 20, 1993.

[122] S. Otten and R. Lagraauw. *Critical current degradation under transverse compressive stress in YBCO-coated superconductive tapes*. Bachelor dissertation, University of Twente, The Netherlands, 2012.

[123] J. W. Ekin, S. L. Bray, and W. L. Bahn. Effect of transverse stress on the critical current of bronze_process and internal_tin Nb_3Sn. *Journal of Applied Physics*, 69(8), page:4436-4438, 1991.

[124] P. Bauer, K. Ewald, and J. Ozelis. Design of a sample holder for measurement of Nb_3Sn cable critical current under transverse loading conditions. *Fermilab Technical Division note TD-99-051**, 1999.

[125] P. Bauer and D. Dietderich. Critical current measurements of superconducting cables at the National High Magnetic Field laboratory - documentation / user guide version 1.0. *Fermilab Technical Division note TD-99-039**, 1999.

[126] A. G. Prodell and A. Arn. A facility for evaluating superconductors above atmospheric pressure at 1.8 K. *Adv. in Cryog. Eng.*, 43, 1998.

[127] G. Ambrosio, N. Andreev, S. E. Bartlett, E. Barzi, C.-H. Denarie, D. Dietderich, A. K. Ghosh, A. P. Verweij, and A. V. Zlobin. Critical current and instability threshold measurement of Nb_3Sn cables for high field accelerator magnets. *IEEE Trans. Appl. Supercond.*, 15(2), 2005.

[128] B. Bordini, F. Regis, O. Crettiez, P. Fessia, M. Guinchard, J. C. Perez, and I. Sexton. Conceptual design of a new sample holder for the FRESCA cable test station. *IEEE Trans. Appl. Supercond.*, 20(3), 2010.

[129] H. H. J. ten Kate, H. Weijers, and J. M. van Oort. Critical current degradation in Nb_3Sn cables under transverse pressure. *IEEE Trans. Appl. Supercond.*, 3(1), page:1334-1337, 1993.

[130] A. P. Verweij and A. K. Ghosh. Critical current measurements of the main LHC superconducting cables. *IEEE Trans. Appl. Supercond.*, 17(2), 2007.

[131] S. Caspi, S. Gourlay, R. Hafalia, A. Lietzke, J. ONeill, C. Taylor, and A. Jackson. The use of pressurized bladders for stress control of superconducting magnets. *IEEE Trans. Appl. Supercond.*, 16(2), 2006.

[132] W. van de Camp. *Critical current versus transverse stress and thermal stability of a RRP Nb_3Sn Rutherford cable*. Master thesis, University of Twente, The Netherlands, 2012.

[133] F. Grilli, E. Pardo, W. Yuan, and F. Gömöry. Computation of losses in HTS under the action of varying magnetic fields and currents. *IEEE Trans. Appl. Supercond.*, 24(1), 2014.

[134] Y. Wang, X. Guan, and J. Dai. Review of AC loss measuring methods for HTS tape and unit. *IEEE Trans. Appl. Supercond.*, 24(5), 2014.

[135] S. Mukoyama, N. Amemiya, K. Watanabe, Y. Iijima, N. Mido, T. Masuda, T. Morimura, M. Oya, T. Nakano, and K. Yamamoto. Study on AC loss measurements of HTS power cable for standardizing. *Journal of Physics: Conference Series*, 897(conference 1), 2017.

[136] A. P. Verweij. *Electrodynamics of superconducting cables in accelerator magnets*. PhD dissertation, University of Twente, The Netherlands, 1995.

[137] J. Souc, F. Gömöry, and M. Vojenčiak. Calibration free method for measurement of the AC magnetization loss. *Supercond. Sci. Technol.*, 18(5), 2005.

[138] B. van Nugteren. *Detecting coupling currents in HTS Roebel cables*. Master dissertation, University of Twente, The Netherlands, 2016.

[139] J. M. C. Martínez. *Analysis of AC losses in superconducting electrical components for application in the design of electrical systems*. PhD dissertation, University of Extremadura, Spain, 2010.

[140] C. Daum, J. Geerinck, R. Heller, P. Schmuser, and P.A.M. Bracke. Superconducting correction magnets for the HERA proton storage ring. *IEEE Transaction on Magnetics*, 24(2), 1988.

[141] J. van Nugteren, B. van Nugteren, P. Gao, L. Bottura, M. Dhallé, W. Goldacker, A. Kario, H. ten Kate, G. Kirby, E. Krooshoop, G. de Rijk, L. Rossi, C. Senatore, S. Wessel, K. Yagotintsev, and Y. Yang. Measurement and numerical evaluation of AC loss in a *Re*BCO Roebel cable at 4.5 K. *IEEE Trans. Appl. Supercond.*, 26(3), 2016.

[142] Mass Flow Meter for low pressure drop or corrosive gas service. F-100d, Bronkhorst high-tech B.V.

[143] D. Tommasini, D. Arbelaez, B. Auchmann, H. Bajas, M. Bajko, A. Ballarino, E. Barzi, G. Bellomo, M. Benedikt, S. Izquierdo Bermudez, B. Bordini, L. Bottura, L. Brower, M. Buzio, B. Caiffi, S. Caspi, M. Dhalle, M. Durante, G. de Rijk, P. Fabbricatore, S. Farinon, P. Ferracin, P. Gao, S. Gourlay, M. Juchno, V. Kashikhin, F. Lackner, C. Lorin, M. Marchevsky, V. Marinozzi, T. Martinez, J. Munilla, I. Novitski, T. Ogitsu, R. Ortwein, J. Carlos Perez, C. Petrone, S. Prestemon, M. Prioli, Jean-Michel Rifflet, E. Rochepault, S. Russenschuck, T. Salmi, F. Savary, D. Schoerling, M. Segreti, C. Senatore, M. Sorbi, A. Stenvall, E. Todesco, F. Toral, A. P. Verweij, S. Wessel, F. Wolf, and Alexander V. Zlobin. Status of the 16 T dipole development program for a Future Hadron Collider. *IEEE Trans. Appl. Supercond.*, 28(3), 2018.

[144] J. S. Murtomaki, J. van Nugteren, G. Kirby, L. Rossi, J. Ruuskanen, and A. Stenvall. Mechanical effects of the nonuniform current distribution on HTS coils for accelerators wound with *Re*BCO Roebel cable. *IEEE Trans. Appl. Supercond.*, 27(4), 2017.

[145] G. A. Kirby, L. Rossi, A. Badel, M. Bajko, A. Ballarino, L. Bottura, M. Dhallé, M. Durante, P. Fazilleau, J. Fleiter, W. Goldacker, E. Härö, J. Himbele, A. Kario, S. Langeslag, C. Lorin, J. Murtzomaki, J. van Nugteren, G. de Rijk, T. Salmi, C. Senatore, A. Stenvall, P. Tixador, A. Usoskin, G. Volpini, Y. Yang, and N. Zangenberg. Status of the demonstration magnets for the EuCARD-2 future magnets project. *IEEE Trans. Appl. Supercond.*, 26(3), 2016.

[146] F. Wolf, P. Ehermann, F. Lackner, D. Mosbach, C. Scheuerlein, K. Schladitz, and D. Schoerling. Characterization of the stress distribution on Nb_3Sn Rutherford cables under transverse compression. *IEEE Trans. Appl. Supercond.*, 28(3), 2018.

[147] A. J. Wuis, B. Bordini, A. Ballarino, L. Oberli, and H. H. J. ten Kate. Characterization of Nb_3Sn Rutherford cables for the LHC 11-T dipole magnet. *IEEE Trans. Appl. Supercond.*, 24(3), 2014.

[148] E. W. Collings, M. D. Sumption, M. A. Susner, D. R. Dietderich, E. Barzi, A. V. Zlobin, Y. Ilyin, and A. Nijhui. Influence of a stainless steel core on coupling loss, interstand contact resistance, and magnetization of an Nb_3Sn Rutherford cable. *IEEE Trans. Appl. Supercond.*, 18(2), 2008.

[149] M. Bajko, B. Bordini, S. Canfer, G. Ellwood, J. Feuvrier, M. Guinchard, M. Karppinen, C. Kokkinos, P. Manil, A. Milanese, L. Oberli, J. C. Perez, F. Regis, and G. de Rijk. The Short Model Coil (SMC) dipole: An R&D program towards Nb_3Sn accelerator magnets. *IEEE Trans. Appl. Supercond.*, 22(3), 2012.

[150] B. Bordini, A. Ballarino, J. Fleiter, M. Macchini, and D. Richter. 11 T conductor performance. https://indico.cern.ch/event/493351/contributions/1171933/, Review of the 11 T dipoles at collimator section for the HL-LHC, CERN, 2016.

[151] B. Bordini, J. E. Duvauchelle, M. Dhalle, P. Gao, C. Senatore, L. Gamperle, and C. Barth. Conductor studies. https://indico.cern.ch/event/661257/contributions/2739628/, 2nd review of the EuroCirCol WP5, CERN, 2017.

[152] W. Goldacker. HTS Roebel cable rearch from KIT and partners, 12th European Conf. on Applied Superconductivity (Lyon, France).

[153] A. V. Zlobin, N. Andreev, G. Apollinari, B. Auchmann, E. Barzi, R. Bossert, M. Karppinen, F. Nobrega, I. Novitski, L. Rossi, D. Smekens, D. Turrioni, and R. Yamada. Design and fabrication of a single-aperture 11 T Nb_3Sn dipole model for LHC upgrade. *IEEE Trans. Appl. Supercond.*, 22(3), 2012.

[154] M. Segreti, C. Lorin, and M. Durante. ECC block design. https://indico.cern.ch/event/689854/contributions/2832770, EuroCirCol WP5 coordination meeting 31, CERN, 2018.

[155] J. W. Ekin. Strain scaling law for flux pinning in practical superconductors. Part 1: Basic relationship and application to Nb_3Sn conductors. *Cryogenics*, 20(11), page: 611-624, 1980.

[156] A. Nijhuis. *Mechanical and electro-magnetic performance of Nb_3Sn superconductors for fusion*. PhD dissertation, University of Twente, The Netherlands, 2016.

[157] J. W. Ekin. Effect of transverse compressive stress on the critical current and upper critical field of Nb_3Sn wires. *Journal of Applied Physics*, 62(12), 1987.

[158] G. Mondonico, B. Seeber, A. Ferreira, B. Bordini, L. Oberli, L. Bottura, A. Ballarino, R. Flükiger, and C. Senatore. Effect of quasi-hydrostatical radial pressure on I_c of Nb_3Sn wires. *Supercond. Sci. Technol.*, 25(11), 2017.

[159] B. Jakob, G. Pasztor, M. Bona, and A. Asner. Reduced sensitivity of Nb_3Sn epoxy-impregnated cable to transverse stress. *Cryogenics*, 31(5), page: 390-391, 1991.

[160] H. Boschman, A. P. Verweij, S. Wessel, H. H. J. ten Kate, and L. J. M. van de Klundert. The effect of transverse loads up to 300 MPa on the critical currents of Nb_3Sn cables. *IEEE Transactions on Magnetics*, 27(2), 1991.

[161] D. Uglietti, R. Wesche, and P. Bruzzone. Effect of transverse load on the critical current of a coated conductor Roebel cable. *Supercond. Sci. Technol.*, 26(7), 2013.

[162] C. M. Bayer, P. V. Gade, C. Barth, A. Preuß, A. Jung, and K. P. Weiß. Mechanical reinforcement for RACC cables in high magnetic background fields. *Supercond. Sci. Technol.*, 29(2), 2016.

[163] S. Otten, M. Dhallé, P. Gao, W. Wessel, A. Kario, A. Kling, and W. Goldacker. *Enhancement of the transverse tolerance of ReBCO Roebel cables by epoxy impregnation*. *Supercond. Sci. Technol.*, 28(6), 2015.

[164] G. Kirby, V. I. Datskov, S. Clement, A. Chiuchiolo, P. Fessia, R. Gauthier, G. Lynch, J. Murtomaki, J. van Nugteren, Francois-Olivier Pincot, J. C. Perez, L. Rossi, G. de Rijk, S. Tavares, and V. Venturi. Thermal contraction, experimental data and fits for the thermal contraction of future magnet materials at cryogenic temperatures, Internal document of CERN, 2016.

[165] Araldite MY740 / HY918 / DY062. Vantico ltd., July 2000.

[166] Araldite MY740 / HY906 / DY070. Huntsman Advanced Materials, Sept. 2007.

[167] P. A. Hudson and H. Jones. High field facilities and services of the clarendon laboratory. *IEEE Transactions on Magnetics*, 17(5), 1981.

[168] M. T. G. van der Laan, R. B. Tax, and H. H. J. ten Kate. A 1 T, 0.33 m bore superconducting magnet operating with cryocoolers at 12 K. *IEEE Transactions on Magnetics*, 28(1), 1992.

[169] A. den Ouden, S. Wessel, E. Krooshoop, R. Dubbeldam, and H. H. J. ten Kate. An experimental 11.5 T Nb_3Sn LHC type of dipole magnet. *IEEE Transactions on Magnetics*, 30(4), 1994.

[170] W. A. J. Wessel, A. den Ouden, H. J. G. Krooshoop, H. H. J. ten Kate, J. Wieland, and P. J . M. van der Slot. A conduction-cooled, 680-mm-long warm bore, 3 T Nb_3Sn solenoid for a cerenkov free electron laser. *IEEE Trans. Appl. Supercond.*, 9(2), 1999.

[171] CTD-101K. Cryogenic, low viscosity and long pot life, excellent for impregnation of large coils. *Composite Technology Development, Lafayette, CO, USA*, 2014.

[172] A. V. Zlobin, G. Ambrosio, N. Andreev, E. Barzi, B. Bordini, R. Bossert, R. Carcagno, D. R. Chichili, J. DiMarco, L. Elementi, S. Feher, V. S. Kashikhin, V. V. Kashikhin, R. Kephart, M. Lamm, P. J. Limon, I. Novitski, D. Orris, Yu. Pischalnikov, P. Schlabach, R. Stanek, J. Strait, C. Sylvester, M. Tartaglia, J. C. Tompkins, D. Turrioni, G. Velev, R. Yamada, and V. Yarba. R&D of Nb_3Sn accelerator magnets at Fermilab. *IEEE Trans. Appl. Supercond.*, 15(2), 2005.

[173] G. Kirby, V. I. Datskov, S. Clement, A. Chiuchiolo, P. Fessia, R. Gauthier, G. Lynch, J. Murtomaki, J. van Nugteren, Francois-Olivier Pincot, J. C. Perez, L. Rossi, G. de Rijk, and S. Tavares. Thermal contraction of future magnet materials at cryogenic temperatures, CERN, 2015.

[174] S. Otten. *Transverse pressure dependence of the critical current in epoxy impregnated ReBCO Roebel cables*. Master thesis, University of Twente, The Netherlands, 2014.

[175] S. Otten, A. Kario, A. Kling, and W. Goldacker. Bending properties of different *Re*BCO coated conductor tapes and Roebel cables at T=77K. *Supercond. Sci. Technol.*, 29(12), 2016.

[176] S. Yazaki, A. Karasawa, T. Kotoyori, A. Ishiyama, and N. Miyahara. Critical current degradation in High-Temperature superconducting tapes caused by temperature rise. *IEEE Trans. Appl. Supercond.*, 23(3), 2013.

[177] Measurements and error analysis. University of North Carolina. https://www.webassign.net/question_assets/unccolphysmechl1/measurements/manual.html, 2011. Accessed 11-06-2019.

[178] H. Boschman. *On the resistive transition of composite superconductors*. PhD dissertation, University of Twente, The Netherlands, 1991.

[179] J.R. Rumble Ed. *CRC Handbook of Chemistry and Physics*. CRC Press, 2018. ISBN: 9781138561632- CAT# K43481.

[180] A. P. Verweij. *De Invloed van Transversale Druk op de Spanning-Stroom Karakteristiek van Nb_3Sn-Kabels tot 340 MPa en tot 11 T*. Master thesis, University of Twente, The Netherlands, 1990.

[181] A. Godeke, F. Hellman, H. H. J. ten Kate, and M. G. T. Mentink. Fundamental origin of the large impact of strain on superconducting Nb_3Sn. *Supercond. Sci. Technol.*, 31(10), 2018.

[182] T. Wang, L. Chiesa, M. Takayasu, and B. Bordini. Modeling of the critical-current behavior of Nb_3Sn subsized cables under transverse load using 2D finite element analysis and a strain scaling law. *IEEE Trans. Appl. Supercond.*, 24(3), 2014.

[183] Q. Xu, M. Iio, T. Nakamoto, and A. Yamamoto. Analysis of strain distribution in A15-type superconducting coils under compressive stress. *IEEE Trans. Appl. Supercond.*, 24(3), 2014.

[184] G. Vallone, B. Bordini, and P. Ferracin. Computation of the reversible critical current degradation in Nb_3Sn Rutherford cables for particle accelerator magnets. *IEEE Trans. Appl. Supercond.*, 28(4), 2018.

[185] P. Ebermann, J. Bernardi, J. Fleiter, F. Lackner, F. Meuter, M. Pieler, C. Scheuerlein, D. Schoerling, F. Wolf, A. Ballarino, L. Bottura, D. Tommasini, F. Savary, and M. Eisterer. Irreversible degradation of Nb_3Sn Rutherford cables due to transverse compressive stress at room temperature. *Supercond. Sci. Technol.*, 31(6), 2018.

[186] M. Daly, C. H. Loffler, D. Smekens, A.T. Fontenla, O.S. De Frutos, M. Guinchard, and F. Savary. Multiscale approach to the mechanical behavior of epoxy impregnated Nb_3Sn coils for the 11 T dipole. *IEEE Trans. Appl. Supercond.*, 28(3), 2018.

[187] K. Konstantopoulou, M. Sarazin, X. Granados, J. Y. Pastor, and X. Obradors. Effect of the axial stress and the magnetic field on the critical current and the electric resistance of the joints between HTS coated conductors. *Supercond. Sci. Technol.*, 28(6), 2015.

[188] H. S. Shin, A. Nisay, M. B. de Leon, and M. J. Dedicatoria. Joining of ReBCO coated conductor tapes using ultrasonic welding method. *IEEE Trans. Appl. Supercond.*, 25(3), 2015.

[189] N. Bagrets, G. Celentano, A. Augieri, R. Nast, and K. P. Weiss. Investigation of soldered ReBCO tape–copper joints for superconducting applications. *IEEE Trans. Appl. Supercond.*, 26(4), 2016.

[190] K. Bäuml and S. Großmann. Investigations on different joining techniques regarding electrical joints with normal conducting material and YBCO coated conductors. *IEEE Trans. Appl. Supercond.*, 26(3), 2016.

[191] J. Fleiter and A. Ballarino. In-field electrical resistance at 4.2 K of *Re*BCO splices. *IEEE Trans. Appl. Supercond.*, 27(4), 2017.

[192] Y. Pan, J. Sheng, W. Wu, Y. Wang, W. Zeng, Y. Zhao, Z. W. Zhang, Z. Li, Z. Hong, and Z. Jin. Numerical study on simplified resistive joints of coated conductors is there a lower limit of the joint resistance. *IEEE Trans. Appl. Supercond.*, 27(4), 2017.

[193] J. Zheng, H. Ma, R. He, Y. Lu, H. Song, C. Cui, Y. Zhang, C. Bai, Y. Guo, Z. Liu, and C. Cai. Low-resistance and strong-adhesion soldering of second-generation high-temperature superconductor tapes within a short time. *IEEE Trans. Appl. Supercond.*, 27(5), 2017.

[194] N. Bagrets, K. P. Weiss, R. Nast, and R. Heller. Correlation between resistances of face-to-face soldered joints and interface resistance between layers in superconducting tapes. *IEEE Trans. Appl. Supercond.*, 28(4), 2018.

[195] H. S. Shin, M. A. Diaz, Z. M. Bautista, and S. Awaji. Joint resistance characteristics in ultrasonic weld ReBCO CC tapes at various temperatures and magnetic fields. *IEEE Trans. Appl. Supercond.*, 28(4), 2018.

[196] D. G. Yang, Y. H. Choi, D. H. Kang, Y. J. Park, and H. G. Lee. Effect of partial insulation winding scheme on discharge characteristics of GdBCO coils. *Current Appl. Phys.*, 15(2), 2015.

[197] S. Honda, M. Iwakuma, Y. Fukumoto, K. Yoshida, S. Sato, T. Izumi, A. Tomioka, and M. Konno. Current-sharing properties in parallel conductors composed of ReBCO superconducting tapes. *IEEE Trans. Appl. Supercond.*, 27(4), 2017.

[198] J. Lu, R. Goddard, K. Han, and S. Hahn. Contact resistance between two *Re*BCO tapes under load and load cycles. *Supercond. Sci. Technol.*, 30(4), 2017.

[199] J. Lu, J. Levitan, D. McRae, and R. Walsh. Contact resistance between two ReBCO tapes the effects of cyclic loading and surface coating. *Supercond. Sci. Technol.*, 31(8), 2018.

[200] M. Bonura, C. Barth, A. Joudrier, J. F. Troitino, A. Fête, and C. Senatore. Systematic study of the contact resistance between ReBCO tapes pressure dependence in the case of no-insulation, metal co-winding and metal-insulation. *IEEE Trans. Appl. Supercond.*, 29(5), 2019.

[201] A. Augieri, G. De Marzi, G. Celentano, L. Muzzi, G. Tomassetti, F. Rizzo, A. Anemona, A. Bragagni, M. Seri, C. Bayer, N. Bagrets, and A. della Corte. Electrical characterization of ENEA high temperature superconducting cable. *IEEE Trans. Appl. Supercond.*, 25(3), 2015.

[202] G. P. Willering, D. C. van der Laan, H. W. Weijers, P. D. Noyes, G. E. Miller, and Y. Viouchkov. Effect of variations in terminal contact resistances on the current distribution in high-temperature superconducting cables. *Supercond. Sci. Technol.*, 28(3), 2015.

[203] T. Mulder, J. Fleiter, G. Willering, A. Dudarev, M. Mentink, M. Dhallé, and H. Ten Kate. Demonstration of the ReBCO CORC 47kA@10T/4.2K Cable-In-Conduit-Conductor and its joint terminals at 4.5 and 77 K. *IEEE Trans. Appl. Supercond.*, 27(4), 2017.

[204] J. S. Murtomäki, G. Kirby, J. van Nugteren, P. A. Contat, O. Sacristan de Frutos, J. Fleiter, F. O. Pincot, G. de Rijk, L. Rossi, J. Ruuskanen, A. Stenvall, and F. J. Wolf. 10 kA joints for HTS Roebel cables. *IEEE Trans. Appl. Supercond.*, 28(3), 2018.

[205] M. N. Wilson. *Superconducting magnets*. Clarendon press Oxford, 1983. ISBN: 978-0198548102.

[206] Y. Iwasa. *Case Studies in Superconducting Magnets, Design and Operational Issues*. Springer, 2009. ISBN: 978-0-387-09800-5.

[207] E. Pardo and F. Grilli. Numerical simulations of the angular dependence of magnetization AC losses: coated conductors, Roebel cables and double pancake coils. *Supercond. Sci. Technol.*, 25(1), 2012.

[208] Y. Sogabe, M. Nii, T. Tsukamoto, T. Nakamura, and N. Amemiya. Electromagnetic field analyses of ReBCO Roebel cables wound into coil configurations. *IEEE Trans. Appl. Supercond.*, 24(3), 2014.

[209] H. Noji. AC loss calculation of ReBCO cables by the combination of electric circuit model and 2D finite element method. *Physics Procedia*, 81, 2016.

[210] N. Bykovsky, G. De Marzi, D. Uglietti, P. Bruzzone, and L. Muzzi. Magnetization loss for stacks of ReBCO tapes. *Supercond. Sci. Technol.*, 30(2), 2017.

[211] W. Zhou, Z. Jiang, M. Staines, W. Song, C. W. Bumby, R. A. Badcock, N. J. Long, and J. Fang. Magnetization loss in ReBCO Roebel cables with varying strand numbers. *IEEE Trans. Appl. Supercond.*, 28(3), 2018.

[212] W. Song, Z. Jiang, M. Staines, R. A. Badcock, and J. Fang. Experimental and numerical transport AC losses in a four-strand Roebel cable bifilar stack. *Supercond. Sci. Technol.*, 31(11), 2018.

[213] W. Ta, T. Shao, and Y. Gao. Comparison study of cable geometries and superconducting tape layouts for high-temperature superconductor cables. *Cryogenics*, 91, 2018.

[214] J. W. Ekin. Strain dependence of the critical current and critical field in multifilamentary Nb_3Sn composites. *IEEE Trans. Magn.*, 15(1), 1979.

[215] W. A. Fietz and W. W. Webb. Hysteresis in superconducting alloys – temperature and field dependence of dislocation pinning in niobium alloys. *Phys. Rev.*, 178(2), 1969.

[216] L. Bottura and B. Bordini. Jc(B,T,ϵ) parameterization for the ITER Nb_3Sn production. *IEEE trans. Appl. Supercond.*, 19(3), 2009.

[217] A. Godeke, M. C. Jewell, C. M. Fischer, A. A. Squitieri, P. J. Lee, and D. C. Larbalestier. The upper critical field of filamentary Nb_3Sn conductors. *Journal of Applied Physics*, 97(9), 2005.

[218] W. D. Markeiwicz. Invariant strain analysis of the critical temperature T_c of Nb_3Sn. *IEEE Trans. Appl. Supercond.*, 15(2), 2005.

[219] M. G. T. Mentink. *An experimental and computational study of strain sensitivity in superconducting Nb_3Sn*. PhD dissertation, University of Twente, The Netherlands, 2014.

[220] M. G. T. Mentink, M. Dhallé, D. R. Dietderich, A. Godeke, E. Hellman, and H. H. J. ten Kate. The effects of disorder on the normal state and superconducting properties of Nb_3Sn. *Supercond. Sci. Technol.*, 30(2), 2017.

[221] M. Sadd. *Elasticity: theory, applications and numerics*. Academic Press, 2014. ISBN: 978-0-12-408136-9.

[222] T. Wang, L. Chiesa, M. Takayasu, and B. Bordini. A novel modeling to predict the critical current behavior of Nb_3Sn PIT strand under transverse load based on a scaling law and Finite Element Analysis. *Cryogenics*, 63, 2014.

[223] Y. Zhai, L. D'Hauthuille, C. Barth, and C. Senatore. Finite-element analysis of transverse compressive and thermal loads on Nb_3Sn wires with voids. *IEEE Trans. Appl. Supercond.*, 26(4), 2016.

[224] J. M. van Oort. *Critical current degradation in Nb_3Sn superconductors in accelerator magnets*. PhD dissertation, University of Twente, The Netherlands, 2000.

[225] P. Bauer, H. Rajainmaki, and E. Salpietro. EFDA material data complication for superconductor simulation. *Inside document*, 2007.

[226] J. G. Hust, D. H. Weitzel, and R. L. Powell. Thermal conductivity, electrical resistivity, and thermopower of aerospace alloys from 4 to 300 K. *NIST Journal of Research – A*, 75(4), 1971.

[227] C. Zhou. *Intra wire resistance and strain affecting the transport properties of Nb_3Sn strands in Cable-in-Conduit Conductors*. PhD dissertation, University of Twente, The Netherlands, 2014.

[228] T. Holúbek, M. Dhallé, and P. Kováč. Current transfer in MgB_2 wires with different sheath materials. *Supercond. Sci. Technol.*, 20(3), 2007.

[229] M. Polak, P. N. Barnes, and G. A. Levin. YBCO/Ag boundary resistivity in YBCO tapes with metallic substrates. *Cryogenics*, 33(3), 1993.

[230] S. P. Ashworth, C. Beduz, K. Harrison, R. G. Scurlock, and Y. Yang. Investigation of the interface between a normal metal and high temperature superconductor. *Advanced in Cryogenic Engineering (Materials)*, 36(ptA), 1990.

[231] E. J. Lucas, Z. J. J. Stekly, C. Layerick, and G. Pewitt. Current transfer in contacts involving superconductors. 1965.

[232] R. A. Matula. Electrical resistivity of copper, gold, palladium, and silver. *Journal of Physical and Chemical Reference Data*, 8(4), 1979.

[233] C. P. Bean. Magnetization on hard superconductors. *Physical Review Letters*, 8, 1962.

[234] G. H. Morgan. Theoretical behavior of twisted multicore superconducting wire in a time-varying uniform magnetic field. *J. Appl. Phys.*, 41(8), 1970.

[235] M. N. Wilson, C. R. Walters, J. D. Lewin, and P. F. Smith. Experimental and theoretical studies of filamentary superconducting composites: I. basic ideas and theory. *J. Phys. D: Appl. Phys.*, 3(11), 1970.

[236] E. H. Brandt and M. Indenbom. Type-II superconducting strip with current in perpendicular magnetic field. *Phys. Rev. B*, 48(17), 1993.

[237] C. P. Bean. Magnetization of high-field superconductors. *Rev. Mod. Phys. 36*, 1964.

[238] A. Wuis. *AC magnetization loss: The role of dimensionality*. Master dissertation, University of Twente, The Netherlands, 2009.

[239] B. ten Haken, J.-J. Rabbers, and H. H. J. ten Kate. Magnetization and AC loss in a superconductor with an elliptical cross-section and arbitrary aspect ratio. *Physica C*, 377(1-2), 2002.

[240] W. J. Carr. *AC loss and macroscopic theory of superconductors*. 2nd ed.,Taylor & Francis Inc, New York, 2001. ISBN: 978-0415267977.

[241] F. Grilli and E. Pardo. Simulation of AC loss in Roebel coated conductor cables. *Supercond. Sci. Technol.*, 23(11), 2010.

[242] L. S. Lakshmi, M. P. Staines, K. P. Thakur, R. A. Badcock, and N. J. Long. Frequency dependence of magnetic ac loss in a five strand YBCO Roebel cable. *Supercond. Sci. Technol.*, 23(6), 2010.

[243] H. Norder. *Inter-strand resistance and coupling losses in YBCO Roebel cables*. Master dissertation, University of Twente, The Netherlands, 2017.

[244] V. M. R. Zermeno, F. Grilli, and F. Sirois. A full 3D time-dependent electromagnetic model for Roebel cables. *Supercond. Sci. Technol.*, 26(5), 2013.

[245] J. A. Parrell, Y. Z. Zhang, M. B. Field, P. Cisek, and S. Hong. High field Nb_3Sn conductor development at Oxford Superconducting Technology. *IEEE Trans. Appl. Supercond.*, 13(2), 2003.

[246] J. E. Kunzler, E. Buehler, F. S. L. Hsu, and J. H. Wernick. Superconductivity in Nb_3Sn at high current density in a magnetic field of 88 kgauss. *Phys. Rev. Lett.*, 6(3), 1961.

[247] W. B. Sampson, S. Kiss, K. E. Robins, and A. D. McInturff. Nb_3Sn dipole magnets. *IEEE Trans. On Magnetics*, 15(1), 1979.

[248] R. McClusky, K. E. Robins, and W. B. Sampson. A Nb_3Sn high field dipole. *IEEE Trans. On Magnetics*, 27(2), 1991.

[249] G. Amhrosio, N. Andreev, E. Barzi, P. Bauer, K. Bwald, J. Ozelis, and G. Sabbi. Study of the react and wind technique for a Nb_3Sn common coil dipole. *IEEE Trans. Appl. Supercond.*, 10(1), 2000.

[250] G. Ambrosio, N. Andreev, E. Barzi, P. Bauer, D. R. Chichili, K. Ewald, S. Feher, L. Imbasciati, V. V. Kashikhin, P. J. Limon, L. Litvinenko, I. Novitski, J. M. Rey, R. M. Scanlan, S. Yadav, R. Yamada, and A. V. Zlobin. R&D for a single-layer Nb_3Sn common coil dipole using the react-and-wind fabrication technique. *IEEE Trans. Appl. Supercond.*, 12(2), 2002.

[251] V. S. Kashikhin, N. Andreev, J. DiMarco, S. Feher, V. V. Kashikhin, M. Lamm, I. Novitski, D. Orris, P. Schlabach, C. Sylvester, M. Tartaglia, G. Velev, and A. V. Zlobin. Field quality measurements of Fermilab Nb_3Sn common coil dipole model. *IEEE Trans. Appl. Supercond.*, 14(2), 2004.

[252] R. Gupta, M. Anerella, J. Cozzolino, J. Escallier, G. Ganetis, A. Ghosh, M. Harrison, J. Muratore, W. Sampson, and P. Wanderer. React and wind Nb_3Sn common coil dipole. *IEEE Trans. Appl. Supercond.*, 17(2), 2007.

[253] A. Asner, R. Perin, S. Wenger, and F. Zerobin. First Nb_3Sn, 1m long superconducting dipole model magnets for LHC break the 10 Tesla field threshold. *11_{th} International Conference on Magnet Technology (MT-11), Tsukuba 1989*, 27(2), Elsevier Applied Science, pp: 36-41, 1990.

[254] H. H. J. ten Kate, A. den Ouden, D. ter Avest, S. Wessel, and R. Dubbeldad. Development of an experimental 10 t Nb_3Sn dipole magnet for the CERN LHC. *IEEE Trans. on Magnetics*, 27(2), 1991.

[255] E. Krooshoop A. den Ouden, S. Wessel and H. ten Kate. Application of Nb_3Sn superconductors in high-field accelerator magnets. *IEEE Trans. Appl. Supercond.*, 7(2), 1997.

[256] R. Gupta, K. Chow, D. Dietderich, S. Gourlay, G. Millos, A. McInturff, and R. Scanlan. A high field magnet design for a future hadron collider. *IEEE Trans. Appl. Supercond.*, 9(2), 1999.

[257] A. F. Lietzke, S. Caspi, L. Chiesa, M. Coccoli, D. R. Dietderich, P. Ferracin, S. A. Gourlay, R. R. Hafalia, A. D. McInturff, G. Sabbi, and R. M. Scanlan. Test results of RD3c, a Nb_3Sn common-coil racetrack dipole magnet. *IEEE Trans. Appl. Supercond.*, 13(2), 2003.

[258] A. V. Zlobin, G. Ambrosio, N. Andreev, E. Barzi, R. Bossert, R. Carcagno, D. R. Chichili, L. Elementi, S. Feher, V. S. Kashikhin, V. V. Kashikhin, M. J. Lamm, I. Novitski, Yu. Pischalnikov, C. Sylvester, M. Tartaglia, and R. Yamada. Development and test of Nb_3Sn cos-theta dipoles based on PIT strands. *IEEE Trans. Appl. Supercond.*, 15(2), 2005.

[259] P. Manil, B. Baudouy, S. Clément, M. Devaux, M. Durante, P. Fazilleau, P. Ferracin, P. Fessia, J. E. Munoz Garcia, L. Garcia, R. Gauthier, L. Oberli, J. C. Perez, S. Pietrowicz, J. M. Rifflet, G. de Rijk, F. Rondeaux, and E. Todesco. Development and coil fabrication test of the Nb_3Sn dipole magnet FRESCA2. *IEEE Trans. Appl. Supercond.*, 24(3), 2014.

[260] S. Caspi, D. Arbelaez, L. Brouwer, S. Gourlay, S. Prestemon, and B. Auchmann. Design of a canted-cosine-theta superconducting dipole magnet for future colliders. *IEEE Trans. Appl. Supercond.*, 27(4), 2017.

[261] J. Cabanes, M. Garlasche, B. Bordini, and A. Dallocchio. Simulation of the cabling process for Rutherford cables: an advanced finite element model. *Cryogenics*, 80(3), 2016.

[262] S. Peggiani. *Analysis of Nb_3Sn Rutherford cable production and strand deformations*. Master dissertation, Polytechnic University of Milan, Italy,, 2017.

[263] L. Rossi. Manufacturing and testing of accelerator superconducting magnets. *CERN Yellow Report CERN-2014-005*, 2014.

[264] D. Pulikowski, F. Lackner, C. Scheuerlein, D. Meinel, F. Savary, D. Tommasini, and M. Pajor. Testing mechanical behavior of Nb_3Sn Rutherford cable during coil winding. *IEEE Trans. Appl. Supercond.*, 27(4), 2017.

[265] E. Barzi, D. Turrioni, and A. V. Zlobin. Progress in Nb_3Sn RRP strand studies and Rutherford cable development at FNAL. *IEEE Trans. Appl. Supercond.*, 24(3), 2014.

[266] B. Bordini, L. Bottura, L. Oberli, L. Rossi, and E. Takala. Impact of the Residual Resistivity Ratio on the Nb_3Sn stability of magnets. *IEEE Trans. Appl. Supercond.*, 22(3), 2012.

[267] M. Brown, C. Tarantini, W. Starch, W. Oates, P. J. Lee, and D. C. Larbalestier. Correlation of filaments distortion and RRR degradation in drawn and rolled PIT and RRP Nb_3Sn wires. *Supercond. Sci. Technol.*, 29(8), 2016.

[268] D. Turrioni, E. Barzi, M. Bossert, V. V. Kashikhin, A. Kikuchi, R. Yamada, and A. V. Zlobin. Study of effects of deformation in Nb_3Sn multifilamentary strands. *IEEE Trans. Appl. Supercond.*, 17(2), 2007.

[269] B. Bordini, A. Ballarino, M. Macchini, D. Richter, B. Sailer, M. Thoener, and K. Schlenga. The bundle-barrier PIT wire developed for the Hilumi LHC project. *IEEE Trans. Appl. Supercond.*, 27(4), 2017.

[270] B. Howlett. Method of fabricating a composite superconductor, patent US 3728165, 1973.

[271] A. R. Kaufman and J. J. Pickett. The deviatoric strain description of the critical properties of Nb_3Sn conductors. *Bull. Am. Phys. Soc.*, 15(833), 1970.

[272] B. Jakob and G. Pasztor. Effect of transverse compressive stress on the critical current of cabled Nb_3Sn conductor. *IEEE Trans. on Magn.*, 25(2), 1989.

[273] B. Jakob, G. Pasztor, M. Bona, and A. Asner. Reduced sensitivity of Nb_3Sn epoxy-impregnated cable to transverse stress. *Cryogenics*, 31(5), 1991.

[274] N. Andreev, E. Barzi, E. Borissov, L. Elementi, V. S. Kashikhin, V. Lombardo, A. Rusy, D. Turrioni, R. Yamada, and A. V. Zlobin. Development of Rutherford-type cables for high field accelerator magnets at Fermilab. *IEEE Trans. Appl. Supercond.*, 17(2), 2007.

[275] G. P. Willering, A. P. Verweij, C. Scheuerlein, A. den Ouden, and H. H. J. ten Kate. Difference in stability between edge and center in a Rutherford cable. *IEEE Trans. Appl. Supercond.*, 18(2), 2008.

[276] G. Pasztor, A. Anghel, B. Jakob, and R. Wesche. Transverse stress effects in Nb_3Sn cables. *IEEE Trans. on Magn.*, 3(4), 1994.

[277] W. K. McDonald, C. W. Curtis, R. M. Scanlan, D. C. Larbalestier, K. Marken, and D. B. Smathers. Manufacture and evaluation of Nb_3Sn conductors fabricated by the MJR method. *IEEE Trans. Magn.*, MAG-19(3), 1983.

[278] Y. Hashimoto, K. Yoshizaki, and M. Tanaka. Processing and properties of superconducting Nb_3Sn filamentary wires. *Proceedings of the 5th International Cryogenic Engineering Conference, Kyoto, Japan*, p.332, 1974.

[279] D. R. Dietderich, R. M. Scanlan, R. P. Walsh, and J. R. Miller. Critical current of superconducting Rutherford cable in high magnetic fields with transverse pressure. *IEEE Trans. Appl. Supercond.*, 9(2), 1999.

[280] A. den Ouden, S. Wessel, H. ten Kate, G. Kirby, T. Taylor, and N. Siegel. Conductor development for a wire bore 10 T Nb_3Sn model dipole magnet. *IEEE Trans. Appl. Supercond.*, 10(1), 2000.

[281] E. Barzi, T. Wokas, and A. V. Zlobin. Sensitivity of Nb_3Sn Rutherford-type cables to transverse pressure. *IEEE Trans. Appl. Supercond.*, 15(2), 2000.

[282] B. Bordini. Self-field correction in critical current measurements of superconducting wires tested on ITER VAMAS barrels. *CERN Internal Note*, EDMS Nr: 1105765, 2010.

[283] A. Godeke, M. C. Jewell, C. M. Fischer, A. A. Squitieri, P. J. Lee, and D. C. Larbalestier. The upper critical field of filamentary Nb_3Sn conductors. *Journal of Applied Physics*, 97(9), 2005.

[284] A. Godeke, B. ten Haken, H. H. J. ten Kate, and D. C. Larbalestier. A general scaling relation for the critical current density in Nb_3Sn. *Supercond. Sci. Technol.*, 19(10), 2006.

[285] J. Fleiter, A. Bonasia, B. Bordini, and A. Ballarino. Rutherford cable design approach and experience at CERN. https://indico.cern.ch/event/596114/contributions /2409586/, US-EuroCirCol cable meeting, CERN, 2017.

[286] A. Ballarino and L. Bottura. Targets for R&D on Nb_3Sn conductor for High Energy Physics. *IEEE Trans. Appl. Supercond.*, 25(3), 2015.

[287] P. Gao, W.A.J. Wessel, M. Dhallé, S. Otten, A. Kario, J. van Nugteren, G. Kirby, L. Bottura, and H. H. J. ten Kate. Effect of resin impregnation on the transverse-pressure dependence of the critical current in ReBCO Roebel cables. *Supercond. Sci. Technol.*, 32(5), 2019.

[288] A. Kario, A. Kling, S. Otten, W. Goldacker, A. Usoskin, A. Molodyk, N. Long, C. Kovacs, M. Dhalle, P. Gao, G. Kirby, J. van Nugteren, J. Fleiter, L. Bottura, L. Rossi, C. Lorin, T. Lecrevisse, and M. Durante. Coated conductor Roebel cable at magnet applications-past, presence and the future, ASC 2018, Seattle, USA, 2018.

[289] T. Puig. Progress in the development of nanostructured coated conductors through chemical process, 4th workshop on accelerator magnets in HTS, Casa Convalescència, Barcelona, Spain, 2017.

[290] C. Senatore, M. Alessandrini, A. Lucarelli, R. Tediosi, D. Uglietti, and Y. Iwasa. Progresses and challenges in the development of high-field solenoidal magnets based on RE123 coated conductors. *Supercond. Sci. Technol.*, 27(10), 2014.

[291] C. Barth, N. Bagrets, K.-P. Weiss, C. M. Bayer, and T. Bast. Degradation free epoxy impregnation of ReBCO coils and cables. *Supercond. Sci. Technol.*, 26(5), 2013.

[292] N. Bagrets, S. Otten, K.-P. Weiss, A. Kario, and W. Goldacker. Thermal and mechanical properties of advanced impregnation materials for HTS cables and coils. *IOP Conf. Series: Materials Science and Engineering*, 102, 2015.

[293] M. Lao, J. Hecher, M. Sieger, P. Pahlke, M. Bauer, R. Hühne, and M. Eisterer. Planar current anisotropy and field dependence of J_c in coated conductors assessed by scanning hall probe microscopy. *Supercond. Sci. Technol.*, 30(2), 2016.

[294] K. Higashikawa, X. Guo, M. Inoue, Z. Jiang, R. Badcock, N. Long, and T. Kiss. Characterization of critical current distribution in Roebel cable strands based on reel-to-reel scanning hall-probe microscopy. *IEEE Trans. Appl. Supercond.*, 27(4), 2017.

[295] E. Moser, E. Laistler, F. Schmitt, and G. Kontaxis. Ultra-High Field NMR and MRI - The Role of Magnet Technology to Increase Sensitivity and Specificity. *Front. Phys.*, 2017.

[296] C. Senatore, C. Barth, M. Bonura, M. Kulich, and G. Mondonico. Field and temperature scaling of the critical current density in commercial *Re*BCO coated conductors. *Supercond. Sci. Technol.*, 29(1), 2015.

[297] CTD-101G. Cryogenic, alumina filled, anhydride cured epoxy. http://www.ctd-materials.com, Composite Technology Development, 2006.

[298] J. Pelegrin, I. Falorio, E. A. Yong, Y. Yang, A. Kario, W. Goldacker, J. van Nugteren, G. Kirby, L. Bottura, A. Ballarino, and M. M. J. Dhallé. AC loss measurements superconducting composite conductors, Internal presentation, 2016.

[299] Y. Yang, J. Pelegrin, I. Falorio, E. A. Young, A. Kario, W. Goldacker, M. M. J. Dhallé, J. van Nugteren, G. Kirby, L. Bottura, and A. Ballarino. Magnetization losses of Roebel cable samples with 2G YBCO coated conductor strands. *IEEE Trans. Appl. Supercond.*, 26(3), 2016.

Summary

This thesis seeks to expand the understanding of the transverse pressure effects on state-of-the-art Nb_3Sn Rutherford and *Re*BCO Roebel cables for application in accelerator magnets. Various cable samples are exposed to transverse pressure and their critical current is measured at 4.2 K in a perpendicular applied magnetic field of 10 to 10.5 T. For impregnated *Re*BCO Roebel cables, the inter-strand resistance at 4.2 and 77 K, as well as the AC magnetization loss at 4.2 K for different applied magnetic field direction were measured as well.

In view of accelerator upgrades such as the High-Luminosity Large Hadron Collider (HL-LHC) or plans for next-generation machines such as the Future Circular Collider, the magnetic field generated by the dipole magnets needs to be enhanced from the present 8.33 to 11 and to 16 T, respectively. NbTi can no longer deliver these magnetic fields. Instead, the latest Nb_3Sn wire technology, offering a non-copper critical current density in excess of 2500 A/mm^2 at 4.2 K and 12 T, is used to assemble Restacked-Rod-Process (RRP) and Powder-In-Tube (PIT) based Rutherford cables. However, since the electronic properties of Nb_3Sn are strain-sensitive and furthermore the material is mechanically brittle, it is a significant challenge to construct high-field dipole magnets with these advanced conductors. The correspondingly high Lorentz force results in a perpendicular stress level of 120 to 200 MPa that act on the wide face of the Rutherford cables. Such a stress causes a significant reversible reduction and eventually even a permanent degradation of the critical current. This thesis sets out to examine the critical current and the upper critical field of resin-impregnated state-of-the-art RRP and PIT cables in terms of transverse pressure at 4.2 K in a background magnetic field of 10 T. Also possible variation of the critical current and upper critical field due to thermal- and mechanical cycling is investigated. For reference, the magnetic field-dependent critical current of witness wires has been measured as well.

Two epoxy resins, CIBA GEIGY Araldite and CTD-101K, are successfully used for the vacuum impregnation of Nb_3Sn Rutherford cables prepared at CERN. Key-stoned 40-strand PIT-114 cables with wire diameter of 0.7 mm designed for the HL-LHC 11 T dispersion suppression magnets, were impregnated with the CIBA GEIGY Araldite resin. Rectangular 18-strand Short Model Coil (SMC) cables comprising 1 mm diameter RRP-132/169 or PIT-192 strands were impregnated with CTD-101K. The latter epoxy resin is better suited for impregnating large-sized coils due to its substantially longer pot life. Glass sleeve for electrical turn-to-turn insulation causes a decrease of the thermal contraction difference between the resins and the reacted cables.

The measured non-copper critical current density at 4.2 K, 12 T for the RRP and PIT witness strands is 3100 and 2500 A/mm^2, respectively. Critical current degradation due to cabling is found to be negligible. Under transverse pressure, the intrinsic and reversible critical current reduction reaches 10% at 130 and at 70 to 100 MPa for the RRP- and the PIT-type SMC cables, respectively. Irreversible degradation of the critical current for both cable types sets in at a transverse pressure larger than 190 MPa and 90 to 150 MPa, respectively. The RRP cable samples are thus concluded to be more robust than similar PIT cables and are suitable for the construction of high-field dipole magnets. However, the experiments also reveal significant critical current reduction due to stress concentrations when the pressure anvil and the impregnated cable surface are misaligned as little as 0.2°, illustrating that great care is needed to avoid stress concentrations during Nb_3Sn coil assembly.

*Re*BCO Roebel cables represent one of the promising routes towards future accelerators that operate with bending magnetic fields beyond 16 T. The Lorentz force generated in such magnets leads to sizeable transverse pressure on the cables of the order of 100 to 150 MPa in the present 15 to 20 T magnet designs. Contrary to single *Re*BCO coated conductors, bare Roebel cables start to degrade already at 40 MPa due to their uneven surface and corresponding local stress concentrations. Proper vacuum impregnation with a suitable epoxy resin strongly improves the transverse pressure susceptibility of *Re*BCO Roebel cables in the first instance, independent of the tape- and cable layout.

Both CY5538 Araldite with silica filler and CTD-101K with glass-fiber sleeve are found to be suitable for vacuum impregnation of *Re*BCO Roebel cables. Six cable samples with an architecture that is directly relevant for CERN's Feather demonstrator magnets were investigated exposed to a variable transverse pressure at 4.2 K in a perpendicular magnetic field of 10.5 T. Three cables comprise 10 SuperPower strands with a transposition length of 126 mm. Two were impregnated with CY5538 Araldite while the third one is a bare control sample. A further three cables comprise 15 strands of either SuperPower or Bruker tape and feature a relatively long transposition length of 226 mm. One of the SuperPower cables was impregnated with the filled Araldite, the others using CTD-101K.

The measurements show that the critical current of the SuperPower Roebel strands is limited by the local critical current density in the 'crossover' sections, which is 42 kA/mm^2 at 4.2 K and 10.8 T. Compared to these 'crossovers', the critical current density reduction of the straight sections of the SuperPower *Re*BCO Roebel cables is insignificant with an appropriate strand punching and cable assembly process. The critical current density at 4.2 K, 11 T of the Bruker-tape cable is 30% higher than in SuperPower-tape with a similar architecture. Remarkably, no critical current reduction was observed up to transverse pressure levels exceeding 170 MPa in the 10-strand SuperPower cables. In the 15-strand cables, transverse pressure limits as high as ≥400 MPa for the SuperPower tape and 455 MPa for Bruker tape were observed for the first time. These values by far satisfy the design requirements of the presently envisaged 20 T class accelerator demonstrator magnets.

For accelerator magnets, also the dynamic magnetic field quality is a key parameter which is affected by the cable's inter-strand resistance R_a. Therefore, direct transport measurements of inter-strand resistance in impregnated *Re*BCO Roebel cables were carried out at 4.2 and 77 K. These data also constitute essential input for cable simulation models. Various intra-strand contributions to the overall inter-strand resistance value are estimated with a straightforward electrical network model. The measured inter-strand resistances are used to estimate AC coupling losses in different magnetic field orientations. For validation, the AC loss of Roebel cables is also measured at 4.2 K. Three analytical models are used to calculate the hysteresis loss and the results are compared with the measured data.

The average inter-strand resistance of the cable samples impregnated with the unfilled epoxy resin CTD-101K ranges from 3 to 18 $\mu\Omega$ at 77 K and from 1 to 10 $\mu\Omega$ at 4.2 K, respectively. The corresponding contact surface resistivity is estimated at 1 to 20 nΩ m^2 at 77 K and 0.5 to 10 nΩ m^2 at 4.2 K, respectively. The copper to copper interface between the tapes dominates the overall inter-strand resistance between the *Re*BCO layers in the impregnated Roebel cables.

Both analytical estimates and measured data on the CTD-101K impregnated Roebel cable show that the AC coupling loss is lower than the hysteresis loss throughout the investigated measurement range. However, a similar cable impregnated with the alumina-filled resin CTD-101G

showed considerable coupling loss when exposed to magnetic field parallel to the wide cable face of the cable. The AC loss in both cables was also measured in terms of the applied magnetic field angle, using an orthogonal set of pick-up coils to record the in- and out-of-plane components of the magnetization separately. Somewhat surprisingly, the loss at intermediate magnetic field angles can be predicted quite well by considering the perpendicular and parallel components of the applied magnetic field separately and by taking the sum of the corresponding losses.

Samenvatting (Summary in Dutch)

Het werk in dit proefschrift streeft een beter begrip na van het effect van transversale druk op de meest recente supergeleidende Nb_3Sn-Rutherford en *Re*BCO-Roebel kabels voor versnellermagneten. Voor dit onderzoek zijn verschillende testkabels transversaal onder druk gezet en is hun kritieke stroom gemeten bij 4,2 K in een loodrecht magneetveld van 10,0 tot 10,5 T. Van de geïmpregneerde *Re*BCO Roebel kabels is ook de elektrische weerstand tussen individuele draden gemeten bij 4,2 en 77 K, alsook de AC-magnetisatieverliezen bij 4,2 K in verschillende veld oriëntaties.

Het opwaarderen van bestaande deeltjesversnellers, zoals de 'High-Luminosity Large Hadron Collider' (HL-LHC); of nieuwe versnellers die op de tekentafel liggen, zoals de 'Future Circular Collider' (FCC), vereist een fikse verhoging van het magneetveld in de dipoolmagneten, van de huidige 8,33 T naar 11 T (HL-LHC) en zelfs 16 T (FCC). NbTi-supergeleiders kunnen zulke hoge velden niet leveren. In plaats daarvan worden de nieuwste generatie Nb_3Sn draden gebruikt, met kritieke stroomdichtheden van 2500 A/mm^2 in een magneetveld van 12 T. Deze supergeleidende draden worden geproduceerd met het 'Restacked-Rod-Process' (RRP), of met de 'Powder-In-Tube' methode (PIT) en worden dan tot Rutherford kabels geslagen. De elektrische eigenschappen van Nb_3Sn variëren sterk wanneer het materiaal vervormd wordt en bovendien is Nb_3Sn bros. Dit maakt het uitdagend om met deze kabels hoog-veld dipoolmagneten te maken. De Lorentzkrachten in de geplande magneten resulteren in een mechanische druk van 120 tot 200 MPa loodrecht op de brede zijde van de Rutherford kabels. Deze druk veroorzaakt eerst een omkeerbare afname en later een permanente degradatie van de kritieke stroom. Dit proefschrift draagt bij aan het wetenschappelijke onderzoek om deze afname beter te begrijpen, door de kritieke stroom en het kritieke veld van RRP en PIT kabelmonsters te meten na impregnatie onder vacuüm met epoxyhars als functie van de transversale druk bij 4,2 K en in een achtergrondveld van 10,0 T. Ook de mogelijke invloed van cyclische variatie in temperatuur en druk op de kritieke stroom en het kritieke veld wordt onderzocht. Ter vergelijking is ook de veldafhankelijke kritieke stroom gemeten in onbelaste, maagdelijke draden na dezelfde warmtebehandeling als de kabels.

Om de Nb_3Sn Rutherford kabels met succes te impregneren onder vacuüm gebruikt CERN twee epoxyharsen, CIBA GEIGY Araldite en CTD-101K. De eerste hars is gebruikt in de 40-aderige PIT-114 kabels met een trapeziumvormige doorsnede ('keystoned') en een draaddiameter van 0,7 mm, die ontworpen is voor de HL-LHC 11 T dispersie-onderdrukkin-gsmagneten. De 18-aderige rechthoekige kabels voor de 'Short Model Coil' (SMC), geslagen uit 1 mm dikke RRP-132/169- of PIT-192-draden, zijn geïmpregneerd met CTD-101K. Deze laatste hars is beter geschikt voor het impregneren van grote spoelen vanwege de langere verwerkingstijd in vloeibare toestand. De glasvezelkous die om de kabel wordt geschoven om deze elektrisch te isoleren verkleint het verschil in thermische contractie tussen het hars-glas mengsel en de metallische kabel.

De kritieke stroomdichtheid van de maagdelijke referentiedraden werd bij 4.2 K en 12 T gemeten als 3100 A/mm^2 voor de RRP en 2500 A/mm^2 voor de PIT draden. De afname in kritieke stroom bij het slaan tot een kabel blijkt verwaarloosbaar klein. Onder transversale druk bedraagt de intrinsieke, omkeerbare afname in kritieke stroom 10% bij 130 MPa voor de RRP- en 10% bij 70 tot 100 MPa voor de PIT-SMC kabels. Een onomkeerbare afname van de kritieke stroom treedt op bij een transversale druk boven 190 MPa voor de RRP- en van 90 tot 150 MPa voor de PIT kabels. RRP kabels zijn dus robuster en daarom beter geschikt voor gebruik in

hoogveld-dipoolmagneten. De experimenten tonen echter ook aan dat spanningsconcentraties een significante afname van de kritieke stroom kunnen veroorzaken wanneer het drukblok en het oppervlak van de geïmpregneerde kabel niet goed zijn uitgelijnd. Dit treedt al op bij een hoekafwijking van 0,2°, zodat grote zorg is geboden om te voorkomen dat zulke spanningsconcentraties ook in werkelijke Nb_3Sn spoelen een probleem vormen.

Het gebuik van *Re*BCO Roebel-type kabel is een veelbelovende optie voor toekomstige deeltjesversnellers waarvoor magneetvelden ver boven de 16 T nodig zijn. De Lorentzkracht in zulke magneten leidt tot een transversale druk van 100 tot 150 MPa. In tegenstelling tot enkelvoudige *Re*BCO tapes, degradeert de kritieke stroom van kale, niet met hars geimpregneerde, meeraderige Roebel kabels al bij zo'n 40 MPa omdat het niet perfect vlakke kabel oppervlak lokale spanningsconcentraties op de geleiders veroorzaakt. De tolerantie van *Re*BCO-Roebelkabels voor hoge transversale druk kan echter sterk worden verbeterd door de kabel te impregneren met een passende epoxyhars, onafhankelijk van het ontwerp van de tape en van de kabel.

Zowel CY5538 Araldite gevuld met SiO_2 of Al_2O_3 als CTD-101K met glasvezelkous zijn geschikt voor het vacuüm impregneren van *Re*BCO-Roebel kabels. Zes kabelmonsters van een type dat direct relevant is voor CERN's 'Feather' demonstratiemagneten zijn blootgesteld aan een variabele transversale druk bij 4,2 K in een loodrecht magneetveld van 10,5 T. Drie monsters bestaan uit 10 SuperPower tapes, verkabeld met een spoed van 126 mm. Twee ervan zijn geïmpregneerd met CY5538 Araldite, een derde is een niet-geïmpregneerde referentie kabel. De andere drie monsters van 15-aderige kabels van SuperPower of Bruker tape en hebben een relatief lange spoed van 226 mm. Één van de SuperPower kabels werd geïmpregneerd met Araldite, de andere met CTD-101K.

De gemeten kritieke stroom van de met SuperPower tapes gemaakte kabel wordt begrensd door de plaatselijke kritieke stroomdichtheid daar waar de geleider van de ene naar de andere kant van de kabel springt (42 kA/mm^2 bij 4,2 K en 10,8 T). Vergeleken met deze dwarsstukken is de afname in de kritieke stroomdichtheid van de rechte delen van de SuperPower *Re*BCO-Roebel kabels verwaarloosbaar, mits een correcte pons- en wikkelmethode wordt gevolgd. De kritieke stroomdichtheid bij 4,2 K en 11,0 T van de Bruker-tape kabel is 30% hoger dan die van de SuperPower-tape kabel met een vergelijkbaar ontwerp. De 10-aderige SuperPower kabels laten geen afname zien van de kritieke stroom tot dat de druk hoger is dan 170 MPa. De druk op de 15-aderige kabels kan worden opgevoerd tot 400 MPa (SuperPower) en zelfs 455 MPa (Bruker) voordat de kritieke stroom significant afneemt. Deze waardes overtreffen ruim de eisen aan de geleiders voor toepassing in 20 T versnellermagneten.

De dynamische veldkwaliteit is een belangrijke parameter voor versnellermagneten, die wordt beïnvloed door de elektrische contactweerstand tussen naast elkaar gelegen tapes in de kabel. Daarom werd deze contactweerstand met een directe transportmethode gemeten in geïmpregneerde *Re*BCO-Roebel kabels bij zowel 4,2 als 77 K. De resultaten leveren essentiële gegevens die nodig zijn voor elektromagnetische simulaties van de kabels. De bijdrages van de verschillende lagen in de tape structuur aan de totale weerstand tussen twee naburige *Re*BCO lagen zijn afgeschat met een eenvoudig elektrisch netwerkmodel. De gemeten contactweerstand is ook gebruikt om de koppelverliezen onder invloed van een alternerend magneetveld in verschillende oriëntaties af te schatten. Om het kabelsimulatiemodel te valideren zijn AC-verliezen van Roebel kabels gemeten bij 4,2 K. Ook drie analytische modellen zijn gebruikt om de hysteresever liezen af te schatten en te vergelijken met de meetgegevens.

De gemiddelde contactweerstand in de kabelmonsters geïmpregneerd met CTD-101K varie-ert van 3 tot 18 $\mu\Omega$ bij 77 K en van 1 tot 10 $\mu\Omega$ bij 4,2 K. De bijbehorende contactweerstand wordt geschat op 1 tot 20 nΩm^2 bij 77 K en 0,5 tot 10 nΩm^2 bij 4,2 K. Het koperen buitenoppervlak van de tapes is dominant in de totale contactweerstand tussen de *Re*BCO lagen in geïmpregneerde Roebel kabels.

Zowel de analytische modelvoorspellingen als de meetgegevens van de met CTD-101K geïmpregneerde Roebel kabels tonen aan dat binnen het gemeten bereik, de koppelverliezen lager zijn dan de hystereseverliezen. Een vergelijkbare kabel geïmpregneerd met SiO_2-gevulde CTD-101G toont hogere koppelverliezen wanneer het magneetveld parallel staat aan het brede kabeloppervlak. AC-verliezen in beide kabels zijn ook gemeten als functie van de richting van het aangebrachte magneetveld, waarbij twee magnetisatie-componenten afzonderlijk werden gemeten met een orthogonaal stel oppikspoelen. Verrassend genoeg wordt het verlies bij tussenliggende hoeken redelijk voorspeld door de parallelle en loodrechte componenten van het magneetveld apart te beschouwen en de corresponderende verliezen eenvoudigweg op te tellen.

Acknowledgments

Doing a doctoral is like climbing a mountain, to see a landscape that very few gets to see, you have to overcome various difficulties and obstacles during the journey. It was a great challenge for me, and fortunately, I have met the most amazing people who taught me courage, patience, perseverance, gratitude and how I can be positive, but also think carefully before taking any action and enjoy the little luxury in life. When I look back at the 6.5 years of study of life I spent in the Energy, Materials and Systems (EMS) group at the University of Twente, with no doubt, the dissertation has been a team work with a large effort and encouragement of many people who have earned my sincere gratitude.

First and foremost, I would like to express my deepest gratitude to my daily supervisor, Dr. Marc Dhallé, for offering me the opportunity to be a visitor in the EMS group for the first two years (Oct. 2012 to Oct. 2014) and to pursue my Ph.D. research for the last 4.5 years, to lead me in the correct direction at the start of my research, stimulating me to broaden my knowledge on applied superconductivity and to do much more than necessary by encouraging and showing patience throughout my research work, and by sharing with me his valuable experience in life and academic research. I would also like to extend my deepest gratitude to my promotor, Prof. Herman ten Kate, for providing valuable advice and suggestions for my research, and for the constructive criticism I have received on my dissertation. Thanks to Herman's patient guidance, I was able to gradually improve my writing skills. The dissertation would not have been possible in a relatively short time without your extraordinary support. Also thank you for your intimate concern when I was struggling with writing in a stressful time. I'm also very grateful to my co-supervisor, Dr. Anna Kario, who left no stone unturned to help me improving my articles and dissertation, providing me tremendous support on the corrections of my journal papers. The two papers would not have been published in such a short time without your substantial effort. They are the best examples for me in my future life.

I would like thank Prof. Marcel ter Brake for the invaluable help in accomplishing my training and professionalization. I have been fortunate to have the chance to spend a few years of my life in research on applied superconductivity in your group, and it is one of the most important memories of my whole life.

I am also grateful to Dr. Srinivas Vanapalli for giving me all the useful advice on writing skills and research, as well as on life. Your flashes of humor impressed me a lot and I feel so happy to work with you in the EMS group. I would also like to thank Dr. Arend Nijhuis for unconditionally sharing of knowledge and ideas about the experiments and data analysis using analytical models. I also wish to thank Dr. Chao Zhou for providing me great opportunities to work with him on the strain effect of various superconductors, teaching me the method of using the U-spring setup. I learned quite a lot from the adequate communications that we had.

I am grateful to my excolleagues Dr. Nir Tzabar, Dr. Tiemo Winkler and Dr. Michiel van Limbeek for the encouragement, support and sensible suggestions during my research and paper writing. I would also like to thank Dr. Jeroen van Nugteren for the fruitful discussions on the AC loss of impregnated *Re*BCO Roebel cables, and the extensive sharing of knowledge about the HTS demonstrator dipole magnet when I visited CERN in 2016. I must also thank Dr. Konstantyn Yagotintsev, Dr. Simon Otten, Dr. Tim Mulder, as working together with you in the lab was a pleasant experience for me. There is always much to gain from communicating with you. Tim, I also enjoyed the mountaineering experience we gained in France after the

EUCAS-2017 conference.

I would like to thank my colleagues Sander Wessel and Eric Krooshoop for their solid technical support and solutions to the various problems with the experiments during my research. In particular, I am grateful to Sander for the substantial help I received in the lab, because I would undoubtedly not have repaired the damaged superconducting transformer in two weeks without your patience and guidance. I also very much appreciate your timely assistance in measuring the DS-RRP Nb_3Sn Rutherford cables, when I struggled with my dissertation.

I would also like to thank my colleagues Ruben Lubkemann and Cris Vermeer, for offering a lot of help in measuring the critical current and Residual Resistance Ratio (RRR) of Nb_3Sn witness strands. During the lab work we also had a lot of fun making jokes, discussing cultural differences and sharing traveling experiences. I am really happy to have worked with you in the lab and it will be a permanent memory to me.

My thanks go to Wilco van de Camp, Bas van Nugteren and Hidde Norder. Wilco, thanks for the extensive help with the transverse pressure measurements at the start of my research. Bas and Hidde, it was my pleasure to work with you on AC loss and inter-strand resistance measurements on impregnated *Re*BCO Roebel cables.

My thanks go to Jaap Kosse and Nando Tolboom for their substantial help in printing my dissertation and translating the summary. Jaap, we had a lot of fun when you visited Chengdu in 2014. I feel really guilty that I did not spend all of my time to guide you and thank you for your understanding. I also have to thank you for providing me important support in my COMSOL modelling work, sharing knowledge and ideas with me. Nando, you are such a humorous friend who always made me happy. I love the time we have worked together over a lot of weekends and thank you for giving so much help in life trivia.

I very much appreciate our secretary, Mrs. Ans Veenstra, for the enormous support I have received in handling my VISA, the reimbursement of conference expenses and many other warming help. I would also like to thank Sahil Jagga, Anne Bergen, Anvar Valiyaparambil and Jianfeng Huang, for the enjoyable leisure time in the social corner. I am especially grateful to Anne for organizing so many activities for the whole group, which gave us much more opportunities to understand each other.

Working in the EMS group was a wonderful experience because of all the friendly members. Here I would like to thank Harry, Izak, Tommaso, Jeroen, Concalo, Koen, Thomas, Michel, Ruben, Baby, Pieter, Rick, Sohrab, Bas, Rik, Teun, Jasper, Jaric, Fabrice and Abhishek for the fruitful discussions during the fortnightly colloquium and the unforgettable group excursion.

Regarding the close collaboration with CERN, I would like to thank Dr. Bernardo Bordini, Dr. Glyn Kirby and Dr. Sandra Tavares for offering the test samples and sharing the knowledge on superconducting cables, as well as the method of using CTD-101K for vacuum impregnation.

Special thanks go to my master supervisors Prof. Yong Zhao and Dr. Xinsheng Yang of the Superconductivity R&D Center at Southwest Jiaotong University. Thanks to their consistent support that I have had the opportunity to study abroad, as well as the many useful suggestions regarding my career.

In addition to my research life, the friends I met in Enschede made my daily life much more colorful. My gratitude goes to Haishan Cao, Yingzhe Wu, Li Liu, Xiaokui Zhang, Zhou Lu,

Yan Cheng, Dongfang Liu, Lin Lin, Wanshu Zhang, Ye Wei, Wei Fang, Michel Temming, Luman Zhan, Zhao Wang, Lantian Chang, Ying Du, Yin Tao, Bingxi Xue, Jun Wang, Yongdi Feng, Weian Wang, Feng Qiu, Jin Kou, Miao Tian, Youwen Fan, Yong Fang and many others. We had a lot of fun during the 6.5 years in the Netherlands, especially the time we spent in Macandra will be an unforgettable memory in my life. I send my greetings and blessings to you and your family, wishing you all a bright future.

Finally, I would like to thank my parents and parents-in-law, as well as my younger brother for all their love, encouragement, selfless contribution and understanding in difficult times in my doctoral journey. The completion of my dissertation would not have been possible without your unconditional support. Last but not least, I am very grateful to my wife Zunyu Huang for her unconditional love, encouragement and patience. I am so happy that you are part of my life, without you consistently taking care of our little family, I am pretty sure I would not have made it. I love you all.